



ALMA MATER STUDIORUM  
UNIVERSITÀ DI BOLOGNA

**DOTTORATO DI RICERCA IN**  
**Biologia Cellulare e Molecolare**

Ciclo XXXVI

**Settore Concorsuale:** 05/A2 – Fisiologia Vegetale

**Settore Scientifico Disciplinare:** BIO/04 – Fisiologia Vegetale

STUDY OF PHOTOSYNTHETIC AND STRESS-RELATED ENZYMES:  
FROM FUNCTIONAL CHARACTERIZATION TO PHYSIOLOGICAL ROLES

**Presentata da:** Dr.ssa Maria Meloni

**Coordinatore Dottorato**

Prof. Vincenzo Scarlato

**Supervisore**

Prof. Paolo Trost

**Co-supervisor**

Prof. Mirko Zaffagnini

Dr. Pierre Crozet

Esame finale anno 2024



## Abstract

As we all know, climate change poses new challenges, particularly concerning our ability to cultivate plants for food, feed, and energy in adverse environmental circumstances. In this context, a major issue regards the productivity of agricultural crops. On the one hand, plant productivity depends on plant capacity to accumulate biomass, and on the other hand, it relies on their ability to cope with both biotic and abiotic stress conditions. The thorough understanding of the molecular mechanisms underlying plant physiology is a key step in laying the foundation for future improvement.

This thesis work focuses on the study of five enzymes involved in carbon metabolism. Three of them, namely glyceraldehyde 3-phosphate dehydrogenase (GAPDH), ribulose-5-phosphate-3-epimerase (RPE) and phosphoribulokinase (PRK) participate in the Calvin-Benson-Bassham cycle, the metabolic pathway ensuring the major input of carbon into the organic world and closely influencing the planet's primary productivity. The other two enzymes, namely alcohol dehydrogenase (ADH) and nitrosogluthathione reductase (GSNOR) are involved in plant adaptation to stress conditions. Specifically, ADH is directly implicated in acclimation to oxygen deficiency, while GSNOR serves as a key regulator of intracellular levels of nitrosogluthathione, a critical signalling molecule involved in stress response.

The approach here employed integrates multidisciplinary analyses focused on the structural and biochemical characterization of recombinant enzymes, with a special emphasis on the investigation of potential cysteine-based regulatory mechanisms. Alongside, *in vivo* and *ex vivo* analyses have offered insights into the elucidation of the role of these enzymes in their physiological context.

# Table of contents

<b>INTRODUCTION</b> .....	<b>1</b>
<b>PART I</b> .....	<b>1</b>
1. CARBON: THE MOLECULE AT THE BASE OF OUR BIOSPHERE .....	1
2. THE OXYGENIC PHOTOSYNTHESIS.....	2
2.1. <i>The photochemical phase</i> .....	2
2.2. <i>The metabolic phase</i> .....	4
3. THE MAIN REDOX REGULATORY SYSTEMS OF CBB CYCLE .....	6
3.1. <i>Cysteines and their role in redox regulation</i> .....	7
3.2. <i>The ferredoxin-thioredoxin system</i> .....	7
3.3. <i>The GAPDH-CP12-PRK complex</i> .....	9
3.4. <i>Proteomic approaches revealed other relevant redox PTMs</i> .....	10
4. FOCUS ON THREE CBB CYCLE ENZYMES .....	10
4.1. <i>Glyceraldehyde-3-phosphate dehydrogenase</i> .....	10
4.2. <i>Ribulose-5-phosphate 3-epimerase</i> .....	12
4.3. <i>Phosphoribulokinase</i> .....	14
5. PHOTOSYNTHESIS AND CROP YIELD .....	16
<b>PART II</b> .....	<b>18</b>
6. PLANTS AND STRESS: THE ROLE OF TWO FUNDAMENTAL ENZYMES BELONGING TO THE SUPERFAMILY OF ALCOHOL DEHYDROGENASES 18	
6.1. <i>ADH and its role in oxygen deprivation conditions</i> .....	21
6.2. <i>GSNOR as a key controller of intracellular GSNO levels</i> .....	24
REFERENCES .....	26
<b>CHAPTER I: “STRUCTURAL SNAPSHOTS OF NITROSOGLUTATHIONE BINDING AND REACTIVITY UNDERLYING S-NITROSYLATION OF PHOTOSYNTHETIC GAPDH”</b> .....	<b>34</b>
SUMMARY .....	35
RESULTS .....	37
<i>Comparing CrGAPA sequence with plastidial GAPDHs from photosynthetic organisms</i> .....	37
<i>Domain organization, cofactor-binding, and catalytic sites of CrGAPA</i> .....	39
<i>CrGAPA specifically undergoes S-nitrosylation in the presence of GSNO</i> .....	42
<i>Structural analysis of GSNO-CrGAPA interactions by molecular dynamics</i> .....	45
<i>Structural snapshots of the GSNO-dependent S-nitrosylation of CrGAPA</i> .....	47
DISCUSSION .....	48
MATERIAL AND METHODS .....	53
<i>Chemicals and enzymes</i> .....	53
<i>Crystallization and data collection</i> .....	53
<i>Structure solution and refinement</i> .....	54
<i>Activity assay</i> .....	54
<i>Treatment of CrGAPA with GSNO</i> .....	54
<i>MALDI-TOF (matrix-assisted laser-desorption ionization-time-of-flight) mass spectrometry</i> .....	55
<i>Molecular dynamics simulations</i> .....	55
<i>Quantum mechanical/molecular mechanical calculations</i> .....	56
<i>Accession numbers</i> .....	56
REFERENCES .....	57
<b>CHAPTER II: “CHARACTERIZATION OF CHLOROPLAST RIBULOSE-5-PHOSPHATE-3-EPIMERASE FROM THE MICROALGA CHLAMYDOMONAS REINHARDTII”</b> .....	<b>63</b>
SUMMARY .....	64
RESULTS .....	65
<i>Quaternary structure of recombinant and native CrRPE1</i> .....	65

<i>CrRPE1 folds as an <math>\alpha_8\beta_8</math> triose-phosphate isomerase (TIM) barrel</i> .....	66
<i>CrRPE1 packs as a trimer of dimers</i> .....	67
<i>CrRPE1 is a metal-containing protein with a conserved catalytic pocket</i> .....	68
<i>Kinetic analysis of CrRPE1 in the epimerization of Ru5P to Xu5P</i> .....	69
<i>Kinetic properties of CrRPE1 catalyzing the conversion of Xu5P to Ru5P</i> .....	72
<i>CrRPE1 displays a limited intrinsic instability and redox sensitivity to reducing agents</i> .....	73
<i>Redox response of CrRPE1 to oxidative treatments</i> .....	73
<i>Post-translational phosphorylation sites</i> .....	75
DISCUSSION .....	76
MATERIALS AND METHODS.....	79
<i>Cloning and protein preparation</i> .....	79
<i>Analytical size-exclusion chromatography</i> .....	79
<i>Small angle X-rays scattering</i> .....	80
<i>Crystallization, structure determination and model refinement</i> .....	80
<i>Circular dichroism spectroscopy</i> .....	81
<i>In vitro reporter assays of CrRPE1 activity</i> .....	81
<i>Protein stability and redox sensitivity</i> .....	82
<i>Metal stability and requirement</i> .....	83
<i>Extraction of algal proteins</i> .....	83
<i>Western blot</i> .....	83
<i>Replicates and statistical analyses</i> .....	84
<i>Accession Numbers</i> .....	84
REFERENCES .....	85
<b>CHAPTER III: “PHOSPHORIBULOKINASE ABUNDANCE IS NOT LIMITING THE CALVIN-BENSON-BASSHAM CYCLE IN CHLAMYDOMONAS REINHARDTII”</b> .....	<b>89</b>
SUMMARY .....	90
RESULTS .....	92
<i>The absence of PRK impacts the growth of Chlamydomonas</i> .....	92
<i>Overexpression of PRK does not affect cell growth</i> .....	94
DISCUSSION .....	97
MATERIALS AND METHODS.....	99
<i>Strains, media and growth conditions</i> .....	99
<i>Plasmid construction</i> .....	99
<i>Chlamydomonas transformation</i> .....	100
<i>Chlamydomonas genotyping</i> .....	100
<i>Protein extraction</i> .....	100
<i>Western blot</i> .....	101
<i>Spot tests</i> .....	101
<i>Growth analysis in photobioreactor</i> .....	101
<i>Enzymatic activity</i> .....	101
REFERENCES .....	103
<b>CHAPTER IV: “STRUCTURAL AND BIOCHEMICAL CHARACTERIZATION OF ARABIDOPSIS ALCOHOL DEHYDROGENASES REVEALS DISTINCT FUNCTIONAL PROPERTIES BUT SIMILAR REDOX SENSITIVITY”</b> .....	<b>107</b>
SUMMARY .....	108
RESULTS .....	110
<i>Arabidopsis ADH1 and GSNOR share a similar fold with identical domain organization</i> .....	110
<i>Structural and catalytic zinc ions in Arabidopsis ADHs</i> .....	112
<i>Structural comparison of ADH1 and GSNOR in apo- and holo-forms</i> .....	113
<i>ADH1 and GSNOR exhibit non-redundant catalytic properties</i> .....	116
<i>Catalytic activity of ADH1 and GSNOR with long-chain alcohols</i> .....	117
<i>Cysteine conservation, accessibility, and reactivity in Arabidopsis ADHs</i> .....	118
.....	120

<i>Arabidopsis ADH1 and GSNOR are both sensitive to the thiol-modifying agent MMTS</i> .....	121
<i>H<sub>2</sub>O<sub>2</sub>-induced oxidation causes irreversible inhibition of ADH1 and GSNOR</i> .....	121
DISCUSSION .....	124
MATERIALS AND METHODS .....	127
<i>Cloning, expression, and purification of A. thaliana ADH1 and GSNOR</i> .....	127
<i>Activity assays</i> .....	127
<i>DTNB-based thiol titration</i> .....	128
<i>Cysteine-modifying treatments</i> .....	128
<i>Zinc ion quantification</i> .....	128
<i>Turbidity measurements</i> .....	129
<i>Protein crystallization and data collection</i> .....	129
<i>Structure solution and refinement</i> .....	129
<i>Structure analysis</i> .....	130
<i>Circular dichroism analysis</i> .....	130
<i>Replicates and statistical analyses</i> .....	131
REFERENCES .....	132
<b>CHAPTER V: “IN-DEPTH DISSECTION OF BIOCHEMICAL FEATURES OF ALCOHOL DEHYDROGENASE FROM ARABIDOPSIS THALIANA AND RELATED PHYSIOLOGICAL INSIGHTS”</b> .....	<b>137</b>
SUMMARY .....	138
RESULTS .....	139
<i>Biochemical analyses of ADH identify NADH-dependent acetaldehyde reduction as the catalytically favored reaction</i> .....	139
<i>Computational analysis displays thermodynamic differences in the propensity of MeCHO/EtOH to bind the catalytic pocket of ADH</i> .....	143
<i>Ex-vivo analysis confirm the hypoxic ADH induction and identify the NADH-dependent MeCHO reduction as the prominent ADH-related activity</i> .....	145
<i>Identification of a new MeCHO detoxification system based on the reductive power of NADPH</i> .....	148
DISCUSSION .....	152
MATERIALS AND METHODS .....	154
<i>Expression and purification of recombinant AtADH</i> .....	154
<i>Activity measurements</i> .....	155
<i>Determination of kinetic parameters</i> .....	155
<i>Thermodynamic calculations</i> .....	155
<i>Growth of Arabidopsis seedlings</i> .....	156
<i>Protein extracts</i> .....	156
<i>Ex vivo activity measurements</i> .....	156
<i>Immunodetection analyses</i> .....	157
<i>Replicates and statistical analyses</i> .....	157
<b>CONCLUSIONS</b> .....	<b>166</b>

## Introduction

\*This section is based on the following published works:

Meloni M. et al., “**Ribulose-1,5-bisphosphate regeneration in the Calvin-Benson-Bassham cycle: Focus on the last three enzymatic steps that allow the formation of Rubisco substrate.**” *Frontiers in plant science* vol. 14 1130430. 16 Feb. 2023, doi:10.3389/fpls.2023.1130430;

Meloni M. et al., “**Characterization of chloroplast ribulose-5-phosphate-3-epimerase from the microalga *Chlamydomonas reinhardtii*.**” *Plant physiology* vol. 194,4 29 Mar. 2024, 2263-2277. doi:10.1093/plphys/kiad680;

Meloni M. et al., “**Structural and biochemical characterization of Arabidopsis alcohol dehydrogenases reveals distinct functional properties but similar redox sensitivity.**” *The Plant journal*, 10.1111/tpj.16651. 2 Feb. 2024, doi:10.1111/tpj.16651.

### Part I

#### 1. Carbon: the molecule at the base of our biosphere

Carbon is a molecule whose versatility has no equals. Having four valence electrons, it can form up to four covalent bonds at once. These covalent bonds can be single, double or triple, broadening the possibility of construction of different molecules. In addition, carbon has a strong tendency to bind to other carbon atoms, forming long chains differently organized in the space (*i.e.*, linear, circular, branched). These crucial characteristics make it the molecule at the base of our biosphere.

Autotrophic organisms are responsible for the entry of inorganic carbon into the biosphere, underlying all trophic chains, thereby being termed “primary producers”. In fact, they can assimilate carbon from inorganic sources such as CH<sub>4</sub> and CO<sub>2</sub>, providing the building blocks for carbohydrates and other organic compounds. Heterotrophic organisms, instead, can only rely on organic sources and are therefore termed “consumers”.

Primary producers are categorized into two major groups: photoautotrophs and chemoautotrophs. They differ on the base of the energy source used to form organic molecules, a process that requires the formation of chemical bonds against the chemical equilibrium. In fact, photoautotrophs use the

energy of light (*i.e.*, electromagnetic radiation) in the process of photosynthesis, while chemoautotrophic organisms use the energy entrapped in inorganic compounds.

This work will be focused on oxygenic photosynthesis carried out by eukaryotic photoautotrophs. Oxygenic photosynthesis emerged when water has started to be used as electron donor, leading to the release of molecular oxygen in the atmosphere as a by-product. Such incredible event happened approximately 2.4 billion years ago, completely changing the features of life on Earth as it was before.

## 2. The Oxygenic Photosynthesis

Among the photosynthetic strategies, oxygenic photosynthesis represents the dominant one. In photosynthetic eukaryotes it takes place in devoted organelles called chloroplasts. Chloroplasts are limited by an envelope composed of two membranes, separating the cytoplasm from the internal compartment, called *stroma*. Inside the stroma, another membrane system forms structures called thylakoids, encapsulating a second compartment, the *lumen*.

At the level of thylakoid membranes, the energy of light is used to move water-derived electrons through the membrane in the so-called photosynthetic electron transport (PET), with the simultaneous generation of a proton gradient ( $\Delta\text{pH}$ ) across the membrane used as electrochemical energy source for the synthesis of ATP. This process constitutes the light phase or photochemical phase of photosynthesis and gathers reducing power in form of NADPH and energy in form of ATP. NADPH and ATP are subsequently used in the metabolic phase of photosynthesis, also called Calvin-Benson-Bassham (CBB) cycle, where a series of enzymatic reactions in the stroma incorporate inorganic  $\text{CO}_2$  into organic 3-carbon sugars. The fine tuning and reciprocal balance of the light and metabolic phases are fundamental for optimal photosynthetic output and for the redox homeostasis of the cell.

For this reason, many regulatory mechanisms are involved, as will be discussed in Paragraph 3.

### 2.1. The photochemical phase

In the first phase of photosynthesis, protein complexes (Oxygen Evolving Complex, Photosystem II, Cytochrome b6f complex, Photosystem I and ATP synthase) and several metallo-organic cofactors act concertedly for the transport through the thylakoidal membrane of the electrons and protons derived from photo-oxidation of water. This whole process leads to the conversion of electromagnetic energy into chemical energy.

Photosystems are structures composed of pigments and proteins embedded in the thylakoidal membrane. They are composed of two fundamental functional parts: the antenna complex (Light

Harvesting Complex, LHC) and the reaction centers (RC), which dynamically interact according to environmental conditions. The main function of LHCs is to collect light energy through photosynthetic pigments and to transfer it to the RCs. Here, a couple of special chlorophylls carry out the photochemical reaction, whereby the collected energy is used to release the excited electrons that will take part in the PET. The reconfiguration of light-harvesting apparatus (*i.e.*, state transition) in response to changing light conditions maximizes the efficiency of light-harvesting, adjusting the distribution of excitation energy between photosystem I and photosystem II.

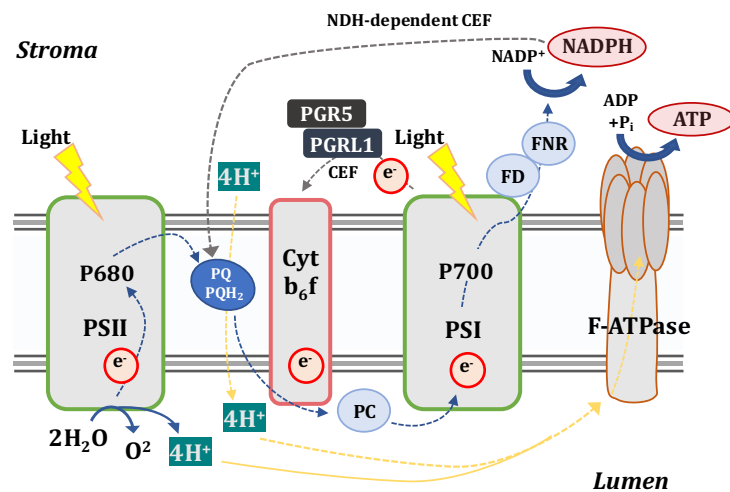


**Figure 1:** Linear electron flow (LEF) and cyclic electron flow (CEF). Abbreviations: PSII, photosystem II; PQ, oxidized plastoquinone; PQH<sub>2</sub>, reduced plastoquinone; Cyt b<sub>6</sub>f, cytochrome b<sub>6</sub>f; PC, plastocyanin; PSI, photosystem; Fd, ferredoxin; FNR, ferredoxin-NADP<sup>+</sup> reductase; PGR5, proton gradient regulation5; PGRL1, PGR5-like protein1; NDH, NAD(P)H dehydrogenase like complex.

The RCs of the two photosystems are called P680 and P700, differing functionally according to their ability to optimally absorb photons at two different wavelengths (680 nm and 700 nm, respectively). The first photochemical reaction occurs in photosystem II (**Figure 1**). Here a network of chlorophyll pigments collects light energy that will be addressed through dipole-dipole interactions (Förster resonance energy transfer, FRET) to the reaction center P680. The excitation energy is employed by the special chlorophyll couple for charge separation, releasing an electron (P680\* → P680<sup>+</sup> + e<sup>-</sup>) (M. P. Johnson, 2016). The generated positive charge on P680<sup>+</sup> is neutralized with another electron provided by water through the OEC. Concomitantly, the excited electron is transferred across the PSII through a series of cofactors. Once reached the plastoquinone (PQ), excited electrons are piped into the so-called Q-cycle, where the reduction and the oxidation of plastoquinone/plastoquinol is carried out by the cytochrome b<sub>6</sub>f complex. From here, electrons move from the copper-containing protein plastocyanin (PC) located in the luminal side of the thylakoid, to photosystem I. At this stage

the electromagnetic energy collected by the system of pigments of PSI induces the translocation of the electrons from the reaction center P700 to ferredoxin (FD) located in the stroma, on the opposite side of the thylakoidal membrane. From FD, electrons are transferred to  $\text{NADP}^+$  through ferredoxin-NADPH reductase (FNR), eventually gathering NADPH.

Along with the PET, protons are pumped across the membrane from the stroma towards the lumen, generating an electro-chemical potential that will be exploited by the ATP synthase to produce ATP through phosphorylation of ADP.

This electron transfer pathway is called linear electron flow (LEF) and generates 2 molecules of NADPH and 2.57 ATP molecules every 4 electrons transferred (Seelert et al., 2000). However, in particular environmental conditions or developmental stages, electrons can be re-routed from FD to the PQ via the PROTON GRADIENT REGULATION5 (PGR5) and PGR5-LIKE PROTEIN1 (PGRL1) proteins (Munekage et al., 2002) or through the NAD(P)H dehydrogenase-like (NDH) complex (Ifuku et al., 2011), in a process called cycling electron flow (CEF) (Suorsa, 2015) (**Figure 1**). As a result of CEF, the transmembrane electrochemical potential is generated, leading to the production of only ATP without concomitant reduction of  $\text{NADP}^+$ , thus increasing the ATP/NADPH ratio.

## *2.2. The metabolic phase*

The CBB cycle enables the fixation of atmospheric carbon dioxide ( $\text{CO}_2$ ) and thus plays a key role in plant metabolism by providing metabolic intermediates for starch and sucrose biosynthesis (Ruan, 2014; Pfister and Zeeman, 2016). On a systemic level, it represents one of the most crucial metabolic processes in the world, fixing most of the carbon in most of the biomass on Earth (Mcfarlane, 2019).

At its core, the CBB cycle involves a series of enzymatic reactions that in photosynthetic eukaryotic organisms take place in the stroma of plant cells. These reactions can be broadly categorized into three main phases: carbon fixation, reduction, and regeneration of ribulose-1,5-bisphosphate (RuBP).



the enzyme phosphoglycerate kinase (PGK) consumes ATP to phosphorylate 3PGA into 1,3-bisphosphoglycerate (1,3-BPGA). Subsequently, 1,3-BPGA is reduced by the enzyme glyceraldehyde-3-phosphate dehydrogenase (GAPDH) using NADPH as electron donor, yielding G3P.

RuBP regeneration phase of the cycle is carried out by eight enzymes catalyzing intersecting reaction paths. In particular, five enzymes function cooperatively to transform the G3P into two types of 5-carbon sugars, namely xylulose-5-phosphate (Xu5P) and ribose-5-phosphate (R5P). Following this step, the regeneration phase leads to the formation of ribulose-5-phosphate (Ru5P) through separated reactions catalyzed by ribulose-5-phosphate epimerase (RPE) and ribose-5-phosphate isomerase (RPI). Finally, the last step involves the enzyme phosphoribulokinase (PRK) which catalyzes the ATP-dependent conversion of Ru5P into RuBP, the substrate for Rubisco.

Based on the functional features of the enzyme, the Rubisco-dependent carboxylation reaction is considered a limiting step in the cycle as a whole (Andralojc et al., 2018). In fact, as opposed to its critical importance, Rubisco is a rather inefficient enzyme due to slow turnover rate and low substrate specificity. In particular, Rubisco catalyzes a side-reaction using atmospheric O<sub>2</sub> as a substrate instead of CO<sub>2</sub>, leading to the production of 2-phosphoglycolate (2-PG) which is metabolized with critical consume of ATP in a process called photorespiration.

However, recent modelling studies and experimental evidence have highlighted that in some conditions the efficiency of the CBB cycle is co-limited by the regeneration of the Rubisco substrate (*i.e.*, RuBP) (Andralojc et al., 2018; Raines, 2022).

### **3. The main redox regulatory systems of CBB cycle**

Photosynthesis works under constantly changing environmental conditions due to the sessile nature of land plants, thereby requiring fine regulation. This regulation, influenced by external *stimuli*, intersects with another level of regulation, directed at the fine coordination of the light-dependent phase with the CBB cycle, which is critical for redox homeostasis in the chloroplast.

The molecular strategies involved are multiple, based on redox, allosteric or physico-chemical mechanisms. Here, the regulatory mechanisms inherent to my research will be addressed, mostly regarding redox-based signaling.

### 3.1. Cysteines and their role in redox regulation

Cysteines are critical residues due to the presence of a thiol group in their side chain providing high functional versatility. In fact, they can mediate the formation of intra and inter-molecular disulfide bonds, essential for the stabilization of tertiary and quaternary structures. Moreover, cysteines are also crucial components of catalytic sites and are often involved in the stabilization of metal ions (e.g., zinc or copper ions). Finally, they are involved in fundamental regulatory mechanisms based on their ability to be target of redox-mediated post translational modifications (PTMs). Dithiol-disulfide exchange represents one of the most physiologically relevant PTM and is regulated by a class of oxidoreductases called thioredoxins (TRXs).

In the last decades, other redox modification involving reactive molecular species (RMS) started to emerge as important regulatory mechanisms of enzyme function, as will be discussed in following paragraphs.

### 3.2. The ferredoxin-thioredoxin system

The first regulatory process of photosynthesis was discovered in the 60s, when several enzymes of the CBB cycle were found to be regulated by light. This mechanism, called ferredoxin/thioredoxin (FD/TRX) system (Buchanan, 1991; Buchanan et al., 2002), permits the fine-tuning of the two phases of photosynthesis according to the redox state of the chloroplast, which in turn is influenced by many environmental constrains, *in primis* by light availability.

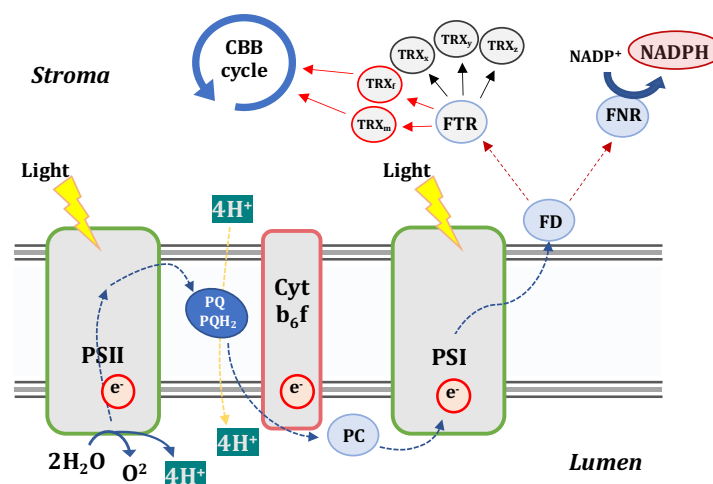


**Figure 3:** Electron flow reducing the thioredoxin pool. From ferredoxin (FD), electrons can reach ferredoxin-NADPH reductase (FNR) or ferredoxin-thioredoxin reductase (FTR). FTR can reduce the thioredoxin (TRX) pool. TRX<sub>m</sub> and TRX<sub>f</sub> isoforms reside in the chloroplast and mediate the regulation of CBB cycle.

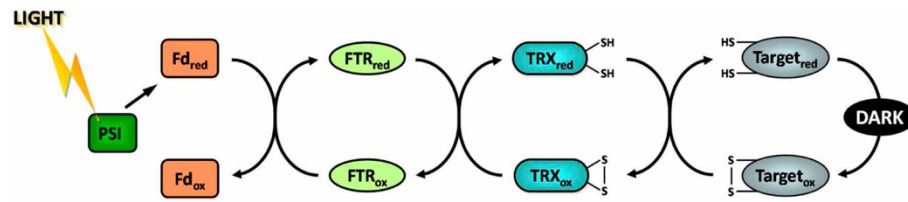


**Figure 4.:** The ferredoxin/thioredoxin system. *Fd*, ferredoxin; *FTR*, ferredoxin thioredoxin reductase; *PSI*, photosystem I; *ox*, oxidized; *red*, reduced. Adapted from Michelet et al., 2013.

This system is composed of three stromal proteins: ferredoxin (FD), ferredoxin/thioredoxin reductase (FTR) and thioredoxin (TRX) (**Figure 3**). TRXs are ubiquitous small thiol oxidoreductases, containing a canonical WCGPC active site responsible for dithiol-disulfide exchanges in target proteins. Typically, TRX targets are oxidized in the dark and reduced in the light. In most cases, the reduction of regulatory disulfide bonds on target proteins leads to the transition from low active to fully active state.

Under light conditions, electrons coming from PSI reduce FD, which represents a metabolic crossroad due to its ability to distribute electron(s) to several biosynthetic and regulatory pathways according to the specific metabolic requirements (Knaff, 1996; Winkler et al., 2010). Under optimal light conditions, most of the electron flux is directed from FD towards the ferredoxin/NADPH reductase (FNR), serving to the production of NADPH required by the CBB cycle. However, part of the electron flux reduces the metalloenzyme FTR which represents the hub between FD and the chloroplast TRX pool. In fact, FTR mediates the electron transfer from FD to TRX disulfide through its [4Fe-4S] cluster, thereby converting the light signal entrusted in the electron flux, into a thiol-dependent biochemical signal. Once reduced, TRX reduces regulatory disulfide on specific target proteins, thereby tuning their activity (**Figure 4**). Land plants possess five main types of chloroplast TRXs (*TRX<sub>f</sub>*, *TRX<sub>m</sub>*, *TRX<sub>x</sub>*, *TRX<sub>y</sub>*, *TRX<sub>z</sub>*), each of them usually containing several isoforms. The diversity of the TRX pool permits highly specific responses influencing many metabolic processes, from carbon fixation to redox homeostasis and antioxidant responses. Most of the CBB cycle enzymes are targeted by *TRX<sub>f</sub>* and *TRX<sub>m</sub>* types, where the former is the most effective.

The enzymes of the CBB cycle targeted by the Fd/TRX system, whose molecular regulatory mechanism is well defined, are five: the two kinases PRK and PGK, the two phosphatases fructose-1,5-bisphosphatase (FBPase) and sedoheptulose-1,7-bisphosphatase (SBPase), and the dehydrogenase GAPDH (Gurrieri et al., 2019; Gütle et al., 2016; Michelet et al., 2013). However, proteomic approaches in several photosynthetic organisms identified all the CBB cycle enzymes as

putative targets of TRXs, although the functional role of this interactions still remains to be explored (Zaffagnini et al., 2019 ARS review).

### 3.3. The GAPDH-CP12-PRK complex

As already mentioned, redox switches can influence target catalysis and interactions with other macromolecules. An established CBB cycle regulatory mechanism influenced by the redox state of the TRX pool, is the formation of a supramolecular complex between the enzymes GAPDH, PRK and the regulatory protein CP12 (**Figure 5**).

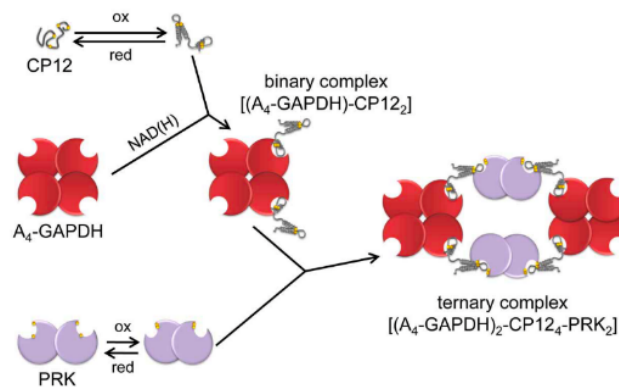


**Figure 5:** Schematic representation of the assembly of the GAPDH<sub>2</sub>-CP12<sub>4</sub>-PRK<sub>2</sub> supramolecular complex induced by oxidizing conditions. Adapted from Michelet et al, 2013.

CP12 is a protein found in almost all the organisms with a CBB cycle, with no defined structural organization under native conditions and therefore defined as a conditionally disordered protein. It contains two pairs of cysteine residues at C- and N-termini, able to perform dithiol-disulfide exchanges (Marri et al., 2008). The formation of the C-terminal disulfide bond stabilizes a local structural motif allowing the interaction with GAPDH (Fermani et al., 2012). This interaction is stabilized only when GAPDH is bound to NAD(H) instead of NADP(H) and leads to the folding of the N-terminus into a stable two-helix bundle (Gurrieri et al., 2021). The CP12-GAPDH interaction represents the first step of the hierarchical assembly of the ternary complex with PRK, where the final organization of the complex consists of two GAPDH tetramers and two PRK dimers linked by four oxidized CP12s (**Figure 5**). The atomic structures of the complex were recently obtained from the cyanobacterium *Thermosynechococcus elongatus* (Mcfarlane, 2019) and from the land plant *Arabidopsis thaliana* (Yu et al., 2020). In the ternary complex, GAPDH and PRK catalysis are highly

inhibited, since CP12 blocks 100% of PRK and 50% of GAPDH active sites, interfering with coenzyme binding in the remaining GAPDH subunits (Gurrieri et al., 2021).

The redox state of the TRX pool and the ratio of tris-phosphorylated (NADP<sup>+</sup> and NADPH) over bis-phosphorylated pyridine nucleotides (NAD<sup>+</sup> and NADH) are the main factors controlling the stability of the complex. These variables are in turn influenced by light/dark or stress conditions, therefore the assembly of the ternary complex represents a link between regulation of CBB cycle enzymes and environmental constrains (Zaffagnini et al., 2019).

### ***3.4. Proteomic approaches revealed other relevant redox PTMs***

In the last decades, several proteomic studies revealed all the CBB cycle enzymes as target of multiple redox PTMs. Besides TRX-dependent thiol switches, S-glutathionylation and S-nitrosylation are two redox PTMs that were found to act as possible regulatory mechanisms of CBB cycle enzymes (Morisse et al., 2014; Zaffagnini et al., 2012). S-glutathionylation consists in the formation of a mixed disulfide between a molecule of glutathione (GSH) and a thiol group of protein cysteines. S-nitrosylation, on the other hand, consists in the formation of a nitrosothiol (-SNO) between NO and a redox-reactive protein cysteine. Both modifications are induced by the perturbation of the redox homeostasis consisting in over-production of reactive molecular species, particularly hydrogen peroxide (H<sub>2</sub>O<sub>2</sub>) and nitric oxide (NO). A recent study employing *Chlamydomonas* as a model organism conducted a comparative analysis among different types of redox PTM, revealing a strong overlap between putative targets of TRXs and S-glutathionylation/S-nitrosylation, hinting at the fact that multiple redox modifications can occur on the same protein (Pérez-Pérez et al., 2017). To this regard, the concept of redox signaling network has recently emerged, indicating the possible crosstalk between different thiol-switching mechanisms leading to highly specific physiological responses. However, the understanding of the redox network that possibly regulates the CBB cycle is far from being conclusive, thereby requiring further investigation.

## **4. Focus on three CBB cycle enzymes**

### ***4.1. Glyceraldehyde-3-phosphate dehydrogenase***

GAPDH is a ubiquitous enzyme that participates in the glycolytic pathway and in photosynthetic organisms also works in the reductive step of the CBB cycle. Plants typically contain four types of genes (*gapA*, *gapB*, *gapC*, and *gapCp*) encoding the different GAPDH isoforms. The products of *gapA* and *gapB* genes give rise to NADP(H)/NAD(H)-dependent A<sub>2</sub>B<sub>2</sub>- and A<sub>4</sub>-GAPDH

photosynthetic isozymes, while *gapC* and *gapCp* encode for the NAD(H)-dependent GAPC and GAPCp glycolytic isoforms.

Concerning photosynthetic GAPDH, land plants mostly contain the AB-containing isoform (Howard, Lloyd, & Raines, 2011; Scagliarini, Trost, Pupillo, & Valenti, 1993), while green algae, red algae and cyanobacteria only contain the A<sub>4</sub>-GAPDH (Petersen et al., 2006).

The reaction accomplished by the photosynthetic isozymes consists in the reduction of the organic acid bisphosphoglycerate (BPGA) using NADPH as electron donor and yielding the sugar G3P, the main output product of the CBB cycle. Contrary to A<sub>4</sub>-GAPDH, whose TRX-mediated regulation occurs exclusively through the ternary GAPDH-CP12-PRK complex, AB-GAPDH can be autonomously regulated through its C-terminal extension (CTE). In fact, the oxidation of a cysteine pair located in the CTE along with the substitution of NADP(H) with NAD(H) in the cofactor binding domain permits the reversible inactivation of AB-GAPDH. This type of regulation is accompanied by a change in the oligomerization state of the enzyme, which leads to the assembly of multiple multimeric assemblies, in particular the A<sub>8</sub>B<sub>8</sub> complex. Oligomeric AB-GAPDH has low activity and accumulates in chloroplasts in the dark (Scagliarini et al., 1993; Baalman et al., 1994).

TRX-mediated reduction of the CTE or the presence of ligands such as NADP(H), ATP, or BPGA allow the recovery of protein activity by reducing the regulatory disulfide or restoring the tetrameric folding, respectively (Trost et al., 2006). The tridimensional structure of GAPDH is known and well conserved in all GAPDH isoforms, having an active tetrameric organization (**Figure 6**). In photosynthetic GAPDH, each subunit contains a catalytic domain binding the substrate and a cofactor-binding domain that accommodates either NAD(H) or NADP(H).

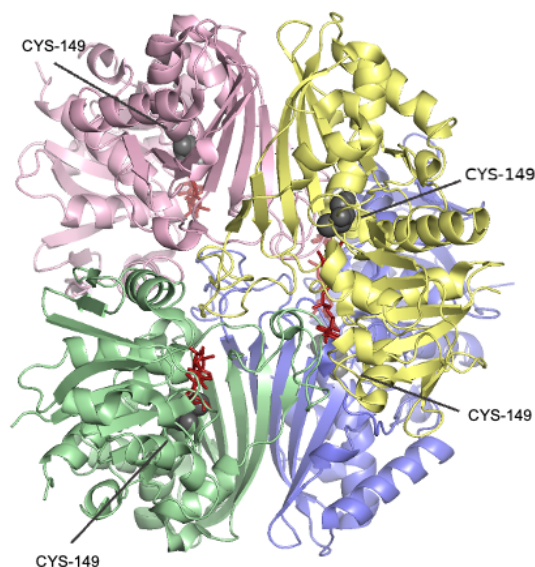


**Figure 6:** Crystal structure of photosynthetic A4 isoform glyceraldehyde-3-phosphate dehydrogenase from *Arabidopsis thaliana* complexed with NAD (PDB code: 3K2B). The four monomers are represented with different colors (yellow, pink, green, lilac). The catalytic cysteine (CYS 149) are highlighted in dark grey dots. NAD is represented as red sticks. Figure generated with Pymol (The PyMOL Molecular Graphics System, Schrödinger, LLC).

The active site harbors a reactive cysteine in position 149 (Cys149, *Chlamydomonas* numbering) that mediates the nucleophilic attack on the substrate, therefore being fundamental for GAPDH catalysis. The stabilization of the thiolate form ( $-S^-$ ) of this residue highly enhances its reactivity and is favored by the interaction with the proximal His176. Besides being required for catalysis, the deprotonation of Cys149 makes it sensitive to S-nitrosylation and other redox modifications (e.g., S-glutathionylation, and sulfenic acid formation) (Bedhomme et al., 2012; Holtgreffe et al., 2008; Zaffagnini et al. 2007; Zaffagnini, Fermani, et al., 2016). This makes Cys149 a critical residue for further possible regulatory mechanisms, although experimental validation of these processes has yet to be carried out.

#### **4.2. Ribulose-5-phosphate 3-epimerase**

Enzyme-driven regeneration of RuBP is crucial to sustain Rubisco catalysis and requires epimerization of xylulose-5-phosphate (Xu5P) into ribulose-5-phosphate (Ru5P) at its chiral carbon 3. This reaction is catalyzed by RPE (enzyme class 5.1.3.1), which is generally considered to be a metalloenzyme belonging to the ribulose phosphate binding superfamily (Chen et al., 1998).

Over the last decades, several studies characterized RPE isoforms from different organisms including protozoan parasites, photosynthetic and non-photosynthetic bacteria, yeast, mammals, and land plants, showing rather different structural and functional features. At the biochemical level, the sole enzymatic activity monitored so far is the conversion of Ru5P to Xu5P (*i.e.*, the PPP-type activity) and the corresponding Michaelis-Menten constants ( $K_M$ ) for Ru5P determined for plant and non-plant RPEs revealed large variations, from high to low affinities (0.2-15 mM range) (Kieli et al., 1973; Akana et al., 2006). Similarly, turnover numbers ( $k_{cat}$ ) are highly variable, ranging from  $\sim 0.1$  to  $10^4$   $\text{sec}^{-1}$  (Teige et al., 1998; Chen et al., 1999). Focusing on plant enzymes, the recombinant form of spinach RPE exhibited a  $k_{cat}$  of  $7,100$   $\text{sec}^{-1}$  and a  $K_M$  for Ru5P of  $0.22$  mM (Chen et al., 1998; Chen et al., 1999), whereas the catalytic parameters of RPE purified from spinach leaf chloroplasts were estimated at  $0.138$   $\text{sec}^{-1}$  and  $0.25$  mM for  $k_{cat}$  and  $K_M$ , respectively (Teige et al., 1998). These values reflected a similar affinity for the substrate while turnover numbers deviate by four orders of

magnitude. Consequently, derived catalytic efficiencies ( $k_{\text{cat}}/K_{\text{M}}$ ) strikingly differ from  $3.23 \times 10^7 \text{ M}^{-1} \text{ sec}^{-1}$  for the recombinant enzyme to  $5.53 \times 10^2 \text{ M}^{-1} \text{ sec}^{-1}$  for the native enzyme.

Recent proteomic studies employed *Chlamydomonas* as a model organism to identify protein targets undergoing post-translational modifications such as thiol-based redox modifications and serine-threonine phosphorylations. Redox modifications included S-glutathionylation and S-nitrosylation (Morisse et al., 2014), and thioredoxin-mediated disulfide/dithiol exchange (Pérez-Pérez et al., 2017). Likewise, RPE from *Chlamydomonas* was found to undergo multiple phosphorylations on three sites at residues Ser50, Thr220, and Ser239 (Wang et al., 2014). Nevertheless, the effective modulation of protein activity through post-translational modifications is still to be proven.

To date, structures of 23 RPE orthologs are reported in the Protein Data Bank, among which four from *Homo sapiens* (Liang et al., 2011), one from *Streptococcus pyogenes* (Akana et al., 2006), one from *Plasmodium falciparum* (Caruthers et al., 2006), and one from *Trypanosoma cruzi* (Gonzalez et al., 2017). Three RPE structures were determined from photosynthetic organisms: one from the cyanobacterium *Synechocystis sp.* PCC 6803 (Wise et al., 2004), one cytosolic isoform from *Oryza sativa* (Jelakovic et al., 2003), and one chloroplast isoform from *Solanum tuberosum* solved at 2.3 Å resolution (Kopp et al., 1999) (**Figure 7**). All known RPEs from both plant and non-plant sources fold as an  $\alpha_8\beta_8$  barrel of the triose-phosphate isomerase (TIM-barrel) superfamily. The carboxy-end of the eight parallel  $\beta$ -strands in the barrel defines a shallow surface onto which a metal ion is chelated by a conserved tetrad of two aspartates and two histidines. Xu5P and Ru5P substrate ligands are typically accommodated in the vicinity of the metal site where reversible epimerization is catalyzed. The identity of the metal was determined for RPE from *Escherichia coli* (Sobota and Imlay, 2011) and attributed to iron II ( $\text{Fe}^{2+}$ ), while other structural data locate a zinc ion at this position (Jelakovic et al., 2003; Wise et al., 2004; Akana et al., 2006). The structural analysis of chloroplast RPE from *Solanum tuberosum* revealed the absence of a metal ion, but instead, a molecule of water was accommodated in the active site center (Kopp et al., 1999). Overall, previous studies show great variance in the determination of enzyme kinetic parameters and metal allocation.

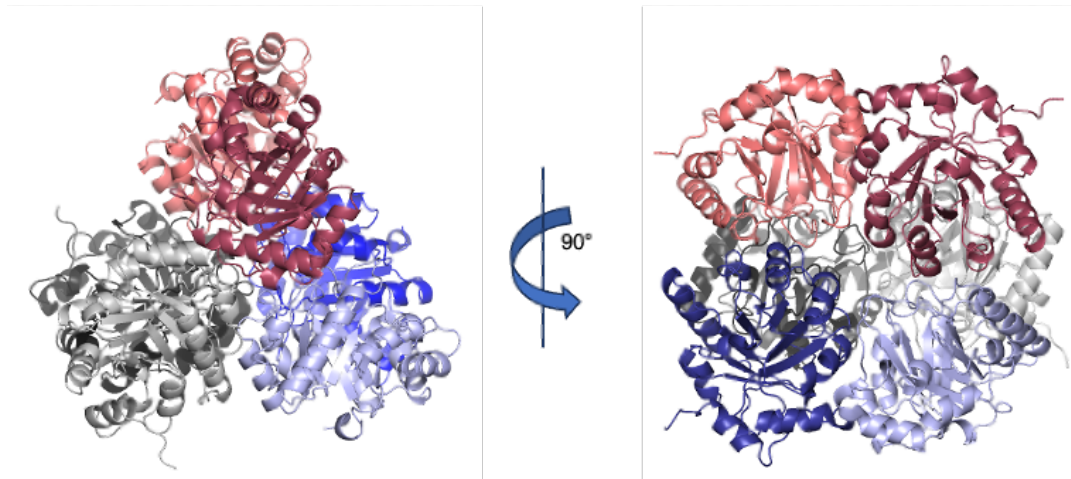


**Figure 7:** Crystal structure of chloroplastic isoform of ribulose-5-phosphate 3-epimerase from *Solanum tuberosum* (PDB code: 1RPX). Two orientations of the homohexamer are shown where each monomer is represented in a different color (blue, lilac, pink, ruby, gray, dark gray). Figure generated with Pymol (The PyMOL Molecular Graphics System, Schrödinger, LLC).

### 4.3. Phosphoribulokinase

PRK (enzyme class 2.7.1.19.) is the enzyme responsible for the catalysis of the last step of CBB cycle, belonging to the subgroup of nucleoside monophosphate (NMP) kinase superfamily characterized by an ATP binding domain. PRK catalyzes the formation of the substrate for Rubisco (*i.e.*, RuBP), consisting in the ATP-dependent phosphorylation of Ru5P which yields RuBP, ADP, and inorganic phosphate.

As already mentioned, PRK is one of the four enzymes of the CBB cycle to be regulated by the TRX system (Michelet et al., 2013; Gurrieri et al., 2021) according to dark/light cycles and to the redox state of the chloroplast. Its activation is preferentially mediated by TRXf (Gurrieri et al., 2019) but TRXz can also fulfil this function, although with lower efficiency (Le Moigne, Gurrieri, et al., 2021). TRX-mediated regulation occurs through dithiol/disulfide exchange reactions involving two conserved cysteine pairs, located in the N- terminal and C-terminal portions of the protein (Cys16-Cys55 and Cys243-Cys249 in CrPRK). Under reducing conditions, TRXs catalyze the reduction of Cys16-Cys55 disulfide, allowing proper binding of ATP and thus triggering catalytic activation of PRK. On the other hand, the formation of Cys16-Cys55 disulfide induced by oxidative conditions blocks the entry of substrates in the active site, although this oxidized PRK form exhibits basal activity (Marri et al., 2005).

In addition, in plants and algae PRK is involved in the formation of a supramolecular regulatory complex with the protein CP12 and the CBB cycle enzyme glyceraldehyde 3-phosphate GAPDH (**Figure 4**) (Pohlmeier et al., 1996; Wedel and Soll, 1998). Whether the redox state of PRK disulfides impacts the complex formation is not yet clear, however the disulfide bond between C-terminal Cys243-Cys249 may fix PRK in a favorable conformation for ternary complex assembly (McFarlane et al., 2019; Yu et al., 2020). In the complex, oxidized CP12 occupies the Ru5P binding site, therefore blocking PRK catalysis (Gurrieri et al., 2021). Besides the established TRX-dependent regulation, PRK activity could be regulated by other type of redox modifications as suggested by proteomic studies along with *in vitro* biochemical analyses involving GSNO and H<sub>2</sub>O<sub>2</sub> as oxidant molecules (Marri et al., 2014). However, the actual redox regulation mediated by these compounds has yet to be explored *in vivo*.

A number of biochemical studies revealed the kinetic parameters of photosynthetic PRK (*i.e.*, cyanobacterial, algal and land plant isoforms). In particular,  $K_m$  for Ru5P has been reported to be in a range from 50 to 270 mM, while the affinity for Mg<sup>2+</sup>-ATP similarly varies from 34 to 280 mM (Anderson, 1973; Hurwitz et al., 1956; Michels et al., 2005; Roesler & Ogren, 1990; Surek et al., 1985; Thieulin-pardo et al., 2015; Wadano et al., 1995). Likewise, specific activities reported for the different plant-type PRKs are comparable, ranging from 218 to 588  $\mu\text{mol min}^{-1} \text{mg}^{-1}$  (Kono et al., 2017; Tabita, 1988).

3D-structures of photosynthetic PRK belonging to *Chlamydomonas* (**Figure 8**), *Arabidopsis*, and *Synechococcus elongatus* are available (Gurrieri et al., 2019; Wilson et al., 2019; Yu et al., 2020). In addition, structures of PRK into the ternary GAPDH-CP12-PRK complex from the cyanobacterium *Thermosynechococcus elongatus* and from *Arabidopsis* have been solved (McFarlane et al., 2019; Yu et al., 2020).

When considering the structural features of PRK, it displays a quaternary organization consisting of a dimer of two identical monomers. The C-terminal portions contain the dimer interface, composed by an extended central mixed  $\beta$ -sheet. The N-terminal regions, located at the edges of the dimer, harbor the active sites, showing the characteristic nucleoside/nucleotide kinase superfamily fold. A flexible structural element called P-loop is present, allowing the proper placement of the  $\gamma$ -phosphate of ATP close to carbon 1 of the sugar substrate, *i.e.*, Ru5P (Yu et al., 2020). ATP binding requests the presence of the nucleoside triphosphate complexed to magnesium ions (Mg<sup>2+</sup>), although other bivalent cations (*e.g.*, Mn<sup>2+</sup> and Ca<sup>2+</sup>) can fulfil its role, at the expense of optimal catalysis (Hurwitz et al., 1956; Marsden & Codd, 1984).

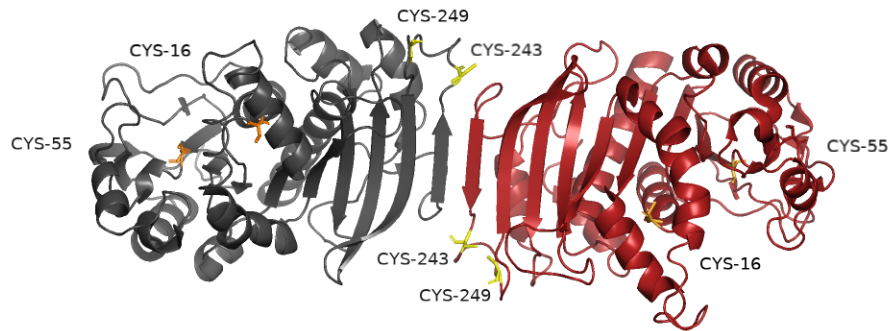


**Figure 8:** Crystal structure of redox-sensitive phosphoribulokinase (PRK) from the green alga *Chlamydomonas reinhardtii* (PDB code: 6H7G). The structure exhibits a dimer, where one monomer is represented in black and the other is represented in ruby. N-terminal (CYS-16 and CYS-55) and C-terminal (CYS-246 and CYS-249) cysteine residues are highlighted in orange and yellow sticks, respectively. Figure generated with Pymol (The PyMOL Molecular Graphics System, Schrödinger, LLC).

## 5. Photosynthesis and crop yield

Over the past 50 years, following the Green Revolution, world population doubled from around 4 billion to 8 billion people today. This massive growth population has been caused primarily by the increase of food supply enabled by advances in agronomic approaches and classical breeding, together with the widespread use of chemical fertilizers, pesticides, and access to controlled irrigation and improved mechanization.

Looking at the future, it has been estimated that by 2050 world population will reach 10 billion people. This growth will get along with a massive increase of need for resources, requiring between a 70% and a 100% increase in the yield of the major food crops (*i.e.*, wheat, rice, soy, potato, maize) (D.Dewbre et al., 2014; Simkin et al., 2019; Tilman & Clark, 2015). However, increase in yields of the major crops has generally plateaued, and the possibility of engaging new arable land is hindered by the need to slow further deforestation and land degradation. Furthermore, approximately one-third of all greenhouse gas emissions are attributed to crop production (Burney et al., 2010), rendering the current agriculture sector highly impactful on climate change.

For all this reason, we as world citizens need a collective effort to reverse this course by questioning our current way of producing and consuming. As a scientific community, we should ask governments to question our current economic system, considering infinite economic growth as not possible to achieve in a world of finite material resources. Along with this, new technological solutions are needed to reduce agriculture's competition with natural resources (*e.g.*, land, water, nutrient inputs).

The maximum yield attainable from a crop in its best adapted variety is called yield potential, which is determined by light availability, light capture, energy conversion and plant architecture (Evans &

Fischer, 1999). Of these constraints, energy conversion, intended as plant's capacity of using the captured light to produce biomass, is the one with highest room for improvement (Long et al., 2006), and is strictly connected to the efficiency of CO<sub>2</sub> assimilation. Over the last decades, many efforts have been made to this regard, focusing on attempts of amelioration of both the photochemical and the metabolic phase of photosynthesis. Many studies demonstrated the possibility of improving CO<sub>2</sub> assimilation through metabolic engineering aimed at the manipulation of the CBB cycle, photorespiration, and photosynthetic electron transport (Simkin et al., 2019). As mentioned before, the CBB cycle is co-limited by the efficiency of Rubisco and the regeneration of RuBP.

Overall, transgenic studies suggested that flux control in the CB cycle, intended as the influence that a single reaction has on the other reactions in the network (Janasch et al., 2019), depends not on a single enzymatic step but is rather shared between all of the CBB cycle enzymes according to the specific environmental conditions and developmental stages (Simkin et al., 2019).

The precise identification of the controlling steps in the flux of CBB cycle would be a pivotal step in the quest for improvement (Raines, 2003)(Boisset et al., 2023), although this achievement is challenging especially when considering the wide range of environmental and biological factors that could influence them.

One powerful tool that would provide a system-wide analysis of metabolic flux control according to a range of many possible variables (*e.g.*, light intensity, CO<sub>2</sub> concentration, influence of other carbon-related pathways) is mathematic modeling. This *in silico* step would be pivotal to address the future biotechnological and metabolic engineering efforts. To this regard, the importance of reliable empirical data must be taken into consideration. In fact, experimental information is crucial for creating accurate and meaningful models, providing the foundation for model validation and predictive power accuracy of the system dynamic behavior (Jablonsky et al., 2011). Basic research aimed at a thorough functional characterization of the CBB cycle enzymes becomes essential to this purpose (Raines, 2022). Once identified the most promising targets by coupling experimental information and modeling, subsequent biotechnological intervention may have the double purpose of modifying protein amount (*i.e.*, genetic up or down-regulation approaches) or acting on the kinetic and regulatory properties of target enzymes.

## Part II

### 6. Plants and stress: the role of two fundamental enzymes belonging to the superfamily of alcohol dehydrogenases

Plants, being sessile organisms, can face stressful situations through a variety of metabolic rearrangements and adaptation strategies activated by complex signaling pathways. How these intricate pathways cross and diverge giving rise to distinct responses still represents a matter of research and debate. One established common event in the stress response appears to be the production of reactive molecular species (RMS) able to work upstream and downstream of other signaling components (Sewelam et al., 2016). In biological systems, the most relevant RMS derive from oxygen (Reactive Oxygen Species, hereafter named ROS) and nitrogen (Reactive Nitrogen Species, hereafter named RNS). Hydrogen peroxide ( $H_2O_2$ ), being the most prevalent, is the ROS with the greater physiological relevance, while nitric oxide ( $\bullet NO$ ) is the prototypical RNS. RMS are passively released as by-products of cell metabolism but can also be transiently synthesized due to their role as signaling molecules. The signaling action is accomplished through their ability to induce redox post-translational modifications (PTMs) in specific target proteins, modulating their activity, localization, or interactions with other biological macromolecules. Redox-based PTMs mainly occur at the level of cysteine residues, considered as the primary sensors of ROS and RNS thanks to the special chemical reactivity and structural flexibility of their sulfur atom. Except for few cases, deprotonated state of cysteines (from thiol,  $-SH$  to thiolate,  $-S^-$ ) is required for the modification to occur (**Figure 9**), as deprotonation greatly enhances cysteine reactivity. The tendency to deprotonation depends mainly on  $pK_a$ , which in turn is influenced by the local protein microenvironment.  $pK_a$  is a thermodynamic parameter denoting the pH at which the populations of thiol- and thiolate-bearing molecules are equal, therefore the lower it is, the higher is the tendency at deprotonation under a specific pH (Poole, 2015). In proteins, the lowering  $pK_a$  is favored by specific hydrogen bond donors and an electropositive local environment which stabilizes the negatively charged thiolate anion. Except for few cases, deprotonated state of cysteines (from thiol,  $-SH$  to thiolate,  $-S^-$ ) is required for the modification to occur (**Figure 9**) greatly enhance cysteine reactivity. Cysteines can mediate the formation of intra and inter-molecular disulfide bonds, thereby being essential for the stabilization of tertiary and quaternary structures. Moreover, they are also crucial components of catalytic sites and are often involved in the stabilization of metal ions such as zinc or copper ions. Being polyfunctional amino acids, reversible changes over cysteine residues can modulate protein functionality, giving rise to regulatory mechanisms.

The main thiol-based redox modifications are dithiol-disulphide exchanges ( $-S-S-$ ), S-nitrosylation ( $-SNO$ ), S-glutathionylation ( $-SSG$ ), S-sulphenylation ( $-SOH$ ), S-sulphinylation ( $-SO_2H$ ), and S-sulphonylation ( $-SO_3H$ ) (Troost et al., 2017) (**Figure 9**).

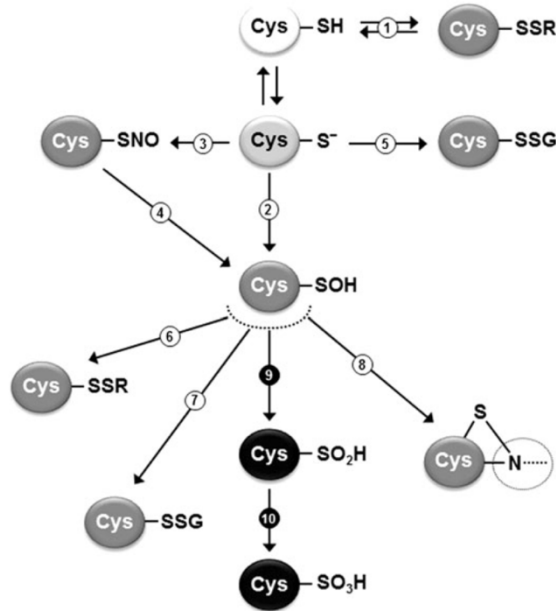


**Figure 9:** Overview of the major redox PTMs of proteins involving cysteines in the thiol ( $-SH$ ), thiolate ( $-S^-$ ), or sulphenylate ( $-SOH$ ) form. Reversible and irreversible redox modifications are indicated with dark-gray and black circles, respectively. Adapted from Troost et al., 2017.

Depending on the target protein and the specific cysteine site, each redox PTM can lead to different effects, rendering significant the plethora of possible outcomes in response to exogenous and endogenous cues, which becomes even more relevant when considering the possible crosstalk between different PTMs.

In plants, many sources for production of ROS have been identified, including non-enzymatic sources such as photosynthesis, photorespiration and respiratory electron transport chains, and enzymatic routes involving NADPH oxidase, amine oxidase, and cell wall-bound peroxidases (Zaffagnini et al., 2019; Mittler, 2002). Contrary to ROS, whose producing mechanisms are well described, there is lack of information regarding the production of NO (Crawford et al., 2006; Zemojtel et al., 2006). Nitrite and nitrate reductase (NIR and NR, respectively) are proposed as the principal systems of production of NO in plants (Morisse et al., 2014; Baudouin, 2011). However recently an oxidative pathway of NO production mediated by peroxidase enzyme has been unveiled in Arabidopsis (López-Gómez et al., 2024). NO and NO-related molecules control a wide range of developmental processes and is

highly involved in stress responses (Del Castello et al., 2019; Neill et al., 2008). In the presence of GSH, NO can lead to the formation of nitrosoglutathione (GSNO), which is considered as the major mobile NO reservoir in the cell due to its chemical stability, and the main agent capable of inducing protein S-nitrosylation. (Morisse et al., 2014). As an important signalling molecule capable of triggering many physiological responses, GSNO concentration must be finely regulated. A pivotal role in the control of cellular GSNO concentration is played by the enzyme S-nitrosoglutathione reductase (GSNOR, enzyme number 1.1.1.284), which catalyzes the degradation/reduction of GSNO using NADH as a source of reducing power. GSNOR, acting as a GSNO scavenging system, indirectly controls the extent of S-nitrosylation in target proteins (Jahnová et al., 2019), thereby influencing the whole downstream signaling cascades.

Concertedly with the fine-tuned accumulation of RMS as signaling molecules, stress situations elicit significant metabolic reorganization as a coping strategy. One intriguing example of this mechanism is the switch from a metabolism based on oxidative phosphorylation as the main source of cellular energy, to a fermentation-based metabolism, which is triggered by hypoxia/anoxia states and other specific stress (*e.g.*, cold, drought, and salt stress). One of the main players in this kind of response is the enzyme alcohol dehydrogenase (ADH, enzyme code 1.1.1.1), which catalyzes in plants the NADH-dependent reduction of acetaldehyde (MeCHO) to ethanol (EtOH) in the process of alcoholic fermentation, thereby concurring in the production of NAD<sup>+</sup> necessary to sustain the glycolytic process (*i.e.*, glyceraldehyde-3-phosphate dehydrogenase-based reaction).

Overall, ADH and GSNOR are crucial enzymes for plant adaptation to stress conditions, both belonging to the protein superfamily called medium-length dehydrogenase/reductases (MDRs) (Persson et al., 2008). ADH and GSNOR are cysteine-rich enzymes, with these residues representing ~4% of total amino acids, a value that is nearly the double of the average content in the proteome of eukaryotic organisms based on UniProt database (The UniProt Consortium, 2021). This abundance of cysteine residues suggests the possibility of a thiol-dependent regulation that could modulate their activity in response to varying physiological conditions. In fact, recent studies revealed ADH/GSNOR as putative targets of S-sulfenylation (Huang et al., 2019b, Wei et al., 2020), S-nitrosylation (Fares et al., 2011, Frungillo et al., 2014, Guerra et al., 2016, Zhan et al., 2018, Zhang et al., 2020), while other redox modifications, such as S-glutathionylation and thioredoxin-mediated dithiol/disulfide interchanges, were found only in the case of ADH (Yamazaki et al., 2004, Dixon et al., 2005).

### 6.1. ADH and its role in oxygen deprivation conditions

The condition where the concentration of oxygen limits aerobic respiration, being in a range between 1% and 5%, is termed hypoxia and represents a stress condition to which plants are often subjected. Acute hypoxia is typically generated by environmental conditions such as flooding, which can lead to waterlogging (submerged roots) or even submergence (submerged roots and aerial parts) of plants. In such conditions, the main cellular responses consist in morpho-physiological modifications (*e.g.*, formation of aerenchyma) and major metabolic rearrangements. In fact, while in aerobic conditions plants account on oxidative phosphorylation as the main strategy to produce energy, upon the establishment of hypoxic conditions the production of ATP is entrusted exclusively to glycolysis coupled with NAD<sup>+</sup> regenerative pathways, which include ethanolic fermentation (**Figure 10**).

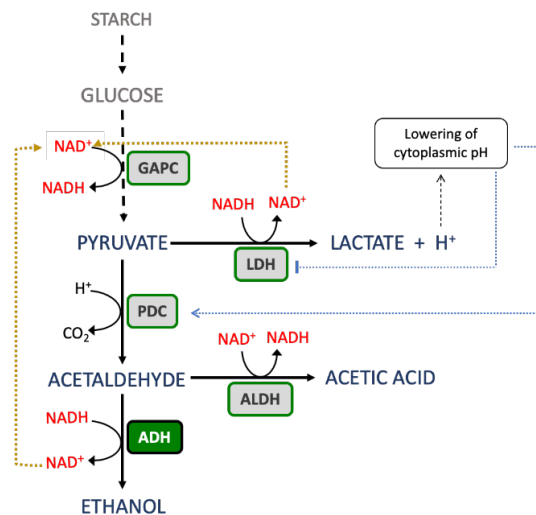


**Figure 10:** Schematic representation of ethanolic and lactic fermentation and their interaction with glycolysis. Abbreviations: GAPC: glycolytic glyceraldehyde-3-phosphate dehydrogenase; LDH: lactate dehydrogenase; ALDH: aldehyde dehydrogenase; PDC: pyruvate decarboxylase; ADH: alcohol dehydrogenase.

Despite this metabolic strategy loses effectiveness (*i.e.*, carbohydrates degradation coupled with glycolysis permits the formation of 2 molecules of ATP, as opposed to the 36 molecules produced through oxidative phosphorylation) (Perata & Alpi, 1993), it is fundamental for the cellular response to this stressful circumstance.

The central node connecting oxygen sensing and downstream responses is represented by a group of transcription factors called hypoxia-associated ethylene response factor group VII (ERF-VII) which respond to a Cys-branch of an N-degron pathway (Licausi et al., 2011). In normoxic conditions, ERF-VIIs are continuously oxidized through the activity of a class of plant enzymes named Plant Cysteine Oxidases (PCOs), triggering a signaling cascade that eventually leads to ERF-VIIs degradation *via* proteasome. Conversely, this mechanism is hindered when the level of oxygen falls, with consequent

stabilization of ERF-VIIs (Pucciariello & Perata, 2017). When stabilized, ERF-VIIs lead to the expression of a cluster of genes called Hypoxia-Responsive Genes (HRGs) (Loreti & Perata, 2020), mainly involved in anaerobic fermentation, saccharose metabolism, control of reactive species and transcriptional control (Gasch et al., 2016). In this context, the fermentative metabolism assumes the important role of restoring the pool of oxidized pyridine nucleotides (*i.e.*,  $\text{NAD}^+$ ) necessary to sustain glycolysis. In particular, lactic fermentation is carried out through the enzyme lactate dehydrogenase (LDH; EC 1.1.1.27), while ethanolic fermentation occurs through the action of two enzymes, namely pyruvate decarboxylase (PDC, EC 4.1.1.1) and ADH (**Figure 10**).

The role of PDC and ADH in oxygen deprivation conditions has been widely demonstrated through genetic evidence in plant species such as maize (J. R. Johnson et al., 1994), rice (Saika et al., 2006) and *Arabidopsis thaliana* (Mithran et al., 2014; Shiao et al., 2002). In *Arabidopsis*, *adh1* null mutants has a lower resistance to hypoxia, whilst its overexpression does not gather a better flooding survival. (Ismond et al., 2003) (**Figure 11**). Moreover, recent experiments on *Arabidopsis* have demonstrated the importance of ADH and PDC for plant growth and development under aerobic conditions, where hypoxic niches are nevertheless maintained (Ventura et al., 2020).

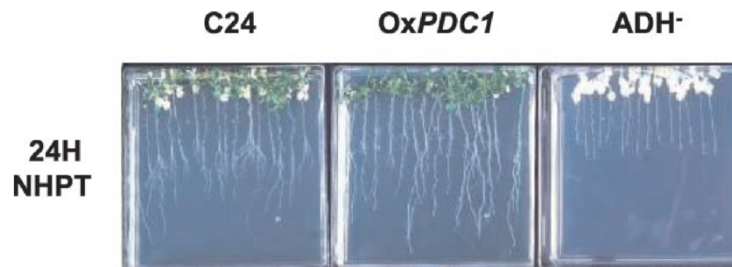


**Figure 11.** Survival assay of *Arabidopsis* seedlings in wild type (C24), PDC overexpressor (*OxPDC1*) and *adh1* mutant (*ADH*<sup>-</sup>) after 24 h of hypoxic treatment with 0.1% [v/v]  $\text{O}_2$  (24H NHPT). Adapted from Ismond et al., 2003.

In the context of ethanolic fermentation, plant ADH catalyzes the  $\text{NADH}$ -dependent conversion of  $\text{MeCHO}$  into  $\text{EtOH}$ , with the dual goal of yielding one molecule of  $\text{NAD}^+$  while detoxifying  $\text{MeCHO}$ . ADH is also able of catalyzing the opposite reaction (*i.e.*, conversion of  $\text{EtOH}$  into  $\text{MeCHO}$ ), which has been the main reaction ascribed to non-plant ADHs investigated so far. It has been hypothesized that the conversion of  $\text{EtOH}$  into  $\text{MeCHO}$  could be physiologically relevant in the conditions where aerobic metabolism is restored after oxygen deprivation, reducing carbon loss by recycling acetaldehyde to eventually produce acetyl-CoA (Thomson & Greenway, 1991).

Recently, it has been shown that the activity of Arabidopsis ADH can be modulated by oxidizing molecules such as  $\text{H}_2\text{O}_2$  and the NO-donor diethylamine NONOate (DEA/NO) (Dumont et al., 2018), suggesting the possible role of cysteine residues in redox-based regulatory mechanisms.

The structural comparison of ADHs has been deeply investigated and many 3D-structures are available in Protein Data Bank, including plant isoforms in the apo (*i.e.*, ligand-free) conformation or complexed with  $\text{NAD}^+$  (**Figure 12**), but lacking the NADH-bound form.

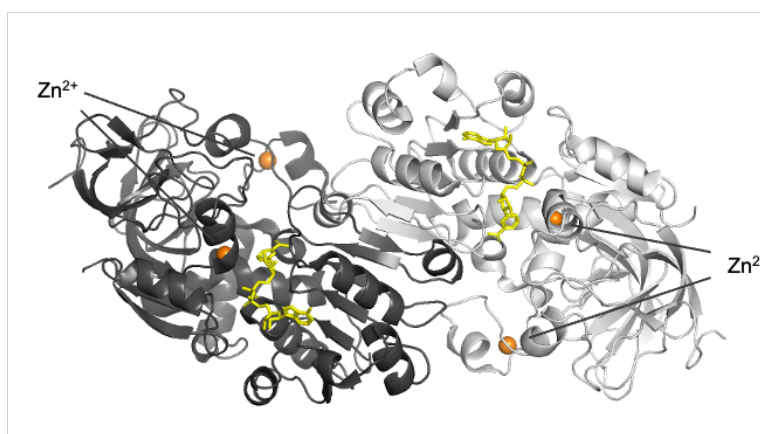


**Figure 12:** crystal structure of Arabidopsis thaliana alcohol Dehydrogenase in complex with  $\text{NAD}^+$  (PDB code: 4RQU). The structure exhibits a dimer, where the two monomers are represented in different colors (black and grey). Zinc ions are represented as orange dots, while NAD as yellow sticks. Figure generated with Pymol (The PyMOL Molecular Graphics System, Schrödinger, LLC).

In general, the active form of ADH is a homodimer where each monomer weights about 40 kDa and contains two domains. The catalytic domain accommodating the substrate is constituted by the N-terminal portion and the C-terminal tail of the protein, while the cofactor binding domain consists of a typical Rossmann Fold and is involved in the oligomerization. Each monomer contains two zinc ions that play a fundamental role in both structure and catalysis. While the structural zinc ion is coordinated by four cysteine residues, the catalytic one is stabilized by two cysteine residues, a histidine, and a water molecule or a glutamate (Strommer, 2011). Analysis of the crystallographic structures of the apo and holo (*i.e.*, complexed to the cofactor) forms of mammalian ADH showed that the binding of cofactors  $\text{NAD}^+$  or NADH causes a conformational change that plays an important role in catalysis (Eklund et al., 1976; Plapp, 2010). Specifically, when one of the two subunits binds the cofactor, it acquires a closed conformation, while the other subunit assumes an open conformation due to the rotation of the catalytic domain, with the apo-form as an intermediate conformation.

## 6.2. GSNOR as a key controller of intracellular GSNO levels

GSNOR belongs to the class-III alcohol dehydrogenase family, highly conserved in most bacteria and all eukaryotes including photosynthetic organisms (Shafqat et al., 1996; Liu et al., 2001). The study of evolutionary patterns suggested that the classical ADHs found in animals and plants has emerged from this enzymatic class (Shafqat et al., 1996).

GSNOR was originally identified as a glutathione-dependent formaldehyde dehydrogenase and then reclassified as an S-(hydroxymethyl)glutathione (HMGSH) dehydrogenase (Liu et al., 2001; Zaffagnini, De Mia, et al., 2016). Lately, it was found to participate in GSNO catabolism through its ability to catalyze the NADH-dependent GSNO reduction yielding N-hydroxysulfinamide (GSNHOH), that in the presence of reduced glutathione (GSH) forms oxidized glutathione (GSSG) and hydroxylamine (Zaffagnini, De Mia, et al., 2016). The pivotal role GSNOR in controlling the intracellular concentration of GSNO has been confirmed through genetic evidence in photosynthetic and non-photosynthetic eukaryotes. Specifically, mouse, yeast, *Arabidopsis thaliana* and *Lotus japonicus* deficient mutants for GSNOR showed increased levels of protein S-nitrosothiols (SNOs) (Feechan et al., 2005; Foster et al., 2009; Liu et al., 2001; Matamoros et al., 2019). In plants, the lack of GSNOR is associated with pleiotropic phenotypes, including lower fertility, impaired growth and thermotolerance defects (Lee et al., 2008), and a compromised activation of defense immune system (Feechan et al., 2005). On the other hand, plants overexpressing GSNOR showed decreased levels of SNO, associated with a higher resistance to H<sub>2</sub>O<sub>2</sub>-triggered leaf cell death (Lin et al., 2012).

Plant GSNOR is a homodimer with subunits of around 40 kDa, each presenting a distal catalytic domain and cofactor-binding domain located at the interface of the two monomers (Kubienová et al., 2013; Tagliani et al., 2021). In human GSNOR, the binary complex with NAD<sup>+</sup> induces a semi-open conformation of the catalytic domain (Sanghani et al., 2000), while in *Solanum lycopersicum* the binding of NADH causes a domain closure (Kubienová et al., 2013). As observed for ADH, two zinc atoms are incorporated in each monomer (**Figure 13**), one having a catalytic role, while the other is thought to have a structural significance (Sanghani et al., 2000). These atoms are coordinated by specific sets of four amino acids, specifically the catalytic zinc binds two cysteines, one histidine, and a glutamate, while the structural atom is stabilized by four cysteines (Kubienová et al., 2013).

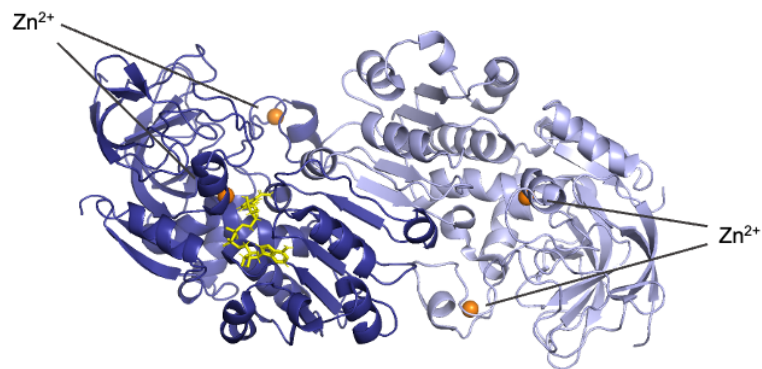


**Figure 13:** Crystal Structure of S-Nitrosoglutathione Reductase from *Arabidopsis thaliana* in complex with NADH (PDB code: 3UKO). The structure exhibits a dimer, where the two monomers are represented in different colors (purple and lilac). Zinc ions are represented as orange dots, while NADH as yellow sticks. Figure generated with Pymol (The PyMOL Molecular Graphics System, Schrödinger, LLC).

Recent studies revealed that the catalytic activity of GSNOR is negatively and reversibly regulated by S-nitrosylation in Arabidopsis, human and budding yeast. This dynamic regulation of GSNOR catalysis is proposed to transiently allow GSNO accumulation and the following NO-dependent signaling cascades. Finally, plant GSNOR resulted to be inhibited by H<sub>2</sub>O<sub>2</sub> (Kovacs et al., 2016; Tichá et al., 2017), providing evidence for crosstalk between ROS and NO signaling.

## References

- Anderson, L. E. (1973). Regulation of pea leaf ribulose-5-phosphate kinase activity. *Biochimica et Biophysica Acta (BBA)-Enzymology*, *321*(2), 484–488.
- App, A. A., & Meiss, A. N. (1958). Effect of aeration on rice alcohol dehydrogenase. *Archives of Biochemistry and Biophysics*, *77*(1), 181–190.
- Baudouin, E. (2011). The language of nitric oxide signalling. *Plant Biology*, *13*(2), 233–242. <https://doi.org/https://doi.org/10.1111/j.1438-8677.2010.00403.x>
- Bedhomme, M., Adamo, M., Marchand, C. H., Couturier, J., Rouhier, N., Lemaire, S. D., Zaffagnini, M., & Trost, P. (2012). Glutathionylation of cytosolic glyceraldehyde-3-phosphate dehydrogenase from the model plant *Arabidopsis thaliana* is reversed by both glutaredoxins and thioredoxins in vitro. *Biochemical Journal*, *445*(3), 337–347.
- Boisset, N. D., Favoino, G., Meloni, M., Jomat, L., Cassier-Chauvat, C., Zaffagnini, M., Lemaire, S. D., & Crozet, P. (2023). Phosphoribulokinase abundance is not limiting the Calvin-Benson-Bassham cycle in *Chlamydomonas reinhardtii*. *Frontiers in Plant Science*, *14*(August), 1–12. <https://doi.org/10.3389/fpls.2023.1230723>
- Buchanan, B. B. (1991). Regulation of CO<sub>2</sub> assimilation in oxygenic photosynthesis: The ferredoxin/thioredoxin system: Perspective on its discovery, present status, and future development. *Archives of Biochemistry and Biophysics*, *288*(1), 1–9. [https://doi.org/https://doi.org/10.1016/0003-9861\(91\)90157-E](https://doi.org/https://doi.org/10.1016/0003-9861(91)90157-E)
- Buchanan, B. B., Schürmann, P., Wolosiuk, R. A., & Jacquot, J.-P. (2002). The ferredoxin/thioredoxin system: from discovery to molecular structures and beyond. *Photosynthesis Research*, *73*(1), 215–222. <https://doi.org/10.1023/A:1020407432008>
- Bui, L. T., Novi, G., Lombardi, L., Iannuzzi, C., Rossi, J., Santaniello, A., Mensuali, A., Corbineau, F., Giuntoli, B., Perata, P., Zaffagnini, M., & Licausi, F. (2019). Conservation of ethanol fermentation and its regulation in land plants. *Journal of Experimental Botany*, *70*(6), 1815–1827. <https://doi.org/10.1093/jxb/erz052>
- Burney, J. A., Davis, S. J., & Lobell, D. B. (2010). Greenhouse gas mitigation by agricultural intensification. *Proceedings of the National Academy of Sciences of the United States of America*, *107*(26), 12052–12057. <https://doi.org/10.1073/pnas.0914216107>
- Crawford, N. M., Galli, M., Tischner, R., Heimer, Y. M., Okamoto, M., & Mack, A. (2006). Response to Zemojtel *<em>et al</em>*: Plant nitric oxide synthase: back to square one. *Trends in Plant Science*, *11*(11), 526–527. <https://doi.org/10.1016/j.tplants.2006.09.007>
- D.Dewbre, C. J., Soglo, Production, F., Cervantes-Godoy, J., PIN, Amegnaglo, Y. Y., Akpa, A. F., Bickel, M., Sanyang, S., Ly, S., Kuiseu, J., Ama, S., Gautier, B. P., Officer, E. S., Officer, E. S., Eberlin, R., Officer, P., Branch, P. A., Oduro-ofori, E., ... Swanson, B. E. (2014). The future of food and agriculture: trends and challenges. In *The future of food and agriculture: trends and challenges* (Vol. 4, Issue 4).
- Del Castello, F., Nejamkin, A., Cassia, R., Correa-Aragunde, N., Fernández, B., Foresi, N., Lombardo, C., Ramirez, L., & Lamattina, L. (2019). The era of nitric oxide in plant biology: Twenty years tying up loose ends. *Nitric Oxide*, *85*, 17–27. <https://doi.org/https://doi.org/10.1016/j.niox.2019.01.013>

- Dennis, E. S., Dolferus, R., Ellis, M., Rahman, M., Wu, Y., Hoeren, F. U., Grover, A., Ismond, K. P., Good, A. G., & Peacock, W. J. (2000). Molecular strategies for improving waterlogging tolerance in plants. *Journal of Experimental Botany*, *51*(342), 89–97. <https://doi.org/10.1093/jexbot/51.342.89>
- Dolferus, R., Jacobs, M., Peacock, W. J., & Dennis, E. S. (1994). Differential interactions of promoter elements in stress responses of the Arabidopsis Adh gene. *Plant Physiology*, *105*(4), 1075–1087. <https://doi.org/10.1104/pp.105.4.1075>
- Dolferus, R., Van Den Bossche, D., & Jacobs, M. (1990). Sequence analysis of two null-mutant alleles of the single Arabidopsis Adh locus. *Molecular and General Genetics MGG*, *224*(2), 297–302. <https://doi.org/10.1007/BF00271565>
- Dumont, S., Bykova, N. V., Khaou, A., Besserour, Y., Dorval, M., & Rivoal, J. (2018). Arabidopsis thaliana alcohol dehydrogenase is differently affected by several redox modifications. *PLoS ONE*, *13*(9). <https://doi.org/10.1371/journal.pone.0204530>
- Eklund, H., Nordström, B., Zeppezauer, E., Söderlund, G., Ohlsson, I., Boiwe, T., Söderberg, B.-O., Tapia, O., Brändén, C.-I., & Åkeson, Å. (1976). Three-dimensional structure of horse liver alcohol dehydrogenase at 2.4 Å resolution. *Journal of Molecular Biology*, *102*(1), 27–59. [https://doi.org/https://doi.org/10.1016/0022-2836\(76\)90072-3](https://doi.org/https://doi.org/10.1016/0022-2836(76)90072-3)
- Evans, L. T., & Fischer, R. A. (1999). Yield Potential: Its Definition, Measurement, and Significance. *Crop Science*, *39*(6), 1544–1551. <https://doi.org/https://doi.org/10.2135/cropsci1999.3961544x>
- Feechan, A., Kwon, E., Yun, B.-W., Wang, Y., Pallas, J. A., & Loake, G. J. (2005). A central role for S-nitrosothiols in plant disease resistance. *Proceedings of the National Academy of Sciences*, *102*(22), 8054–8059. <https://doi.org/10.1073/pnas.0501456102>
- Fermani, S., Trivelli, X., Sparla, F., Thumiger, A., Calvaresi, M., Marri, L., Falini, G., Zerbetto, F., & Trost, P. (2012). Conformational Selection and Folding-upon-binding of Intrinsically Disordered Protein CP12 Regulate Photosynthetic Enzymes Assembly\*. *Journal of Biological Chemistry*, *287*(25), 21372–21383. <https://doi.org/https://doi.org/10.1074/jbc.M112.350355>
- Foster, M. W., Liu, L., Zeng, M., Hess, D. T., & Stamler, J. S. (2009). A Genetic Analysis of Nitrosative Stress. *Biochemistry*, *48*(4), 792–799. <https://doi.org/10.1021/bi801813n>
- Gasch, P., Funding, M., Müller, J. T., Lee, T., Bailey-Serres, J., & Mustroph, A. (2016). Redundant ERF-VII transcription factors bind to an evolutionarily conserved cis-motif to regulate hypoxia-responsive gene expression in arabidopsis. *Plant Cell*. <https://doi.org/10.1105/tpc.15.00866>
- Gurrieri, L., Del, A., Demitri, N., Falini, G., Viorel, N., & Zaffagnini, M. (2019). *Arabidopsis and Chlamydomonas phosphoribulokinase crystal structures complete the redox structural proteome of the Calvin – Benson cycle*. 1–6. <https://doi.org/10.1073/pnas.1820639116>
- Gurrieri, L., Fermani, S., Zaffagnini, M., Sparla, F., & Trost, P. (2021). Calvin–Benson cycle regulation is getting complex. *Trends in Plant Science*, *26*(9), 898–912. <https://doi.org/10.1016/j.tplants.2021.03.008>
- Güttele, D. D., Roret, T., Müller, S. J., Couturier, J., Lemaire, S. D., Hecker, A., Dhalleine, T., Buchanan, B. B., Reski, R., Einsle, O., & Jacquot, J. P. (2016). Chloroplast FBPase and SBPase are thioredoxin-linked enzymes with similar architecture but different evolutionary histories. *Proceedings of the National Academy of Sciences of the United States of America*, *113*(24), 6779–6784. <https://doi.org/10.1073/pnas.1606241113>

- Holtgrefe, S., Gohlke, J., Starmann, J., Druce, S., Klocke, S., Altmann, B., Wojtera, J., Lindermayr, C., & Scheibe, R. (2008). Regulation of plant cytosolic glyceraldehyde 3-phosphate dehydrogenase isoforms by thiol modifications. *Physiologia Plantarum*, *133*(2), 211–228.
- Hurwitz, J., Weissbach, A., Horecker, B. L., & Smyrniotis, P. Z. (1956). Spinach phosphoribulokinase. *Journal of Biological Chemistry*, *218*(2), 769–783.
- Ifuku, K., Endo, T., Shikanai, T., & Aro, E.-M. (2011). Structure of the chloroplast NADH dehydrogenase-like complex: nomenclature for nuclear-encoded subunits. *Plant and Cell Physiology*, *52*(9), 1560–1568.
- Ismond, K. P., Dolferus, R., De Pauw, M., Dennis, E. S., & Good, A. G. (2003). Enhanced low oxygen survival in Arabidopsis through increased metabolic flux in the fermentative pathway. *Plant Physiology*, *132*(3), 1292–1302. <https://doi.org/10.1104/pp.103.022244>
- Jablonsky, J., Bauwe, H., & Wolkenhauer, O. (2011). Modeling the Calvin-Benson cycle. *BMC Systems Biology*, *5*. <https://doi.org/10.1186/1752-0509-5-185>
- Jahnová, J., Luhová, L., & Petřivalský, M. (2019). S-nitrosoglutathione reductase—the master regulator of protein S-nitrosation in plant NO signaling. *Plants*, *8*(2), 48.
- Janasch, M., Asplund-Samuelsson, J., Steuer, R., & Hudson, E. P. (2019). Kinetic modeling of the Calvin cycle identifies flux control and stable metabolomes in Synechocystis carbon fixation. *Journal of Experimental Botany*, *70*(3), 1017–1031. <https://doi.org/10.1093/jxb/ery382>
- Johnson, J. R., Cobb, B. G., & Drew, M. C. (1994). Hypoxic induction of anoxia tolerance in roots of Adh1 null Zea mays L. *Plant Physiology*, *105*(1), 61–67. <https://doi.org/10.1104/pp.105.1.61>
- Johnson, M. P. (2016). Photosynthesis. *Essays in Biochemistry*, *60*(3), 255–273. <https://doi.org/10.1042/EBC20160016>
- Knaff, D. B. (1996). Ferredoxin and ferredoxin-dependent enzymes. In *Oxygenic photosynthesis: the light reactions* (pp. 333–361). Springer.
- Kono, T., Mehrotra, S., Endo, C., Kizu, N., Matusda, M., Kimura, H., Mizohata, E., Inoue, T., Hasunuma, T., Yokota, A., Matsumura, H., & Ashida, H. (2017). A RuBisCO-mediated carbon metabolic pathway in methanogenic archaea. *Nature Communications*, *8*(1), 14007. <https://doi.org/10.1038/ncomms14007>
- Kovacs, I., Holzmeister, C., Wirtz, M., Geerlof, A., Fröhlich, T., Römling, G., Kuruthukulangarakoola, G. T., Linster, E., Hell, R., Arnold, G. J., Durner, J., & Lindermayr, C. (2016). ROS-Mediated Inhibition of S-nitrosoglutathione Reductase Contributes to the Activation of Anti-oxidative Mechanisms . In *Frontiers in Plant Science* (Vol. 7). <https://www.frontiersin.org/articles/10.3389/fpls.2016.01669>
- Kubienová, L., Kopečný, D., Tylichová, M., Briozzo, P., Skopalová, J., Šebela, M., Navrátil, M., Tâche, R., Luhová, L., Barroso, J. B., & Petřivalský, M. (2013). Structural and functional characterization of a plant S-nitrosoglutathione reductase from Solanum lycopersicum. *Biochimie*, *95*(4), 889–902. <https://doi.org/https://doi.org/10.1016/j.biochi.2012.12.009>
- Lee, U., Wie, C., Fernandez, B. O., Feelisch, M., & Vierling, E. (2008). Modulation of Nitrosative Stress by S-Nitrosoglutathione Reductase Is Critical for Thermotolerance and Plant Growth in Arabidopsis . *The Plant Cell*, *20*(3), 786–802. <https://doi.org/10.1105/tpc.107.052647>
- Licausi, F., Kosmacz, M., Weits, D. A., Giuntoli, B., Giorgi, F. M., Voesenek, L. A. C. J., Perata, P., & Van Dongen, J. T. (2011). Oxygen sensing in plants is mediated by an N-end rule pathway for protein destabilization. *Nature*, *479*(7373), 419–422. <https://doi.org/10.1038/nature10536>

- Lin, A., Wang, Y., Tang, J., Xue, P., Li, C., Liu, L., Hu, B., Yang, F., Loake, G. J., & Chu, C. (2012). Nitric Oxide and Protein S-Nitrosylation Are Integral to Hydrogen Peroxide-Induced Leaf Cell Death in Rice. *Plant Physiology*, *158*(1), 451–464. <https://doi.org/10.1104/pp.111.184531>
- Liu, L., Hausladen, A., Zeng, M., Que, L., Heitman, J., & Stamler, J. S. (2001). A metabolic enzyme for S-nitrosothiol conserved from bacteria to humans. *Nature*, *410*(6827), 490–494. <https://doi.org/10.1038/35068596>
- Long, S. P., ZHU, X., Naidu, S. L., & Ort, D. R. (2006). Can improvement in photosynthesis increase crop yields? *Plant, Cell & Environment*, *29*(3), 315–330.
- López-Gómez, P., Buezo, J., Urra, M., Cornejo, A., Esteban, R., de Los Reyes, J. F., Urarte, E., Rodríguez-Dobrevá, E., Chamizo-Ampudia, A., & Eguaras, A. (2024). A new oxidative pathway of nitric oxide production from oximes in plants. *Molecular Plant*, *17*(1), 178–198.
- Loreti, E., & Perata, P. (2020). The Many Facets of Hypoxia in Plants. *Plants*, *9*(6), 745. <https://doi.org/10.3390/plants9060745>
- Marri, L., Trost, P., Trivelli, X., Gonnelli, L., Pupillo, P., & Sparla, F. (2008). Spontaneous assembly of photosynthetic supramolecular complexes as mediated by the intrinsically unstructured protein CP12. *The Journal of Biological Chemistry*, *283*(4), 1831–1838. <https://doi.org/10.1074/jbc.M705650200>
- Marsden, W. J. N., & Codd, G. A. (1984). Purification and molecular and catalytic properties of phosphoribulokinase from the cyanobacterium *Chlorogloeopsis fritschii*. *Microbiology*, *130*(4), 999–1006.
- Matamoros, M., Cutrona, M., Wienkoop, S., Begara Morales, J., Sandal, N., Orera, I., Barroso, J., Stougaard, J., & Becana, M. (2019). Altered Plant and Nodule Development and Protein S-Nitrosylation in *Lotus japonicus* Mutants Deficient in S-Nitrosoglutathione Reductases. *Plant & Cell Physiology*, *61*. <https://doi.org/10.1093/pcp/pcz182>
- Mcfarlane, C. (2019). Structural basis of light-induced redox regulation in the Calvin–Benson cycle in cyanobacteria. *Proceedings of the National Academy of Sciences*, *116*. <https://doi.org/10.1073/pnas.1906722116>
- Meloni, M., Gurrieri, L., Fermani, S., Velie, L., Sparla, F., Crozet, P., Henri, J., & Zaffagnini, M. (2023). Ribulose-1,5-bisphosphate regeneration in the Calvin-Benson-Bassham cycle: Focus on the last three enzymatic steps that allow the formation of Rubisco substrate. *Frontiers in Plant Science*, *14*(February), 1–13. <https://doi.org/10.3389/fpls.2023.1130430>
- Michelet, L., Zaffagnini, M., Morisse, S., Sparla, F., Pérez-Pérez, M. E., Francia, F., Danon, A., Marchand, C. H., Fermani, S., Trost, P., & Lemaire, S. D. (2013). Redox regulation of the Calvin-Benson cycle: Something old, something new. *Frontiers in Plant Science*, *4*(NOV), 1–21. <https://doi.org/10.3389/fpls.2013.00470>
- Michels, A. K., Wedel, N., & Kroth, P. G. (2005). Diatom plastids possess a phosphoribulokinase with an altered regulation and no oxidative pentose phosphate pathway. *Plant Physiology*, *137*(3), 911–920.
- Mithran, M., Paparelli, E., Novi, G., Perata, P., & Loreti, E. (2014). Analysis of the role of the pyruvate decarboxylase gene family in *Arabidopsis thaliana* under low-oxygen conditions. *Plant Biology*, *16*(1), 28–34. <https://doi.org/10.1111/plb.12005>
- Mittler, R. (2002). Oxidative stress, antioxidants and stress tolerance. *Trends in Plant Science*, *7*(9), 405–410. [https://doi.org/10.1016/S1360-1385\(02\)02312-9](https://doi.org/10.1016/S1360-1385(02)02312-9)

- Morisse, S., Zaffagnini, M., Gao, X. H., Lemaire, S. D., & Marchand, C. H. (2014). Insight into protein S-nitrosylation in *Chlamydomonas reinhardtii*. *Antioxidants & Redox Signaling*, *21*(9), 1271–1284. <https://doi.org/10.1089/ars.2013.5632>
- Munekage, Y., Hojo, M., Meurer, J., Endo, T., Tasaka, M., & Shikanai, T. (2002). PGR5 is involved in cyclic electron flow around photosystem I and is essential for photoprotection in *Arabidopsis*. *Cell*, *110*(3), 361–371.
- Neill, S., Barros, R., Bright, J., Desikan, R., Hancock, J., Harrison, J., Morris, P., Ribeiro, D., & Wilson, I. (2008). Nitric oxide, stomatal closure, and abiotic stress. *Journal of Experimental Botany*, *59*(2), 165–176. <https://doi.org/10.1093/jxb/erm293>
- Perata, P., & Alpi, A. (1993). Plant responses to anaerobiosis. *Plant Science*, *93*(1), 1–17. [https://doi.org/https://doi.org/10.1016/0168-9452\(93\)90029-Y](https://doi.org/https://doi.org/10.1016/0168-9452(93)90029-Y)
- Pérez-Pérez, M. E., Mauriès, A., Maes, A., Tourasse, N. J., Hamon, M., Lemaire, S. D., & Marchand, C. H. (2017). The Deep Thioredoxome in *Chlamydomonas reinhardtii*: New Insights into Redox Regulation. *Molecular Plant*, *10*(8), 1107–1125. <https://doi.org/10.1016/j.molp.2017.07.009>
- Persson, B., Hedlund, J., & Jörnvall, H. (2008). Medium- and short-chain dehydrogenase/reductase gene and protein families : the MDR superfamily. *Cellular and Molecular Life Sciences : CMLS*, *65*(24), 3879–3894. <https://doi.org/10.1007/s00018-008-8587-z>
- Plapp, B. V. (2010). Conformational changes and catalysis by alcohol dehydrogenase. *Archives of Biochemistry and Biophysics*, *493*(1), 3–12. <https://doi.org/10.1016/j.abb.2009.07.001>
- Poole, L. B. (2015). The basics of thiols and cysteines in redox biology and chemistry. *Free Radical Biology and Medicine*, *80*, 148–157. <https://doi.org/10.1016/j.freeradbiomed.2014.11.013>
- Pucciariello, C., & Perata, P. (2012). Flooding tolerance in plants. *Plant Stress Physiology*, 148–170.
- Pucciariello, C., & Perata, P. (2017). *New insights into reactive oxygen species and nitric oxide signalling under low oxygen in plants*. 473–482. <https://doi.org/10.1111/pce.12715>
- Raines, C. A. (2003). The Calvin cycle revisited. *Photosynthesis Research*, *75*(1), 1–10. <https://doi.org/10.1023/A:1022421515027>
- Raines, C. A. (2022). Improving plant productivity by re-tuning the regeneration of RuBP in the Calvin–Benson–Bassham cycle. *New Phytologist*, *236*(2), 350–356. <https://doi.org/10.1111/nph.18394>
- Roesler, K. R., & Ogren, W. L. (1990). *Chlamydomonas reinhardtii* phosphoribulokinase: Sequence, purification, and kinetics. *Plant Physiology*, *93*(1), 188–193.
- Saika, H., Matsumura, H., Takano, T., Tsutsumi, N., & Nakazono, M. (2006). A Point Mutation of Adh1 Gene is Involved in the Repression of Coleoptile Elongation under Submergence in Rice. *Breeding Science - BREEDING SCI*, *56*, 69–74. <https://doi.org/10.1270/jsbbs.56.69>
- Sanghani, P. C., Stone, C. L., Ray, B. D., Pindel, E. V., Hurley, T. D., & Bosron, W. F. (2000). Kinetic Mechanism of Human Glutathione-Dependent Formaldehyde Dehydrogenase. *Biochemistry*, *39*(35), 10720–10729. <https://doi.org/10.1021/bi9929711>
- Schwartz, D. (1971). Genetic control of alcohol dehydrogenase—a competition model for regulation of gene action. *Genetics*, *67*(3), 411.
- Seelert, H., Poetsch, A., Dencher, N. A., Engel, A., Stahlberg, H., & Müller, D. J. (2000). Proton-powered turbine of a plant motor . *Nature*, *405*(6785), 418–419. <https://doi.org/10.1038/35013148>

- Sewelam, N., Kazan, K., & Schenk, P. M. (2016). Global plant stress signaling: Reactive oxygen species at the cross-road. *Frontiers in Plant Science*, 7(FEB2016), 1–21. <https://doi.org/10.3389/fpls.2016.00187>
- Shafqat, J., El-Ahmad, M., Danielsson, O., Martínez, M. C., Persson, B., Parés, X., & Jörnvall, H. (1996). Pea formaldehyde-active class III alcohol dehydrogenase: Common derivation of the plant and animal forms but not of the corresponding ethanol-active forms (classes I and P). *Proceedings of the National Academy of Sciences of the United States of America*, 93(11), 5595–5599. <https://doi.org/10.1073/pnas.93.11.5595>
- Shiao, T., Ellis, M. H., Dolferus, R., Dennis, E. S., & Doran, P. M. (2002). Overexpression of alcohol dehydrogenase or pyruvate decarboxylase improves growth of hairy roots at reduced oxygen concentrations. *Biotechnology and Bioengineering*, 77(4), 455–461. <https://doi.org/https://doi.org/10.1002/bit.10147>
- Simkin, A. J., López-Calcagno, P. E., & Raines, C. A. (2019). Feeding the world: Improving photosynthetic efficiency for sustainable crop production. *Journal of Experimental Botany*, 70(4), 1119–1140. <https://doi.org/10.1093/jxb/ery445>
- Smith, E. N., Schwarzländer, M., Ratcliffe, R. G., & Kruger, N. J. (2021). Shining a light on NAD- and NADP-based metabolism in plants. *Trends in Plant Science*, 26(10), 1072–1086. <https://doi.org/https://doi.org/10.1016/j.tplants.2021.06.010>
- Steinbeck, J., Fuchs, P., Negroni, Y. L., Elsässer, M., Lichtenauer, S., Stockdreher, Y., Feitosa-Araujo, E., Kroll, J. B., Niemeier, J. O., Humberg, C., Smith, E. N., Mai, M., Nunes-Nesi, A., Meyer, A. J., Zottini, M., Morgan, B., Wagner, S., & Schwarzländer, M. (2020). In vivo nadh/nad1 biosensing reveals the dynamics of cytosolic redox metabolism in plants. *Plant Cell*, 32(10), 3324–3345. <https://doi.org/10.1105/tpc.20.00241>
- Strommer, J. (2011). The plant ADH gene family. *Plant Journal*, 66(1), 128–142. <https://doi.org/10.1111/j.1365-313X.2010.04458.x>
- Suorsa, M. (2015). Cyclic electron flow provides acclimatory plasticity for the photosynthetic machinery under various environmental conditions and developmental stages . In *Frontiers in Plant Science* (Vol. 6). <https://www.frontiersin.org/articles/10.3389/fpls.2015.00800>
- Surek, B., Heilbronn, A., Austen, A., & Latzko, E. (1985). Purification and characterization of phosphoribulokinase from wheat leaves. *Planta*, 165, 507–512.
- Tabita, F. R. (1988). Molecular and cellular regulation of autotrophic carbon dioxide fixation in microorganisms. *Microbiological Reviews*, 52(2), 155–189.
- Tagliani, A., Rossi, J., Marchand, C. H., De Mia, M., Tedesco, D., Gurrieri, L., Meloni, M., Falini, G., Trost, P., Lemaire, S. D., Fermani, S., & Zaffagnini, M. (2021). Structural and functional insights into nitrosogluthathione reductase from *Chlamydomonas reinhardtii*. *Redox Biology*, 38(November 2020). <https://doi.org/10.1016/j.redox.2020.101806>
- Thieulin-pardo, G., Lignon, S., & Gontero, B. (2015). *Molecular BioSystems Phosphoribulokinase from Chlamydomonas reinhardtii : a Benson – Calvin cycle enzyme enslaved to its cysteine residues*. 14, 1134–1145. <https://doi.org/10.1039/c5mb00035a>
- Thompson, C. E., Freitas, L. B., & Salzano, F. M. (2018). Molecular evolution and functional divergence of alcohol dehydrogenases in animals, fungi and plants. *Genetics and Molecular Biology*, 41(1), 341–354. <https://doi.org/10.1590/1678-4685-GMB-2017-0047>

- Thomson, C. J., & Greenway, H. (1991). Metabolic Evidence for Stelar Anoxia in Maize Roots Exposed to Low O<sub>2</sub> Concentrations 1. *Plant Physiology*, *96*(4), 1294–1301. <https://doi.org/10.1104/pp.96.4.1294>
- Tichá, T., Lochman, J., Činčalová, L., Luhová, L., & Petřivalský, M. (2017). Redox regulation of plant S-nitrosoglutathione reductase activity through post-translational modifications of cysteine residues. *Biochemical and Biophysical Research Communications*, *494*(1), 27–33. <https://doi.org/https://doi.org/10.1016/j.bbrc.2017.10.090>
- Tilman, D., & Clark, M. (2015). Food, Agriculture & the Environment: Can We Feed the World & Save the Earth? *Daedalus*, *144*(4), 8–23. [https://doi.org/10.1162/DAED\\_a\\_00350](https://doi.org/10.1162/DAED_a_00350)
- Treffon, P., Rossi, J., Gabellini, G., Trost, P., Zaffagnini, M., & Vierling, E. (2021). Quantitative proteome profiling of a S-nitrosoglutathione reductase (GSNOR) null mutant reveals a new class of enzymes involved in nitric oxide homeostasis in plants. *Frontiers in Plant Science*, *12*, 787435.
- Trost, P., Fermani, S., Calvaresi, M., & Zaffagnini, M. (2017). Biochemical basis of sulphenomics: how protein sulphenic acids may be stabilized by the protein microenvironment. *Plant Cell and Environment*, *40*(4), 483–490. <https://doi.org/10.1111/pce.12791>
- Ventura, I., Brunello, L., Iacopino, S., Valeri, M. C., Novi, G., Dornbusch, T., Perata, P., & Loreti, E. (2020). Arabidopsis phenotyping reveals the importance of alcohol dehydrogenase and pyruvate decarboxylase for aerobic plant growth. *Scientific Reports*, *10*(1), 16669. <https://doi.org/10.1038/s41598-020-73704-x>
- Wadano, A., Kamata, Y., Iwaki, T., Nishikawa, K., & Hirahashi, T. (1995). Purification and characterization of phosphoribulokinase from the cyanobacterium *Synechococcus* PCC7942. *Plant and Cell Physiology*, *36*(7), 1381–1385.
- Weits, D. A., Kunkowska, A. B., Kamps, N. C. W., Portz, K. M. S., Packbier, N. K., Nemeč Venzá, Z., Gaillochet, C., Lohmann, J. U., Pedersen, O., & van Dongen, J. T. (2019). An apical hypoxic niche sets the pace of shoot meristem activity. *Nature*, *569*(7758), 714–717.
- Williamson, D. H., Lund, P., & Krebs, H. A. (1967). The redox state of free nicotinamide-adenine dinucleotide in the cytoplasm and mitochondria of rat liver. *Biochemical Journal*, *103*(2), 514–527. <https://doi.org/10.1042/bj1030514>
- Winkler, M., Hemschemeier, A., Jacobs, J., Stripp, S., & Happe, T. (2010). Multiple ferredoxin isoforms in *Chlamydomonas reinhardtii* – Their role under stress conditions and biotechnological implications. *European Journal of Cell Biology*, *89*(12), 998–1004. <https://doi.org/https://doi.org/10.1016/j.ejcb.2010.06.018>
- Yu, A., Xie, Y., Pan, X., Zhang, H., Cao, P., Su, X., Chang, W., & Li, M. (2020). Photosynthetic Phosphoribulokinase Structures: Enzymatic Mechanisms and the Redox Regulation of the Calvin-Benson-Bassham Cycle[OPEN]. *The Plant Cell*, *32*(5), 1556–1573. <https://doi.org/10.1105/tpc.19.00642>
- Zaffagnini, M., Bedhomme, M., Groni, H., Marchand, C. H., Puppo, C., Gontero, B., Cassier-Chauvat, C., Decottignies, P., & Lemaire, S. D. (2012). Glutathionylation in the Photosynthetic Model Organism *Chlamydomonas reinhardtii*: A Proteomic Survey\*. *Molecular & Cellular Proteomics*, *11*(2), M111.014142. <https://doi.org/https://doi.org/10.1074/mcp.M111.014142>
- Zaffagnini, M., De Mia, M., Morisse, S., Di Giacinto, N., Marchand, C. H., Maes, A., Lemaire, S. D., & Trost, P. (2016). Protein S-nitrosylation in photosynthetic organisms: A comprehensive overview with future

perspectives. *Biochimica et Biophysica Acta (BBA) - Proteins and Proteomics*, 1864(8), 952–966.  
<https://doi.org/https://doi.org/10.1016/j.bbapap.2016.02.006>

Zaffagnini, M., Fermani, S., Calvaresi, M., Orrù, R., Iommarini, L., Sparla, F., Falini, G., Bottoni, A., & Trost, P. (2016). Tuning Cysteine Reactivity and Sulfenic Acid Stability by Protein Microenvironment in Glyceraldehyde-3-Phosphate Dehydrogenases of *Arabidopsis thaliana*. *Antioxidants and Redox Signaling*, 24(9), 502–517. <https://doi.org/10.1089/ars.2015.6417>

Zaffagnini, M., Fermani, S., Marchand, C. H., Costa, A., Sparla, F., Rouhier, N., Geigenberger, P., Lemaire, S. D., & Trost, P. (2019). Redox Homeostasis in Photosynthetic Organisms: Novel and Established Thiol-Based Molecular Mechanisms. *Antioxidants and Redox Signaling*, 31(3), 155–210.  
<https://doi.org/10.1089/ars.2018.7617>

Zaffagnini, M., Morisse, S., Bedhomme, M., Marchand, C. H., Festa, M., Rouhier, N., Lemaire, S. D., & Trost, P. (2013). Mechanisms of nitrosylation and denitrosylation of cytoplasmic glyceraldehyde-3-phosphate dehydrogenase from *Arabidopsis thaliana*. *Journal of Biological Chemistry*, 288(31), 22777–22789.

Zemojtel, T., Fröhlich, A., Palmieri, M. C., Kolanczyk, M., Mikula, I., Wyrwicz, L. S., Wanker, E. E., Mundlos, S., Vingron, M., Martasek, P., & Durner, J. (2006). Plant nitric oxide synthase: a never-ending story? *Trends in Plant Science*, 11(11), 524–525. <https://doi.org/10.1016/j.tplants.2006.09.008>

Zhou, J.-Y., Hao, D.-L., & Yang, G.-Z. (2021). Regulation of Cytosolic pH: The Contributions of Plant Plasma Membrane H<sup>+</sup>-ATPases and Multiple Transporters. In *International Journal of Molecular Sciences* (Vol. 22, Issue 23). <https://doi.org/10.3390/ijms222312998>

## CHAPTER I: “Structural snapshots of nitrosoglutathione binding and reactivity underlying S-nitrosylation of photosynthetic GAPDH”

**Edoardo Jun Mattioli<sup>a,1</sup>, Jacopo Rossi<sup>b,1</sup>, Maria Meloni<sup>b</sup>, Marcello De Mia<sup>c</sup>, Christophe H. Marchand<sup>c,d</sup>, Andrea Tagliani<sup>b,c,2</sup>, Silvia Fanti<sup>a</sup>, Giuseppe Falini<sup>a</sup>, Paolo Trost<sup>b</sup>, Stéphane D. Lemaire<sup>c,e</sup>, Simona Fermani<sup>a,f,\*</sup> Matteo Calvaresi<sup>a,f,\*</sup>, and Mirko Zaffagnini<sup>b,\*</sup>**

<sup>a</sup> Department of Chemistry “G. Ciamician”, University of Bologna, I-40126 Bologna, Italy

<sup>b</sup> Department of Pharmacy and Biotechnologies, University of Bologna, I-40126 Bologna, Italy

<sup>c</sup> CNRS, Sorbonne Université, Institut de Biologie Physico-Chimique, UMR8226, F-75005, Paris, France

<sup>d</sup> CNRS, Institut de Biologie Physico-Chimique, Plateforme de Protéomique, FR550, F-75005, Paris, France

<sup>e</sup> Sorbonne Université, CNRS, Institut de Biologie Paris-Seine, Laboratory of Computational and Quantitative Biology, UMR7238, F-75005, Paris, France

<sup>f</sup> CIRI Health Sciences & Technologies (HST), University of Bologna, I-40064 Bologna, Italy

<sup>1</sup> These authors contributed equally to this work

<sup>2</sup> Current address: Department of Biosciences, Università degli Studi di Milano, 20133 Milan, Italy

*This work has been published in 2022 on **Redox Biology** and is available at:*

DOI: 10.1016/j.redox.2022.102387

*Supplemental materials are available at:*

<https://www.sciencedirect.com/science/article/pii/S2213231722001598?via%3Dihub>

## Summary

Nitric oxide ( $\bullet\text{NO}$ , hereafter referred to as NO) is a relatively stable free radical recognized to act as a signaling molecule in controlling multiple physiological processes in both animal and plant systems. The biological effects of NO are thought to be primarily linked to a redox PTM named S-nitrosylation (also referred to as protein S-nitrosation). This oxidative modification consists in the formation of a nitrosothiol (-SNO) between NO and a redox-reactive protein cysteine and results in the alteration of enzyme activities, protein conformation and stability, as well as interactions with other macromolecules including proteins and nucleic acids. The formation of nitrosothiols can occur through the direct reaction of NO with thiyl radical ( $-\text{S}\bullet$ ), or they can derive from the addition of a nitrosonium group ( $\text{NO}^+$ ) to a cysteine thiolate ( $-\text{S}^-$ ). At the physiological level, dinitrogen trioxide ( $\text{N}_2\text{O}_3$ ) and nitrosoglutathione (GSNO) are considered the prominent nitrosylating agents due to their ability to donate their  $\text{NO}^+$  moiety to a target cysteine. While the reaction of  $\text{N}_2\text{O}_3$  with cysteine residues does not seem to require specific structural constraints, the interaction of GSNO with target cysteines is supposed to be assisted by the presence of acidic and basic residues flanking or surrounding the protein thiol in the primary or tertiary sequence, respectively. This structural feature has been named GSNO binding motif and it functions to both enhance proton release from the cysteine thiol and ensure a proper binding of the nitrosylating agent. The identification of a -SNO consensus motif in target proteins has been sought, but a universal pattern has not been established yet. Besides acting as a trans-nitrosylating agent, GSNO can also induce S-glutathionylation, a reversible redox modification consisting in the formation of a mixed disulfide between glutathione and a protein cysteine, which shares with S-nitrosylation the capacity to tune protein function and conformation. In the last decades, proteomic-based approaches identified hundreds of proteins undergoing S-nitrosylation in plants, highlighting the importance of this redox modification in the control of multiple cellular processes such as pathogen resistance, immune response, and carbon-related metabolic pathways. Notwithstanding the numerous putative targets, glyceraldehyde-3-phosphate dehydrogenase (GAPDH) has been found as a prominent target and widely used to study the molecular mechanisms underlying NO-dependent thiol modifications. In plants, GAPDH comprises several isoforms participating in the glycolytic pathway in the cytoplasm and the stroma (NAD(H)-dependent GAPC and GAPCp isoforms, respectively), and in the Calvin-Benson-Bassham (CBB) cycle in the stroma (NADP(H)-dependent GAPA and GAPA/B isozymes). The reaction accomplished by the photosynthetic GAPDH is part of the reductive phase of the CBB cycle and consists in the NADPH-dependent reduction of the organic acid bisphosphoglycerate (BPGA) yielding the sugar G3P, the main output product of the CBB cycle.

Regardless of their metabolic function, the catalytic mechanism of GAPDH enzymes strictly depends on a reactive cysteine located in the active site. The reactivity of this residue (hereafter numbered as Cys149, is crucial for the nucleophilic attack on the substrate and it is fostered by an interaction with the proximal His176 that attracts the proton from the sulfur atom stabilizing the thiolate state ( $-S^-$ ). Besides being required for the catalysis, the deprotonation of Cys149 makes it sensitive to S-nitrosylation and other redox modifications (*e.g.*, S-glutathionylation, persulfidation, and sulfenic acid formation), which unavoidably alter its functionality. Considering the prominent role of GSNO as a mediator of NO-dependent biological activities and the thiol-dependent regulatory switch of GAPDH activity, we sought to elucidate the structural determinants that control GSNO binding and reactivity as well as the molecular mechanisms underlying the GSNO-dependent oxidation of plant GAPDH. To this aim, we employed a combination of biochemical, structural, and computational approaches to investigate the regulatory role of GSNO on GAPDH from *Chlamydomonas reinhardtii* (CrGAPDH). Exposure to GSNO led to reversible CrGAPDH inactivation via S-nitrosylation of its catalytic cysteine, fully prevented by the binding of CrGAPDH substrate (*i.e.*, 1,3-bisphosphoglycerate, BPGA). In contrast, the cofactor NADP<sup>+</sup> causes a partial protection delaying the inactivation kinetics. Determination of the crystal structures of CrGAPDH bound to both NAD<sup>+</sup> and NADP<sup>+</sup> allowed the comparison with other structurally known plant GAPDH, and it was instrumental to establish the protein residues involved in the GSNO binding using molecular dynamics (MD). The reaction between GSNO and the catalytic cysteine was investigated using a quantum mechanical/molecular mechanical (QM/MM) approach. Based on our findings, we provide mechanistic insights into the response of a photosynthetic GAPDH to GSNO-dependent regulation, possibly extending this analysis to cysteine microenvironments from other proteins that are susceptible to be oxidatively modified by GSNO.

## Results

### Comparing CrGAPA sequence with plastidial GAPDHs from photosynthetic organisms

Multiple sequence alignments reveal that CrGAPA shows a relatively high similarity with photosynthetic GAPDH from land plants and microalgae (76-80% sequence identity; **Supplemental Figures 1 and 2**), while the sequence identity slightly decreases (64-68%) when we compared CrGAPA with homologs from cyanobacterial species (**Supplemental Figures 3**). Among photosynthetic GAPDH isoforms, the catalytic dyad Cys149/His176 and the majority of residues participating in the stabilization of the cofactors NADP(H) and NAD(H) and specificity towards NADP(H) are fully conserved (see below and **Supplemental Figures 1-3**). Multiple alignment of primary sequences was also instrumental to assess Cys conservation in photosynthetic GAPDH. CrGAPA shows in its primary structure four cysteines (Cys) at position 18, 149, 153, and 285 (**Supplemental Figure 1**). Cys18 and Cys149 are strictly conserved in photosynthetic GAPA isozymes, while Cys153 and Cys285 are absent in two microalgal species (*i.e.*, *Ostreococcus tauri* and *Micromonas pusilla*) and cyanobacterial enzymes (*i.e.*, *Synechococcus elongatus* PCC7942 and *Thermosynechococcus elongatus*), respectively, and are both replaced by glycine residues (**Supplemental Figures 1-3**).

### Three-dimensional structure of CrGAPA and structural comparison with photosynthetic GAPDH isoforms

In order to determine the structural features of CrGAPA, the enzyme was expressed in *E. coli* and purified to homogeneity by metal affinity chromatography. The recombinant protein contains 349 amino acids (mature protein plus the MHHHHHMH peptide) with a calculated molecular weight of 38103.8 Da consistent with SDS-PAGE analysis (**Supplemental Figure 4**). The crystal structures of CrGAPA complexed with both cofactors NADP<sup>+</sup> and NAD<sup>+</sup> (NADP- and NAD-CrGAPA) have been determined at a resolution of 1.5 and 2.2 Å, respectively (**Supplemental Table 1**). An additional structure of the enzyme complexed with NADP<sup>+</sup> and showing the catalytic Cys149 oxidized to sulphinate/sulphonate (-SO<sub>2</sub><sup>-</sup>/-SO<sub>3</sub><sup>-</sup>) is also reported (**Supplemental Table 1**). All crystals are isomorphous and their asymmetric unit contains a dimer (chains named O and R) generating the whole tetramer by a crystallographic 2-fold axis corresponding to a molecular symmetry axis (**Figure 1**). The superimposition of the two independent chains determines a root mean square deviation (rmsd) of 0.21 Å (326 aligned C<sub>α</sub> atoms) and 0.30 Å (335 aligned C<sub>α</sub> atoms) in the case of NADP- and NAD-CrGapA, respectively. In reduced and oxidized NADP-CrGAPA structure, the well-

defined electron density allowed the building of the whole non-cleavable His-tag (MHHHHHHM) at the N-terminal end of chain R. This portion disordered in chain O, breaks the 222 symmetry of the tetrameric structure which became a dimer of dimers (C2 symmetry) and is stabilized by interactions with symmetry related molecules (Supplemental **Figure 5A, B**).

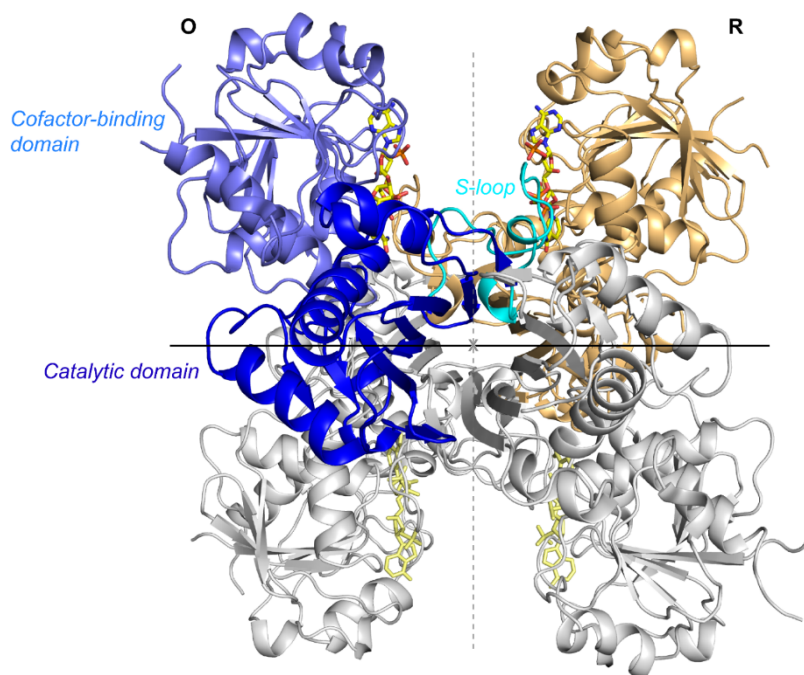


**Figure 1:** Crystal structure of CrGAPA tetramer. Ribbon representation of the CrGAPA tetramer. The dimer OR corresponds to the asymmetric unit, while the dimer generated by the 2-fold crystallographic axis, is reported in gray. The crystallographic symmetry axis is coincident with one of the symmetry molecular axis (in black), the other two symmetry molecular axes are represented with dashed lines (gray). In chain O, the different domains are highlighted: cofactor-binding domain in light blue, catalytic domain in blue and S-loop in cyan. The cofactor (NADP<sup>+</sup>) bound to each monomer, is represented in stick.

Besides CrGAPA, the crystal structures of photosynthetic GAPDH isoforms have been determined for spinach and Arabidopsis enzymes (SoGAPA and AtGAPA, respectively) (Fermani et al., 2001; Falini et al., 2003; Camara-Artigas et al., 2006; Fermani et al., 2010) and for homologs from two cyanobacteria (*Synechococcus elongatus* PCC7942 and *Thermosynechococcus elongatus*; (Kitatani et al., 2006, 2006; Matsumura et al., 2011; McFarlane et al., 2019). As expected from the high sequence homology (64-80%), the 3D structure of photosynthetic GAPDH is highly conserved. The superimpositions of CrGAPA crystal structures with those of SoGAPA and AtGAPA give an average rmsd of 0.43-0.56 Å for monomers and 0.87 Å for tetramers. Structural conservation is also observed when we compared CrGAPA with cyanobacterial NADP(H)-dependent GAPDH, displaying rmsd ranging from 0.55 to 0.77 Å for monomer and from 0.84 to 1.18 Å for tetramer superimpositions.

## Domain organization, cofactor-binding, and catalytic sites of CrGAPA

Like in other GAPDH (Skarzynski et al., 1987; Fermani et al., 2001; Fermani et al., 2010), each CrGAPA monomer consists of a cofactor-binding domain and a catalytic domain. The first one comprises residues 1-147 and 313-334 and shows the structurally conserved Rossmann fold motif typical of enzymes using nucleotide cofactors and an additional antiparallel  $\beta$ -sheet (**Figure 1**). The catalytic domain stretching from residues 148 to 312, is composed by a seven-stranded mixed  $\beta$ -sheets, three  $\alpha$ -helices, and an ordered loop named S-loop (residues 177 to 203) which forms the interface with the adjacent subunit and contributes to the set-in place and binding of the cofactor (**Figure 1**). Based on the electron density, we recognized that each CrGAPA monomer contains the coenzyme (NADP<sup>+</sup> or NAD<sup>+</sup>) bound in an extended conformation through hydrogen bonds and electrostatic interactions with protein residues and water molecules (**Figure 2A**).

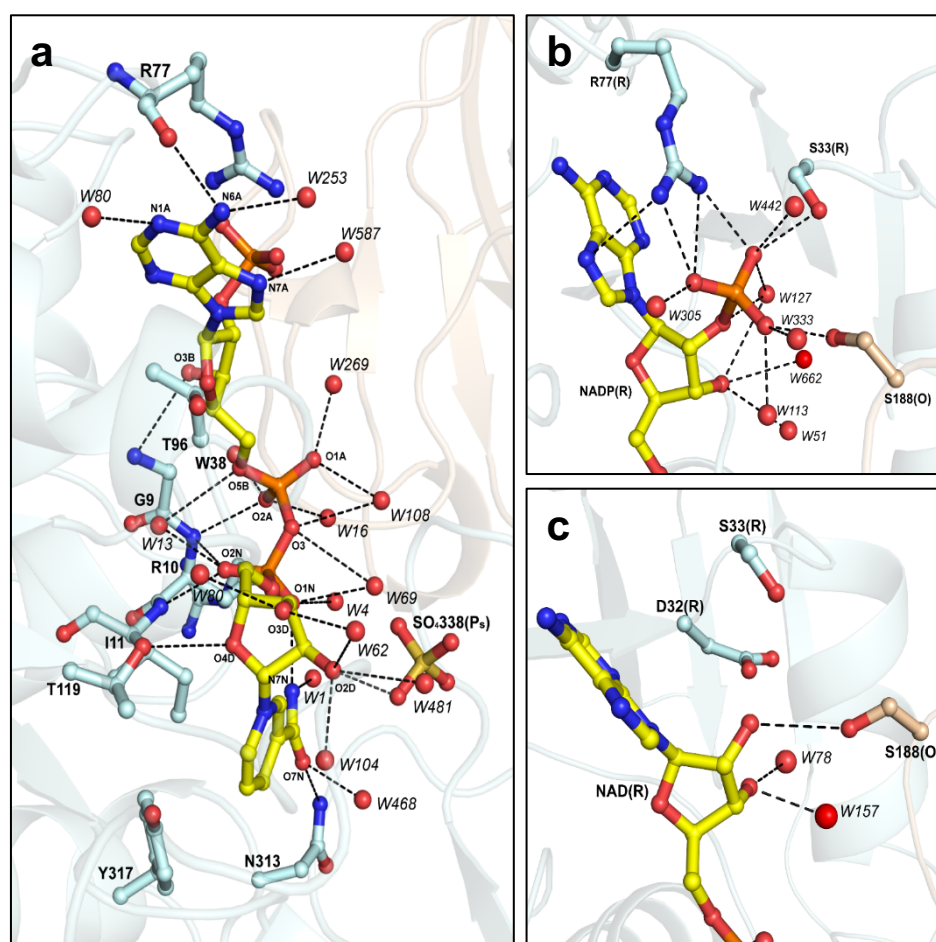


**Figure 2:** Cofactor interactions in CrGAPA. (a) Hydrogen bonds and electrostatic interactions (distance  $\leq 3.5$  Å) between the CrGAPA cofactor (NADP<sup>+</sup> or NAD<sup>+</sup>) and protein residues or water molecules. The cofactor bound to chain R of NADP<sup>+</sup>-structure is shown as a representative case. (b) Focus on the interactions (distance  $\leq 3.5$  Å)

between the 2'-phosphate group of NADP<sup>+</sup> and protein residues or water molecules. (c) Focus on the interactions (distance  $\leq 3.5$  Å) between the adenine ribose hydroxyl groups of NAD<sup>+</sup> and protein residues or water molecules.

The adenine and nicotinamide rings are roughly perpendicular to the average planes of the neighboring riboses. The first one is sandwiched between the methyl group of Thr96 and the guanidium group of Arg77 in the NADP-bound structure or the hydroxyl group of Ser33 in the NAD-bound structure (**Figures 2A-C**). The nicotinamide ring orientation is determined by an intramolecular hydrogen bond between the N7 and the O1 of the nicotinamide moiety (NO1-NN7 = 2.9 Å in both subunits of NADP-CrGAPA and 3.1 and 2.8 Å in O and R subunits of NAD-CrGAPA), and hydrophobic interactions with side chains of the strictly conserved Ile11 and Tyr317 (**Figure 2A**). The backbone nitrogen atoms of Gly9, Arg10, and Ile11 are involved in the stabilization of the central phosphate groups. The 2'-phosphate group in the adenine ribose of NADP<sup>+</sup> forms a salt-bridge with the Arg77 and hydrogen bonds with Ser33 and Ser188 of the adjacent subunit, and various water molecules (**Figure 2B**). When NAD<sup>+</sup> binds to the enzyme the hydroxyl groups of the adenine ribose form hydrogen bonds with water molecules and uniquely in chain R, with Ser188 of the adjacent subunit O (**Figure 2C**). Unlike other photosynthetic GAPDH (*i.e.*, GAPA from spinach, Arabidopsis, and the cyanobacterium *Thermosynechococcus elongatus*), the highly conserved Asp32 (**Supplemental Figures 1-3**), which is involved in the stabilization of NAD(H) (Falini et al., 2003; Fermani et al., 2010; McFarlane et al., 2019), does not participate in the cofactor binding in CrGAPA lying at more than 4.5 Å from the hydroxyl groups of the adenine ribose (**Figure 2C**). The replacement of the catalytically preferred cofactor NADP<sup>+</sup> with NAD<sup>+</sup> does not significantly alter either the monomer or the tetramer folding. Indeed, the superimpositions of monomers and tetramers give a rmsd of 0.23-0.36 Å (333 aligned C<sub>α</sub> atoms) and 0.32 Å (1326 aligned C<sub>α</sub> atoms), respectively. Even the protein portion 31-36, which was observed to undergo conformational changes depending on the bound cofactor in photosynthetic GAPA from spinach (Falini et al., 2003), perfectly superimposes in NADP- and NAD-CrGAPA structures.

The catalytic domain hosts the enzyme active pocket formed by the dyad Cys149/His176, the nicotinamide ring of the cofactor (NADP<sup>+</sup> or NAD<sup>+</sup>), and two sites named P<sub>s</sub> and P<sub>i</sub> hosting the phosphate group(s) of the substrates during catalysis (*i.e.*, BPGA or glyceraldehyde-3-phosphate, G3P) and occupied in all presented structures by sulfate ions coming from the crystallization solution. The reactivity (*i.e.*, nucleophilicity) of the catalytic Cys149 thiol group is ensured by the interaction with the basic imidazole ring of His176 (Cys149 SG – His176 NE2 = 3.3 – 3.4 Å) and by hydrogen bond formation with the backbone amino group and side chain hydroxyl group of Thr150 (Cys149 SG – Thr150 N = 3.2 – 3.3 Å and Cys149 SG – Thr150 OG1 = 3.9 – 4.2 Å) (**Figure 3A**). The same

residues are also responsible of the stabilization of the sulfinylated/sulfonylated Cys149 (Cys-SO<sub>2</sub><sup>-</sup>/SO<sub>3</sub><sup>-</sup>) observed in the oxidized NADP<sup>+</sup>-CrGAPA structure (Supplemental **Figure 6**). This evidence indicates that the catalytic Cys is prone to oxidation just increasing the pH of the medium. The position of the P<sub>s</sub> and P<sub>i</sub> sites is superimposable in NADP<sup>+</sup> and NAD<sup>+</sup> structures and all residues involved in their stabilization are strictly conserved in photosynthetic GAPDH sequences (**Figure 3B** and **Supplemental Figure 1-3**). In particular, the P<sub>s</sub> site lies close to the cofactor nicotinamide ribose and one of its hydroxyl group interacts with the sulfate ion (**Figure 2A**). Further stabilization is provided by salt-bridges with Arg195 and Arg231, and by hydrogen bonds with the side chain of Thr179 and water molecules (**Figure 3B**). The P<sub>i</sub> site is instead stabilized only by hydrogen bonds with the backbone amino groups of the segment Thr208-Ala210, the hydroxyl groups of Ser148 and Thr208, and water molecules (**Figure 3B**).

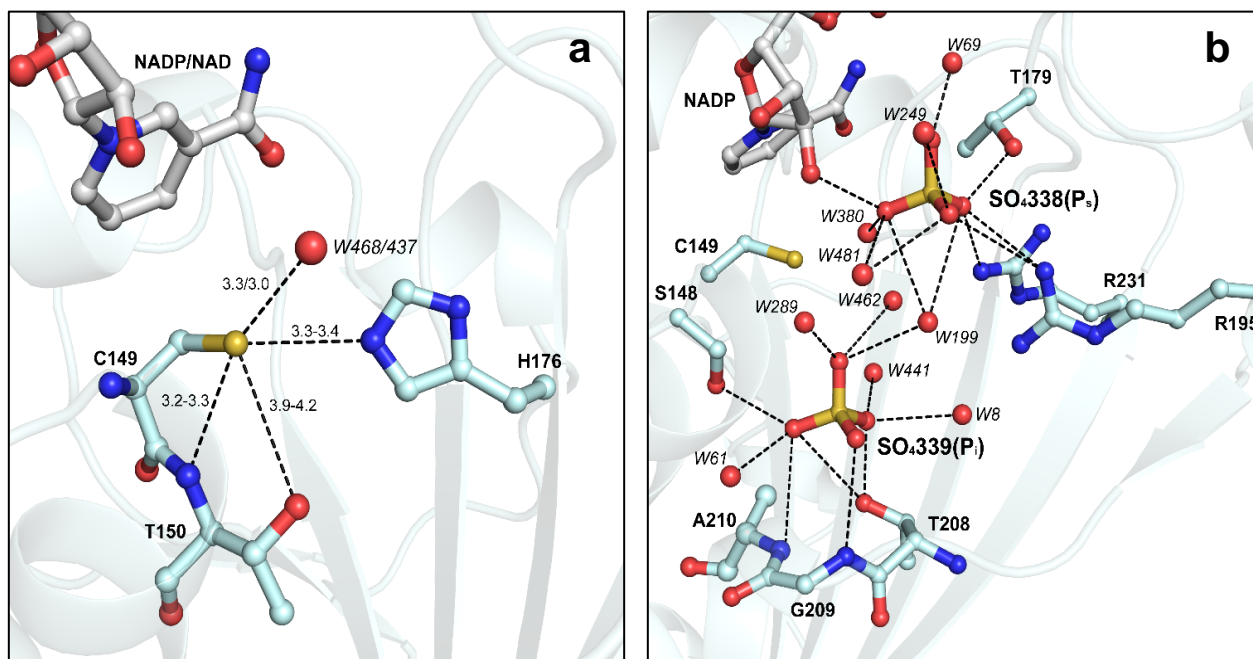


**Figure 3.** Catalytic site of CrGAPA. (a) The catalytic dyad Cys149/His176 and interactions of Cys149 that stabilize the thiolate form, are shown. The ranges of values reported refer to the distances observed in chains O and R of NADP<sup>+</sup> or NAD<sup>+</sup> structures. (b) The P<sub>s</sub> and P<sub>i</sub> sites and the hydrogen bonds and electrostatic interactions (distance  $\leq 3.5$  Å) with protein residues or water molecules, are shown. P<sub>s</sub> and P<sub>i</sub> sites are occupied in all CrGAPA structures here presented, by sulphate ions coming from the crystallization solution.

## CrGAPA specifically undergoes S-nitrosylation in the presence of GSNO

In a previous study, we demonstrated that CrGAPA activity is sensitive to oxidative modifications mediated by hydrogen peroxide ( $\text{H}_2\text{O}_2$ ), GSSG, and GSNO (Marri et al., 2014). Whereas the molecular mechanisms underlying  $\text{H}_2\text{O}_2$ - and GSSG-dependent oxidation have been extensively investigated, the nature and type of redox modification induced by GSNO remains elusive.

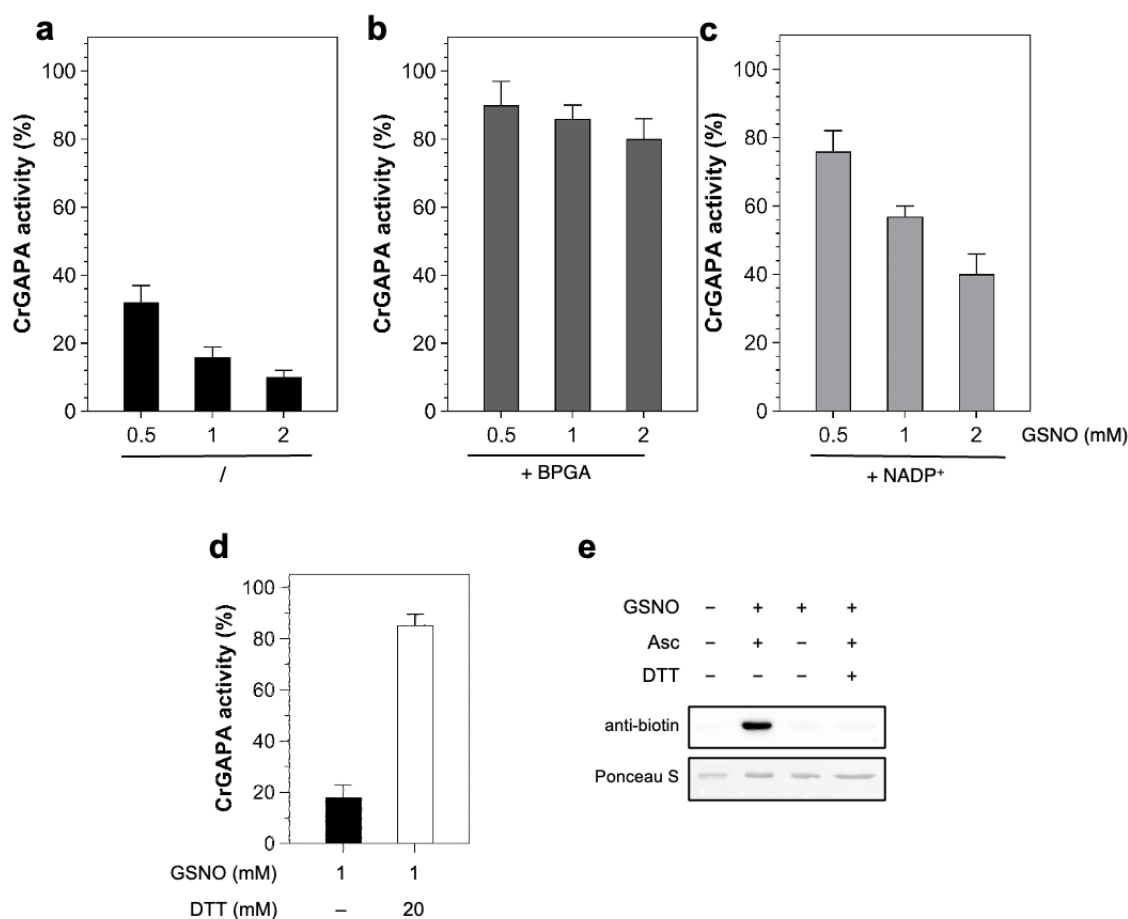


**Figure 4.** GSNO-mediated S-nitrosylation of CrGAPA. (a) Incubation of CrGAPA with GSNO. The enzyme was incubated (30 min) with different concentration of GSNO. (b) Substrate (b) and cofactor (c) protection of GSNO-treated CrGAPA. CrGAPA was pre-incubated with BPGA-generating system or 0.2 mM  $\text{NADP}^+$  prior to exposure to 2 mM GSNO (see “Material and Methods” for further details). (d) The reversibility of CrGAPA inactivation by GSNO (2 mM, black bar) was assessed after incubation in the presence of 20 mM DTT (white bar). For panels a-d, data are represented as mean  $\pm$  SD ( $n = 3$ ) of control activity. (e) S-nitrosylation of CrGAPA. The enzyme was treated for 30 min in the presence of 2 mM GSNO and nitrosylation was visualized using the BST followed by anti-biotin western blots as described in “Material and Methods”. The red-ponceau (ponceau S) staining of the membrane shows equal loading in each lane.

Here, we analyzed the effect of variable GSNO amounts on CrGAPA activity and observed a strong inactivation of the enzyme which retains ~30%, 15%, and 10% of residual activity after exposure (30 min) to 0.5, 1, and 2 mM GSNO, respectively (**Figure 4A**). As mentioned before, CrGAPA has four cysteines showing different accessibility as assessed by their accessible surface area (ASA) (**Figure 5**). In NADP-CrGAPA, Cys285 is the most exposed (average residue and thiol group ASAs equal to 67 Å<sup>2</sup> and 20 Å<sup>2</sup>, respectively), while the catalytic Cys149 is less accessible (average residue and thiol group ASAs equal to 9 Å<sup>2</sup> and 6 Å<sup>2</sup>, respectively). In contrast, Cys18 and Cys153 are almost buried (average residue and thiol group ASAs equal to 2 Å<sup>2</sup> and 0 Å<sup>2</sup> for Cys18 and both 0 Å<sup>2</sup> for Cys153). Therefore, Cys accessibility values and protein inactivation strongly suggest that GSNO could interact with the catalytic Cys149 and likely Cys285. To establish the specific involvement of the catalytic cysteine, the enzyme was incubated in the presence of the substrate BPGA prior to treatment with GSNO. As shown in **Figure 4B**, the GSNO-dependent inactivation was almost completely blocked in agreement with the fact that BPGA covalently binds to catalytic Cys149 and therefore, its presence allows full protection from redox alterations as previously established (Bedhomme et al., 2012; Zaffagnini et al., 2013). Incubation of CrGAPA with NADP<sup>+</sup> partially prevented inhibition of the enzyme by GSNO (**Figure 4C**), suggesting that NADP<sup>+</sup>, bound to the active site, might interfere with the GSNO-dependent inactivation process likely through steric hindrance. Consistently, if the cofactor is removed from the structure the accessibility of Cys149 increases (average residue and thiol group ASAs equal to 28 Å<sup>2</sup> and 21 Å<sup>2</sup>, respectively).

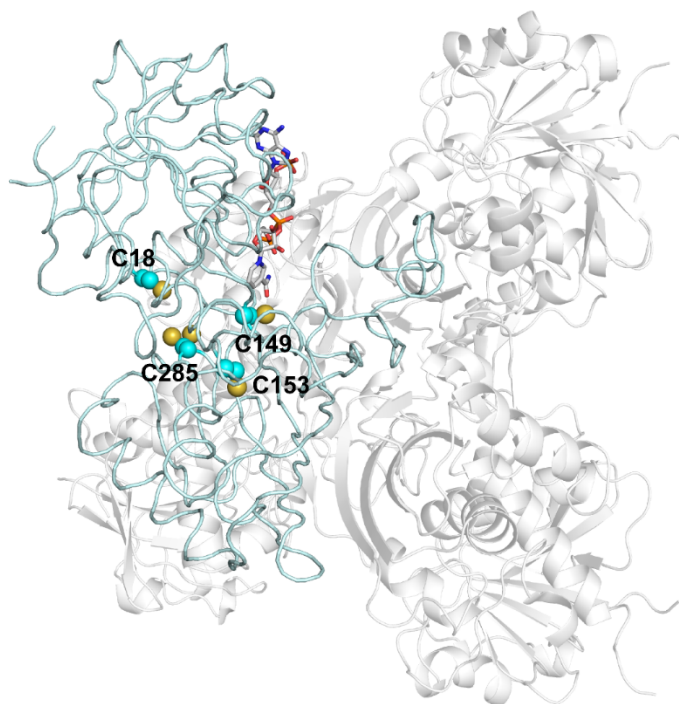


**Figure 5.** Cysteine residues position and accessibility in CrGAPA monomer. The position of cysteines in the monomer of CrGAPA is shown. Based on accessible surface area (ASA), Cys18 and 153 are buried (2 and 0 Å<sup>2</sup>,

and 0 and 0 Å<sup>2</sup> for average residue and thiol group, respectively), the catalytic Cys149 shows a low accessibility (9 Å<sup>2</sup> and 6 Å<sup>2</sup> for average residue and thiol group, respectively), while Cys285 that shows in the crystal structure a double conformation is the most accessible (67 Å<sup>2</sup> and 20 Å<sup>2</sup> for average residue and thiol group, respectively).

It is known that GSNO can react with protein thiols inducing S-nitrosylation or S-glutathionylation. Based on activity measurements, we cannot distinguish which of the two redox modifications alter the redox state of CrGAPA catalytic cysteine. To establish the type of redox alteration induced by GSNO, we employed MALDI-TOF mass spectrometry (MS) coupled to the biotin switch technique (BST) and anti-biotin western blots. It is noteworthy that MALDI-TOF mass spectrometry can easily detect S-glutathionylation typically resulting in a 305 Da shift of the mass of the protein, while the labile SNO bond is lost during the laser-induced ionization process. Consequently, the S-nitrosylated protein is indistinguishable from its unmodified form. MALDI-TOF analysis was performed on CrGAPA after incubation (30 min) with 1 mM GSNO (**Supplemental Figure 7**). The spectrum recorded for GSNO-treated CrGAPA (observed protein mass: 38,136.5 Da) was comparable with unmodified protein (calculated protein mass: 38,103,81 Da), indicating that GSNO is unable to induce S-glutathionylation. In addition, no change in protein mass was observed after exposure of GSNO-treated CrGAPA with DTT (observed protein mass: 38,124.8 Da). Despite the absence of significant mass shift, activity measurements revealed that GSNO causes CrGAPA inhibition (**Figure 4D**). In addition, reducing treatments almost restored full activity (**Figure 4D**). Using the biotin-switch technique coupled to anti-biotin western blot, we evaluated the nitrosylated state of GSNO-treated CrGAPA (**Figure 4E**). After incubation of CrGAPA for 30 min in the presence of 1 mM GSNO, we observed a strong signal after ascorbate-dependent SNO reduction indicating that GSNO induces S-nitrosylation of CrGAPA (**Figure 4E**). Consistently, no signal was observed either when ascorbate reduction was omitted (*i.e.*, lack of nitrosothiols reduction and biotin labeling) or when DTT was applied to GSNO-treated CrGAPA prior to the thiol blocking step (*i.e.*, complete reduction of nitrosothiols and subsequent reaction of nascent thiols with thiol-modifying agents) (**Figure 4E**).

Taken together, these results indicate that (i) CrGAPA activity is reversibly inhibited by GSNO; (ii) GSNO causes CrGAPA inhibition solely through S-nitrosylation as revealed by BST and MALDI-TOF MS analyses; (iii) incubation with BPGA fully protects CrGAPA inhibition indicating that the catalytic Cys149 is targeted by GSNO; and (iv) NADP<sup>+</sup> partially hampers GSNO-dependent S-nitrosylation likely affecting GSNO binding and/or reactivity.

## Structural analysis of GSNO-CrGAPA interactions by molecular dynamics

After establishing that CrGAPA undergoes S-nitrosylation in the presence of GSNO, we carried out molecular dynamics (MD) simulations to gain insight into the dynamics of the GSNO-dependent trans-nitrosylation process of CrGAPA at the molecular level. To evaluate possible variations of the glutathione binding mode prior and after the reaction with the enzyme, we performed two different MD simulations of (i) CrGAPA in complex with GSNO and (ii) S-nitrosylated CrGAPA in complex with glutathione thiolate ( $\text{GS}^-$ ), *i.e.*, the leaving group formed after the transfer of the NO moiety to the enzyme (Zaffagnini et al., 2016). By a decomposition analysis of the trajectories according to the MM-GBSA scheme, we quantified the contribution of each amino acids to the binding of GSNO/ $\text{GS}^-$ , identifying at the atomic level the GSNO/ $\text{GS}^-$  binding motif.

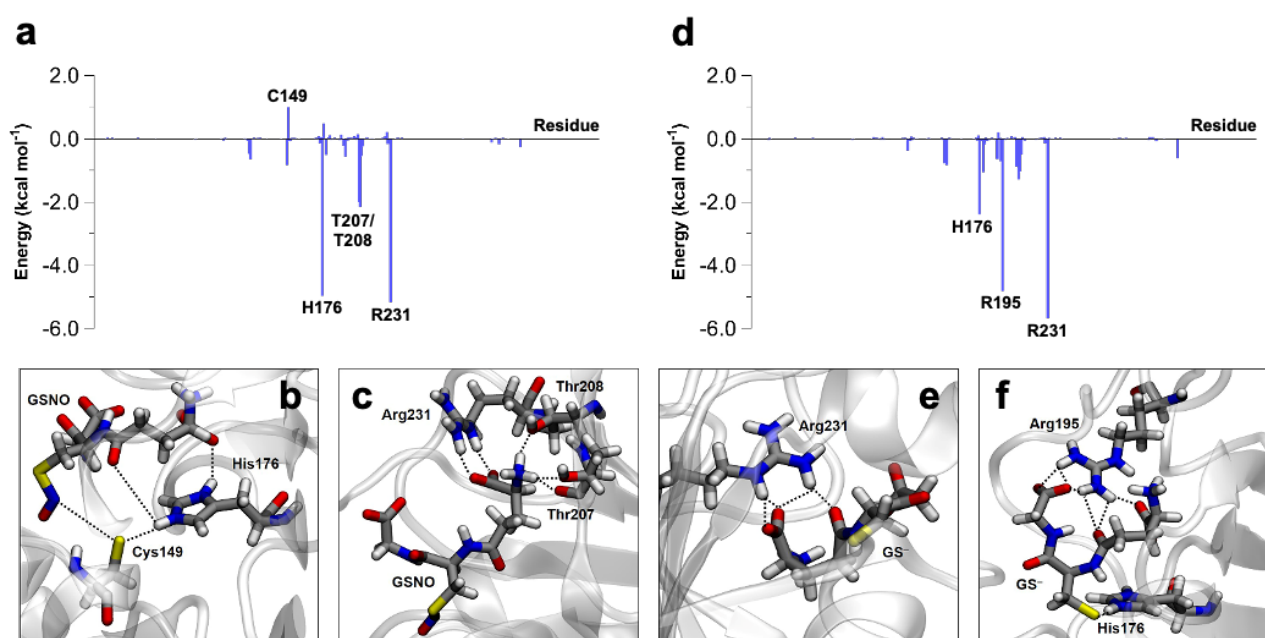


**Figure 6.** Structural interactions of CrGAPA with GSNO and  $\text{GS}^-$ . (a)  $\Delta G_{\text{binding}}$  between CrGAPA and GSNO, decomposed per residue. (b) Interaction between His176 and GSNO. (c) interactions of Thr207, Thr208, Arg231, and GSNO. (d)  $\Delta G_{\text{binding}}$  between S-nitrosylated CrGAPA and  $\text{GS}^-$ , decomposed per residue. (e) Interaction between Arg231 and  $\text{GS}^-$ . (f) Interactions between His176, Arg195, and  $\text{GS}^-$ .

The binding of GSNO to CrGAPA involves several protein residues including His176, Thr207, Thr208, and Arg231 (**Figure 6A**). His176 forms the catalytic dyad (Cys149/His176) and it is responsible for the deprotonation of Cys149 and consequent stabilization of the thiolate ( $-\text{S}^-$ ) (**Figure 6B**). Therefore, His176 is found in a protonated form with the imidazolium ring bearing two NH groups and a positive net charge. Furthermore, His176 participates to the binding of GSNO as it

strongly interacts with the  $\gamma$ -glutamate of GSNO forming a salt bridge and a hydrogen bond with its carboxylate group. Intriguingly, we can note that His176 bridges Cys149 and GSNO, the two groups involved in the NO transfer, by forming two distinct hydrogen bonds through its NH groups. As aforementioned, Thr207, Thr208, and Arg231 also participate in the anchoring process with GSNO interacting with the  $\gamma$ -glutamate group (**Figure 6C**). Thr207/Thr208 form hydrogen bonds, acting as acceptors, with the N-terminal amino group of GSNO, while Arg231 interacts with the  $\gamma$ -glutamate carboxylate moiety via the typical donor-bifurcated hydrogen bonding/salt bridge. Remarkably, Cys149 by itself has a negative effect on GSNO binding, due to electrostatic repulsion between the negative Cys149 thiolate and glutathione –SNO group.

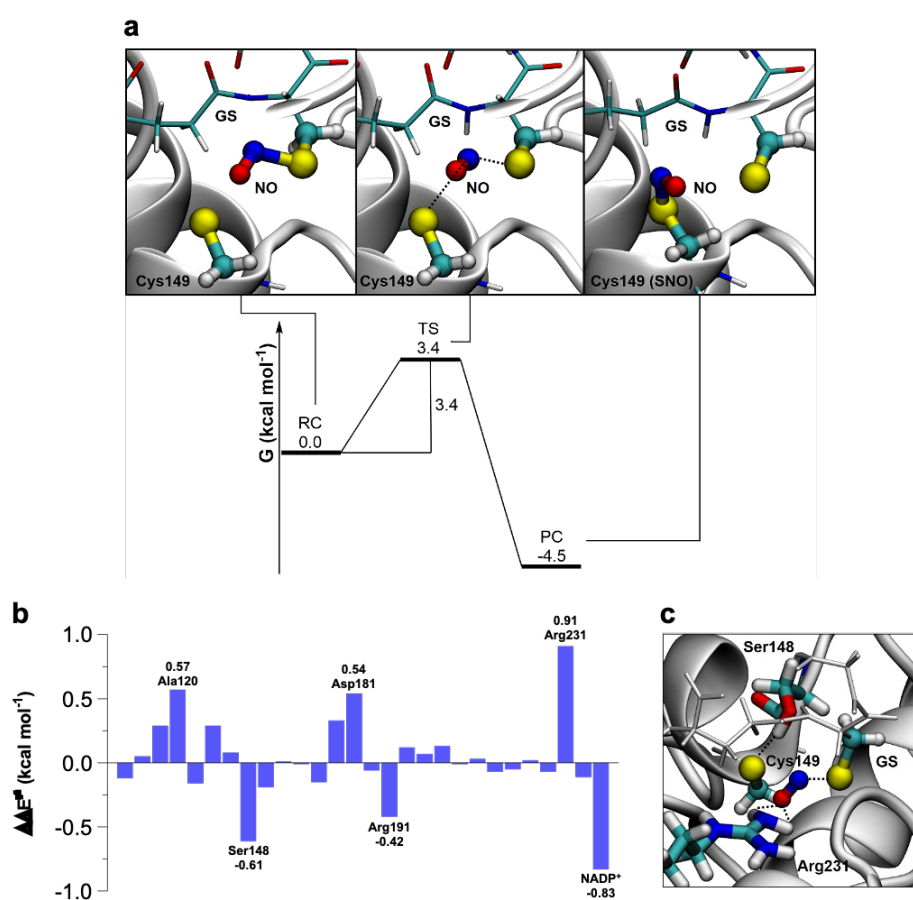


**Figure 7.** Quantum mechanical analysis of GSNO-dependent S-nitrosylation of CrGAPA. (a) Free energy surface (FES) for the trans-nitrosylation process in CrGAPA. Activation barrier and reaction energies are expressed in kcal mol<sup>-1</sup>. In the squares, a blow-up of the critical points. From left to right: reactive complex (RC), transition state (TS), and product complex (PC). (b) Stabilizing/destabilizing effect of single amino acids in the activation barrier for the GSNO-dependent trans-nitrosylation process of CrGAPA. (c) Interaction between Ser148, Arg231, and the QM reactive system in TS (i.e., Cys149-SNO-GS<sup>-</sup>).

The energy contribution of CrGAPA residues interacting with  $\text{GS}^-$  after the transfer of NO from GSNO to Cys149 has occurred is shown in **Figure 6D**. Arg231 maintains its interaction with the  $\gamma$ -glutamate of GSNO whereas His176, although still involved  $\text{GS}^-$  binding, undergoes major variations. Notably, Cys149, which originally formed a strong hydrogen bond with His176, loses its negative charge and His176 moves to stabilize by hydrogen bonding the newly formed thiolate in the  $\text{GS}^-$ . In the conformational rearrangement induced by the NO transfer, Arg195 intervenes to stabilize the C-terminal carboxylate of the  $\text{GS}^-$  glycine moiety, while Thr207 and Thr208 no longer participate in the stabilization of  $\text{GS}^-$ .

As described above, the transfer of the NO moiety from GSNO to Cys149 causes a consistent rearrangement of charges between the two Cys residues involved in the trans-nitrosylation reaction, triggering a reorganization of the network of interactions between the CrGAPA protein and the “GS” scaffold. If GSNO is anchored to CrGAPA mainly by the  $\gamma$ -glutamate residue and kept close to the target Cys149 by His176, a redistribution of the interaction throughout  $\text{GS}^-$  occurs after the trans-nitrosylation reaction. The analysis of the rmsd (*i.e.*, mobility) of the three amino acids comprising the glutathione moiety in the GSNO/CrGAPA( $\text{S}^-$ ) and  $\text{GS}^-$ /CrGAPA(SNO) complexes, during the MD simulations, neatly reflects this behavior. In the GSNO/CrGAPA complex,  $\gamma$ -glutamate is characterized by a rmsd of 0.76 Å, CysNO of 1.01 Å, and glycine of 1.54 Å, demonstrating that the anchoring of GSNO to the protein mainly involves the  $\gamma$ -glutamate residue. After NO transfer has occurred, the rmsd of glycine decreases to 1.18 Å, while the rmsd values for Cys and  $\gamma$ -glutamate increase (1.23 Å and 1.39 Å, respectively), showing a rigidification of the C-terminal glycine due to the binding with Arg195 and an increase of the flexibility of the Cys and  $\gamma$ -glutamate moieties. Besides, we also noted an increased overall molecular mobility of glutathione which shifts from 1.03 Å for GSNO to 1.29 Å for  $\text{GS}^-$ .

### Structural snapshots of the GSNO-dependent S-nitrosylation of CrGAPA

Because MD simulations cannot provide information about reactive processes, a deeper understanding of the trans-nitrosylation reaction was obtained by calculating the energetic profile of the NO transfer from GSNO to Cys149 in the CrGAPA protein environment using a QM/MM approach. Overall, QM/MM calculations are instrumental to get mechanistic insights into reaction profiles providing both thermodynamic parameters (*i.e.*, activation barrier and reaction-free energy) and the relative contribution of protein residues to activation barriers (*i.e.*, fingerprinting analysis). Before analyzing the trans-nitrosylation reaction in the protein microenvironment, we examined the reaction in conventional media (**Supplemental Figure 8**). While trans-nitrosylation in gas phase is

typically a two-step barrierless process (**Supplemental Figure 8A**), it is a single-step process in water (**Supplemental Figure 8B**) characterized by an activation energy of  $12.6 \text{ kcal mol}^{-1}$ . Both processes are isoenergetic due to the symmetry of the reagents and products. In contrast, when we considered the protein environment, the transfer of NO from GSNO to Cys149 is an exoergonic single-step process characterized by an activation energy of  $3.4 \text{ kcal mol}^{-1}$  (**Figure 7A**). Therefore, the protein environment lowers significantly the barrier of the trans-nitrosylation process and differentiates the energies of the two nitrosylated cysteines, favoring in this case the S-nitrosylation of Cys149. In the transition state (TS), the net negative charge on the sulfur atom of Cys149 is reduced by the approaching of NO and the formation of the incipient S-NO bond, while conversely the cysteine of GS(NO) is becoming a thiolate.

The relative contribution of each specific amino acid to activation barriers was quantified by fingerprint analysis (**Figure 7B**). Through specific interactions, Ser148 plays an important role in destabilizing the TS while Arg231 has an opposite effect (*i.e.*, stabilization of the TS). Specifically, Arg231 acts as a shuttle that assists the NO moiety moving from GSNO to Cys149 (**Figure 7C**), stabilizing the TS through hydrogen bonding and electrostatic interactions, as already observed in some transferases (Marforio et al., 2015; Gesteira et al., 2021). Before the reaction with GSNO, Ser148 is strongly hydrogen bonded to the thiolate of Cys149. In the TS, however, Cys149 gradually loses its negative charge (**Figure 7C**) weakening the hydrogen bond with Ser148 resulting in a destabilizing effect on the TS. All the other amino acids identified by the fingerprint analysis are charged residues (Asp181, Arg191) or residues characterized by strong dipoles (C=O and N-H in Ala120), and all are very close to the reaction site. Their net effect is due to the charge rearrangement between the two Cys residues, passing from the reagent to the transition state (activation barrier). In addition to protein residues, also  $\text{NADP}^+$  plays an important role by acting as a destabilizing factor of the TS and thus affecting the S-nitrosylation reaction electrostatically.

## Discussion

Photosynthetic GAPDH is an important enzyme that fulfils major metabolic functions through its participation in the carbon fixation pathway (Troost et al., 2006). Unlike land plants, *Chlamydomonas* along with other green microalgae and cyanobacteria only contains homotetrameric photosynthetic GAPDH isoform composed by A-type subunits (*i.e.*, GAPA). This isoform differs from photosynthetic AB-GAPDH as it is not subjected to autonomous light-dependent redox regulation (Michelet et al., 2013; Gurrieri et al., 2021).

The enzymatic activity of GAPDH isoforms is dependent on the presence of a reactive Cys that performs a nucleophilic attack on the substrate (Troost et al., 2006; Zaffagnini et al., 2007; Zaffagnini et al., 2013). As observed in other GAPDH from plant and non-plant sources, the crystal structure of CrGAPA revealed that the catalytic Cys149 is located in close proximity to a histidine residue (*i.e.*, His176) crucial for thiol deprotonation and thiolate stabilization (**Figure 3A**). Besides the catalytic Cys149/His176 dyad, CrGAPA shares with other photosynthetic GAPDH an almost identical native folding and a superimposable domain organization. The folding conservation is also accompanied by a strict conservation of residues involved in cofactor(s) and substrate binding. Furthermore, we observed no structural rearrangements related to the accommodation and stabilization of the two cofactors (*i.e.*, NAD<sup>+</sup> and NADP<sup>+</sup>).

Among redox PTMs, S-nitrosylation plays an important role in providing ubiquitous mechanisms for thiol-mediated regulatory and signaling pathways. This redox modification is typically induced by the interaction of reactive Cys thiols with GSNO and consistently, accumulation of protein nitrosothiols was observed in mutant plants lacking GSNO reductase (GSNOR), the main enzyme controlling the intracellular concentration of GSNO (Lindermayr, 2017; Zaffagnini et al., 2019). Based on recent evidences, GSNO was found to modulate GAPDH catalysis. Notably, activity modulation by GSNO was observed for GAPDH-related activities when assayed in *Arabidopsis* protein extracts (Lindermayr et al., 2005), and for the recombinant forms of glycolytic GAPC from *Arabidopsis thaliana* (Zaffagnini et al., 2013) and photosynthetic GAPDH from *Chlamydomonas reinhardtii* (Marri et al., 2014).

To gain insight into the atomic details of S-nitrosylation, we employed photosynthetic CrGAPA which we demonstrated to specifically undergo GSNO-dependent S-nitrosylation on its catalytic cysteine with consequent reversible inhibition of enzyme activity. Based on the here presented NADP<sup>+</sup>-crystal structure, we carried out computational calculations to determine the protein residues contributing to the binding and stabilization of GSNO within the active site. Intriguingly, we observed that the catalytic His176 participates in GSNO accommodation while interacting with the catalytic Cys149 thiolate (**Figure 6B**). Therefore, His176 appears crucial in NO transfer and in bypassing the electrostatic repulsion between the Cys149 thiolate and the -SNO group of GSNO, both involved in the reaction process. The binding of GSNO also encompasses two threonines (Thr207 and Thr208) and Arg231, all interacting with the  $\gamma$ -glutamate moiety of GSNO (**Figure 6C**). Overall, the multiple interactions between GSNO and CrGAPA are crucial in ensuring effective recognition of GSNO in the active site of the protein, an essential step to trigger the trans-nitrosylation process. The positioning and stabilization of the “GS” scaffold in the active site of CrGAPA is mainly mediated by the  $\gamma$ -glutamate of GSNO. Its prominent role was previously observed in the S-glutathionylated

glycolytic AtGAPC1 (Zaffagnini et al., 2019). In the crystal structure of glutathionylated AtGAPC1, the glutathione molecule covalently bound to the catalytic cysteine is set in place mainly through the interaction between the  $\gamma$ -glutamate moiety and various active site residues, while the C-terminal carboxylate of the glycine is free and seems dispensable in the GSH stabilization. Moreover, we show that a rearrangement of the interaction network occurs in the binding of glutathione thiolate ( $\text{GS}^-$ ), which results from the reaction of GSNO with Cys149. This change is functional to the release of  $\text{GS}^-$  and the consequent stabilization of the nitrosothiol on the catalytic Cys149. While Arg231 maintains the bifurcated interaction with the  $\gamma$ -glutamate carboxylate, the two threonines are no longer involved in its stabilization inducing an increase in the mobility of  $\text{GS}^-$  (**Figure 6E**). Besides, His176 moves away from the neutral nitrosylated Cys149 and interacts with the thiolate of glutathione, while the C-terminal carboxylic group of the glutathionyl glycine interacts with Arg195, which is not engaged in GSNO binding (**Figure 6F**). As a result, the leaving group  $\text{GS}^-$  is more mobile than GSNO.

Taken together, these observations highlight the importance of positively charged (His and Arg) and polar residues (Thr) in determining the redox sensitivity of CrGAPA to GSNO-dependent S-nitrosylation by (i) deprotonating the catalytic cysteine, (ii) supporting the NO transfer, and (iii) stabilizing the GSNO/ $\text{GS}^-$  molecules. Our findings partially deviate from previous studies that, based on protein sequence analysis, predicted the propensity of a given Cys to undergo S-nitrosylation on the basis of consensus motifs comprising acidic (*i.e.*, glutamate and aspartate) and basic (*i.e.*, arginine, histidine, and lysine) residues flanking the target cysteine (Stamler et al., 1997; Hess et al., 2005; Bignon et al., 2018; Stomberski et al., 2019; Kolbert and Lindermayr, 2021). Despite being proposed in the GSNO binding motif, acidic residues were not detected in the stabilization and accommodation of GSNO in the proximity of CrGAPA Cys149. Therefore, it seems clear that a more thorough investigation based on the three-dimensional structure is needed to elucidate the importance of structural and molecular determinants in Cys propensity to S-nitrosylation (Marino and Gladyshev, 2010).

QM/MM calculations revealed that the GSNO-dependent trans-nitrosylation of CrGAPA has a  $\sim 4$ -fold lower activation energy compared to the trans-nitrosylation reaction in aqueous solution (**Figure 8A and Supplemental Figure 8B**). Protein-mediated trans-nitrosylation further differs from the reaction in water as it is an exoergonic process since there is no symmetry between reactants ( $\text{GSNO} + \text{Cys149-S}^-$ ) and products ( $\text{Cys149-SNO} + \text{GS}^-$ ). Thus, the newly formed Cys149-SNO has a lower energy compared to GSNO indicating that the nitrosothiol is more stable in CrGAPA compared to the nitrosylating agent. In addition, it is known that exothermicity determines the amount of reagent required to induce the reaction, while the height of the energy barrier determines the reaction rate.

Therefore, we can hypothesize that, *in vivo*, GSNO (*i.e.*, the reagent) induces a fast CrGAPA S-nitrosylation, regardless of its intracellular concentration.

The activation barrier for the trans-nitrosylation reaction is modulated by the protein microenvironment and fingerprint analysis was instrumental to unravel the relative contribution of CrGAPA residues. Intriguingly, only polar or charged residues (Ser148, Asp181, Arg191, and Arg231) were identified to influence the stability of the TS ( $\text{GS}\cdots\text{NO}\cdots\text{S-Cys149}$ ) thus modulating the energy barrier of the reaction (**Figure 7B**). While Ser148 and Arg191 have a destabilizing effect with the hydroxyl group of Ser148 involved in Cys149 thiolate stabilization, Asp181 and Arg231 contribute to stabilize the TS. Besides protein residues, we found that also  $\text{NADP}^+$  destabilizes the TS thus increasing the energy barrier of the trans-nitrosylation reaction. On this basis, the role of the cofactor in partially preventing the GSNO-dependent CrGAPA inhibition can be ascribed more to electrostatic interactions than to steric hindrance affecting GSNO binding.

In conclusion, we propose a structurally-based computationally-derived GSNO binding motif in which binding and stabilization of GSNO/GS<sup>-</sup> mainly involve basic and hydroxyl residues that mainly interact with the double charged N-terminal  $\gamma$ -glutamate group (*i.e.*, positive N-terminal amine and negative carboxylic group). Among identified residues (**Figure 6**), His176, Arg195, Thr208, and Arg231 play also an essential role in modulating the catalytic and redox reactivity of Cys149 and in the stabilization of the substrate. Thus, it appears clear that catalytic properties along with redox sensitivity to GSNO-mediated oxidation are operated by the same network of residues. Moreover, we found that the energy profile of CrGAPA S-nitrosylation is modulated by the native protein environment involving both short- and long-distance electrostatic and polar interactions (**Figure 7**). The importance of charge interconnections, even at long distance, was previously observed in Arabidopsis GAPC1 and GAPA, where they contributed to tune cysteine reactivity towards  $\text{H}_2\text{O}_2$ -dependent primary oxidation (*i.e.*, sulfenic acid formation) (Zaffagnini et al., 2016).

Albeit cysteines are unique molecular switches and highly responsive sensors of the cellular redox state, the molecular mechanisms underlying thiol oxidative modifications are still not fully elucidated. Computational analyses coupled to structural and biochemical studies appear essential for understanding the oxidation sensitivity of reactive Cys and the complex mechanisms underpinning oxidative modifications (Bignon et al., 2018), which are fundamental PTMs for the functioning and regulation of cellular networks alongside other more studied modifications such as phosphorylation.

Here we demonstrate that GSNO-mediated nitrosothiol formation affects the functioning of photosynthetic CrGAPA. However, the physiological impact of S-nitrosylation on the algal enzyme remains to be investigated and related to this, also the NO-dependent redox modulation of the carbon

fixation pathway in microalgae and other photosynthetic organisms is still unexplored. To note, all enzymes participating in the carbon fixation pathway were identified as putative targets of S-nitrosylation (Morisse et al., 2014) but molecular evidence of NO-dependent regulation of CBB enzymes is still limited (Marri et al., 2014; Zaffagnini et al., 2014). To date, only GAPA was demonstrated to undergo S-nitrosylation, which could act as a reversible regulatory mechanism of protein activity under physiological conditions. However, we should also consider that S-nitrosylation can cause irreversible inhibition by acting as a redox switch that promotes the covalent modification of catalytic cysteine by NAD(H), as demonstrated both in the presence of the isolated enzyme and under cellular conditions (Mohr et al., 1996; Broniowska and Hogg, 2010). Numerous studies revealed that animal GAPDH can acquire moonlighting functions specifically triggered by redox modifications of the catalytic cysteine which redirect the enzyme to new and completely unrelated functions (Zaffagnini et al., 2013). In particular, nuclear translocation of S-nitrosylated animal GAPDH can control apoptosis but also regulation of gene expression and it was demonstrated to act as a trans-nitrosylase of nuclear proteins (Zaffagnini et al., 2013). Whether photosynthetic GAPDH also possesses additional functions is still an open question and further studies are required to shed light on the possibility that this enzyme might be involved in S-nitrosylation-dependent regulatory cascades in green algae and other photosynthetic organisms.

## Material and Methods

### Chemicals and enzymes

N-[6-(Biotinamido)hexyl]-3'-(2'-pyridyldithio)propionamide (HPDP-biotin) was purchased from Pierce Biotechnology. GSNO was prepared freshly as described previously (Treffon et al., 2021). All other chemicals and enzymes were obtained from Merck Life Science unless otherwise specified. Recombinant CrGAPA was expressed and purified according to (Marri et al., 2014). The concentration of purified CrGAPA was determined spectrophotometrically using a molar extinction coefficient at 280 nm ( $\epsilon_{280}$ ) of  $36,565 \text{ M}^{-1} \text{ cm}^{-1}$ . Before each treatment, the enzyme was pre-reduced as described in (Marri et al., 2014).

### Crystallization and data collection

Purified CrGapA was concentrated to 10 mg/ml in 30 mM Tris-HCl, 1 mM EDTA (pH 7.9), and 1 mM  $\text{NAD}^+$  or  $\text{NADP}^+$  and crystallized by the hanging drop vapor-diffusion method at 293 K. Protein solution aliquots of 2  $\mu\text{l}$  were mixed to an equal volume of reservoir and the final drop was equilibrated against 750  $\mu\text{l}$  reservoir solution. Aggregate crystals appeared in 10-15 days using 1.8-2.0 M  $(\text{NH}_4)_2\text{SO}_4$  as precipitant and 0.1 M Tris-HCl pH 7.5-8.5 or HEPES-NaOH pH 7.5, thus the conditions were optimized decreasing the precipitant concentration or protein concentration or both. Best crystals used for further diffraction experiments, grew with a protein concentration ranging from 5 to 10 mg/ml, 1.2-1.6 M  $(\text{NH}_4)_2\text{SO}_4$ , 0.1 M Tris-HCl pH 7.5-8.5 or 0.1 M Bicine pH 9.5 (only for oxidized  $\text{NADP}^+$ -CrGapA). Crystals were harvest by a cryo-loop, briefly soaked in the cryo-protectant solution (1.6 M  $(\text{NH}_4)_2\text{SO}_4$ , 20% glycerol, and 2 mM  $\text{NAD}^+$  or  $\text{NADP}^+$ ) and finally frozen in liquid nitrogen.

Diffraction data were collected at the Elettra synchrotron radiation source (Trieste, beam line XRD1) at 100 K using a wavelength of 1.0 Å, an oscillation angle ( $\Delta\Phi$ ) of  $0.5^\circ$  for  $\text{NAD}^+$ - and oxidized  $\text{NADP}^+$ -CrGapA and  $0.3^\circ$  for  $\text{NADP}^+$ -CrGapA, and a sample-to-detector (Pilatus 2M) distance (d) of 160, 190 and 200 mm for  $\text{NADP}^+$ -, oxidized  $\text{NADP}^+$ - and  $\text{NAD}^+$ -CrGapA, respectively. Data were processed using XDS (Kabsch, 2010) and scaled with AIMLESS (Evans and Murshudov, 2013). The correct space group was determined with POINTLESS (Evans, 2006) and confirmed in the structure solution stage. Unit cell parameters and statistics are reported in Supplemental Table 1.

## Structure solution and refinement

CrGapA structures were solved by molecular replacement using the program MOLREP (Vagin and Teplyakov, 2010) from CCP4 package (Winn et al., 2011), using the structure of SoGAPA (PDB ID code: 1JN0; (Fermani et al., 2001)) excluding non-proteins atoms and water molecules, as a search model. The refinement was performed with REFMAC5 7.1.004 (Murshudov et al., 1997) from CCP4 package (Winn et al., 2011), selecting 5% of reflection for  $R_{\text{free}}$  calculation. The molecular graphic software COOT (Emsley and Cowtan, 2004) was used for manual rebuilding and modelling of the missing atoms in the electron density map and to add solvent molecules. Water molecules were automatically added and, after a visual inspection, confirmed in the model if the relative electron density value in the  $(2F_o - F_c)$  maps exceeded  $0.19 \text{ e-}\text{\AA}^{-3}$  ( $1.0 \sigma$ ) and if they fell into an appropriate hydrogen bonding environment. Inspection of the Fourier difference maps of CrGapA crystals clearly showed additional electron densities attributed to the cofactors ( $\text{NAD}^+$  or  $\text{NADP}^+$ ) and to an oxidized thiol group ( $-\text{SO}_3$ ) of the catalytic Cys149. For  $\text{NADP}^+$ -CrGapA structures the last refinement cycle was performed with PHENIX (Adams et al., 2010). Final refinement statistics are reported in Supplemental Table 1.

The superpositions among structures have been performed by LSQKAB (Krissinel and Henrick, 2004) from CCP4 package (Winn et al., 2011). The structures have been validated using MolProbity (Chen et al., 2010). Figures were generated using Pymol (The PyMOL Molecular Graphics System, Schrödinger, LLC).

## Activity assay

CrGAPA activity was monitored as described previously (Sparla et al., 2004; Zaffagnini et al., 2007). Briefly, the reaction was measured spectrophotometrically at 340 nm and 25 °C in an assay mixture containing 50 mM Tris-HCl (pH 7.5), 1 mM EDTA, 5 mM  $\text{MgCl}_2$ , 3 mM 3-phosphoglycerate, 5 units/ml of yeast 3-phosphoglycerate kinase, 2 mM ATP, and 0.2 mM NADPH.

## Treatment of CrGAPA with GSNO

CrGAPA (2  $\mu\text{M}$ ) was incubated in 50 mM Tris-HCl buffer (pH 7.9) in the presence of different concentrations of GSNO. After 30 min incubation, an aliquot of the sample (5  $\mu\text{l}$ ) was withdrawn for the assay of enzyme activity. Substrate protection was performed by pre-incubating (5 min) the protein in the presence of a 1,3-bisphosphoglycerate-generating system (3 mM 3-phosphoglycerate, 5 units/ml of 3-phosphoglycerate kinase, and 2 mM ATP) or in the presence of 0.2 mM  $\text{NADP}^+$ . The

reversibility of GSNO-mediated CrGAPA inactivation was assessed by measuring protein activity after incubation for 10 min in the presence of 20 mM dithiothreitol (DTT). The S-nitrosylation signal of GSNO-treated CrGAPA was assessed using the biotin switch technique as described in (Zaffagnini et al., 2013). Control experiments were carried out to demonstrate that (i) untreated protein is irresponsive to anti-biotin antibodies, (ii) the biotin labeling is strictly dependent upon ascorbate-dependent reduction, and (iii) DTT treatment, carried out before the thiol-blocking step, fully restores the reduced state of CrGAPA cysteines, thus resulting in the absence of biotin labeling even after ascorbate treatment.

### **MALDI-TOF (matrix-assisted laser-desorption ionization-time-of-flight) mass spectrometry**

CrGAPA was treated for 30 min with 1 mM GSNO and MALDI-TOF mass spectrometry analysis was performed before and after incubation with 20 mM DTT for 30 min. The samples were analyzed as described in (Zaffagnini et al., 2019; Tagliani et al., 2021).

### **Molecular dynamics simulations**

*Setting the MD simulation.* MD simulations were performed using the AMBER 16 package (Case et al., 2005). The FF14SB force field (Maier et al., 2015) was used to model CrGAPA, GSNO and GS<sup>-</sup>. For the nitrosylated cysteine an *ad hoc* force field developed by Han (Han, 2008) was used. NADP<sup>+</sup> was modelled with force field parameters calculated by (Holmberg et al., 1999). The charges of GSNO and GS<sup>-</sup> were determined using the Merz-Singh-Kollman scheme (Bayly et al., 1993). All simulations were performed with explicit solvent by using the TIP3P water model (Mahoney and Jorgensen, 2000).

*Minimization, equilibration and MD production.* 500 steps of steepest descent minimization, followed by additional 9500 steps of conjugate gradient minimization were performed with PMEMD (Case et al., 2005). The minimized structure was used as starting point for the equilibration process. Particle Mesh Ewald summation was used throughout (with cut off radius of 10.0 Å), H-atoms were considered by the SHAKE algorithm and a time step of 2 fs was applied in all MD runs. 1 ns of heating to 298 K within an NPT ensemble and temperature coupling according to Andersen was used to equilibrate the system. A MD trajectory of 100 ns is then produced. Snapshot structures were saved into individual trajectory files every 1000-time steps, *i.e.*, every 2 ps of molecular dynamics.

*Post Processing of Trajectories.* Trajectories obtained from MD simulations were post-processed using CPPTRAJ. (Mahoney and Jorgensen, 2000; Roe and Cheatham, 2013) 1000 snapshots were

extracted from the calculated trajectory (1 snapshot each 100 ps) to estimate the contributions to the binding free energy of the single amino acids of CrGAPA with GSNO and GS<sup>-</sup>, using the MM/GBSA approach (Kollman et al., 2000).

### **Quantum mechanical/molecular mechanical calculations**

*Determination of the potential energy surface (PES) of the transnitrosylation reaction.* QM/MM calculations were carried out according to ONIOM scheme (Vreven et al., 2003) as implemented in Gaussian16 (Frisch et al., 2016). The inner QM layer consists in the reacting part of the system, *i.e.*, H<sub>3</sub>CS<sup>-</sup> + CH<sub>3</sub>SNO and was described at the DFT level using the M06-2X functional (Tomasi et al., 2005) and the 6-311++G\*\* basis set (Frisch et al., 2016). The outer layer was described at the molecular mechanics (MM) level employing the parameters used in the MD simulations. The structure of the various critical points (minima and saddle points) was fully optimized. Frequency calculations were carried out at the same level of theory to check the nature of critical points and, to calculate Gibbs free energies. Water solvation was modelled using PCM model as implemented in Gaussian (Tomasi et al., 2005).

*Fingerprint analysis.* To quantify the catalytic effect of the residues surrounding the cysteines (within 5 Å) involved in the transnitrosylation process we recomputed the activation energy of the transnitrosylation reaction, calculating the electrostatic (Coulomb) effect of the *i*th residue on the QM region in the reactant and in the transition state (fingerprint analysis) (Stenta et al., 2008; Stenta et al., 2009; Calvaresi et al., 2012). The analyses demonstrate the stabilizing/destabilizing effects exerted by the various residues.

### **Accession numbers**

The atomic coordinates and structure factors of CrGapA structures have been deposited in the Protein Data Bank with the accession codes: 7ZQ3, 7ZQK, and 7ZQ4 for NADP<sup>+</sup>-, NAD<sup>+</sup>- and oxidized NADP<sup>+</sup>-CrGapA, respectively.

## References

- Adams PD, Afonine PV, Bunkoczi G, Chen VB, Davis IW, Echols N, Headd JJ, Hung LW, Kapral GJ, Grosse-Kunstleve RW, McCoy AJ, Moriarty NW, Oeffner R, Read RJ, Richardson DC, Richardson JS, Terwilliger TC, Zwart PH (2010) PHENIX: a comprehensive Python-based system for macromolecular structure solution. *Acta Crystallogr D Biol Crystallogr* 66: 213-221
- Aroca A, Schneider M, Scheibe R, Gotor C, Romero LC (2017) Hydrogen Sulfide Regulates the Cytosolic/Nuclear Partitioning of Glyceraldehyde-3-Phosphate Dehydrogenase by Enhancing its Nuclear Localization. *Plant Cell Physiol* 58: 983-992
- Bayly CI, Cieplak P, Cornell W, Kollman PA (1993) A well-behaved electrostatic potential based method using charge restraints for deriving atomic charges: the RESP model. *The Journal of Physical Chemistry* 97: 10269-10280
- Bedhomme M, Adamo M, Marchand CH, Couturier J, Rouhier N, Lemaire SD, Zaffagnini M, Trost P (2012) Glutathionylation of cytosolic glyceraldehyde-3-phosphate dehydrogenase from the model plant *Arabidopsis thaliana* is reversed by both glutaredoxins and thioredoxins in vitro. *Biochem J* 445: 337-347
- Bignon E, Allegra MF, Lucchetta M, Tiberti M, Papaleo E (2018) Computational Structural Biology of S-nitrosylation of Cancer Targets. *Front Oncol* 8: 272
- Broniowska KA, Hogg N (2010) Differential mechanisms of inhibition of glyceraldehyde-3-phosphate dehydrogenase by S-nitrosothiols and NO in cellular and cell-free conditions. *Am J Physiol Heart Circ Physiol* 299: H1212-1219
- Calvaresi M, Stenta M, Garavelli M, Altoé P, Bottoni A (2012) Computational Evidence for the Catalytic Mechanism of Human Glutathione S-Transferase A3-3: A QM/MM Investigation. *ACS Catalysis* 2: 280-286
- Camara-Artigas A, Hirasawa M, Knaff DB, Wang M, Allen JP (2006) Crystallization and structural analysis of GADPH from *Spinacia oleracea* in a new form. *Acta Crystallogr Sect F Struct Biol Cryst Commun* 62: 1087-1092
- Case DA, Cheatham TE, 3rd, Darden T, Gohlke H, Luo R, Merz KM, Jr., Onufriev A, Simmerling C, Wang B, Woods RJ (2005) The Amber biomolecular simulation programs. *J Comput Chem* 26: 1668-1688
- Chen VB, Arendall WB, 3rd, Headd JJ, Keedy DA, Immormino RM, Kapral GJ, Murray LW, Richardson JS, Richardson DC (2010) MolProbity: all-atom structure validation for macromolecular crystallography. *Acta Crystallogr D Biol Crystallogr* 66: 12-21
- Emsley P, Cowtan K (2004) Coot: model-building tools for molecular graphics. *Acta Crystallogr D Biol Crystallogr* 60: 2126-2132
- Evans P (2006) Scaling and assessment of data quality. *Acta Crystallogr D Biol Crystallogr* 62: 72-82
- Evans PR, Murshudov GN (2013) How good are my data and what is the resolution? *Acta Crystallogr D Biol Crystallogr* 69: 1204-1214
- Falini G, Fermani S, Ripamonti A, Sabatino P, Sparla F, Pupillo P, Trost P (2003) Dual coenzyme specificity of photosynthetic glyceraldehyde-3-phosphate dehydrogenase interpreted by the crystal structure of A4 isoform complexed with NAD. *Biochemistry* 42: 4631-4639
- Fermani S, Ripamonti A, Sabatino P, Zanotti G, Scagliarini S, Sparla F, Trost P, Pupillo P (2001) Crystal structure of the non-regulatory A(4) isoform of spinach chloroplast glyceraldehyde-3-phosphate dehydrogenase complexed with NADP. *J Mol Biol* 314: 527-542
- Fermani S, Sparla F, Marri L, Thumiger A, Pupillo P, Falini G, Trost P (2010) Structure of photosynthetic glyceraldehyde-3-phosphate dehydrogenase (isoform A4) from *Arabidopsis thaliana* in complex with NAD. *Acta Crystallogr Sect F Struct Biol Cryst Commun* 66: 621-626
- Frisch MJ, Trucks GW, Schlegel HB, Scuseria GE, Robb MA, Cheeseman JR, Scalmani G, Barone V, Petersson GA, Nakatsuji H, Li X, Caricato M, Marenich AV, Bloino J, Janesko BG, Gomperts R, Mennucci B, Hratchian HP, Ortiz JV, Izmaylov AF, Sonnenberg JL, Williams, Ding F, Lipparini F, Egidi F, Goings J, Peng B, Petrone A, Henderson T, Ranasinghe D, Zakrzewski VG, Gao J, Rega N, Zheng G, Liang W, Hada M, Ehara M, Toyota K, Fukuda R, Hasegawa J, Ishida M, Nakajima T, Honda Y, Kitao O, Nakai H, Vreven T, Throssell K, Montgomery Jr. JA, Peralta JE, Ogliaro F, Bearpark MJ, Heyd JJ, Brothers EN, Kudin KN, Staroverov VN, Keith TA, Kobayashi R, Normand J, Raghavachari K, Rendell AP, Burant JC, Iyengar SS, Tomasi J, Cossi M, Millam JM, Klene M, Adamo C, Cammi R, Ochterski JW, Martin RL, Morokuma K, Farkas O, Foresman JB, Fox DJ (2016) Gaussian 16 Rev. C.01. *In*, Wallingford, CT
- Gesteira TF, Marforio TD, Mueller JW, Calvaresi M, Coulson-Thomas VJ (2021) Structural Determinants of Substrate Recognition and Catalysis by Heparan Sulfate Sulfotransferases. *ACS Catalysis* 11: 10974-10987

- Gurrieri L, Fermani S, Zaffagnini M, Sparla F, Trost P (2021) Calvin-Benson cycle regulation is getting complex. *Trends Plant Sci* 26: 898-912
- Han S (2008) Force field parameters for S-nitrosocysteine and molecular dynamics simulations of S-nitrosated thioredoxin. *Biochem Biophys Res Commun* 377: 612-616
- Hess DT, Matsumoto A, Kim SO, Marshall HE, Stamler JS (2005) Protein S-nitrosylation: purview and parameters. *Nature Reviews. Molecular Cell Biology* 6: 150-166
- Holmberg N, Ryde U, Bulow L (1999) Redesign of the coenzyme specificity in L-lactate dehydrogenase from *Bacillus stearothermophilus* using site-directed mutagenesis and media engineering. *Protein Eng* 12: 851-856
- Holtgreffe S, Gohlke J, Starmann J, Druce S, Klocke S, Altmann B, Wojtera J, Lindermayr C, Scheibe R (2008) Regulation of plant cytosolic glyceraldehyde 3-phosphate dehydrogenase isoforms by thiol modifications. *Physiol Plant* 133: 211-228
- Kabsch W (2010) Xds. *Acta Crystallogr D Biol Crystallogr* 66: 125-132
- Kitatani T, Nakamura Y, Wada K, Kinoshita T, Tamoi M, Shigeoka S, Tada T (2006) Structure of apo-glyceraldehyde-3-phosphate dehydrogenase from *Synechococcus* PCC7942. *Acta Crystallogr Sect F Struct Biol Cryst Commun* 62: 727-730
- Kitatani T, Nakamura Y, Wada K, Kinoshita T, Tamoi M, Shigeoka S, Tada T (2006) Structure of NADP-dependent glyceraldehyde-3-phosphate dehydrogenase from *Synechococcus* PCC7942 complexed with NADP. *Acta Crystallogr Sect F Struct Biol Cryst Commun* 62: 315-319
- Kolbert Z, Lindermayr C (2021) Computational prediction of NO-dependent posttranslational modifications in plants: Current status and perspectives. *Plant Physiol Biochem* 167: 851-861
- Kollman PA, Massova I, Reyes C, Kuhn B, Huo S, Chong L, Lee M, Lee T, Duan Y, Wang W, Donini O, Cieplak P, Srinivasan J, Case DA, Cheatham TE, 3rd (2000) Calculating structures and free energies of complex molecules: combining molecular mechanics and continuum models. *Acc Chem Res* 33: 889-897
- Krissinel E, Henrick K (2004) Secondary-structure matching (SSM), a new tool for fast protein structure alignment in three dimensions. *Acta Crystallogr D Biol Crystallogr* 60: 2256-2268
- Lindermayr C (2017) Crosstalk between reactive oxygen species and nitric oxide in plants: Key role of S-nitrosogluthathione reductase. *Free Radic Biol Med*
- Lindermayr C, Saalbach G, Durner J (2005) Proteomic identification of S-nitrosylated proteins in *Arabidopsis*. *Plant Physiol* 137: 921-930
- Lindermayr C, Sell S, Muller B, Leister D, Durner J (2010) Redox regulation of the NPR1-TGA1 system of *Arabidopsis thaliana* by nitric oxide. *Plant Cell* 22: 2894-2907
- Mahoney MW, Jorgensen WL (2000) A five-site model for liquid water and the reproduction of the density anomaly by rigid, nonpolarizable potential functions. 112: 8910-8922
- Maier JA, Martinez C, Kasavajhala K, Wickstrom L, Hauser KE, Simmerling C (2015) ff14SB: Improving the Accuracy of Protein Side Chain and Backbone Parameters from ff99SB. *J Chem Theory Comput* 11: 3696-3713
- Marforio TD, Giacinto P, Bottoni A, Calvaresi M (2015) Computational Evidence for the Catalytic Mechanism of Tyrosylprotein Sulfotransferases: A Density Functional Theory Investigation. *Biochemistry* 54: 4404-4410
- Marino SM, Gladyshev VN (2010) Structural analysis of cysteine S-nitrosylation: a modified acid-based motif and the emerging role of trans-nitrosylation. *J Mol Biol* 395: 844-859
- Marri L, Thieulin-Pardo G, Lebrun R, Puppo R, Zaffagnini M, Trost P, Gontero B, Sparla F (2014) CP12-mediated protection of Calvin-Benson cycle enzymes from oxidative stress. *Biochimie* 97: 228-237
- Matsumura H, Kai A, Maeda T, Tamoi M, Satoh A, Tamura H, Hirose M, Ogawa T, Kizu N, Wadano A, Inoue T, Shigeoka S (2011) Structure basis for the regulation of glyceraldehyde-3-phosphate dehydrogenase activity via the intrinsically disordered protein CP12. *Structure* 19: 1846-1854
- McFarlane CR, Shah NR, Kabasakal BV, Echeverria B, Cotton CAR, Bubeck D, Murray JW (2019) Structural basis of light-induced redox regulation in the Calvin-Benson cycle in cyanobacteria. *Proc Natl Acad Sci U S A* 116: 20984-20990
- Michelet L, Zaffagnini M, Morisse S, Sparla F, Pérez-Pérez ME, Francia F, Danon A, Marchand CH, Fermani S, Trost P, Lemaire SD (2013) Redox regulation of the Calvin-Benson cycle: something old, something new. *Front Plant Sci* 4: 470
- Mohr S, Stamler JS, Brune B (1996) Posttranslational modification of glyceraldehyde-3-phosphate dehydrogenase by S-nitrosylation and subsequent NADH attachment. *J Biol Chem* 271: 4209-4214

- Morisse S, Zaffagnini M, Gao XH, Lemaire SD, Marchand CH (2014) Insight into protein S-nitrosylation in *Chlamydomonas reinhardtii*. *Antioxid Redox Signal* 21: 1271-1284
- Muller-Schussele SJ, Bohle F, Rossi J, Trost P, Meyer AJ, Zaffagnini M (2021) Plasticity in plastid redox networks: evolution of glutathione-dependent redox cascades and glutathionylation sites. *BMC Plant Biol* 21: 322
- Murshudov GN, Vagin AA, Dodson EJ (1997) Refinement of macromolecular structures by the maximum-likelihood method. *Acta Crystallogr D Biol Crystallogr* 53: 240-255
- Roe DR, Cheatham TE (2013) PTRAJ and CPPTRAJ: Software for Processing and Analysis of Molecular Dynamics Trajectory Data. *Journal of Chemical Theory and Computation* 9: 3084-3095
- Skarzynski T, Moody PC, Wonacott AJ (1987) Structure of holo-glyceraldehyde-3-phosphate dehydrogenase from *Bacillus stearothermophilus* at 1.8 Å resolution. *J Mol Biol* 193: 171-187
- Sparla F, Fermani S, Falini G, Zaffagnini M, Ripamonti A, Sabatino P, Pupillo P, Trost P (2004) Coenzyme site-directed mutants of photosynthetic A4-GAPDH show selectively reduced NADPH-dependent catalysis, similar to regulatory AB-GAPDH inhibited by oxidized thioredoxin. *J Mol Biol* 340: 1025-1037
- Stamler JS, Toone EJ, Lipton SA, Sucher NJ (1997) (S)NO signals: translocation, regulation, and a consensus motif. *Neuron* 18: 691-696
- Stenta M, Calvaresi M, Altoe P, Spinelli D, Garavelli M, Bottoni A (2008) The catalytic activity of proline racemase: a quantum mechanical/molecular mechanical study. *J Phys Chem B* 112: 1057-1059
- Stenta M, Calvaresi M, Altoe P, Spinelli D, Garavelli M, Galeazzi R, Bottoni A (2009) Catalytic Mechanism of Diaminopimelate Epimerase: A QM/MM Investigation. *J Chem Theory Comput* 5: 1915-1930
- Stomberski CT, Hess DT, Stamler JS (2019) Protein S-Nitrosylation: Determinants of Specificity and Enzymatic Regulation of S-Nitrosothiol-Based Signaling. *Antioxid Redox Signal* 30: 1331-1351
- Tada Y, Spoel SH, Pajerowska-Mukhtar K, Mou Z, Song J, Wang C, Zuo J, Dong X (2008) Plant immunity requires conformational changes [corrected] of NPR1 via S-nitrosylation and thioredoxins. *Science* 321: 952-956
- Tagliani A, Rossi J, Marchand CH, De Mia M, Tedesco D, Gurrieri L, Meloni M, Falini G, Trost P, Lemaire SD, Fermani S, Zaffagnini M (2021) Structural and functional insights into nitrosogluthathione reductase from *Chlamydomonas reinhardtii*. *Redox Biol* 38: 101806
- Tomasi J, Mennucci B, Cammi R (2005) Quantum mechanical continuum solvation models. *Chem Rev* 105: 2999-3093
- Treffon P, Rossi J, Gabellini G, Trost P, Zaffagnini M, Vierling E (2021) Quantitative Proteome Profiling of a S-Nitrosogluthathione Reductase (GSNOR) Null Mutant Reveals a New Class of Enzymes Involved in Nitric Oxide Homeostasis in Plants. *Front Plant Sci* 12: 787435
- Trost P, Fermani S, Calvaresi M, Zaffagnini M (2017) Biochemical basis of sulphenomics: how protein sulphenic acids may be stabilized by the protein microenvironment. *Plant Cell Environ* 40: 483-490
- Trost P, Fermani S, Marri L, Zaffagnini M, Falini G, Scagliarini S, Pupillo P, Sparla F (2006) Thioredoxin-dependent regulation of photosynthetic glyceraldehyde-3-phosphate dehydrogenase: autonomous vs. CP12-dependent mechanisms. *Photosynth Res* 89: 263-275
- Vagin A, Teplyakov A (2010) Molecular replacement with MOLREP. *Acta Crystallogr D Biol Crystallogr* 66: 22-25
- Vreven T, Morokuma K, Farkas O, Schlegel HB, Frisch MJ (2003) Geometry optimization with QM/MM, ONIOM, and other combined methods. I. Microiterations and constraints. *J Comput Chem* 24: 760-769
- Wendehenne D, Pugin A, Klessig DF, Durner J (2001) Nitric oxide: comparative synthesis and signaling in animal and plant cells. *Trends Plant Sci* 6: 177-183
- Winn MD, Ballard CC, Cowtan KD, Dodson EJ, Emsley P, Evans PR, Keegan RM, Krissinel EB, Leslie AG, McCoy A, McNicholas SJ, Murshudov GN, Pannu NS, Potterton EA, Powell HR, Read RJ, Vagin A, Wilson KS (2011) Overview of the CCP4 suite and current developments. *Acta Crystallogr D Biol Crystallogr* 67: 235-242
- Zaffagnini M, Bedhomme M, Marchand CH, Morisse S, Trost P, Lemaire SD (2012) Redox regulation in photosynthetic organisms: focus on glutathionylation. *Antioxid Redox Signal* 16: 567-586
- Zaffagnini M, De Mia M, Morisse S, Di Giacinto N, Marchand CH, Maes A, Lemaire SD, Trost P (2016) Protein S-nitrosylation in photosynthetic organisms: A comprehensive overview with future perspectives. *Biochim Biophys Acta* 1864: 952-966
- Zaffagnini M, Fermani S, Calvaresi M, Orru R, Iommarini L, Sparla F, Falini G, Bottoni A, Trost P (2016) Tuning Cysteine Reactivity and Sulfenic Acid Stability by Protein Microenvironment in Glyceraldehyde-3-Phosphate Dehydrogenases of *Arabidopsis thaliana*. *Antioxid Redox Signal* 24: 502-517

- Zaffagnini M, Fermani S, Costa A, Lemaire SD, Trost P (2013) Plant cytoplasmic GAPDH: redox post-translational modifications and moonlighting properties. *Front Plant Sci* 4: 450
- Zaffagnini M, Fermani S, Marchand CH, Costa A, Sparla F, Rouhier N, Geigenberger P, Lemaire SD, Trost P (2019) Redox Homeostasis in Photosynthetic Organisms: Novel and Established Thiol-Based Molecular Mechanisms. *Antioxid Redox Signal* 31: 155-210
- Zaffagnini M, Marchand CH, Malferrari M, Murail S, Bonacchi S, Genovese D, Montalti M, Venturoli G, Falini G, Baaden M, Lemaire SD, Fermani S, Trost P (2019) Glutathionylation primes soluble glyceraldehyde-3-phosphate dehydrogenase for late collapse into insoluble aggregates. *Proc Natl Acad Sci U S A* 116: 26057-26065
- Zaffagnini M, Michelet L, Marchand C, Sparla F, Decottignies P, Le Marechal P, Miginiac-Maslow M, Noctor G, Trost P, Lemaire SD (2007) The thioredoxin-independent isoform of chloroplastic glyceraldehyde-3-phosphate dehydrogenase is selectively regulated by glutathionylation. *FEBS J* 274: 212-226
- Zaffagnini M, Michelet L, Sciabolini C, Di Giacinto N, Morisse S, Marchand CH, Trost P, Fermani S, Lemaire SD (2014) High-resolution crystal structure and redox properties of chloroplastic triosephosphate isomerase from *Chlamydomonas reinhardtii*. *Mol Plant* 7: 101-120
- Zaffagnini M, Morisse S, Bedhomme M, Marchand CH, Festa M, Rouhier N, Lemaire SD, Trost P (2013) Mechanisms of nitrosylation and denitrosylation of cytoplasmic glyceraldehyde-3-phosphate dehydrogenase from *Arabidopsis thaliana*. *J Biol Chem* 288: 22777-22789





## **CHAPTER II: “Characterization of chloroplast ribulose-5-phosphate-3-epimerase from the microalga *Chlamydomonas reinhardtii*”**

**Maria Meloni<sup>1,2</sup>, Silvia Fanti<sup>3</sup>, Daniele Tedesco<sup>4</sup>, Libero Gurrieri<sup>1</sup>, Paolo Trost<sup>1</sup>, Simona Fermani<sup>3</sup>, Stéphane D. Lemaire<sup>2</sup>, Mirko Zaffagnini<sup>1,\*</sup>, and Julien Henri<sup>2,\*</sup>**

<sup>1</sup>Laboratory of Molecular Plant Physiology, Department of Pharmacy and Biotechnology, University of Bologna, via Irnerio 42, 40126, Bologna, Italy

<sup>2</sup>Sorbonne Université, CNRS, Laboratoire de Biologie Computationnelle et Quantitative, Institut de Biologie Paris-Seine, UMR 7238, 4 place Jussieu, 75005, Paris, France

<sup>3</sup>Department of Chemistry “G. Ciamician”, University of Bologna, via Selmi 2, 40126, Bologna, Italy

<sup>4</sup>Institute for Organic Synthesis and Photoreactivity, National Research Council (ISOF-CNR), via Gobetti 101, 40129, Bologna, Italy

*This work has been published in 2024 on **Plant Physiology** and is available at:*

<https://doi.org/10.1093/plphys/kiad680>

*Supplementary data available at:*

<https://academic.oup.com/plphys/advance-article/doi/10.1093/plphys/kiad680/7491446#435507956>

## Summary

Carbon fixation relies on Rubisco and ten additional enzymes in the Calvin-Benson-Bassham cycle. Epimerization of xylulose-5-phosphate (Xu5P) into ribulose-5-phosphate (Ru5P) contributes to the regeneration of ribulose-1,5-bisphosphate, the substrate of Rubisco. Ribulose-5-phosphate-3-epimerase (RPE, EC 5.1.3.1) catalyzes the formation of Ru5P, but it can also operate in the pentose phosphate pathway by catalyzing the reverse reaction. The green alga *Chlamydomonas reinhardtii* encodes two RPEs at nuclear genome loci, namely RPE1 and RPE2. RPE1 and RPE2 proteins share 41% sequence identity but RPE2 is predicted to be cytosolic while RPE1 is predicted to be targeted to the chloroplast. Like in plants, the pentose-phosphate pathway (PPP) is duplicated in the chloroplast and the cytosol of *Chlamydomonas*. This suggests that RPE2 contributes to cytosolic PPP while RPE1 is active in both the chloroplast PPP and the CBB cycle.

In the current study, we present a thorough examination of the structural features of RPE1 from *Chlamydomonas* (CrRPE1) by means of SAXS analysis and size-exclusion chromatography coupled with immunoblot analysis of algal protein extracts. The hexameric structure was further confirmed by the resolution of the crystal structure of CrRPE1, determined at a resolution of 1.9 Å. Our model confirms the general features of the epimerase fold and catalytic site, with better resolution compared to the only other known chloroplast isoform from *Solanum tuberosum*. To get insights into the kinetic properties of CrRPE1, we set up and optimized *in vitro* coupled-enzyme assays to monitor the enzymatic conversion of Ru5P to Xu5P (*i.e.*, PPP-related activity), and for the first time, the epimerization of Xu5P to Ru5P (*i.e.*, CBB cycle-related activity). A biochemical comparison with the recombinant form of the spinach homologue was also conducted, showing that the two enzymes have similar kinetic features, in contrast to previous studies. Finally, we monitored the thiol-based redox sensitivity of CrRPE1 and the specific activities of phospho-mimicking mutants to assess possible regulatory mechanisms based on redox and phospho-based modifications, also mapping putative sites on the molecular structure.

To our best knowledge, this study presents for the first time the experimental high-resolution structure of *Chlamydomonas reinhardtii* RPE1, its kinetic properties in the two possible directions of epimerization, and possible regulatory mechanisms, highlighting the physiological relevance of this enzyme that plays a crucial role in carbon metabolism in a photosynthetic model organism.

## Results

### Quaternary structure of recombinant and native CrRPE1

Based on previous findings, chloroplast RPE from land plants assembles in a homohexameric structure (Kopp, Kopriva et al. 1999, Kopriva, Koprivova et al. 2000, Jelakovic, Kopriva et al. 2003), albeit an octameric form was initially assigned (Chen, Hartman et al. 1998, Teige, Melzer et al. 1998). The cytosolic counterpart, however, was incontrovertibly found as a dimer (Karmali, Drake et al. 1983, Kopriva, Koprivova et al. 2000). To assess the oligomerization state of CrRPE1, the enzyme was heterologously expressed, purified to homogeneity, and analyzed by size exclusion chromatography (SEC, **Supplementary Figure 1A**). We observed a single monodisperse peak with an apparent molecular weight of 134 kDa, which corresponds to roughly five times that of a 27 kDa subunit. The oligomeric nature of the protein along with a precise estimate of the number of subunits was further investigated by Small Angle X-ray Scattering (SAXS) (**Supplementary Figure 1B and C**). The X-ray diffusion curve was analyzed by ATSAS PRIMUS-QT which derived a radius of gyration of 35.53 Å and a molecular weight of 166,581 Da corresponding to six subunits per particle. Because SAXS is considered a more rigorous method to estimate protein molecular weights with respect to analytical chromatography, we concluded that CrRPE1 folds as a homohexamer.

To further inspect the oligomerization state of CrRPE, we analyzed the quaternary structure of the native enzyme extracted from *Chlamydomonas* cell cultures. The soluble protein fraction was submitted to analytical SEC (**Supplementary Figure 1D**), and elution fractions were analyzed by western blot using primary polyclonal anti-CrRPE1 antibodies. Fractions containing detectable amounts of RPE corresponded to elution volumes comprised between 15.6 mL and 17.2 mL, with a maximum signal in the 16.0-16.4 mL fraction (**Supplementary Figure 1E**). This elution volume matches that of the recombinant protein (16.25 mL, **Supplementary Figure 1A**) that we observed on the same chromatographic system. We conclude that RPE1 extracted from cultivated algae has the same molecular weight as the pure recombinant protein, and that CrRPE1 assembles as an homohexamer *in vivo*.

### CrRPE1 folds as an $\alpha_8\beta_8$ triose-phosphate isomerase (TIM) barrel

To expand the current knowledge of the structural properties of photosynthetic RPE, so far limited to the RPE isoform of potato, we solved the three-dimensional structure of CrRPE1 by X-ray crystallography at a resolution of 1.9 Å. CrRPE1 crystallized in the monoclinic space group  $P 1 2_1 1$  with twelve subunits that assemble in hexameric structures (**Figure 1**). Crystal packing analysis thus confirmed the homohexameric organization of CrRPE1, in agreement with the quaternary structure assessed by SAXS analysis. All subunits are virtually identical with root mean square deviations (RMSDs) values in the 0.122-0.171 Å range. In the representative chain A, residues Thr31 to Pro260 of mature protein were modelled into continuous electron density. A structural alignment with potato RPE revealed RMSD values ranging from 0.276 Å to 0.347 Å, indicating a native folding substantially conserved between photosynthetic RPE from green algae and land plants.

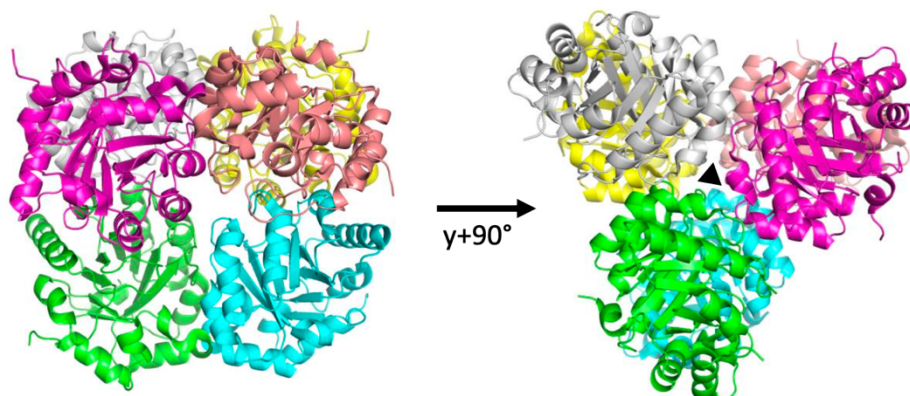


**Figure 1:** Crystal structure of ribulose-5-phosphate 3-epimerase isoform 1 from *Chlamydomonas reinhardtii* (CrRPE1). Quaternary structure of CrRPE1. Subunits of the homo-hexamer are colored. Dimer pairs are colored in green-blue, magenta-salmon, and yellow-white. Trimerization axis is represented with a triangle on the right.

As previously observed in structurally solved RPEs (Meloni, Gurrieri et al. 2023) CrRPE1 monomers adopt a canonical  $(\beta/\alpha)_8$ -barrel fold (TIM-barrel, CATH topology 3.20.20, SCOPe family c.1.2.2) with 8 parallel  $\beta$ -strands forming the central cylindrical  $\beta$ -sheet surrounded by 8  $\alpha$ -helices joined by loops (**Figure 2**). An additional short amino-terminal  $\alpha$ -helix caps the basal, amino-exposing side of the  $\beta$ -barrel. The overall content of secondary elements in the crystal structure (helices: 28.1%; strands: 17.4%; turns: 12.2%; other: 42.3%) reflects the TIM-barrel fold and this was further confirmed by in-solution analysis using CD spectroscopy (**Supplementary Figure 2**). Structural alignment of EBI AlphaFold2 entry A8IKW6 and our independently determined crystal structure yield a RMSD of 0.241 Å. Both models are almost identical except for local loop discrepancies, side

chains rotamers, and the additional information content of crystallography with regards to water molecules, bound ions and quaternary packing. We conclude that CrRPE1 folds similarly to other TIM-barrel RPEs.

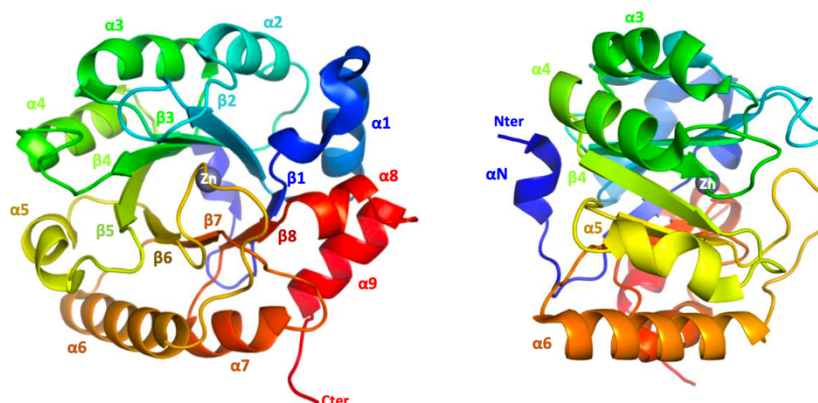


**Figure 2:** CrRPE1 folding. Main chain is traced in cartoon colored from blue (amino-terminus) to red (carboxy-terminus). Secondary structure elements are annotated. A zinc ion is placed in the center top of the  $\beta$ -barrel.

### CrRPE1 packs as a trimer of dimers

Crystal packing analysis identified nearest neighbors in and around the unit cell. EBI-PISA most probable assembly is composed of the six chains ABDFGK, burying a total surface of contact of 14,140 Å<sup>2</sup>. Computed free energy of dissociation is 20.3 kJ.mol<sup>-1</sup>. Three equivalent interfaces form sub-dimers between chains G-A, K-D, and F-B while six additional interfaces form between B-A, D-B, D-A, K-G, G-F, and K-F to trimerize the dimers into the full hexamer (**Figure 1**). In the representative G-A dimer, the interface involves ten hydrogen bonds: Leu56<sub>G</sub>-Ser54<sub>A</sub>, Gly57<sub>G</sub>-Ser54<sub>A</sub>, Gly87<sub>G</sub>-Thr85<sub>A</sub>, Arg79<sub>G</sub>-Glu110<sub>A</sub> (two bonds), Ser54<sub>G</sub>-Leu56<sub>A</sub>, Ser54<sub>G</sub>-Gly57<sub>A</sub>, Thr85<sub>G</sub>-Gly87<sub>A</sub>, Glu110<sub>G</sub>-Arg79<sub>A</sub> (two bonds), and five salt bridges: Arg79<sub>G</sub>-Glu110<sub>A</sub> (three bridges), and the mirror equivalent residues pair Glu110<sub>G</sub>-Arg79<sub>A</sub> (two bridges). The interface significance score is 1, implying it as essential for complex formation. Trimer interfaces such as that of subunits B-A only form with six hydrogen bonds, in residue pairs Ser133<sub>B</sub>-Gln132<sub>A</sub> (two bonds), Ser161<sub>B</sub>-Glu166<sub>A</sub>, Phe80<sub>B</sub>-His137<sub>A</sub>, Asp181<sub>B</sub>-Arg140<sub>A</sub> and the mirror pair Ser163<sub>B</sub>-Ser163<sub>A</sub>. EBI-PISA complex significance score is 0.328, attributing a reliable auxiliary role to these polar interactions in the stabilization of the full complex. The assembly sequence for hexameric CrRPE1 probably starts with the association of dimers, before they can contribute to several weak trimerization contacts that eventually gather the full hexamer altogether. This oligomeric organization was previously described for RPE isoforms from potato, *Synechocystis*, and *Streptococcus pyogenes* (**Supplementary Figure**

3) (Kopp, Kopriva et al. 1999, Wise, Akana et al. 2004, Akana, Fedorov et al. 2006).

### CrRPE1 is a metal-containing protein with a conserved catalytic pocket

RPEs from both plant and non-plant sources typically contain a metal ion which has a stabilizing effect towards the substrate (Liang, Ouyang et al. 2011). However, some RPE isoforms with available crystallographic structures do not contain any metal ion supporting that RPE folding does not require the presence of a specific metal within the active site. What remains to be established is whether enzymes that lack a metal ion are catalytically functional. Crystal structure analysis of CrRPE1 revealed that a spherical electron density is located close to the carboxy-exposing side of the barrel. A zinc ion was modelled into the density (**Figure 2**) and the identity of the metal was further confirmed by anomalous scattering at the Zn K-edge (**Supplementary Figure 4A**). This is in accordance with what was previously observed for cytosolic RPEs from rice (PDB entry: 1H1Z) and from *Streptococcus pyogenes* (PDB entry: 2FLI). The metal attribution is unknown for the structure of the chloroplast ortholog from potato (PDB: 1RPX). The canonical tetrad of residues involved in metal coordination is perfectly conserved in CrRPE1 and comprises His72, Asp74, His105 and Asp216 (CrRPE1 numbering) (**Supplementary Figure 5**). His72 and Asp74 belong to  $\beta$ -strand2, while His105 and Asp216 belong to  $\beta$ -strand 3 and  $\beta$ -strand 7, respectively. Besides stabilizing the metal ion, the two aspartate residues play a crucial role in the catalytic mechanism by exchanging protons with the epimerized carbon atom of the substrate (Chen, Larimer et al. 1999).

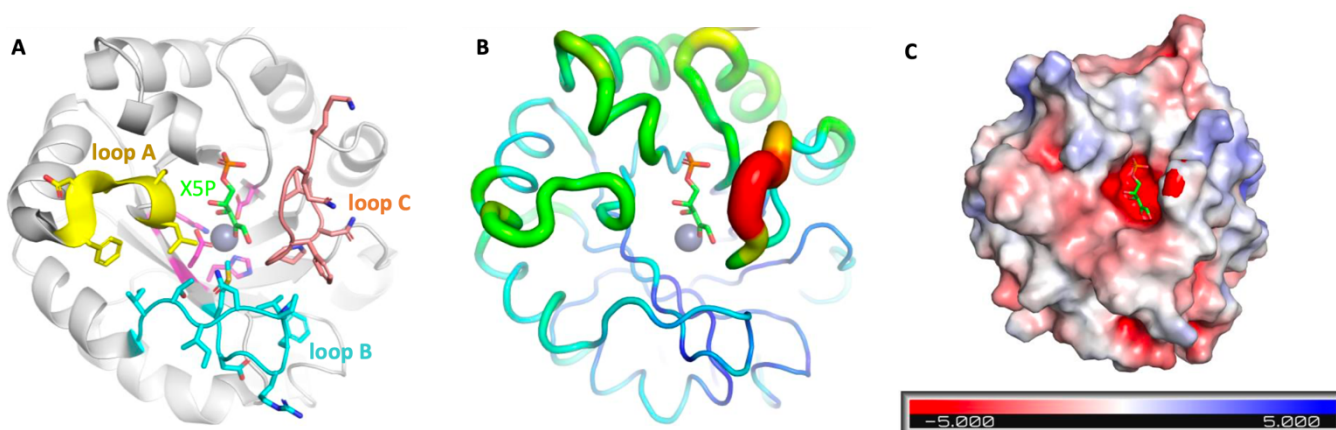


**Figure 3:** CrRPE1 active site model. (A) Cartoon representation of CrRPE1 main chain. Zinc ion is represented as a gray sphere. Xu5P position was inferred by alignment of CrRPE1 structure with that of *Homo sapiens* RPE co-crystallized with Xu5P (3OVR (Liang, Ouyang et al. 2011)). Loops A, B, and C surrounding the active site are colored yellow, cyan, and teal with residue side chains represented in sticks. (B) Local mobility of CrRPE1 is represented by crystallographic B-factors: thin and blue ribbon represents low B-factors, while large and red represents high B-factors. (C) Surface representation of CrRPE1 showing electron density map (red and blue) and a color scale from -5.000 to 5.000.

*ribbon represents high B-factors. (C) CrRPE1 electrostatic surface calculated by PyMOL APBS (Jurrus, Engel et al. 2018) is represented in a gradient from blue (electropositive) to red (electronegative).*

In CrRPE1, the zinc ion is positioned at the bottom of a deep cleft sided by loop A (Leu49- Phe53), loop B (Met76-Gly87), and loop C (Val180-Lys188) (**Figure 3A**). Loops A, B and C respectively project from  $\beta$ -strands 1, 2 and 6. Loops A and B contact each other by hydrophobic bonds between side chains of Leu49 and Thr85, and between side chains of Phe53 and Ile86. Loops B and C make multiple hydrophobic contacts involving the following pairs of residues: Val81-Pro182, Val81-Gly183, Pro82-Gly183, and Pro82-Phe184. The constrained positioning of the three loops restricts the path of an incoming substrate (Xu5P or Ru5P).

Since attempts to crystallize protein in the presence of the substrate have proved unsuccessful, we predicted the substrate binding mode in the active site of CrRPE1 by aligning CrRPE1 crystal structure onto the complex of human RPE (HsRPE) and its substrate Xu5P (PDB entry: 3OVR) with an RMSD = 0.804 Å. Xu5P appears positioned in the space defined between the zinc ion and the three aforementioned loops, respecting the lock-and-key complementarity within the active site cleft (**Figure 3A**). The conformation defined by CrRPE1 specific side chains hence fully accommodates the substrate dimension. The main structural difference between CrRPE1 and HsRPE complexed with Xu5P is the repositioning of the portion Phe184-Ph189 of the highly conserved loop C closer to the substrate. Xu5P binding probably induces a fit of the enzyme that closes around its substrate. Loop Phe184-Phe189 of our model displays the highest crystallographic B-factors of the whole protein, suggesting a functional mobility of these residues upon substrate and product accommodations (**Figure 3B**). Loop between strand  $\beta$ 6 and helix  $\alpha$ 6 was similarly considered important for Xu5P binding in chloroplast ortholog from potato (Kopp, Kopriva et al. 1999). The substrate binding pocket presents an overall electronegative potential (**Figure 3C**). The 5-phosphatidyl group of the modelled substrate is oriented in proximity to main chain aminogroup of Gly217, Gly218, Gly238, and Ser239. Electrostatic interactions between electropositive or hydrogen bond donor amines and negatively charged or hydrogen bond acceptor phosphate favor the alignment of the substrate carbonyl and the hydroxyl group of the C3 substrate at 2.8 Å and 3.4 Å from the zinc ion, respectively. This conformation of the active site appears optimal to ensure efficient Xu5P to Ru5P interconversions.

### **Kinetic analysis of CrRPE1 in the epimerization of Ru5P to Xu5P**

Since kinetic comparison of plant RPE orthologues reveals large discrepancies, we sought to

determine the kinetic features of recombinant CrRPE1. To this end, we replicated and optimized protocols from previous studies (Davis, Lee et al. 1972, Kiely, Stuart et al. 1973, Chen, Larimer et al. 1999, Akana, Fedorov et al. 2006). The initial velocity ( $v_i$ ) of CrRPE1 ascribed to the PPP-related activity (*i.e.*, Ru5P epimerization to Xu5P) was measured by coupling Ru5P epimerization to NADH oxidation via three reporter enzymes (CrTK, CrTPI, and  $\alpha$ -GDH) (**Supplementary Figure 6**). When CrRPE1 was omitted in the assay cuvette, we detected a slow and time-limited NADH consumption likely attributed to Xu5P contamination of Ru5P powder. Consequently, the further oxidation of NADH observed after adding CrRPE1 in the assay mixture indicates that the formation of Xu5P by CrRPE1 is strictly required to allow the continuous functioning of coupled enzymes (*i.e.*, the CrTK-dependent formation of glyceraldehyde-3-phosphate and subsequent catalysis by CrTPI and  $\alpha$ -GDH, **Supplementary Figure 6**). After establishing the enzymatic assay, we analyzed the dependency of CrRPE1 activity on protein concentration and metal ion. As shown in **Figure 4A**, we found that protein activity ( $\Delta\text{Abs}_{340}/\text{min}$ ) displayed a linear relationship with increasing protein concentration in the 2.5-10 nM range, corresponding to a specific activity of  $388 \pm 30 \mu\text{mol min}^{-1} \text{mg}^{-1}$  (**Supplementary Figure 7A**). Exposure of CrRPE1 to chelating agents (*i.e.*, EDTA and TPEN) substantially decreased enzyme catalysis, while treatment with equimolar or higher (10- and 100-fold excess) concentrations of zinc chloride did not enhance CrRPE1 activity (**Supplementary Figures 4B and C**). The kinetic parameters were then determined using variable Ru5P concentrations and activity data were analyzed by non-linear regression using the Michaelis-Menten equation (**Figure 4B**). Enzyme activities plotted versus Ru5P concentration displayed a typical hyperbolic response and CrRPE1 catalyzed the epimerization of Ru5P to Xu5P with a  $K_M$  value of  $1.52 \pm 0.19 \text{ mM}$  and a  $k_{\text{cat}}$  of  $273 \pm 17 \text{ sec}^{-1}$ . By comparing the kinetic properties of CrRPE with recombinant and native RPE from spinach (SoRPE), which is the only plastidial isoform to have been kinetically characterized to date, we noted that the affinity for Ru5P is markedly different as native and recombinant SoRPE showed a ~6-fold lower Michaelis-Menten constant (0.22-0.25 mM) (**Table 1**). A striking diversity was also observed when comparing turnover numbers since CrRPE catalyzes the reaction with a value about 25-fold lower and 2000-fold higher than those previously reported for the recombinant and native form of spinach RPE, respectively (**Table 1**) (Chen, Hartman et al. 1998, Teige, Melzer et al. 1998, Chen, Larimer et al. 1999).

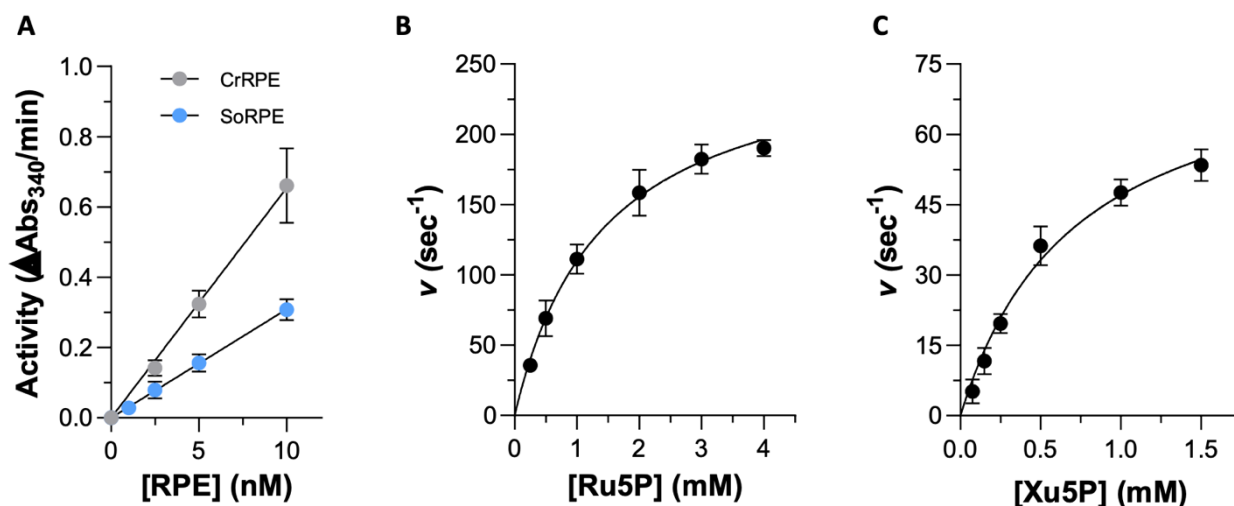


**Figure 4:** *In vitro* enzymatic activity of CrRPE1 and SoRPE. (A) Linear dependence of PPP-related activity on CrRPE1 concentration expressed as  $\Delta\text{Abs}_{340}/\text{min}$ . The data are represented as mean  $\pm$  S.D. ( $n = 3$ ). (B) Variation of apparent turnover number ( $\text{s}^{-1}$ ) catalyzed by 5 nM CrRPE1 in the presence of varying Ru5P concentrations (0-4 mM). (C) Variation of apparent turnover number ( $\text{s}^{-1}$ ) catalyzed by 5 nM CrRPE1 in the presence of varying Xu5P concentrations (0-1.5 mM). For panels (B) and (C), turnover represents moles of NADPH oxidized/s in the presence of 1 mol of CrRPE1. The data are represented as mean  $\pm$  S.D ( $n = 3$ ). The best fit was obtained using the Michaelis-Menten equation.

**Table 1:** Catalytic parameters of RPE from *Chlamydomonas* (*Chlamydomonas reinhardtii*) and spinach (*Spinacia oleracea*).

Source organism	$K_M^{\text{Ru5P}}$ (mM)	$k_{\text{cat}}$ ( $\text{s}^{-1}$ )	$k_{\text{cat}}/K_M^{\text{Ru5P}}$ ( $\text{M}^{-1} \text{s}^{-1}$ )	References
<i>Chlamydomonas reinhardtii</i>	1.52	273	$1.80 \times 10^5$	This work
<i>Spinacia oleracea</i>				
chloroplast extract	0.25	0.1382	553	Teige et al. (1998)
recombinant protein	0.22	7,100	$3.23 \times 10^7$	Chen et al. (1999)
<i>Spinacia oleracea</i>				
recombinant protein	1.56	105	$6.73 \times 10^4$	This work

In view of the values reported here and in previous studies, any comparative conclusion on the catalytic features is risky since the catalytic constants for spinach native and recombinant RPE

isoforms are extremely discordant. One possible explanation was provided by Chen and coauthors who considered the presence of the reducing agent dithiothreitol (DTT), which was used during the purification procedure of the native form, as a destabilizing agent that alters the functionality of the spinach protein (Chen, Hartman et al. 1998). To further inspect the kinetic diversity with SoRPE, we expressed and purified the spinach enzyme and determined its biochemical properties (**Figure 4A**). The recombinant SoRPE catalyzed the epimerization of Ru5P to Xu5P with a specific activity ~2-fold lower compared to CrRPE (**Supplementary Figure 7A**) and exhibited a similar  $K_M$  with respect to CrRPE1 ( $1.56 \pm 0.17$  mM) and 2.5-fold lower  $k_{cat}$  value ( $105.4 \pm 13.5$  sec<sup>-1</sup>) (**Supplementary Figure 7B**). Taken together, our results on spinach enzyme are in contrast to previous studies differing for both substrate affinity and catalytic proficiency (*i.e.*, specific activity or turnover numbers) (**Table 1**). In this regard, several reasons can be proposed that may depend on multiple factors: (i) the functional and redox state of the RPE enzyme, (ii) the source and specificity of the coupled enzymes, and (iii) the purity and integrity of the chemicals used. However, other possible explanations could justify these differences, including the amount of catalytic metal in purified recombinant proteins, and for this reason we do not intend to question further this striking discrepancy.

### **Kinetic properties of CrRPE1 catalyzing the conversion of Xu5P to Ru5P**

Whereas PPP-related RPE activity has been widely employed to dissect the catalytic properties of RPE enzymes, there is a lack of knowledge about the biochemical features of RPE related to the conversion of Xu5P into Ru5P (*i.e.*, CBB cycle-related activity). To assess the catalytic properties related to the catalytic capacity to use Xu5P as substrate, we employed the enzymatic assay typically used to monitor the activity of phosphoribulokinase (PRK) (Gurrieri, Del Giudice et al. 2019). The enzyme catalyzes the ATP-dependent phosphorylation of Ru5P, and in the assay we developed, the substrate of PRK is provided by CrRPE1 through epimerization of Xu5P. We observed that the CrRPE1 amount in the assay cuvette was the only limiting factor of the assay. Consistently, we found that protein activity ( $\Delta\text{Abs}_{340}/\text{min}$ ) displayed a linear relationship with increasing protein concentration in the 2.5-20 nM range. The derived specific activity was  $116 \pm 7$   $\mu\text{mol min}^{-1} \text{mg}^{-1}$ , which is ~3.3-fold lower compared to the PPP-related activity (**Supplementary Figure 7A**).

Kinetic constants were then determined by using variable Xu5P concentrations (0-1.5 mM) and activity data were analyzed by non-linear regression analysis using the Michaelis-Menten equation (**Figure 4C**). As observed for the opposite reaction, enzyme activities plotted versus Xu5P concentration displayed a typical hyperbolic response and CrRPE1 catalyzed the epimerization of

Xu5P to Ru5P with a  $K_M$  value of  $0.716 \pm 0.09$  mM and a  $k_{cat}$  of  $80.7 \pm 7.9$  sec<sup>-1</sup>. Comparing these kinetic data with those obtained from the reverse reaction, CrRPE1 shows a higher affinity for Xu5P compared to Ru5P but displays a lower capacity to convert Xu5P into Ru5P with respect to the reverse reaction. Consequently, derived catalytic efficiencies ( $k_{cat}/K_M$ ) slightly differ from  $1.13 \times 10^5$  M<sup>-1</sup> sec<sup>-1</sup> for the activity employing Xu5P as a substrate to  $1.80 \times 10^5$  M<sup>-1</sup> sec<sup>-1</sup> for the epimerization of Ru5P to Xu5P.

### **CrRPE1 displays a limited intrinsic instability and redox sensitivity to reducing agents**

The stability of a given protein under different cellular conditions (*e.g.*, low temperature or reducing conditions) is a crucial parameter because of the direct connection between structural integrity and functionality. In a previous study, Chen and colleagues showed that the chloroplast SoRPE (recombinant form) was highly unstable when incubated at 4 °C (Chen, Hartman et al. 1998). Moreover, the activity of the recombinant enzyme decreased after exposure to reducing agents such as 2-mercaptoethanol. In relation to this evidence, we investigated the response of CrRPE1 activity to incubation at low temperature (4 °C) and treatments with two chemical reducing agents, namely 2-mercaptoethanol and dithiothreitol (DTT). CrRPE1 activity was not affected by incubation at low temperature (~99% activity compared to control), whereas a loss of activity was observed following exposure with 2-mercaptoethanol (~40% inhibition after 2 h incubation). Intriguingly, no significant alteration of the enzymatic activity was detected upon treatment with DTT. Although DTT and 2-mercaptoethanol share similar reactivity toward protein cysteines, the redox mechanism underlying the inhibitory effect of the latter is unclear. In this regard, it is worth noting that a reductive-based redox mechanism would imply a pre-existing oxidized state of the protein, which would be subsequently modified by reducing treatments. However, this is in contrast with the observation that in the crystal structure all cysteine thiols are found in a reduced state (**Figure 5A**). Therefore, we can assume that the observed inactivation mediated by 2-mercaptoethanol eludes a cysteine-based redox-type mechanism but rather derives from other properties of the molecule likely affecting protein folding and/or metal coordination.

### **Redox response of CrRPE1 to oxidative treatments**

CrRPE1 was identified as a putative target of thioredoxin implying that it might contain cysteine residues involved in the formation of one or more disulfide bonds (Pérez-Pérez, Mauriès et al. 2017). Besides, CrRPE1 was also found to undergo S-nitrosylation (Morisse, Zaffagnini et al. 2014) and S-

glutathionylation (Zaffagnini, Bedhomme et al. 2012). Our crystal structure of CrRPE1 positions the four cysteines with relative surface accessibility of 0.180 for Cys37, 0.076 for Cys150, and 0.000 for both Cys68 and Cys204 (**Figure 5A**). The thiol of Cys37 is the most accessible to the solvent and therefore it is likely able to react with oxidizing molecules, even though minor conformational changes may allow the other cysteines to partially or fully expose their side chains to the solvent. To determine the number of accessible cysteine thiols, we employed the Ellman's reagent (5,5-dithio-bis-(2-nitrobenzoic acid), DTNB) and measured one accessible thiol group *in vitro* ( $1.0 \pm 0.2$ ), suggesting that only one cysteine is likely competent for redox exchange.

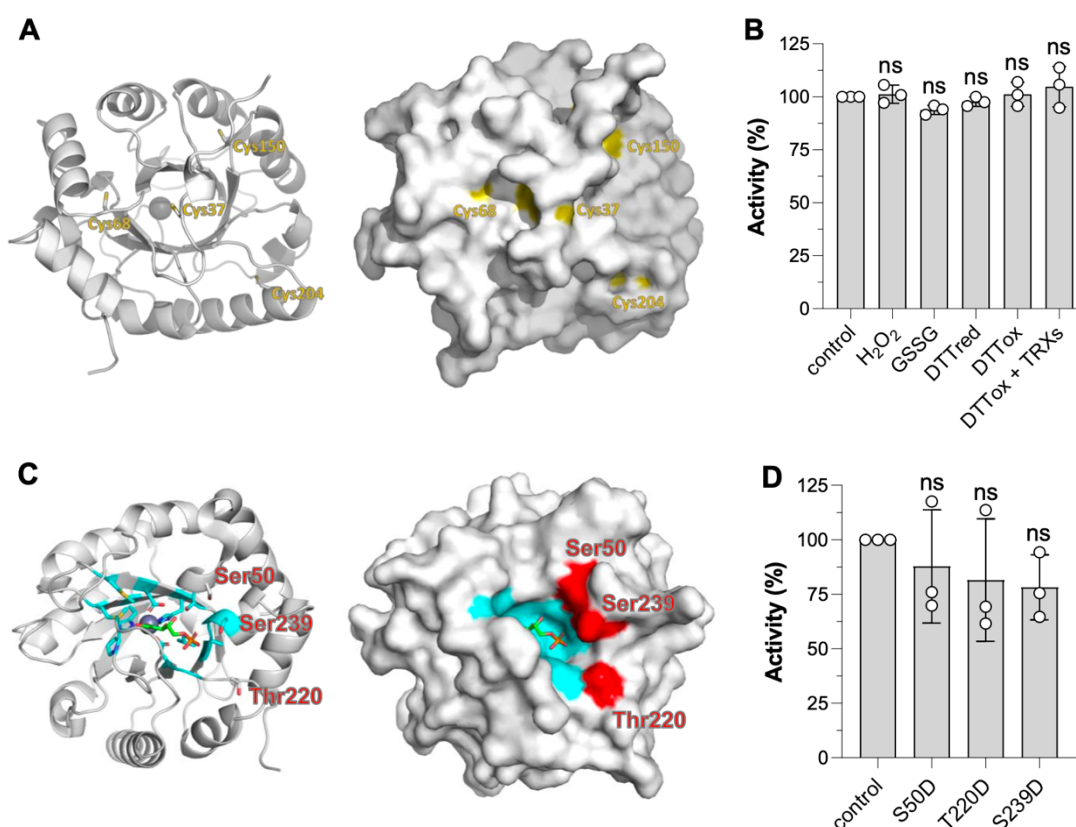


**Figure 5:** Post-translational modification sites of CrRPE1. (A) Cartoon (left) and surface (right) representation of the protein main chain with potential cysteine redox sites highlighted in yellow. (B) Determination of redox sensitivity of CrRPE1 after treatment with oxidizing and reducing compounds (see “Material and Methods” for further details). Control activity was set to 100% and used to calculate the percentage of residual activity of CrRPE1 after incubation (60 min) in the presence of reducing or oxidizing conditions. The data are represented as mean  $\pm$  S.D. ( $n = 3$ ). Statistical analysis was performed using one-way ANOVA followed by a Tukey's post-hoc test for multiple comparisons.  $P$  values reported on graphs as follows: \* $p \leq 0.05$ , \*\* $p \leq 0.01$ , ns: not significant. (C) Cartoon (left) and surface (right) representation of the protein main chain with phosphorylation target amino acids side chains highlighted in red. Xu5P substrate was modelled by alignment with structure 3OVR as in Figure 3. Residues at 4 Å from Xu5P are colored in cyan. (D) Determination of specific activities of phospho-mimicking CrRPE mutants. Purified recombinant CrRPE1 mutants bearing negatively charged aspartate residues replacing

*Ser50, Thr220, or Ser239 were assayed monitoring the PPP-related activity (Ru5P to Xu5P conversion). Activity of wild-type (WT) CrRPE1 was set to 100% and used to calculate the percentage of activity of CrRPE1 mutants. The mutant data are represented as mean  $\pm$  S.D. ( $n = 3$ ). Statistical analysis was performed using one-way ANOVA followed by a Tukey's post-hoc test for multiple comparisons. P values reported on graphs as follows: \* $p \leq 0.05$ , \*\* $p \leq 0.$ , ns: not significant.*

We then examined the redox sensitivity of CrRPE1 after exposure with oxidized DTT alone or in combination with pure recombinant chloroplast thioredoxins from *Chlamydomonas*. As shown in **Figure 5B**, no significant alteration of protein activity was observed indicating that dithiol/disulfide interchanges do not constitute a regulatory mechanism of CrRPE1 activity. The catalytic response of CrRPE1 to oxidative modifications was also assessed in the presence of oxidized glutathione (GSSG), and hydrogen peroxide ( $H_2O_2$ ) alone or in combination with reduced glutathione (GSH). Again, we did not observe any significant variation of CrRPE1 activity with respect to control conditions (**Figure 5B**). Taken together, these results led us to the conclusion that CrRPE1 catalysis is insensitive to possible variations in the redox state of cysteine residues, and this is consistent with the distal positions of the cysteines from the active site (**Figure 5A**).

### **Post-translational phosphorylation sites**

A phosphoproteomic study identified three phosphorylation sites on CrRPE1, namely Ser50, Thr220 and Ser239 (Wang, Gau et al. 2014), which map at the vicinity of the active site, at respectively 11 Å, 17 Å and 13 Å of the zinc ion. In our crystal structure, the three residues expose to solvent their unmodified hydroxyl side chains in a 14 Å arch that aligns at the entrance of the active site (**Figure 5C**). Possible recognition and modification by a kinase are allowed by this solvent exposure. RPE substrates (*i.e.*, Xu5P and Ru5P) are expected to be exchanged with solvent following a path gated by Ser50, Thr220 and Ser239. Phosphorylation of one or more of these sites may hence hinder the formation of the Michaelis-Menten complex, causing a reduction of the enzyme activity.

To assess this hypothesis, we designed and prepared three mutated proteins in which serine or threonine were substituted by aspartates to tentatively mimic with  $\beta$ -carboxylates the introduction of phosphate charges. However, the activity of phospho-mimicking single mutants was not significantly reduced as compared to wild-type (**Figure 5D**) either because phosphorylation introduces more charges and larger steric hindrance than the carboxylate mimics, or because more than one site needs to be modified to affect the enzymatic activity.

## Discussion

In this study we describe the structure of RPE1 from the model microalga *Chlamydomonas reinhardtii* determined by X-ray crystallography at a resolution of 1.9 Å. Recombinant CrRPE1 purifies as a homo-hexamer built from the trimerization of dimers as revealed by in solution analysis and resolution of the 3D structure. We also unveiled that native RPE extracted from algae cultures elutes at the same apparent molecular mass as the purified recombinant protein. Hexamerization is not observed in the crystal structure of non-plant RPE (Liang, Ouyang et al. 2011) but is reported for chloroplastic RPE from potato (*Solanum tuberosum*) (Kopp, Kopriva et al. 1999). Our structural model reveals that the catalytic pocket contains a zinc ion and lies close to both the dimerization and the trimerization interfaces. We propose that the formation of oligomers of RPE supports allosteric cross-talk between subunit active sites, possibly by restricting the mobility of loops around the catalytic pocket. Interestingly, this could contribute to the variation of the enzymatic parameters reported for photosynthetic and non-photosynthetic RPEs. The 3D-structure computes B-factors that quantify the local mobility of the protein in the crystal. We observed four elements of high mobility surrounding the active site (**Figure 3B**), that are good candidates for such an allosteric regulation. The determination of RPE high-resolution structures in the presence of the substrate or in less constrained environments, *e.g.*, by nuclear magnetic resonance (NMR) or single-particle cryogenic electron microscopy (cryo-EM), would provide more information on the dynamic around the active site.

In the chloroplast of Viridiplantae, RPE participates to either PPP or CBB cycle catalyzing the configuration exchange between Ru5P and Xu5P. CrRPE1, which is localized in the chloroplast stroma, likely performs both epimerization reactions given that both pathways co-exist in the same cellular compartment. Catalytic interconversion between Xu5P and Ru5P consists in an acid-base catalysis involving proton abstraction and donation from and to the C3 atom of the substrate and is proposed to occur through the formation of a 2-3-ene-diolate intermediate (Chen, Larimer et al. 1999, Akana, Fedorov et al. 2006). Active site zinc ion along with conserved methionine residues (Met76, Met107, and Met178) participate in the stabilization of this high energy intermediate interacting with carbon 2 and carbon 3 hydroxyl oxygens and carbon 2 oxyanion. Asp74 and Asp216 successively complete the metal coordination sphere and can exchange protons with the reaction intermediates. Depending on the bound substrate, the reaction proceeds with its deprotonation being carried out by one of the two catalytic Asp (*i.e.*, Ru5P to Xu5P conversion) or with the taking of a proton from the second catalytic Asp. Based on the kinetic analysis of CrRPE1 here reported, the algal enzyme has similar affinities for Xu5P and Ru5P with a slightly higher preference for the former. Consequently,

the kinetic direction of the reaction does not depend on the kinetic properties of the enzyme but rather on the intracellular concentration of Xu5P/Ru5P owing to the similar tendency of the two different substrates to bind.

While the enzymatic mechanism is clearly established for several RPE orthologs, it is not yet known whether the enzyme is subject to any regulatory mechanisms. In the present study, we mapped the sites of post-translational modifications that may contribute to the modulation of RPE activity according to the environmental conditions or the energetic demand of the cell. Recent proteomic studies on *Chlamydomonas* cell extracts revealed that RPE has three sites of phosphorylation (Ser50, Thr220, and Ser239) (Wang, Gau et al. 2014, McConnell, Werth et al. 2018). Notwithstanding their distant position in the sequence, all three residues are located in a small area in close proximity to the catalytic pocket. We propose that insertion of one, two or three bulky negatively-charged phosphates might interfere with the binding of the Xu5P/Ru5P substrate and Ru5P/Xu5P product release, thus slowing down RPE catalysis. Phosphorylation sites (Ser50, Thr182, and Ser239) are conserved in other RPE isoforms from photosynthetic organisms and also in the human enzyme, suggesting that phosphorylation might constitute a conserved regulation mode of RPE activity. Future studies are required to shed light on the possible modulation of photosynthetic-related metabolism as other CBB cycle enzymes were identified as putative targets of phosphorylation (Wang, Gau et al. 2014, McConnell, Werth et al. 2018).

Cysteine redox status is coupled with photosystems illumination through the ferredoxin- thioredoxin reduction pathway that was demonstrated to activate several CBB cycle enzymes by reducing regulatory disulfide bonds (for review see (Michelet, Zaffagnini et al. 2013)). In addition, accessible and reactive protein thiols could act as redox sensors of oxidative stress conditions by reacting with reactive oxygen/nitrogen species resulting primarily in S- nitrosylation or S-glutathionylation of proteins (Zaffagnini, Fermani et al. 2019). Considering that CrRPE1 was identified as a putative target of multiple thiol-based redox modifications (Zaffagnini, Bedhomme et al. 2012, Morisse, Zaffagnini et al. 2014, Pérez-Pérez, Mauriès et al. 2017), we evaluated whether CrRPE1 enters these thiol-switching mechanisms due to the redox alteration of its cysteine residues, knowing that only Cys37 is accessible to the solvent. Various attempts made *in vitro*, however, revealed no change in CrRPE1 activity indicating that the redox state of CrRPE1 cysteine(s) is not altered by redox treatments or, alternatively, that cysteine oxidation alone is not sufficient to affect protein catalysis. This is consistent with the position of CrRPE1 cysteines, which are all located far from the catalytic pocket. Overall, this result is reminiscent of the redox sensitivity of triose-phosphate isomerase (TPI), another CBB cycle enzyme. This enzyme was identified as a putative redox target, but no alteration in protein activity was detected upon exposure to various oxidizing treatments (Zaffagnini, Michelet et al.

2014). While being functionally resistant to oxidative modifications, we can hypothesize that alteration of the redox state of CrRPE1 cysteine thiols might induce local conformational changes allowing the enzyme to interact with partner proteins. Such interactions would act as a regulatory mechanism as observed for PRK and glyceraldehyde-3-phosphate dehydrogenase forming an inactive supramolecular complex bridged by CP12 (Gurrieri, Fermani et al. 2021), or alternatively, they might be functional in the formation of larger enzymatic assemblies to channel CBB cycle metabolites and increase metabolic efficiency. In this regard, plant RPE was recently proposed to engage in such an activating complex with RPI (Kuken, Sommer et al. 2018) and to colocalize with CBB cycle enzymes in a liquid partition of the stroma (Wang, Patena et al. 2022, Wang, Patena et al. 2023). Further research on native RPE isolated from algae extracts is needed to evaluate the complexity and dynamics of the RPE proteome and redox-dependent protein-protein interactions.

The current knowledge on kinetic features of plant RPE makes it rather complicated to accurately estimate how the enzyme truly functions in the physiological context of the stroma, which could in turn result into important physiological implications likely to be linked to the substrate to product conversion in the Michaelis-Menten complex. Nonetheless, if we consider the *in vitro* catalytic properties of CrRPE1 related to photosynthetic activity (*i.e.*, CBB cycle-related activity), we can estimate a kinetic modeling in the physiological context of a photosynthetic cell under light conditions. In *Chlamydomonas*, RPE1 concentration was quantified at 3.3  $\mu\text{M}$  (Hammel, Sommer et al. 2020). Considering that (i) RPE1 is the sole isoform present in the chloroplast stroma with a concentration of 3.3  $\mu\text{M}$ , (ii) its substrate Xu5P is available at 10-50  $\mu\text{M}$  (Mettler, Muhlhaus et al. 2014), and (iii) RPE functions with a  $K_M$  of 0.716 mM and a  $k_{cat}$  of 81  $\text{sec}^{-1}$ , we expect an *in vivo* Xu5P to Ru5P flow ranging from 3.7 to 17  $\mu\text{M sec}^{-1}$ . These values are comparable to or lower than those calculated for Rubisco of 18.9  $\mu\text{M sec}^{-1}$  ( $k_{cat} = 5.8 \text{ sec}^{-1}$ ,  $K_M = 0.029 \text{ mM}$  (Tcherkez, Farquhar et al. 2006), [RuBP] = 200  $\mu\text{M}$  (Mettler, Muhlhaus et al. 2014), RbcS stromal concentration of 183  $\mu\text{M}$  (Hammel, Sommer et al. 2020)).

Relying on *in vitro* kinetic constants coupled with metabolome and proteome values of substrates and enzymes concentrations, it appears likely that any increase in RPE protein abundance and optimization of its function may result in improved regeneration efficiency of RuBP and thus increased Rubisco activity as suggested by recent models (Raines 2022) and reported in *Arabidopsis rpe* mutants (Li, Peng et al. 2022). If this was confirmed by further analyses, synthetic biology engineering toolkits available in *Chlamydomonas* and other microalgae (Li, Zhang et al. 2016, Shin, Lim et al. 2016, Crozet, Navarro et al. 2018) could overcome the RPE limitation by either changing protein quantities or altering kinetic features (*i.e.*, substrate affinity and turnover number) to improve catalytic efficiency. Modifying a synthetic CBB cycle from engineering principles will support the

understanding of its physico-chemical properties and open important opportunities to improve photosynthetic efficiency and likely crops yield.

## Materials and methods

### Cloning and protein preparation

*Chlamydomonas* (*Chlamydomonas reinhardtii*) open reading frame of gene Cre02.g116450 of the UniProt entry A8IKW6 was searched for chloroplast transit peptide with ChloroP (Emanuelsson, Nielsen et al. 1999), PredAlgo (Tardif, Atteia et al. 2012) and multiple sequence alignments (**Supplementary Figure 5**). Nucleotide sequence encoding residues 28 to 265 of the predicted mature protein was PCR-amplified from template AV634644 (HC036a02) of *Chlamydomonas* expressed sequence tag database (Kazusa). PCR product was digested by NcoI and BamHI and ligated into pET-3d vector in fusion with an in frame N-terminal hexa- histidine tag, yielding plasmid pET3d-His<sub>6</sub>-CrRPE1. The plasmid was used to transform *Escherichia coli* BL21 Rosetta2 (DE3) expression strain (Merck, Darmstadt, Germany), grown to exponential phase in 1 L lysogeny broth (LB) medium supplemented with 100  $\mu\text{g mL}^{-1}$  ampicillin. Expression was induced by addition of 0.2 mM isopropyl- $\beta$ -D- thiogalactopyranoside (IPTG) for 16 h at 30 °C. Cells were harvested by centrifugation, resuspended in 30 mM Tris-HCl, pH 7.9 (buffer A) and lysed by sonication. Clarified lysate was loaded on 3 mL Ni-NTA resin, washed with buffer A supplemented with 30 mM imidazole and step-eluted with buffer A supplemented with a final imidazole concentration of 250 mM. Eluate was desalted on PD-10 column pre-equilibrated with buffer A and concentrated by ultrafiltration to 5-10 mg mL<sup>-1</sup>. The molecular mass and purity of recombinant protein were examined by SDS-PAGE and the resulting homogeneous protein solutions were stored at -20 °C. Protein concentration was determined spectrophotometrically using a molar extinction coefficient at 280 nm of 14,105 mM<sup>-1</sup> cm<sup>-1</sup> and a molar mass of 26,772.9 Da.

### Analytical size-exclusion chromatography

Recombinant CrRPE1 was injected on a Superose 6 Increase 10/300 GL column (GE Healthcare, Chicago, Illinois) and isocratically eluted in 50 mM Tris-HCl (pH 7.5) and 150 mM KCl at a 0.5 mL min<sup>-1</sup> flow rate. The column was calibrated with standard globular proteins (Bio-Rad,

Hercules, USA), namely bovine thyroglobulin (670 kDa), bovine  $\gamma$ -globulin (158kDa), chicken ovalbumin (44 kDa), and horse myoglobin (17 kDa).

### **Small angle X-rays scattering**

An aliquot of 50  $\mu\text{L}$  of pure CrRPE1 concentrated at 9.5 mg mL<sup>-1</sup> was injected on BioSEC-3 300 size-exclusion chromatography column (Agilent Technologies, Santa Clara, USA) equilibrated in 20 mM Tris-HCl (pH 7.9) and 100 mM NaCl, in line with the small-angle X-ray scattering (SAXS) exposure capillary at the synchrotron beamline SWING (SOLEIL, Saint Aubin, France). Collected diffusion images were analyzed on the application Foxtrot 3.3.4 (Xenocs, Sassenage, France) and the ATSAS 2.8.3 suite (Petoukhov, Franke et al. 2012, Franke, Petoukhov et al. 2017). PrimusQT calculated a radius of gyration of  $35.49 \pm 0.03 \text{ \AA}$  and estimated SAXS CrRPE1 molecular weight at 173,354 Da (Qp), 169,124 Da (MoW), 158,056 Da (Vc), 165,791 Da (size and shape). Oligomeric state was finally computed as mean SAXS molecular weight of 166,581 Da, divided by monomeric recombinant CrRPE1 sequence molecular weight of 26,773 Da and resulting in an estimated number of ~6 subunits per oligomer.

### **Crystallization, structure determination and model refinement**

Sitting drops of 100 nL of pure CrRPE1 concentrated at 9.5 mg mL<sup>-1</sup> were mixed with 100 nL of each of the 384 precipitant conditions of the joint center for structural genomics sparse-matrix screen for crystallization (Qiagen, Hilden, Germany) (Lesley and Wilson 2005). Condition 53 of screen III (160 mM calcium acetate; 80 mM sodium cacodylate pH 6.5; 20% v/v glycerol; 14.4% w/v polyethylene glycol 8,000) yielded macled rods of 100  $\mu\text{m}$  length. Crystals were flash-frozen in cryo-loops and tested for diffraction at ESRF beamline ID30A-3 (Grenoble, France). A collection of 7,200 frames of 0.05° tilt each were collected for a complete dataset of space group P2<sub>1</sub>. Indexation, integration, and scaling were performed with XDS (Kabsch 2010) on the beamline software EDNA (Incardona, Bourenkov et al. 2009). Phases were determined by molecular replacement with PHASER-MR (McCoy, Grosse-Kunstleve et al. 2007) from protomers of CrRPE1 as modelled by homology with PHYRE2 prediction algorithm (Kelley, Mezulis et al. 2015). Twelve subunits were searched for, to respect a solvent content of 48.8 % in the asymmetric unit. Initial density map and structural model were interpreted by iterative cycles of automated building with AUTOBUILD (Terwilliger, Grosse-Kunstleve et al. 2008), manual building with

COOT (Emsley, Lohkamp et al. 2010) and refinement with PHENIX.REFINE (Afonine, Grosse-Kunstleve et al. 2012) until geometry (Ramachandran 97.48% allowed, 2.49% favorable) and statistics ( $R_{\text{work}} = 0.2124$ ;  $R_{\text{free}} = 0.1880$ ) were judged acceptable (Table 1). All other crystallographic utilities were found in the PHENIX package (Adams, Afonine et al. 2010). Images of the crystallographic model were traced with PyMOL (Schrödinger, LLC, New York, USA) version 2.0.6. Relative solvent exposure of cysteine residues was calculated with ASAview (Ahmad, Gromiha et al. 2004) and scaled from 0 (no exposure) to 1 (full exposure). Interface analysis was conducted by PISA (EBI) (Krissinel and Henrick 2007). Crystallographic data are registered at the Protein Data Bank under accession code 7B1W.

### **Circular dichroism spectroscopy**

Samples of CrRPE1 (10.7  $\mu\text{M}$ ) were prepared in buffer A and quantified by spectrophotometric analysis at 280 nm in a 1 cm cell ( $\epsilon_{280} = 13,980 \text{ M}^{-1} \text{ cm}^{-1}$  based on primary structure) (Pace, Vajdos et al. 1995). Far-UV circular dichroism (CD) spectra (250–195 nm) were measured at room temperature on a J-810 spectropolarimeter (Jasco, Japan), using a QS-quartz cell with 0.5 mm optical pathlength (Hellma Analytics, Germany), a 2 nm spectral bandwidth, a 20 nm  $\text{min}^{-1}$  scanning speed, a 4 sec data integration time, a 0.2 nm data interval and an accumulation cycle of 3 scans per spectrum. The resulting CD spectra were blank-corrected and converted to molar units per residue ( $\Delta\epsilon_{\text{res}}$ , in  $\text{M}^{-1} \text{ cm}^{-1}$ ).

### ***In vitro* reporter assays of CrRPE1 activity**

The epimerization of Ru5P into Xu5P (*i.e.*, PPP-related activity) was measured using a 4-step coupled assay as previously described (Nowitzki, Wyrich et al. 1995) (**Supplementary Figure 6**), with minor modifications. As reporter enzymes we used the recombinant transketolase and triose-phosphate isomerase from *Chlamydomonas* (CrTK and CrTPI, respectively) (Zaffagnini, Michelet et al. 2014, Pasquini, Fermani et al. 2017), and the rabbit muscle  $\alpha$ -glycerophosphate dehydrogenase ( $\alpha$ -GDH; Sigma-Aldrich, Saint-Louis, USA). Prior to the activity assays, CrRPE1 was separated by size-exclusion chromatography and eluted fractions corresponding to the hexameric form were pooled and desalted in buffer A. The catalytic activity was assayed spectrophotometrically at 25 °C in a reaction mixture containing 50 mM Tris-HCl (pH 7.9), 15 mM  $\text{MgCl}_2$ , 0.1 mM thiamine pyrophosphate (TPP), 0.1% (w/v) bovine serum albumin, 1  $\mu\text{M}$  CrTK, 4 nM CrTPI, 2 units  $\text{mL}^{-1}$   $\alpha$ -GDH, 2 mM ribose-5-phosphate (R5P), 0.25–4 mM Ru5P, and

0.2 mM NADH. The reaction was initiated by the addition of CrRPE1 and the enzymatic activity was measured by following the decrease in the absorption at 340 nm using a Cary60 UV/Vis spectrophotometer (Agilent Technologies). Previous studies highlighted interferences in the assay derived from traces of Xu5P in the Ru5P powder and from traces of epimerase activity in the auxiliary enzymes from commercial sources (Wood 1979). To establish whether NADH oxidation was effectively dependent upon CrRPE1 catalysis (*i.e.* Xu5P formation and subsequent reactions catalyzed by CrTK, CrTPI and  $\alpha$ -GDH; **Supplementary Figure 6**), we measured the consumption of NADH in the absence of CrRPE1 and found a limited NADH oxidation corresponding to 5% of the initial NADH ( $\sim 10 \mu\text{M}$ ) that we ascribed to Xu5P contamination in the Ru5P solution.

To measure the CBB cycle-related activity, namely the conversion of Xu5P to Ru5P, we employed a recently developed 4-step coupled assay involving three reporter enzymes: the recombinant form of phosphoribulokinase from *Chlamydomonas* (CrPRK, (Gurrieri, Del Giudice et al. 2019)), and commercial pyruvate kinase (PK) and lactate dehydrogenase (LDH) from *Saccharomyces cerevisiae* (Sigma-Aldrich, Saint-Louis, USA) (**Supplementary Figure 6**). The catalytic activity was measured at 25 °C in a reaction mixture containing 50 mM Tris-HCl (pH 7.9), 10 mM  $\text{MgCl}_2$ , 2 mM adenosine triphosphate (ATP), 2.5 mM phosphoenolpyruvate (PEP), 5 units  $\text{mL}^{-1}$  PK, 6 units  $\text{mL}^{-1}$  LDH, 6 units  $\text{mL}^{-1}$  CrPRK, 0.075-1.5 mM Xu5P, and 0.2 mM NADH. The reaction was initiated by the addition of CrRPE1 and monitored at 340 nm using a Cary60 UV/Vis spectrophotometer (Agilent Technologies). CrRPE1-dependent enzymatic activities were determined after subtracting background activities measured in the absence of CrRPE1.

### **Protein stability and redox sensitivity**

The stability of CrRPE1 was assessed by incubating the enzyme (5  $\mu\text{M}$ ) at 4 °C or 25 °C in buffer A. At the indicated times, aliquots (1–2  $\mu\text{l}$ ) were withdrawn to carry out activity measurements as described above. The redox sensitivity of CrRPE1 (5  $\mu\text{M}$ ) was evaluated by treating the enzyme with reducing agents (10 mM 2-mercaptoethanol or 10 mM dithiothreitol, DTT) or oxidizing molecules such as 2 mM oxidized glutathione (GSSG), or 2 mM hydrogen peroxide ( $\text{H}_2\text{O}_2$ ), or 10 mM oxidized DTT in the absence/presence of recombinant chloroplast thioredoxins f2, m, x, y, and z from *Chlamydomonas* (5  $\mu\text{M}$  each) (Lemaire, Tedesco et al. 2018, Marchand, Fermani et al. 2019). All incubations were carried out at 25 °C in buffer A. Control experiments were performed by incubating the enzyme in the presence of buffer alone. At the indicated times, aliquots (1–2  $\mu\text{l}$ ) were withdrawn to carry out activity measurements as described above.

### **Metal stability and requirement**

The stability of the zinc ion in CrRPE1 and the possible activation by exogenous zinc ion were assessed by incubating the protein (10  $\mu\text{M}$ ) in the presence of chelating agents (10 mM EDTA or 10 mM TPEN) or zinc chloride (1, 0.1 and 0.01 mM). All incubations were carried out for 60 min at 25 °C in buffer A. Control experiments were performed by incubating the enzyme in the presence of buffer alone. At the indicated times, aliquots (1–2  $\mu\text{l}$ ) were withdrawn to carry out activity measurements as described above.

### **Extraction of algal proteins**

A single colony of wild-type *Chlamydomonas reinhardtii* strain D66 was grown in 50 mL TAP medium (Gorman and Levine 1965) under continuous 120 rpm agitation and illumination at an intensity of 36  $\mu\text{E s}^{-1} \text{m}^{-2}$ . At  $20 \times 10^6$  cells  $\text{mL}^{-1}$  the culture was harvested by 5 min centrifugation at 3,000 g and stored at -20 °C. Cell pellet (600 mg) was thawed and resuspended in 12 mL of 20 mM Tris-HCl supplemented with 100 mM NaCl (pH 7.9), and lysed by passage through CellD (Constant systems, Daventry, UK) at 30 kPSI. Soluble fraction was separated by 10 min centrifugation at 30,000 g at 4 °C and filtered through 0.2  $\mu\text{m}$  membrane. The resulting suspension (300  $\mu\text{L}$ ) was injected on a Superose 6 Increase 10/300 GL column and eluted isocratically at 0.3  $\text{mL min}^{-1}$  in 20 mM Tris-HCl supplemented with 150 mM KCl (pH 7.5). Elution fractions (400  $\mu\text{L}$ ) were collected, starting from column dead volume 7.2 mL (fraction 18) and up to column total volume 28.0 mL (fraction 70), snap-frozen in liquid nitrogen, and stored at -20 °C for western blot detection using rabbit polyclonal antibodies raised against recombinant CrRPE1 (Covalab, Bron, France).

### **Western blot**

Size-exclusion chromatography of *Chlamydomonas* soluble protein extract fractions 19 to 44 were mixed with reducing Laemmli loading buffer, boiled and resolved by 200 V electrophoresis through SDS-PAGE. Proteins were subsequently transferred to Protran 0.2  $\mu\text{m}$  nitrocellulose membrane (GE Healthcare, Chicago, USA). Efficiency of protein transfer was checked by Ponceau staining. Primary polyclonal anti-CrRPE1 antibody was incubated overnight at a dilution of 1:5,000. Secondary anti-rabbit IgG coupled to peroxidase (Sigma- Aldrich reference A9169, Saint Louis, USA) was incubated 2 h at a dilution of 1:10,000 and revealed by ECL Prime colorimetric assay (GE Healthcare, Chicago, USA).

**Replicates and statistical analyses**

All the results reported are representative of at least three independent biological replicates and expressed as mean  $\pm$  S.D. Statistical analysis was performed using one-way ANOVA followed by a Tukey's post-hoc test for multiple comparisons. P values reported on graphs as follows: \* $p \leq 0.05$ , \*\* $p \leq 0.01$ .

**Accession Numbers**

Sequence data from this article can be found in the EMBL data library under accession number PNW74744.1.

## References

- Adams, P. D., P. V. Afonine, G. Bunkoczi, V. B. Chen, I. W. Davis, N. Echols, J. J. Headd, L. W. Hung, G. J. Kapral, R. W. Grosse-Kunstleve, A. J. McCoy, N. W. Moriarty, R. Oeffner, R. J. Read, D. C. Richardson, J. S. Richardson, T. C. Terwilliger and P. H. Zwart (2010). "PHENIX: a comprehensive Python-based system for macromolecular structure solution." *Acta Crystallogr D Biol Crystallogr* 66(Pt 2): 213-221.
- Afonine, P. V., R. W. Grosse-Kunstleve, N. Echols, J. J. Headd, N. W. Moriarty, M. Mustyakimov, T. C. Terwilliger, A. Urzhumtsev, P. H. Zwart and P. D. Adams (2012). "Towards automated crystallographic structure refinement with phenix.refine." *Acta Crystallogr D Biol Crystallogr* 68(Pt 4): 352-367.
- Ahmad, S., M. Gromiha, H. Fawareh and A. Sarai (2004). "ASAView: database and tool for solvent accessibility representation in proteins." *BMC Bioinformatics* 5: 51.
- Akana, J., A. A. Fedorov, E. Fedorov, W. R. Novak, P. C. Babbitt, S. C. Almo and J. A. Gerlt (2006). "D- Ribulose 5-phosphate 3-epimerase: functional and structural relationships to members of the ribulose-phosphate binding (beta/alpha)<sub>8</sub>-barrel superfamily." *Biochemistry* 45(8): 2493-2503.
- Benson, A. A., J. A. Bassham, M. Calvin, A. G. Hall, H. E. Hirsch, S. Kawaguchi, V. Lynch and N. E. Tolbert (1952). "The path of carbon in photosynthesis. XV. Ribulose and sedoheptulose." *J Biol Chem* 196(2): 703-716.
- Caruthers, J., J. Bosch, F. Buckner, W. Van Voorhis, P. Myler, E. Worthey, C. Mehlin, E. Boni, G. DeTitta, J. Luft, A. Lauricella, O. Kalyuzhnyi, L. Anderson, F. Zucker, M. Soltis and W. G. Hol (2006). "Structure of a ribulose 5-phosphate 3-epimerase from *Plasmodium falciparum*." *Proteins* 62(2): 338- 342.
- Chen, Y. R., F. C. Hartman, T. Y. Lu and F. W. Larimer (1998). "D-Ribulose-5-phosphate 3-epimerase: cloning and heterologous expression of the spinach gene, and purification and characterization of the recombinant enzyme." *Plant Physiol* 118(1): 199-207.
- Chen, Y. R., F. W. Larimer, E. H. Serspersu and F. C. Hartman (1999). "Identification of a catalytic aspartyl residue of D-ribulose 5-phosphate 3-epimerase by site-directed mutagenesis." *J Biol Chem* 274(4): 2132-2136.
- Crozet, P., F. J. Navarro, F. Willmund, P. Mehrshahi, K. Bakowski, K. J. Lauersen, M. E. Perez-Perez, P. Auroy, A. Gorchs Rovira, S. Sauret-Gueto, J. Niemeyer, B. Spaniol, J. Theis, R. Trosch, L. D. Westrich, K. Vavitsas, T. Baier, W. Hubner, F. de Carpentier, M. Cassarini, A. Danon, J. Henri, C. H. Marchand, M. de Mia, K. Sarkissian, D. C. Baulcombe, G. Peltier, J. L. Crespo, O. Kruse, P. E. Jensen, M. Schroda, A.
- G. Smith and S. D. Lemaire (2018). "Birth of a Photosynthetic Chassis: A MoClo Toolkit Enabling Synthetic Biology in the Microalga *Chlamydomonas reinhardtii*." *ACS Synth Biol* 7(9): 2074-2086. Davis, L., N. Lee and L. Glaser (1972). "On the mechanism of the pentose phosphate epimerases." *J Biol Chem* 247(18): 5862-5866.
- Emanuelsson, O., H. Nielsen and G. von Heijne (1999). "ChloroP, a neural network-based method for predicting chloroplast transit peptides and their cleavage sites." *Protein Sci* 8(5): 978-984.
- Emerson, R. and W. Arnold (1932). "The Photochemical Reaction in Photosynthesis." *J Gen Physiol* 16(2): 191-205.
- Emsley, P., B. Lohkamp, W. G. Scott and K. Cowtan (2010). "Features and development of Coot." *Acta Crystallogr D Biol Crystallogr* 66(Pt 4): 486-501.
- Franke, D., M. V. Petoukhov, P. V. Konarev, A. Panjkovich, A. Tuukkanen, H. D. T. Mertens, A. G. Kikhney, N. R. Hajizadeh, J. M. Franklin, C. M. Jeffries and D. I. Svergun (2017). "ATSAS 2.8: a comprehensive data analysis suite for small-angle scattering from macromolecular solutions." *J Appl Crystallogr* 50(Pt 4): 1212-1225.
- Gonzalez, S. N., W. M. Valsecchi, D. Maugeri, J. M. Delfino and J. J. Cazzulo (2017). "Structure, kinetic characterization and subcellular localization of the two ribulose 5-phosphate epimerase isoenzymes from *Trypanosoma cruzi*." *PLoS One* 12(2): e0172405.
- Gorman, D. S. and R. P. Levine (1965). "Cytochrome f and plastocyanin: their sequence in the photosynthetic electron transport chain of *Chlamydomonas reinhardtii*." *Proc Natl Acad Sci U S A* 54(6): 1665-1669.
- Gouet, P., E. Courcelle, D. I. Stuart and F. Metoz (1999). "ESPrift: analysis of multiple sequence alignments in PostScript." *Bioinformatics* 15(4): 305-308.
- Gurrieri, L., A. Del Giudice, N. Demitri, G. Falini, N. V. Pavel, M. Zaffagnini, M. Polentarutti, P. Crozet,

- C. H. Marchand, J. Henri, P. Trost, S. D. Lemaire, F. Sparla and S. Fermani (2019). "Arabidopsis and Chlamydomonas phosphoribulokinase crystal structures complete the redox structural proteome of the Calvin-Benson cycle." *Proc Natl Acad Sci U S A* 116(16): 8048-8053.
- Gurrieri, L., S. Fermani, M. Zaffagnini, F. Sparla and P. Trost (2021). "Calvin-Benson cycle regulation is getting complex." *Trends Plant Sci* 26(9): 898-912.
- Hammel, A., F. Sommer, D. Zimmer, M. Stitt, T. Mühlhaus and M. Schroda (2020). "Overexpression of Sedoheptulose-1,7-Bisphosphatase Enhances Photosynthesis in Chlamydomonas reinhardtii and Has No Effect on the Abundance of Other Calvin-Benson Cycle Enzymes." *Front Plant Sci* 11: 868.
- Incardona, M. F., G. P. Bourenkov, K. Levik, R. A. Pieritz, A. N. Popov and O. Svensson (2009). "EDNA: a framework for plugin-based applications applied to X-ray experiment online data analysis." *J Synchrotron Radiat* 16(Pt 6): 872-879.
- Jakoby, W. B., D. O. Brummond and S. Ochoa (1956). "Formation of 3-phosphoglyceric acid by carbon dioxide fixation with spinach leaf enzymes." *J Biol Chem* 218(2): 811-822.
- Jelakovic, S., S. Kopriva, K. H. Süss and G. E. Schulz (2003). "Structure and catalytic mechanism of the cytosolic D-ribulose-5-phosphate 3-epimerase from rice." *J Mol Biol* 326(1): 127-135.
- Jelakovic, S., S. Kopriva, K. H. Süss and G. E. Schulz (2003). "Structure and catalytic mechanism of the cytosolic D-ribulose-5-phosphate 3-epimerase from rice." *J Mol Biol* 326(1): 127-135.
- Johnson, M. P. (2016). "Photosynthesis." *Essays Biochem* 60(3): 255-273.
- Johnson, X. and J. Alric (2013). "Central carbon metabolism and electron transport in Chlamydomonas reinhardtii: metabolic constraints for carbon partitioning between oil and starch." *Eukaryot Cell* 12(6): 776-793.
- Jurus, E., D. Engel, K. Star, K. Monson, J. Brandi, L. E. Felberg, D. H. Brookes, L. Wilson, J. Chen, K. Liles, M. Chun, P. Li, D. W. Gohara, T. Dolinsky, R. Konecny, D. R. Koes, J. E. Nielsen, T. Head-Gordon,
- W. Geng, R. Krasny, G. W. Wei, M. J. Holst, J. A. McCammon and N. A. Baker (2018). "Improvements to the APBS biomolecular solvation software suite." *Protein Sci* 27(1): 112-128.
- Kabsch, W. (2010). "Xds." *Acta Crystallogr D Biol Crystallogr* 66(Pt 2): 125-132.
- Karmali, A., A. F. Drake and N. Spencer (1983). "Purification, properties and assay of D-ribulose 5-phosphate 3-epimerase from human erythrocytes." *Biochem J* 211(3): 617-623.
- Kelley, L. A., S. Mezulis, C. M. Yates, M. N. Wass and M. J. Sternberg (2015). "The Pyre2 web portal for protein modeling, prediction and analysis." *Nat Protoc* 10(6): 845-858.
- Kiely, M. E., A. L. Stuart and T. Wood (1973). "Partial purification and kinetic properties of ribulose-5-phosphate ketol-isomerase and ribulose-5-phosphate 3-epimerase from various sources." *Biochim Biophys Acta* 293(2): 534-541.
- Kopp, J., S. Kopriva, K. H. Süss and G. E. Schulz (1999). "Structure and mechanism of the amphibolic enzyme D-ribulose-5-phosphate 3-epimerase from potato chloroplasts." *J Mol Biol* 287(4): 761-771. Kopp, J., S. Kopriva, K. H. Süss and G. E. Schulz (1999). "Structure and mechanism of the amphibolic enzyme D-ribulose-5-phosphate 3-epimerase from potato chloroplasts." *J Mol Biol* 287(4): 761-771. Kopriva, S., A. Koprivova and K. H. Süss (2000). "Identification, cloning, and properties of cytosolic D-ribulose-5-phosphate 3-epimerase from higher plants." *J Biol Chem* 275(2): 1294-1299.
- Krissinel, E. and K. Henrick (2007). "Inference of macromolecular assemblies from crystalline state." *J Mol Biol* 372(3): 774-797.
- Kuken, A., F. Sommer, L. Yaneva-Roder, L. C. Mackinder, M. Hohne, S. Geimer, M. C. Jonikas, M. Schroda, M. Stitt, Z. Nikoloski and T. Mettler-Altmann (2018). "Effects of microcompartmentation on flux distribution and metabolic pools in Chlamydomonas reinhardtii chloroplasts." *Elife* 7.
- Lemaire, S. D., D. Tedesco, P. Crozet, L. Michelet, S. Fermani, M. Zaffagnini and J. Henri (2018). "Crystal Structure of Chloroplastic Thioredoxin f2 from Chlamydomonas reinhardtii Reveals Distinct Surface Properties." *Antioxidants (Basel)* 7(12).
- Lesley, S. A. and I. A. Wilson (2005). "Protein production and crystallization at the joint center for structural genomics." *J Struct Funct Genomics* 6(2-3): 71-79.
- Li, X., R. Zhang, W. Patena, S. S. Gang, S. R. Blum, N. Ivanova, R. Yue, J. M. Robertson, P. A. Lefebvre,
- S. T. Fitz-Gibbon, A. R. Grossman and M. C. Jonikas (2016). "An Indexed, Mapped Mutant Library Enables Reverse Genetics Studies of Biological Processes in Chlamydomonas reinhardtii." *Plant Cell* 28(2): 367-387.
- Li, Y., L. Peng, X. Wang and L. Zhang (2022). "Reduction in chloroplastic ribulose-5-phosphate-3-epimerase decreases photosynthetic capacity in Arabidopsis." *Frontiers in Plant Science* 13.

- Liang, W., S. Ouyang, N. Shaw, A. Joachimiak, R. Zhang and Z. J. Liu (2011). "Conversion of D-ribulose 5-phosphate to D-xylulose 5-phosphate: new insights from structural and biochemical studies on human RPE." *Faseb j* 25(2): 497-504.
- Marchand, C. H., S. Fermani, J. Rossi, L. Gurrieri, D. Tedesco, J. Henri, F. Sparla, P. Trost, S. D. Lemaire and M. Zaffagnini (2019). "Structural and Biochemical Insights into the Reactivity of Thioredoxin h1 from *Chlamydomonas reinhardtii*." *Antioxidants (Basel)* 8(1).
- McConnell, E. W., E. G. Werth and L. M. Hicks (2018). "The phosphorylated redox proteome of *Chlamydomonas reinhardtii*: Revealing novel means for regulation of protein structure and function." *Redox Biol* 17: 35-46.
- McCoy, A. J., R. W. Grosse-Kunstleve, P. D. Adams, M. D. Winn, L. C. Storoni and R. J. Read (2007). "Phaser crystallographic software." *J Appl Crystallogr* 40(Pt 4): 658-674.
- Meloni, M., L. Gurrieri, S. Fermani, L. Velie, F. Sparla, P. Crozet, J. Henri and M. Zaffagnini (2023). "Ribulose-1,5-bisphosphate regeneration in the Calvin-Benson-Bassham cycle: Focus on the last three enzymatic steps that allow the formation of Rubisco substrate." *Front Plant Sci* 14: 1130430.
- Merchant, S. S., S. E. Prochnik, O. Vallon, E. H. Harris, S. J. Karpowicz, G. B. Witman, A. Terry, A. Salamov, L. K. Fritz-Laylin, L. Marechal-Drouard, W. F. Marshall, L. H. Qu, D. R. Nelson, A. A. Sanderfoot, M. H. Spalding, V. V. Kapitonov, Q. Ren, P. Ferris, E. Lindquist, H. Shapiro, S. M. Lucas, J. Grimwood, J. Schmutz, P. Cardol, H. Cerutti, G. Chanfreau, C. L. Chen, V. Cognat, M. T. Croft, R. Dent, S. Dutcher, E. Fernandez, H. Fukuzawa, D. Gonzalez-Ballester, D. Gonzalez-Halphen, A. Hallmann, M. Hanikenne, M. Hippler, W. Inwood, K. Jabbari, M. Kalanon, R. Kuras, P. A. Lefebvre, S. D. Lemaire, A. V. Lobanov, M. Lohr, A. Manuell, I. Meier, L. Mets, M. Mittag, T. Mittelmeier, J. V. Moroney, J. Moseley, C. Napoli, A. M. Nedelcu, K. Niyogi, S. V. Novoselov, I. T. Paulsen, G. Pazour, S. Purton, J. P. Ral, D. M. Riano-Pachon, W. Riekhof, L. Rymarquis, M. Schroda, D. Stern, J. Umen, R. Willows, N. Wilson, S. L. Zimmer, J. Allmer, J. Balk, K. Bisova, C. J. Chen, M. Elias, K. Gendler, C. Hauser, M. R. Lamb, H. Ledford, J. C. Long, J. Minagawa, M. D. Page, J. Pan, W. Pootakham, S. Roje, A. Rose, E. Stahlberg, A. M. Terauchi, P. Yang, S. Ball, C. Bowler, C. L. Dieckmann, V. N. Gladyshev, P. Green, R. Jorgensen, S. Mayfield, B. Mueller-Roeber, S. Rajamani, R. T. Sayre, P. Brokstein, I. Dubchak, D. Goodstein, L. Hornick, Y. W. Huang, J. Jhaveri, Y. Luo, D. Martinez, W. C. Ngau, B. Otilar, A. Poliakov, A. Porter, L. Szajkowski, G. Werner, K. Zhou, I. V. Grigoriev, D. S. Rokhsar and A. R. Grossman (2007). "The *Chlamydomonas* genome reveals the evolution of key animal and plant functions." *Science* 318(5848): 245-250.
- Mettler, T., T. Muhlhaus, D. Hemme, M. A. Schottler, J. Rupprecht, A. Idoine, D. Veyel, S. K. Pal, L. Yaneva-Roder, F. V. Winck, F. Sommer, D. Vosloh, B. Seiwert, A. Erban, A. Burgos, S. Arvidsson, S. Schonfelder, A. Arnold, M. Gunther, U. Krause, M. Lohse, J. Kopka, Z. Nikoloski, B. Mueller-Roeber, L. Willmitzer, R. Bock, M. Schroda and M. Stitt (2014). "Systems Analysis of the Response of Photosynthesis, Metabolism, and Growth to an Increase in Irradiance in the Photosynthetic Model Organism *Chlamydomonas reinhardtii*." *Plant Cell* 26(6): 2310-2350.
- Michelet, L., M. Zaffagnini, S. Morisse, F. Sparla, M. E. Pérez-Pérez, F. Francia, A. Danon, C. H. Marchand, S. Fermani, P. Trost and S. D. Lemaire (2013). "Redox regulation of the Calvin-Benson cycle: something old, something new." *Front Plant Sci* 4: 470.
- Morisse, S., M. Zaffagnini, X. H. Gao, S. D. Lemaire and C. H. Marchand (2014). "Insight into protein S- nitrosylation in *Chlamydomonas reinhardtii*." *Antioxid Redox Signal* 21(9): 1271-1284.
- Nowitzki, U., R. Wyrich, P. Westhoff, K. Henze, C. Schnarrenberger and W. Martin (1995). "Cloning of the amphibolic Calvin cycle/OPPP enzyme D-ribulose-5-phosphate 3-epimerase (EC 5.1.3.1) from spinach chloroplasts: functional and evolutionary aspects." *Plant Mol Biol* 29(6): 1279-1291.
- Pace, C. N., F. Vajdos, L. Fee, G. Grimsley and T. Gray (1995). "How to measure and predict the molar absorption coefficient of a protein." *Protein Sci* 4(11): 2411-2423.
- Pasquini, M., S. Fermani, D. Tedesco, C. Sciabolini, P. Crozet, M. Naldi, J. Henri, U. Vothknecht, C. Bertucci, S. D. Lemaire, M. Zaffagnini and F. Francia (2017). "Structural basis for the magnesium- dependent activation of transketolase from *Chlamydomonas reinhardtii*." *Biochim Biophys Acta Gen Subj* 1861(8): 2132-2145.
- Pérez-Pérez, M. E., A. Mauriès, A. Maes, N. J. Tourasse, M. Hamon, S. D. Lemaire and C. H. Marchand (2017). "The Deep Thioredoxome in *Chlamydomonas reinhardtii*: New Insights into Redox Regulation." *Mol Plant* 10(8): 1107-1125.
- Petoukhov, M. V., D. Franke, A. V. Shkumatov, G. Tria, A. G. Kikhney, M. Gajda, C. Gorba, H. D. Mertens, P. V. Konarev and D. I. Svergun (2012). "New developments in the ATSAS program package for small-angle scattering data analysis." *J Appl Crystallogr* 45(Pt 2): 342-350.
- Raines, C. A. (2022). "Improving plant productivity by re-tuning the regeneration of RuBP in the Calvin-Benson-Bassham cycle." *New Phytol*.
- Shin, S. E., J. M. Lim, H. G. Koh, E. K. Kim, N. K. Kang, S. Jeon, S. Kwon, W. S. Shin, B. Lee, K. Hwangbo,

- J. Kim, S. H. Ye, J. Y. Yun, H. Seo, H. M. Oh, K. J. Kim, J. S. Kim, W. J. Jeong, Y. K. Chang and B. R. Jeong (2016). "CRISPR/Cas9-induced knockout and knock-in mutations in *Chlamydomonas reinhardtii*." *Sci Rep* 6: 27810.
- Sobota, J. M. and J. A. Imlay (2011). "Iron enzyme ribulose-5-phosphate 3-epimerase in *Escherichia coli* is rapidly damaged by hydrogen peroxide but can be protected by manganese." *Proc Natl Acad Sci U S A* 108(13): 5402-5407.
- Tardif, M., A. Atteia, M. Specht, G. Cogne, N. Rolland, S. Brugiere, M. Hippler, M. Ferro, C. Bruley, G. Peltier, O. Vallon and L. Cournac (2012). "PredAlgo: a new subcellular localization prediction tool dedicated to green algae." *Mol Biol Evol* 29(12): 3625-3639.
- Tcherkez, G. G., G. D. Farquhar and T. J. Andrews (2006). "Despite slow catalysis and confused substrate specificity, all ribulose biphosphate carboxylases may be nearly perfectly optimized." *Proc Natl Acad Sci U S A* 103(19): 7246-7251.
- Teige, M., M. Melzer and K. H. Suss (1998). "Purification, properties and in situ localization of the amphibolic enzymes D-ribulose 5-phosphate 3-epimerase and transketolase from spinach chloroplasts." *Eur J Biochem* 252(2): 237-244.
- Terwilliger, T. C., R. W. Grosse-Kunstleve, P. V. Afonine, N. W. Moriarty, P. H. Zwart, L. W. Hung, R. J. Read and P. D. Adams (2008). "Iterative model building, structure refinement and density modification with the PHENIX AutoBuild wizard." *Acta Crystallogr D Biol Crystallogr* 64(Pt 1): 61-69.
- Wang, H., B. Gau, W. O. Slade, M. Juergens, P. Li and L. M. Hicks (2014). "The global phosphoproteome of *Chlamydomonas reinhardtii* reveals complex organellar phosphorylation in the flagella and thylakoid membrane." *Mol Cell Proteomics* 13(9): 2337-2353.
- Wang, L., W. Patena, K. A. Van Baalen, Y. Xie, E. R. Singer, S. Gavrilenko, M. Warren-Williams, L. Han, H. R. Harrigan, V. Chen, V. T. N. P. Ton, S. Kyin, H. H. Shwe, M. H. Cahn, A. T. Wilson, J. Hu, D. J. Schnell, C. D. McWhite and M. Jonikas (2022). "A Chloroplast Protein Atlas Reveals Novel Structures and Spatial Organization of Biosynthetic Pathways." *bioRxiv*: 2022.2005.2031.493820.
- Wang, L., W. Patena, K. A. Van Baalen, Y. Xie, E. R. Singer, S. Gavrilenko, M. Warren-Williams, L. Han, H. R. Harrigan, L. D. Hartz, V. Chen, V. Ton, S. Kyin, H. H. Shwe, M. H. Cahn, A. T. Wilson, M. Onishi, J. Hu, D. J. Schnell, C. D. McWhite and M. C. Jonikas (2023). "A chloroplast protein atlas reveals punctate structures and spatial organization of biosynthetic pathways." *Cell* 186(16): 3499- 3518.e3414.
- Wise, E. L., J. Akana, J. A. Gerlt and I. Rayment (2004). "Structure of D-ribulose 5-phosphate 3- epimerase from *Synechocystis* to 1.6 Å resolution." *Acta Crystallogr D Biol Crystallogr* 60(Pt 9): 1687- 1690.
- Wood, T. (1979). "Purification and properties of D-ribulose-5-phosphate 3-epimerase from calf liver." *Biochim Biophys Acta* 570(2): 352-362.
- Zaffagnini, M., M. Bedhomme, H. Groni, C. H. Marchand, C. Puppo, B. Gontero, C. Cassier-Chauvat, P. Decottignies and S. D. Lemaire (2012). "Glutathionylation in the photosynthetic model organism *Chlamydomonas reinhardtii*: a proteomic survey." *Mol Cell Proteomics* 11(2): M111 014142.
- Zaffagnini, M., M. Bedhomme, H. Groni, C. H. Marchand, C. Puppo, B. Gontero, C. Cassier-Chauvat, P. Decottignies and S. D. Lemaire (2012). "Glutathionylation in the photosynthetic model organism *Chlamydomonas reinhardtii*: a proteomic survey." *Mol Cell Proteomics* 11(2): M111.014142.
- Zaffagnini, M., S. Fermani, C. H. Marchand, A. Costa, F. Sparla, N. Rouhier, P. Geigenberger, S. D. Lemaire and P. Trost (2019). "Redox Homeostasis in Photosynthetic Organisms: Novel and Established Thiol-Based Molecular Mechanisms." *Antioxid Redox Signal* 31(3): 155-210.
- Zaffagnini, M., L. Michelet, C. Sciabolini, N. Di Giacinto, S. Morisse, C. H. Marchand, P. Trost, S. Fermani and S. D. Lemaire (2014). "High-resolution crystal structure and redox properties of chloroplastic triosephosphate isomerase from *Chlamydomonas reinhardtii*." *Mol Plant* 7(1): 101-120.

## **CHAPTER III: “Phosphoribulokinase abundance is not limiting the Calvin-Benson-Bassham cycle in *Chlamydomonas reinhardtii*”**

**Nicolas D. Boisset<sup>1, 2, 3,\*</sup>, Giusi Favoino<sup>1,\*†</sup>, Maria Meloni<sup>4</sup>, Lucile Jomat<sup>1</sup>, Corinne Cassier-Chauvat<sup>5</sup>, Mirko Zaffagnini<sup>4</sup>, Stéphane D. Lemaire<sup>1,2,‡</sup> and Pierre Crozet<sup>1,2,6,‡</sup>**

<sup>1</sup>Laboratoire de Biologie Computationnelle et Quantitative, Institut de Biologie Paris-Seine, Sorbonne Université, CNRS, UMR 7238, Paris, France

<sup>2</sup>Laboratoire de Biologie Moléculaire et Cellulaire des Eucaryotes, Institut de Biologie Physico-Chimique, Sorbonne Université, CNRS, UMR 8226, Paris France.

<sup>3</sup>Doctoral School of Plant Sciences, Université Paris-Saclay, Saint-Aubin, France.

<sup>4</sup>Department of Pharmacy and Biotechnology, Bologna, Italy.

<sup>5</sup>CEA, CNRS, Institute for Integrative Biology of the Cell (I2BC), Université Paris-Saclay, Gif-sur-Yvette, France

<sup>6</sup>Polytech-Sorbonne, Sorbonne Université, Paris, France.

\*authors participated equally to this work

*This work was published in 2023 on **Frontiers in Plant Science** and is available at:*

DOI: 10.3389/fpls.2023.1230723

## Summary

Improving photosynthetic efficiency in plants and microalgae is of utmost importance to support the growing demand for food, feed, energy and chemicals while limiting the consume of natural resources (*i.e.*, land, water, nutrients). Notably, limitations in photosynthetic light conversion efficiency can be directly attributed to kinetic bottlenecks within the Calvin-Benson-Bassham cycle (CBB cycle), the main CO<sub>2</sub>-fixing metabolic pathway in photosynthetic organisms. The main limitations in the CBB cycle are known to reside in the carboxylation step catalyzed by the enzyme ribulose-1,5-bisphosphate carboxylase/oxygenase (Rubisco) and in the regeneration phase of the cycle.

Phosphoribulokinase (PRK) is an enzyme unique to the CBB cycle and catalyzes the phosphorylation of ribulose-5-phosphate into ribulose-1,5-bisphosphate (RuBP), generating the substrate of Rubisco. Its active form is a homodimer, where each monomer contains 2 pairs of conserved cysteine residues, located at the N- and C-terminal portions of the polypeptide. The biochemical and regulatory properties of PRK have been extensively investigated *in vitro* (Michelet et al., 2013; Le Moigne et al., 2023; Meloni et al., 2023). These studies have demonstrated that PRK regulation takes place through two main mechanisms, both depending on redox post-translational modifications (PTMs) controlled by an enzymatic class of oxidoreductases called thioredoxins (TRXs). The first regulatory mechanism consists in the direct regulation of PRK catalytic capacity through the TRX system. In this context, the TRX-mediated reduction of the N-terminal PRK disulfide bond triggers enzyme activation by facilitating the entrance of the substrate into the active site. As opposite, the formation of the disulfide bond causes the blockage of catalysis, but the system controlling this oxidative mechanism is yet to be fully understood.

The second system regulating PRK activity involves the formation of a regulatory ternary complex with the protein CP12 and the CBB cycle enzyme glyceraldehyde-3-phosphate dehydrogenase (GAPDH) (Marri et al., 2008; Marri et al., 2009; Thieulin-Pardo et al., 2015; Gurrieri et al., 2021; Gurrieri et al., 2023). This supramolecular complex, induced by oxidizing conditions (*e.g.*, dark conditions) and indirectly regulated by the TRX system, strongly inhibit the catalytic activity of both PRK and GAPDH.

Many studies are present in literature demonstrating the limitations on the CBB cycle flux imposed by the enzymes Rubisco and sedoheptulose-1,7-bisphosphatase (SBPase), but the limitations imposed by the third CBB cycle specific enzyme, PRK, remain largely unexplored. Previous studies focusing on possible limitation on the CBB cycle imposed by PRK were conducted in tobacco. Here, antisense RNA approaches were used to alter the level of PRK, revealing that only plants with a PRK activity

below 15% showed decreased carbon fixation (Paul et al., 1995; Banks et al., 1999). This suggests that endogenous PRK content might not be limiting the CBB cycle in tobacco. In a study conducted in the unicellular green alga *Chlamydomonas reinhardtii*, a strain lacking PRK activity was reported to be inefficient for photosynthetic carbon fixation (Moll and Levine, 1970). However, this mutant was later found to revert spontaneously precluding its use for engineering approaches (Smith, 2000). The present study is focused on the analysis of the possible limitation that PRK could impose on autotrophic growth capacity in the green microalga *Chlamydomonas reinhardtii*. This organism is considered a robust model system for studies regarding photosynthesis. In fact, its genomes are sequenced and annotated, and culture conditions are highly developed together with molecular biology and synthetic techniques (Vavitsas et al., 2019) permitting its efficient manipulation. Moreover, since it is a mixotrophic organism, the generation and maintenance of photosynthetic mutants is possible. Synthetic biology approaches are possible thanks to the generation of a Golden Gate Modular Cloning (MoClo) toolkit specifically optimized for *Chlamydomonas* (Crozet et al., 2018). This tool is based on Type IIS restriction enzymes and allows the easy and fast assembly of complex multigenic constructs starting from basic gene parts (*e.g.*, promoters, CDS, terminators). Moreover, the availability of a genetic library composed of more than 100 gene parts codon-optimized for the *Chlamydomonas* nuclear genome expands the possibilities for development of new synthetic gene constructs.

In this work we have characterized a PRK *knock-out* mutant strain and showed that in the absence of PRK, *Chlamydomonas* cannot grow photoautotrophically while functional complementation with a synthetic construct allowed restoration of photoautotrophy. By employing the MoClo kit we were able to efficiently generate genetic constructs with the aim of obtaining different levels of *in vivo* PRK expression. The use of the Design–Build–Test–Learn cycle permitted us to overcome the initial limitations by improving the design of the transcriptional units. Diverse combinations of DNA parts including PRK endogenous promoter and introns enabled us to obtain mutant lines with PRK levels comparable to the wild type and even higher (overexpressing strains). Eventually, a collection of strains with PRK levels between 25% and 250% of wild type endogenous PRK levels was generated and characterized. Immunoblot and growth assays revealed that the overexpression of PRK did not increase photosynthetic growth, suggesting that the endogenous level of PRK in *Chlamydomonas* is not limiting the Calvin-Benson-Bassham cycle under optimal light conditions.

## Results

### The absence of PRK impacts the growth of *Chlamydomonas*

PRK is an enzyme unique to the CBB cycle encoded by a single gene in *Chlamydomonas reinhardtii* (Cre12.g554800\_4532). To comprehensively investigate the function of the PRK-encoding gene (PRK1), we used the mutant LMJ.RY0402.119555 (hereafter named  $\Delta$ PRK) from the Clip Library, generated by random insertion of the paromomycin resistance gene (Li et al., 2019). This mutant strain harbors an insertion (named CIB1) in the exon 7 of the PRK1 gene (**Figure 1a**) as identified by junction sequencing with a 95% confidence (Li et al., 2019). In the mutant strain, the position of the CIB insertion in exon 7 was verified by PCR analysis with primer couples allowing specific detection of a single band related to either the WT PRK1 gene or the disrupted PRK1 gene containing the CIB1 insertion (**Figure 1b**).

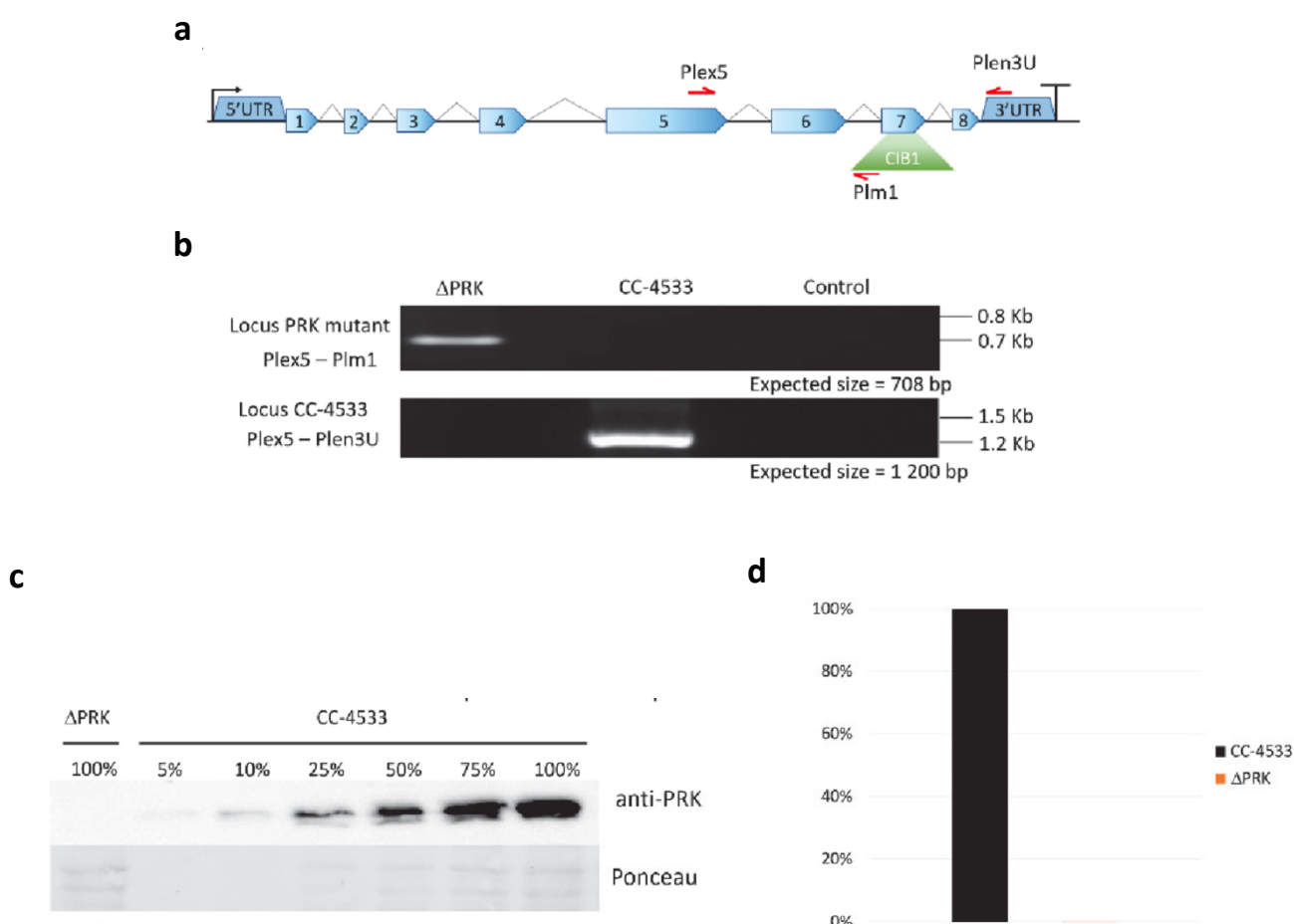


**Figure 1:** Characterization of the PRK mutant. (a) Representation of the PRK genomic locus in the Clip mutant with the CIB1 insertion (containing the paromomycin resistance gene) positioned in exon 7. (b) PCR on genomic DNA to confirm the presence of the CIB1 insertion in the PRK gene in the mutant strain (Locus PRK mutant) and

the presence of the intact PRK locus (Locus CC-4533) in the reference strain. (c) Anti-PRK western blot on total soluble protein extract of CC-4533 and  $\Delta$ PRK strains (100% corresponds to 12  $\mu$ g of total protein). (d) Total activity of reduced PRK. Desalted crude extracts of CC-4533 and  $\Delta$ PRK were reduced with 20 mM DTT prior to activity measurement.

To determine the impact of the CIB1 insertion on PRK protein expression, total protein extracts from the mutant strain ( $\Delta$ PRK) and the reference strain (CC-4533) were analyzed by western blotting. The PRK signal was very strong in the reference strain, while no signal was detected in the mutant strain (**Figure 1c**). To evaluate the detection threshold of our custom made anti-PRK polyclonal antibody, a gradient of total protein from the reference strain CC-4533 was utilized and a PRK signal could still be detected using 5% of the total protein extract (**Figure 1c**). This finding indicates that the mutant strain has a PRK content lower than 5% of that in CC-4533, strongly suggesting that the presence of the CIB insertion disrupts PRK protein expression.

Since PRK activity is unique in Chlamydomonas, the absence of the PRK protein should correlate with a loss of the corresponding enzymatic activity. As PRK is activated by reduction (Marri et al., 2008), we treated the total soluble protein extract from each strain with the strong reducing agent DTT to obtain maximal PRK activity. Consistently, no PRK activity was detected in the mutant strain compared to the reference strain (**Figure 1d**). Consequently, the LMJ.RY0402.119555 strain is a knock-out strain with undetectable levels of both PRK protein and activity.

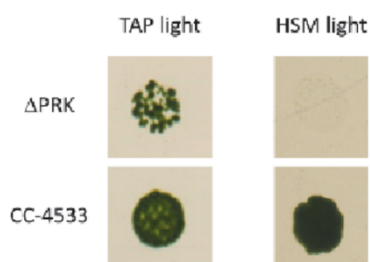


**Figure 2:** Spot test of CC-4533 and  $\Delta$ PRK strains in TAP and minimal (HSM) media under continuous light (25°C, 100  $\mu$ mol photons  $m^{-2} s^{-1}$ ). The reference strain CC-4533 was used as a control.  $10^6$  cells were spotted and incubated for 7 days prior to observation.

To examine the functional consequences of PRK deficiency in Chlamydomonas we analyzed the growth phenotype of the  $\Delta$ PRK mutant under various conditions. Since PRK is central to the CBB cycle, we tested the ability of this mutant to grow in the presence of light and acetate as a carbon source (TAP light, mixotrophic conditions) or in the presence of light in a minimal medium without

acetate (HSM light, strictly photoautotrophic conditions). In solid media, the  $\Delta$ PRK mutant could not grow photoautotrophically but was able to grow in the presence of light and acetate, albeit more slowly than the reference strain (**Figure 2**). To further characterize the growth phenotype of the  $\Delta$ PRK strain in mixotrophic conditions, we monitored its growth over time in a photobioreactor in TAP liquid medium, compared with the CC-4533 reference strain (**Figure 3**).

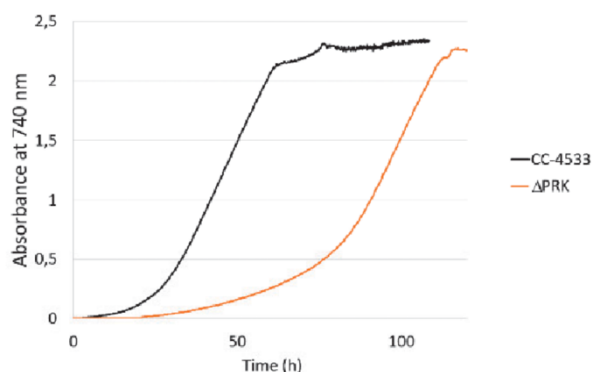


**Figure 3:** Growth profile comparison between PRK and CC-4533. Cultures were inoculated at  $10^5$  cells/mL and incubated in TAP under light ( $25\text{ }^\circ\text{C}$  and  $100\text{ }\mu\text{mol m}^{-2}\text{ s}^{-1}$ ).

The growth profiles revealed a pronounced difference between the two strains. Indeed, the mutant grew much slower than CC-4533, explaining the difference observed on solid media. These data indicate that the  $\Delta$ PRK strain is non-photoautotrophic and strongly imply that the PRK1 gene is essential for photosynthetic carbon fixation, and that the absence of the CBB cycle limits the growth of the knock-out strain. To demonstrate that this phenotype is due to the absence of PRK, we sought to functionally complement the  $\Delta$ PRK strain.

### Overexpression of PRK does not affect cell growth

To verify the possible limitation that PRK could have on Chlamydomonas autotrophic growth capacity, we designed synthetic genetic constructs to obtain overexpressing strains and be able to analyze their relative growth response. To do so, various types of constructs were built and tested, differing on the base of the promoter used (*i.e.*, PSAD or endogenous 5' UTR and promoter) and of the presence or absence of introns in the coding sequence (CDS) of the PRK1 gene. The PSAD genetic elements were chosen since they were previously shown to allow strong constitutive expression of a reporter gene (Crozet et al., 2018).

The following results were obtained by employing the synthetic constructs that incorporate the endogenous PRK1 promoter and its 5'UTR to drive either expression of the PRK1 CDS devoid of introns or the native PRK1 coding sequence containing natural introns (**Figure 4a**). Indeed, it is now well-established that the presence of introns in the synthetic construct is frequently required to ensure high-level expression of a transgene in *Chlamydomonas* (Lumbreras and Purton, 1998; Fuhrmann et al., 1999; Baier et al., 2018). The presence of introns could boost gene expression due to the presence of a transcriptional enhancer, through a process called Intron-mediated enhancement that stimulates transcription in a direct manner or through interaction with the spliceosome (Schroda, 2019; Baier et al., 2020). In this work, an online tool has been developed to design *Chlamydomonas* transgenes with artificial introns (Jaeger et al., 2019).

The PRK1 promoter and the native PRK1 gene coding sequences were amplified by PCR from *Chlamydomonas* CC-4533 genomic DNA and cloned as level 0 MoClo parts. These parts were employed to build the two transcriptional units coupled to the hygromycin resistance gene to generate pCMM-25 and pCMM-26 (**Figure 4a**), which were subsequently introduced into *Chlamydomonas* nuclear genome by transformation through electroporation. The selection of transformants was carried out on TAP solid medium supplemented with hygromycin. Mutant strains subsequently analyzed derived from transformation with the synthetic construct pCMM-26 of either the CC-4533 or the  $\Delta$ PRK *Chlamydomonas* genetic backgrounds (obtaining A2 or  $\beta$ 3 strains, respectively) (**Figure 4b**). Another analyzed mutant strain derived from the transformation of the  $\Delta$ PRK *Chlamydomonas* background with the synthetic construct pCMM-25 (D5 strain) (**Figure 4b**).

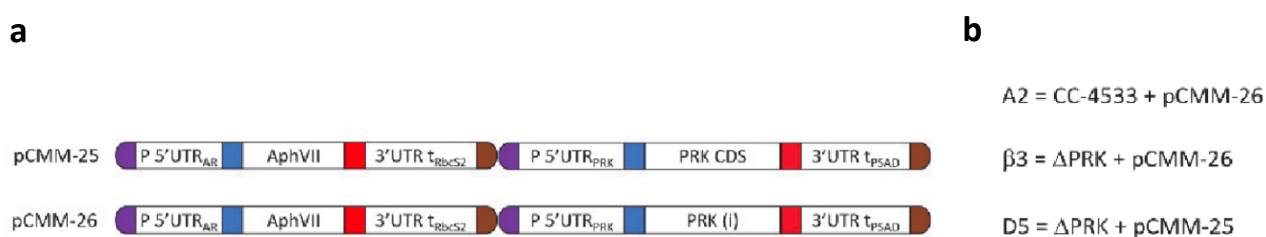


**Figure 4:** Experimental design for overexpression of PRK. (a) Design of the pCMM-25 and pCMM-26 constructs. (b) Design of mutant strains obtained from the insertion of one the two synthetic constructs (pCMM-25 or pCMM-26) in different genetic backgrounds (CC-4533 or  $\Delta$ PRK).

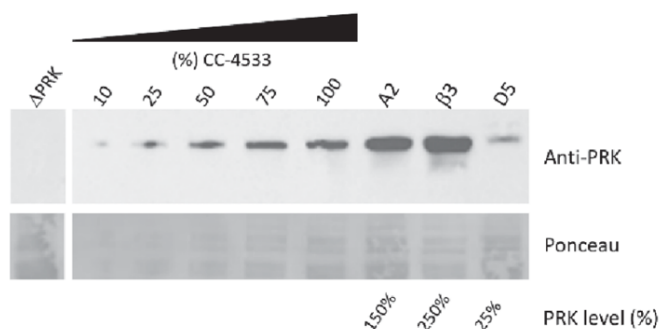


**Figure 5:** Overexpression of PRK. Anti-PRK western blot on total soluble protein extracts of the  $\Delta$ PRK, CC-4533, and transformed strains as indicated. 100% corresponds to 12  $\mu$ g of total protein. A gradient of the total protein extract of the strain CC-4533 was used for the relative quantification of the PRK content in the different complemented strains, indicated as PRK level (%).

To evaluate the level of expression of the transgenic PRK we carried out immunoblot analysis (**Figure 5**). As a result, we observed two strains overexpressing PRK, where the A2 strain accumulates 1.5-fold compared to the reference strain (CC-4533), while  $\beta$ 3 reached an accumulation of 2.5-fold compared to CC-4533. A mutant strain with diminished accumulation of PRK was also obtained (D5) accumulating the 25% of PRK compared to the CC-4533. This indicates that the presence of introns in the PRK1 coding sequence is crucial for achieving high level expression of the transgene, consistently with what observed in previous studies (Lumbreras and Purton, 1998; Fuhrmann et al., 1999; Baier et al., 2018; Lauersen et al., 2018; Schroda, 2019; Baier et al., 2020). Whether the high-level expression is linked to a specific PRK1 intron could be an interesting question to be addressed in future studies.

To determine the autotrophic growth capacity of the different mutant lines, growth analysis was performed in a photobioreactor in liquid HSM medium under three different light intensities (**Figures 6a-c**). The growth of the two overexpressing strains (A2 and  $\beta$ 3) was comparable to the CC-4533 strain. Specifically, at high light intensity (300  $\text{mmol m}^{-2} \text{s}^{-1}$ ) growth of  $\beta$ 3 strain was similar to CC-4533, while at lower light intensities it showed a marginally slower growth kinetics compared to the two other strains. In low light, the A2 strain displayed a slower growth rate, possibly due to the site of random insertion of the transgene. Nonetheless, these results clearly show that overexpression of PRK does not lead to an increased growth. This suggests that the endogenous level of PRK in *Chlamydomonas* is not limiting the Calvin-Benson-Bassham cycle under optimal growth conditions.

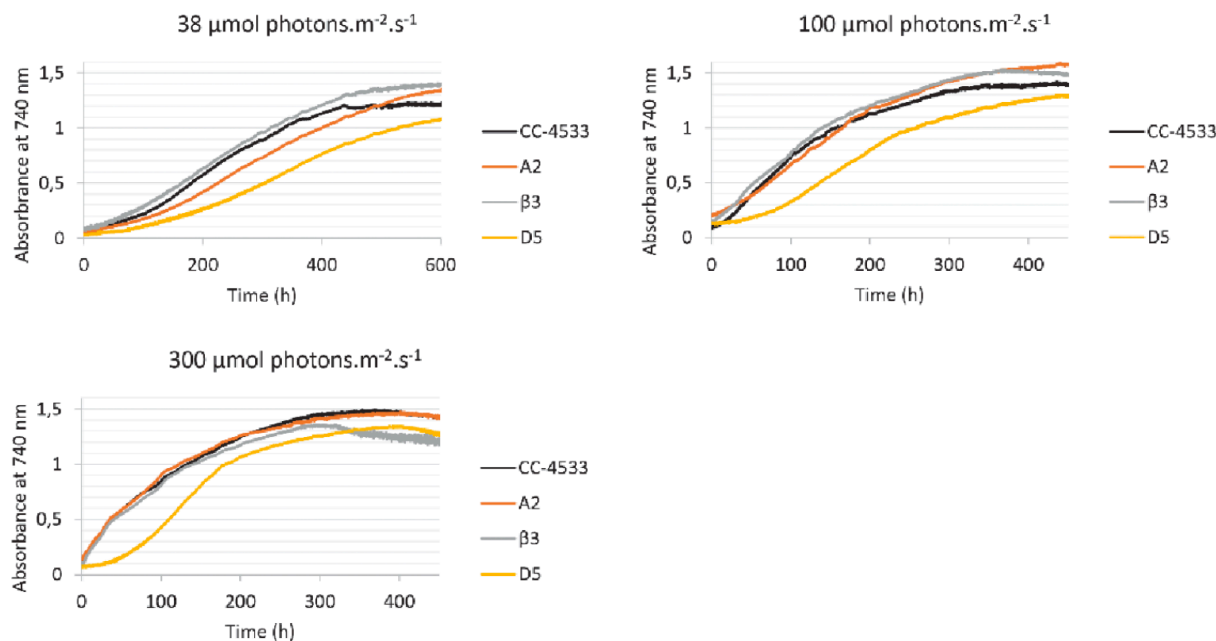


**Figure 6a-c.** Growth curves of CC-4533 and mutant strains. Cultures were inoculated at  $10^5$  cells/mL and incubated in HSM at 25 °C under three distinct light intensities as indicated.

## Discussion

In the present study, we have characterized a PRK knock-out mutant of *C. reinhardtii* and utilized this strain to investigate the limitations imposed by PRK expression level on the CBB cycle. We demonstrated that PRK is essential for photosynthesis in *C. reinhardtii* through a comprehensive analysis of the mutant and its functional complementation. The essentiality of PRK for photoautotrophic growth was previously suggested by a large-scale systematic characterization of gene function in *Chlamydomonas* (Fauser et al., 2022). Previously, the only analyses of PRK deficiency in *Chlamydomonas* were obtained in the F-60 mutant generated by chemical mutagenesis and without a full validation by functional complementation (Moll and Levine, 1970). This mutant was also shown to spontaneously revert ((Smith, 2000) and personal observation of the authors). Through our functional complementation approach, we demonstrated that, in the conditions tested, overexpression of PRK does not improve *Chlamydomonas* growth. This suggests that the endogenous PRK content is not limiting the CBB cycle in this model alga. PRK is therefore in excess but this excess is much more limited than observed in tobacco, where PRK limitation was only observed below 15% of the WT level (Paul et al., 1995; Banks et al., 1999). This implies that a slight decrease of PRK level or PRK activity would be sufficient to limit the CBB cycle in *Chlamydomonas*. This

may allow PRK to play a more prominent role in the control of the CBB cycle turnover in *Chlamydomonas*, for example under conditions leading to light-dependent regulation of PRK activity mediated by thioredoxins and/or CP12 (Gurrieri et al., 2021; Gurrieri et al., 2023). Nevertheless, the CBB cycle functioning is different in algae compared to land plants, particularly because a carbon concentration mechanism (CCM) named pyrenoid increases carbon fixation by Rubisco (Barrett et al., 2021) and likely imposes a stronger requirement for RuBP production by PRK to sustain growth, especially in non-limiting light conditions. Metabolite profiling revealed that RuBP is indeed significantly more concentrated in algae and cyanobacteria compared to land plants (Clapero et al., 2023). This higher concentration of RuBP may be required to ensure that substantial concentration gradients drive rapid diffusion into the CCM compartment that houses Rubisco (Treves et al., 2022). Finally, the PRK knock-out strain along with the genetic elements we have generated may constitute useful tools to explore PRK regulation *in vivo* using functional complementation with PRK variants harboring targeted mutations such as mutations to serine/alanine of regulatory cysteines.

## Materials and methods

### Strains, media and growth conditions

The strains used in this study originate from the CLiP library (Liet al., 2019): the reference strain (CC-4533) and  $\Delta$ PRK (LMJ.RY0402.119555), both obtained from the Chlamydomonas Resource Center. Chlamydomonas cells were grown on agar plates or liquid medium, using Tris-acetate-phosphate (TAP) medium (Gorman and Levine, 1965) or High salt medium (HSM) (Sueoka, 1960) at 25°C, under continuous light (40-60  $\mu\text{mol photons m}^{-2} \text{s}^{-1}$ ) or dark (in particular for the  $\Delta$ PRK strain), and shaking for liquid cultures (130 rpm). Antibiotics used were hygromycin B (10  $\mu\text{g/mL}$ ) and paromomycin (15  $\mu\text{g/mL}$ ). Growth analyses were performed in the Algem® labscale double photobioreactor systems (Algenuity, Stewartby, UK) for large volume cultures (400 mL) or in the Algem® HT-24 (Algenuity) photobioreactor for small volume cultures (25 mL). All chemicals were obtained from Sigma- Aldrich unless otherwise specified.

### Plasmid construction

Protein and nucleic acid designs were performed in silico using Serial Cloner 2.6.1 software. All recipient plasmids are derived from the MoClo original toolkit (Weber et al., 2011). Phosphoribulokinase (PRK) cDNA sequence (Cre12.g554800; Uniprot accession P19824) was obtained by PCR on reverse translated mRNA extracts from a D66 strain (Schnell and Lefebvre, 1993) using primers TTGAAGACTTAATGGCTTTCCTACTATGCGCGC and TTGAAGACAACCCACGGGCACAACGTCC. The resulting PRK coding sequence was designed for the position B3-B4 of the Chlamydomonas MoClo toolkit (Crozet et al., 2018), and cloned into the plasmid pAGM1287 (Weber et al., 2011). Two other constructs were obtained by PCR on genomic DNA of CC-4533 strain using the following primers: TTGAAGACTTCTCAGGAGGCCCTGGGCTTTAGCCCC and AAGAAGACAACCTCGAGTACATGATGCATGTAACAGC AGCAATGAT for the PRK promoter, TTGAAGACTTCTCATACTGCGTCTTGGGTTCGGTGCGCT and CAGAAGACAACCTCGCATTGGTTGCTAACAGCTCGACGC for the PRK 5'UTR, and TTGAAGACTTCTCAAATGGCTTTCCTACTATGCGCGC and TTGAAGACTTCTCAAATGGCTTTCCTACTATGCGCGC for the PRK CDS with introns. Each part was cloned into the plasmid pAGM9121 (Patronet al., 2015). The level 1 plasmids were built in pICH47742 with the endogenous promoter and 5'UTR of PRK and the 3'UTR/ Terminator of PSAD controlling the expression of the PRK CDS with or without its endogenous introns. Level M plasmids

were built in pAGM8031 combining p1-013 (hygromycin resistance gene) (de Carpentier et al., 2020) with the PRK transcriptional unit resulting in pCMM-25 ( $P_{PRK}$ -PRK<sub>CDS</sub>) and pCMM-26 ( $P_{PRK}$ -PRK<sub>(i)</sub>).

### **Chlamydomonas transformation**

Transformations were performed as previously described (Crozet et al., 2018), using 55 fmol of purified cassette after BsaI-HF (for antibiotic screening with pM plasmids) digestion (New England Biolabs) of the corresponding plasmid. The transformation leads to random insertion of the transgene in the nuclear genome. Transformants were selected on HSM-agar medium or TAP-agar containing hygromycin B (20 mg/L). Transformants were analyzed after 5 to 7 days of growth in HSM liquid medium in medium light (50  $\mu\text{mol photons m}^{-2} \text{s}^{-1}$ ).

### **Chlamydomonas genotyping**

Cells were grown in TAP medium up to  $4\text{-}5 \times 10^6$  cells  $\text{mL}^{-1}$ , harvested by centrifugation at 2500 g for 5 min at room temperature (RT), and lysed in 400  $\mu\text{L}$  of extraction buffer (0.2 M Tris-HCl pH 7.5, 200 mM NaCl; 25 mM EDTA; 0.5% SDS) for 10 min at 37 °C under agitation (1400 rpm). After centrifugation at 17000 g for 3 min at RT, the genomic DNA contained in the supernatant was precipitated with one volume of isopropanol for 10 min at room temperature and collected by centrifugation at 17000 g for 10 min at RT. The pellet DNA was then washed with 70% ethanol, spinned (17000 g for 3 min at RT) and the pellet was air-dried prior to resuspension in water. PCR was performed using the Quick- LoadR©Taq2×Master Mix (New England Biolabs) according to the manufacturer's instructions. Primers used were Plex5: AAGGACGCTGACATG, Plm1: CCTGATGGATGGTTC, PLPSAD: TTGAAGACAATCATCTCAATGGGTGTG and Plen3U: AGGTGCCAAAGCAAC.

### **Protein extraction**

Cells were grown in TAP medium up to  $4\text{-}5 \times 10^6$  cells  $\text{mL}^{-1}$ , harvested by centrifugation at 5000 g for 10 min at 4 °C, resuspended in 500  $\mu\text{L}$  of Buffer B (30 mM Tris-HCl pH 7.9, 0.5 mM EDTA, antiprotease complete tablets (Roche)), and lysed twice by using glass beads and vortexing (30 sec vortex, 1 min on ice). The total extract was then clarified by centrifugation (2x10 min at 21000 g) and the concentration of the total soluble protein was determined by BCA Protein Assay using bovine serum albumin (BSA) as standard.

### Western blot

Total soluble proteins were analyzed by western blotting with a custom rabbit polyclonal primary antibody raised against *Chlamydomonas* PRK (Covalab, Bron, France) subsequently detected by secondary anti-rabbit antibody coupled to horseradish peroxidase (Sigma-Aldrich reference A9169, Saint Louis, USA). Detection was done with commercial ECL peroxidase assay (GE Healthcare, Chicago IL USA) with a Chemidoc (Bio-Rad, Hercules CA USA).

### Spot tests

Cells were grown until exponential phase ( $2-6 \times 10^6$  cells  $\text{mL}^{-1}$ ) and serial dilutions in TAP or HSM media were made. The dilution was spotted (10  $\mu\text{L}$ ) onto TAP and HSM agar plates at different light intensities. The plates were then scanned after 7 days using a Perfection V800 Photo scanner (Epson). This analysis was automatized using an Opentrons OT-2.

### Growth analysis in photobioreactor

Growth analyses were performed using the Algem® lab-scale double photobioreactor system (Algenity, Stewartby, United Kingdom) under continuous light ( $100 \mu\text{mol photons m}^{-2} \text{s}^{-1}$ ) and 120 rpm agitation in TAP or high salt medium (HSM). The strains were pre-acclimated for at least 24h in the same medium prior to growth analysis. The absorbance at 740 nm was recorded every 10 min using the built-in sensor. The maximal growth rate was determined as the maximal slope of the growth curve ( $\Delta\text{Abs}/\Delta\text{time}$ ). Growth curves obtained with the AlgemHT24 photobioreactor were performed in autotrophic conditions and with three different light intensities, *i.e.*, low light at  $38 \mu\text{mol.m}^{-2}.\text{s}^{-1}$ , medium light at  $100 \mu\text{mol.m}^{-2}.\text{s}^{-1}$ , and high light at  $300 \mu\text{mol.m}^{-2}.\text{s}^{-1}$ .

### Enzymatic activity

To eliminate metabolites that could interfere with enzymatic activity measurements, the crude extract was desalted in Sephadex G-25 Columns (GE Healthcare) and reduced with 20 mM DTT in 50 mM Tris-HCl (pH 7.5) for 30 min at 30 °C. The PRK activity was measured as previously described (Gurrieri et al., 2019). Briefly, the reaction mixture contained 50 mM Tris-HCl (pH 7.5), 1 mM EDTA, 40 mM KCl, 10 mM  $\text{MgCl}_2$ , 5 U/mL Pyruvate kinase, 6 U/mL Lactate dehydrogenase, 2.5 mM phosphoenolpyruvate, 2 mM ATP, and 0.2 mM NADH. The desalted crude extract was added

and the background was recorded for 1-2 min. PRK activity was then measured by adding 0.5 mM ribulose-5-phosphate and monitoring the oxidation of NADH at 340 nm.

## References

- Adler, L., Diaz-Ramos, A., Mao, Y., Pukacz, K.R., Fei, C., and McCormick, A.J. (2022). New horizons for building pyrenoid-based CO<sub>2</sub>-concentrating mechanisms in plants to improve yields. *Plant Physiol* 190(3), 1609-1627. doi: 10.1093/plphys/kiac373.
- Amthor, J.S., Bar-Even, A., Hanson, A.D., Millar, A.H., Stitt, M., Sweetlove, L.J., et al. (2019). Engineering Strategies to Boost Crop Productivity by Cutting Respiratory Carbon Loss. *Plant Cell* 31(2), 297-314. doi: 10.1105/tpc.18.00743.
- Atkinson, N., Mao, Y., Chan, K.X., and McCormick, A.J. (2020). Condensation of Rubisco into a proto-pyrenoid in higher plant chloroplasts. *Nat Commun* 11(1), 6303. doi: 10.1038/s41467-020-20132-0.
- Baier, T., Jacobebbinghaus, N., Einhaus, A., Lauersen, K.J., and Kruse, O. (2020). Introns mediate post-transcriptional enhancement of nuclear gene expression in the green microalga *Chlamydomonas reinhardtii*. *PLoS Genet* 16(7), e1008944. doi: 10.1371/journal.pgen.1008944.
- Baier, T., Wichmann, J., Kruse, O., and Lauersen, K.J. (2018). Intron-containing algal transgenes mediate efficient recombinant gene expression in the green microalga *Chlamydomonas reinhardtii*. *Nucleic Acids Res* 46(13), 6909-6919. doi: 10.1093/nar/gky532.
- Banks, F.M., Driscoll, S.P., Parry, M.A., Lawlor, D.W., Knight, J.S., Gray, J.C., et al. (1999). Decrease in phosphoribulokinase activity by antisense RNA in transgenic tobacco. Relationship between photosynthesis, growth, and allocation at different nitrogen levels. *Plant Physiol* 119(3), 1125-1136. doi: 10.1104/pp.119.3.1125.
- Bar-Even, A. (2018). Daring metabolic designs for enhanced plant carbon fixation. *Plant Sci* 273, 71-83. doi: 10.1016/j.plantsci.2017.12.007.
- Bar-Even, A., Noor, E., Lewis, N.E., and Milo, R. (2010). Design and analysis of synthetic carbon fixation pathways. *Proc Natl Acad Sci U S A* 107(19), 8889-8894. doi: 10.1073/pnas.0907176107.
- Barrett, J., Girr, P., and Mackinder, L.C.M. (2021). Pyrenoids: CO<sub>2</sub>-fixing phase separated liquid organelles. *Biochim Biophys Acta Mol Cell Res* 1868(5), 118949. doi: 10.1016/j.bbamcr.2021.118949.
- Clapero, V., Arrivault, S., and Stitt, M. (2023). Natural variation in metabolism of the Calvin-Benson cycle. *Semin Cell Dev Biol*. doi: 10.1016/j.semedb.2023.02.015.
- Crozet, P., Navarro, F.J., Willmund, F., Mehrshahi, P., Bakowski, K., Lauersen, K.J., et al. (2018). Birth of a Photosynthetic Chassis: A MoClo Toolkit Enabling Synthetic Biology in the Microalga *Chlamydomonas reinhardtii*. *ACS Synth Biol* 7(9), 2074-2086. doi: 10.1021/acssynbio.8b00251.
- da Fonseca-Pereira, P., Siqueira, J.A., Monteiro-Batista, R.C., Vaz, M., Nunes-Nesi, A., and Araujo, W.L. (2022). Using synthetic biology to improve photosynthesis for sustainable food production. *J Biotechnol* 359, 1-14. doi: 10.1016/j.jbiotec.2022.09.010.
- de Carpentier, F., Le Peillet, J., Boisset, N.D., Crozet, P., Lemaire, S.D., and Danon, A. (2020). Blasticidin S Deaminase: A New Efficient Selectable Marker for *Chlamydomonas reinhardtii*. *Front Plant Sci* 11, 242. doi: 10.3389/fpls.2020.00242.
- Ding, F., Wang, M., Zhang, S., and Ai, X. (2016). Changes in SBPase activity influence photosynthetic capacity, growth, and tolerance to chilling stress in transgenic tomato plants. *Sci Rep* 6, 32741. doi: 10.1038/srep32741.
- Driever, S.M., Simkin, A.J., Alotaibi, S., Fisk, S.J., Madgwick, P.J., Sparks, C.A., et al. (2017). Increased SBPase activity improves photosynthesis and grain yield in wheat grown in greenhouse conditions. *Philos Trans R Soc Lond B Biol Sci* 372(1730). doi: 10.1098/rstb.2016.0384.
- Durao, P., Aigner, H., Nagy, P., Mueller-Cajar, O., Hartl, F.U., and Hayer-Hartl, M. (2015). Opposing effects of folding and assembly chaperones on evolvability of Rubisco. *Nat Chem Biol* 11(2), 148-155. doi: 10.1038/nchembio.1715.
- Eckardt, N.A., Ainsworth, E.A., Bahuguna, R.N., Broadley, M.R., Busch, W., Carpita, N.C., et al. (2023). Climate change challenges, plant science solutions. *Plant Cell* 35(1), 24-66. doi: 10.1093/plcell/koac303.
- Erb, T.J., and Zarzycki, J. (2016). Biochemical and synthetic biology approaches to improve photosynthetic CO<sub>2</sub>-fixation. *Curr Opin Chem Biol* 34, 72-79. doi: 10.1016/j.cbpa.2016.06.026.
- Fang, L., Lin, H.X., Low, C.S., Wu, M.H., Chow, Y., and Lee, Y.K. (2012). Expression of the *Chlamydomonas reinhardtii* sedoheptulose-1,7-bisphosphatase in *Dunaliella bardawil* leads to enhanced photosynthesis and increased glycerol production. *Plant Biotechnol J* 10(9), 1129-1135. doi: 10.1111/pbi.12000.
- Fausser, F., Vilarrasa-Blasi, J., Onishi, M., Ramundo, S., Patena, W., Millican, M., et al. (2022). Systematic characterization of gene function in the photosynthetic alga *Chlamydomonas reinhardtii*. *Nat Genet* 54(5), 705-714. doi: 10.1038/s41588-022-01052-9.
- Ferenczi, A., Pyott, D.E., Xipnitou, A., and Molnar, A. (2017). Efficient targeted DNA editing and replacement in *Chlamydomonas reinhardtii* using Cpf1 ribonucleoproteins and single-stranded DNA. *Proc Natl Acad Sci U S A* 114(51), 13567-13572. doi: 10.1073/pnas.1710597114.
- Fuhrmann, M., Oertel, W., and Hegemann, P. (1999). A synthetic gene coding for the green fluorescent protein (GFP) is a versatile reporter in *Chlamydomonas reinhardtii*. *Plant J* 19(3), 353-361. doi: 10.1046/j.1365-313x.1999.00526.x.

- Garcia, A., Gaju, O., Bowerman, A.F., Buck, S.A., Evans, J.R., Furbank, R.T., et al. (2023). Enhancing crop yields through improvements in the efficiency of photosynthesis and respiration. *New Phytol* 237(1), 60-77. doi: 10.1111/nph.18545.
- Gleizer, S., Ben-Nissan, R., Bar-On, Y.M., Antonovsky, N., Noor, E., Zohar, Y., et al. (2019). Conversion of *Escherichia coli* to Generate All Biomass Carbon from CO<sub>2</sub>. *Cell* 179(6), 1255-1263 e1212. doi: 10.1016/j.cell.2019.11.009.
- Godfray, H.C., Beddington, J.R., Crute, I.R., Haddad, L., Lawrence, D., Muir, J.F., et al. (2010). Food security: the challenge of feeding 9 billion people. *Science* 327(5967), 812-818. doi: 10.1126/science.1185383.
- Gorman, D.S., and Levine, R.P. (1965). Cytochrome f and plastocyanin: their sequence in the photosynthetic electron transport chain of *Chlamydomonas reinhardtii*. *Proc Natl Acad Sci U S A* 54(6), 1665-1669. doi: 10.1073/pnas.54.6.1665.
- Greiner, A., Kelterborn, S., Evers, H., Kreimer, G., Sizova, I., and Hegemann, P. (2017). Targeting of Photoreceptor Genes in *Chlamydomonas reinhardtii* via Zinc-Finger Nucleases and CRISPR/Cas9. *Plant Cell* 29(10), 2498-2518. doi: 10.1105/tpc.17.00659.
- Gurrieri, L., Del Giudice, A., Demitri, N., Falini, G., Pavel, N.V., Zaffagnini, M., et al. (2019). Arabidopsis and *Chlamydomonas* phosphoribulokinase crystal structures complete the redox structural proteome of the Calvin-Benson cycle. *Proc Natl Acad Sci U S A* 116(16), 8048-8053. doi: 10.1073/pnas.1820639116.
- Gurrieri, L., Fermani, S., Zaffagnini, M., Sparla, F., and Trost, P. (2021). Calvin-Benson cycle regulation is getting complex. *Trends Plant Sci* 26(9), 898-912. doi: 10.1016/j.tplants.2021.03.008.
- Gurrieri, L., Sparla, F., Zaffagnini, M., and Trost, P. (2023). Dark complexes of the Calvin-Benson cycle in a physiological perspective. *Semin Cell Dev Biol*. doi: 10.1016/j.semedb.2023.03.002.
- Hammel, A., Sommer, F., Zimmer, D., Stitt, M., Muhlhaut, T., and Schroda, M. (2020). Overexpression of Sedoheptulose-1,7-Bisphosphatase Enhances Photosynthesis in *Chlamydomonas reinhardtii* and Has No Effect on the Abundance of Other Calvin-Benson Cycle Enzymes. *Front Plant Sci* 11, 868. doi: 10.3389/fpls.2020.00868.
- Hennacy, J.H., and Jonikas, M.C. (2020). Prospects for Engineering Biophysical CO<sub>2</sub> Concentrating Mechanisms into Land Plants to Enhance Yields. *Annu Rev Plant Biol* 71, 461-485. doi: 10.1146/annurev-arplant-081519-040100.
- Iwaki, T., Haranoh, K., Inoue, N., Kojima, K., Satoh, R., Nishino, T., et al. (2006). Expression of foreign type I ribulose-1,5-bisphosphate carboxylase/oxygenase (EC 4.1.1.39) stimulates photosynthesis in cyanobacterium *Synechococcus* PCC7942 cells. *Photosynth Res* 88(3), 287-297. doi: 10.1007/s11220-006-9048-x.
- Jaeger, D., Baier, T., and Lauersen, K.J. (2019). Intronserter, an advanced online tool for design of intron containing transgenes. *Algal Research* 42, 101588. doi: <https://doi.org/10.1016/j.algal.2019.101588>.
- Janasch, M., Asplund-Samuelsson, J., Steuer, R., and Hudson, E.P. (2019). Kinetic modeling of the Calvin cycle identifies flux control and stable metabolomes in *Synechocystis* carbon fixation. *J Exp Bot* 70(3), 973-983. doi: 10.1093/jxb/ery382.
- Jin, K., Chen, G., Yang, Y., Zhang, Z., and Lu, T. (2023). Strategies for manipulating Rubisco and creating photorespiratory bypass to boost C(3) photosynthesis: Prospects on modern crop improvement. *Plant Cell Environ* 46(2), 363-378. doi: 10.1111/pce.14500.
- Kim, J., Lee, S., Baek, K., and Jin, E. (2020). Site-Specific Gene Knock-Out and On-Site Heterologous Gene Overexpression in *Chlamydomonas reinhardtii* via a CRISPR-Cas9-Mediated Knock-in Method. *Front Plant Sci* 11, 306. doi: 10.3389/fpls.2020.00306.
- Kubis, A., and Bar-Even, A. (2019). Synthetic biology approaches for improving photosynthesis. *J Exp Bot* 70(5), 1425-1433. doi: 10.1093/jxb/erz029.
- Lauersen, K.J., Wichmann, J., Baier, T., Kampranis, S.C., Pateraki, I., Moller, B.L., et al. (2018). Phototrophic production of heterologous diterpenoids and a hydroxy-functionalized derivative from *Chlamydomonas reinhardtii*. *Metab Eng* 49, 116-127. doi: 10.1016/j.ymben.2018.07.005.
- Le Moigne, T., Boisset, N.D., de Carpentier, F., Crozet, P., Danon, A., Henri, J., et al. (2023). "Chapter 8 - Photoproduction of reducing power and the Calvin-Benson cycle," in *The Chlamydomonas Sourcebook (Third Edition)*, eds. A.R. Grossman & F.-A. Wollman. (London: Academic Press), 273-315.
- Lefebvre, S., Lawson, T., Zakhleniuk, O.V., Lloyd, J.C., Raines, C.A., and Fryer, M. (2005). Increased sedoheptulose-1,7-bisphosphatase activity in transgenic tobacco plants stimulates photosynthesis and growth from an early stage in development. *Plant Physiol* 138(1), 451-460. doi: 10.1104/pp.104.055046.
- Li, X., Patena, W., Fauser, F., Jinkerson, R.E., Saroussi, S., Meyer, M.T., et al. (2019). A genome-wide algal mutant library and functional screen identifies genes required for eukaryotic photosynthesis. *Nat Genet* 51(4), 627-635. doi: 10.1038/s41588-019-0370-6.
- Liang, F., and Lindblad, P. (2016). Effects of overexpressing photosynthetic carbon flux control enzymes in the cyanobacterium *Synechocystis* PCC 6803. *Metab Eng* 38, 56-64. doi: 10.1016/j.ymben.2016.06.005.
- Liang, F., and Lindblad, P. (2017). *Synechocystis* PCC 6803 overexpressing RuBisCO grow faster with increased photosynthesis. *Metab Eng Commun* 4, 29-36. doi: 10.1016/j.meteno.2017.02.002.

- Long, B.M., Hee, W.Y., Sharwood, R.E., Rae, B.D., Kaines, S., Lim, Y.L., et al. (2018). Carboxysome encapsulation of the CO<sub>2</sub>-fixing enzyme Rubisco in tobacco chloroplasts. *Nat Commun* 9(1), 3570. doi: 10.1038/s41467-018-06044-0.
- Long, B.M., Rae, B.D., Rolland, V., Forster, B., and Price, G.D. (2016). Cyanobacterial CO<sub>2</sub>-concentrating mechanism components: function and prospects for plant metabolic engineering. *Curr Opin Plant Biol* 31, 1-8. doi: 10.1016/j.pbi.2016.03.002.
- Long, S.P., Marshall-Colon, A., and Zhu, X.G. (2015). Meeting the global food demand of the future by engineering crop photosynthesis and yield potential. *Cell* 161(1), 56-66. doi: 10.1016/j.cell.2015.03.019.
- Long, S.P., Zhu, X.G., Naidu, S.L., and Ort, D.R. (2006). Can improvement in photosynthesis increase crop yields? *Plant Cell Environ* 29(3), 315-330.
- Lumbreras, V., and Purton, S. (1998). Recent advances in chlamydomonas transgenics. *Protist* 149(1), 23-27. doi: 10.1016/S1434-4610(98)70006-9.
- Mackinder, L.C.M. (2018). The Chlamydomonas CO<sub>2</sub> -concentrating mechanism and its potential for engineering photosynthesis in plants. *New Phytol* 217(1), 54-61. doi: 10.1111/nph.14749.
- Marcus, Y., Altman-Gueta, H., Wolff, Y., and Gurevitz, M. (2011). Rubisco mutagenesis provides new insight into limitations on photosynthesis and growth in Synechocystis PCC6803. *J Exp Bot* 62(12), 4173-4182. doi: 10.1093/jxb/err116.
- Marri, L., Trost, P., Trivelli, X., Gonnelli, L., Pupillo, P., and Sparla, F. (2008). Spontaneous assembly of photosynthetic supramolecular complexes as mediated by the intrinsically unstructured protein CP12. *J Biol Chem* 283(4), 1831-1838. doi: 10.1074/jbc.M705650200.
- Marri, L., Zaffagnini, M., Collin, V., Issakidis-Bourguet, E., Lemaire, S.D., Pupillo, P., et al. (2009). Prompt and easy activation by specific thioredoxins of calvin cycle enzymes of Arabidopsis thaliana associated in the GAPDH/CP12/PRK supramolecular complex. *Mol Plant* 2(2), 259-269. doi: 10.1093/mp/ssn061.
- McFarlane, C.R., Shah, N.R., Kabasakal, B.V., Echeverria, B., Cotton, C.A.R., Bubeck, D., et al. (2019). Structural basis of light-induced redox regulation in the Calvin-Benson cycle in cyanobacteria. *Proc Natl Acad Sci U S A* 116(42), 20984-20990. doi: 10.1073/pnas.1906722116.
- Meloni, M., Gurrieri, L., Fermani, S., Velie, L., Sparla, F., Crozet, P., et al. (2023). Ribulose-1,5-bisphosphate regeneration in the Calvin-Benson-Bassham cycle: Focus on the last three enzymatic steps that allow the formation of Rubisco substrate. *Front Plant Sci* 14, 1130430. doi: 10.3389/fpls.2023.1130430.
- Michelet, L., Zaffagnini, M., Morisse, S., Sparla, F., Perez-Perez, M.E., Francia, F., et al. (2013). Redox regulation of the Calvin-Benson cycle: something old, something new. *Front Plant Sci* 4, 470. doi: 10.3389/fpls.2013.00470.
- Moll, B., and Levine, R.P. (1970). Characterization of a Photosynthetic Mutant Strain of Chlamydomonas reinhardi Deficient in Phosphoribulokinase Activity. *Plant Physiol* 46(4), 576-580. doi: 10.1104/pp.46.4.576.
- Ort, D.R., Merchant, S.S., Alric, J., Barkan, A., Blankenship, R.E., Bock, R., et al. (2015). Redesigning photosynthesis to sustainably meet global food and bioenergy demand. *Proc Natl Acad Sci U S A* 112(28), 8529-8536. doi: 10.1073/pnas.1424031112.
- Patron, N.J., Orzaez, D., Marillonnet, S., Warzecha, H., Matthewman, C., Youles, M., et al. (2015). Standards for plant synthetic biology: a common syntax for exchange of DNA parts. *New Phytol* 208(1), 13-19. doi: 10.1111/nph.13532.
- Paul, M.J., Knight, J.S., Habash, D., Parry, M.A.J., Lawlor, D.W., Barnes, S.A., et al. (1995). Reduction in phosphoribulokinase activity by antisense RNA in transgenic tobacco: effect on CO<sub>2</sub> assimilation and growth in low irradiance. *The Plant Journal* 7(4), 535-542. doi: https://doi.org/10.1046/j.1365-3113X.1995.7040535.x.
- Raines, C.A. (2003). The Calvin cycle revisited. *Photosynth Res* 75(1), 1-10. doi: 10.1023/A:1022421515027.
- Raines, C.A. (2011). Increasing photosynthetic carbon assimilation in C<sub>3</sub> plants to improve crop yield: current and future strategies. *Plant Physiol* 155(1), 36-42. doi: 10.1104/pp.110.168559.
- Raines, C.A. (2022). Improving plant productivity by re-tuning the regeneration of RuBP in the Calvin-Benson-Bassham cycle. *New Phytol* 236(2), 350-356. doi: 10.1111/nph.18394.
- Roell, M.S., Schada von Borzykowski, L., Westhoff, P., Plett, A., Paczia, N., Claus, P., et al. (2021). A synthetic C<sub>4</sub> shuttle via the  $\beta$ -hydroxyaspartate cycle in C<sub>3</sub> plants. *Proc Natl Acad Sci U S A* 118(21). doi: 10.1073/pnas.2022307118.
- Rosenthal, D.M., Locke, A.M., Khozaei, M., Raines, C.A., Long, S.P., and Ort, D.R. (2011). Over-expressing the C<sub>3</sub> photosynthesis cycle enzyme Sedoheptulose-1-7 Bisphosphatase improves photosynthetic carbon gain and yield under fully open air CO<sub>2</sub> fumigation (FACE). *BMC Plant Biol* 11, 123. doi: 10.1186/1471-2229-11-123.
- Salesse-Smith, C.E., Sharwood, R.E., Busch, F.A., Kromdijk, J., Bardal, V., and Stern, D.B. (2018). Overexpression of Rubisco subunits with RAF1 increases Rubisco content in maize. *Nat Plants* 4(10), 802-810. doi: 10.1038/s41477-018-0252-4.
- Salome, P.A., and Merchant, S.S. (2019). A Series of Fortunate Events: Introducing Chlamydomonas as a Reference Organism. *Plant Cell* 31(8), 1682-1707. doi: 10.1105/tpc.18.00952.
- Satanowski, A., Dronsella, B., Noor, E., Vogeli, B., He, H., Wichmann, P., et al. (2020). Awakening a latent carbon fixation cycle in Escherichia coli. *Nat Commun* 11(1), 5812. doi: 10.1038/s41467-020-19564-5.

- Schnell, R.A., and Lefebvre, P.A. (1993). Isolation of the *Chlamydomonas* regulatory gene NIT2 by transposon tagging. *Genetics* 134(3), 737-747. doi: 10.1093/genetics/134.3.737.
- Schroda, M. (2019). Good News for Nuclear Transgene Expression in *Chlamydomonas*. *Cells* 8(12). doi: 10.3390/cells8121534.
- Schwander, T., Schada von Borzyskowski, L., Burgener, S., Cortina, N.S., and Erb, T.J. (2016). A synthetic pathway for the fixation of carbon dioxide in vitro. *Science* 354(6314), 900-904. doi: 10.1126/science.aah5237.
- Shin, S.E., Lim, J.M., Koh, H.G., Kim, E.K., Kang, N.K., Jeon, S., et al. (2016). CRISPR/Cas9-induced knockout and knock-in mutations in *Chlamydomonas reinhardtii*. *Sci Rep* 6, 27810. doi: 10.1038/srep27810.
- Simkin, A.J., Lopez-Calcagno, P.E., and Raines, C.A. (2019). Feeding the world: improving photosynthetic efficiency for sustainable crop production. *J Exp Bot* 70(4), 1119-1140. doi: 10.1093/jxb/ery445.
- Smith, B.D. (2000). *Isolation and analysis of Chlamydomonas reinhardtii phosphoribulokinase mutants and revertants*. Undergraduate Honors Thesis, University of Nebraska
- South, P.F., Cavanagh, A.P., Liu, H.W., and Ort, D.R. (2019). Synthetic glycolate metabolism pathways stimulate crop growth and productivity in the field. *Science* 363(6422), eaat9077. doi: 10.1126/science.aat9077.
- Stitt, M., Lunn, J., and Usadel, B. (2010). Arabidopsis and primary photosynthetic metabolism - more than the icing on the cake. *Plant J* 61(6), 1067-1091. doi: 10.1111/j.1365-313X.2010.04142.x.
- Stitt, M., and Schulze, D. (1994). Does Rubisco control the rate of photosynthesis and plant growth? An exercise in molecular ecophysiology. *Plant, Cell and Environment* 17(5), 465-487. doi: 10.1111/j.1365-3040.1994.tb00144.x.
- Sueoka, N. (1960). Mitotic Replication of Deoxyribonucleic Acid in *Chlamydomonas Reinhardii*. *Proc Natl Acad Sci U S A* 46(1), 83-91. doi: 10.1073/pnas.46.1.83.
- Tamoi, M., Nagaoka, M., Miyagawa, Y., and Shigeoka, S. (2006). Contribution of fructose-1,6-bisphosphatase and sedoheptulose-1,7-bisphosphatase to the photosynthetic rate and carbon flow in the Calvin cycle in transgenic plants. *Plant Cell Physiol* 47(3), 380-390. doi: 10.1093/pcp/pcj004.
- Thieulin-Pardo, G., Remy, T., Lignon, S., Lebrun, R., and Gontero, B. (2015). Phosphoribulokinase from *Chlamydomonas reinhardtii*: a Benson-Calvin cycle enzyme enslaved to its cysteine residues. *Mol Biosyst* 11(4), 1134-1145. doi: 10.1039/c5mb00035a.
- Tilman, D., Balzer, C., Hill, J., and Befort, B.L. (2011). Global food demand and the sustainable intensification of agriculture. *Proc Natl Acad Sci U S A* 108(50), 20260-20264. doi: 10.1073/pnas.1116437108.
- Treves, H., Lucius, S., Feil, R., Stitt, M., Hagemann, M., and Arrivault, S. (2022). Operation of Carbon-Concentrating Mechanisms in Cyanobacteria and Algae requires altered poising of the Calvin-Benson cycle. *bioRxiv*, 2022.2008.2023.504937. doi: 10.1101/2022.08.23.504937.
- Trudeau, D.L., Edlich-Muth, C., Zarzycki, J., Scheffen, M., Goldsmith, M., Khersonsky, O., et al. (2018). Design and in vitro realization of carbon-conserving photorespiration. *Proc Natl Acad Sci U S A* 115(49), E11455-E11464. doi: 10.1073/pnas.1812605115.
- Vavitsas, K., Crozet, P., Vinde, M.H., Davies, F., Lemaire, S.D., and Vickers, C.E. (2019). The Synthetic Biology Toolkit for Photosynthetic Microorganisms. *Plant Physiol* 181(1), 14-27. doi: 10.1104/pp.19.00345.
- Vecchi, V., Barera, S., Bassi, R., and Dall'Osto, L. (2020). Potential and Challenges of Improving Photosynthesis in Algae. *Plants (Basel)* 9(1). doi: 10.3390/plants9010067.
- Wang, L.M., Shen, B.R., Li, B.D., Zhang, C.L., Lin, M., Tong, P.P., et al. (2020). A Synthetic Photorespiratory Shortcut Enhances Photosynthesis to Boost Biomass and Grain Yield in Rice. *Mol Plant* 13(12), 1802-1815. doi: 10.1016/j.molp.2020.10.007.
- Weber, E., Engler, C., Gruetzner, R., Werner, S., and Marillonnet, S. (2011). A modular cloning system for standardized assembly of multigene constructs. *PLoS One* 6(2), e16765. doi: 10.1371/journal.pone.0016765.
- Wilson, R.H., Hayer-Hartl, M., and Bracher, A. (2019). Crystal structure of phosphoribulokinase from *Synechococcus* sp. strain PCC 6301. *Acta Crystallogr F Struct Biol Commun* 75(Pt 4), 278-289. doi: 10.1107/S2053230X19002693.
- Wobbe, L., and Remacle, C. (2015). Improving the sunlight-to-biomass conversion efficiency in microalgal biofactories. *J Biotechnol* 201, 28-42. doi: 10.1016/j.jbiotec.2014.08.021.
- Yoon, D.-K., Ishiyama, K., Suganami, M., Tazoe, Y., Watanabe, M., Imaruoka, S., et al. (2020). Transgenic rice overproducing Rubisco exhibits increased yields with improved nitrogen-use efficiency in an experimental paddy field. *Nature Food* 1(2), 134-139. doi: 10.1038/s43016-020-0033-x.
- Yu, A., Xie, Y., Pan, X., Zhang, H., Cao, P., Su, X., et al. (2020). Photosynthetic Phosphoribulokinase Structures: Enzymatic Mechanisms and the Redox Regulation of the Calvin-Benson-Bassham Cycle. *Plant Cell* 32(5), 1556-1573. doi: 10.1105/tpc.19.00642.
- Zhu, X.G., de Sturler, E., and Long, S.P. (2007). Optimizing the distribution of resources between enzymes of carbon metabolism can dramatically increase photosynthetic rate: a numerical simulation using an evolutionary algorithm. *Plant Physiol* 145(2), 513-526. doi: 10.1104/pp.107.103713.
- Zhu, X.G., Long, S.P., and Ort, D.R. (2010). Improving photosynthetic efficiency for greater yield. *Annu Rev Plant Biol* 61, 235-261. doi: 10.1146/annurev-arplant-042809-112206.

## **CHAPTER IV: “Structural and biochemical characterization of Arabidopsis alcohol dehydrogenases reveals distinct functional properties but similar redox sensitivity”**

**Maria Meloni<sup>a,1</sup>, Jacopo Rossi<sup>a,1</sup>, Silvia Fanti<sup>b,1</sup>, Giacomo Carloni<sup>b</sup>, Daniele Tedesco<sup>c</sup>, Patrick Treffon<sup>d</sup>, Luca Piccinini<sup>e,f</sup>, Giuseppe Falini<sup>b</sup>, Paolo Trost<sup>a</sup>, Elizabeth Vierling<sup>d</sup>, Francesco Licausi<sup>g</sup>, Beatrice Giuntoli<sup>e,f</sup>, Francesco Musiani<sup>a,\*</sup>, Simona Fermani<sup>b,h,\*</sup>, and Mirko Zaffagnini<sup>a,\*</sup>**

<sup>a</sup>Department of Pharmacy and Biotechnology, University of Bologna, 40126 Bologna, Italy

<sup>b</sup>Department of Chemistry “G. Ciamician”, University of Bologna, 40126 Bologna, Italy

<sup>c</sup>Institute for Organic Synthesis and Photoreactivity (ISOF), National Research Council of Italy (CNR), 40129 Bologna, Italy

<sup>d</sup>Department of Biochemistry and Molecular Biology, University of Massachusetts Amherst, Amherst, MA, USA

<sup>e</sup>Department of Biology, University of Pisa, Pisa, 56127, Italy

<sup>f</sup>Center for Plant Sciences, Scuola Superiore Sant’Anna, Pisa, 56124, Italy

<sup>g</sup>Department of Plant Sciences, University of Oxford, Oxford, United Kingdom

<sup>h</sup>Interdepartmental Centre for Industrial Research Health Sciences & Technologies, University of Bologna, 40064 Bologna, Italy

<sup>1</sup>equal contribution

*This work has been published in 2024 on **Plant Journal** and it available at:*

DOI: 10.1111/tpj.16651

## Summary

Alcohol dehydrogenases (ADHs) comprise several classes of metal-containing enzymes belonging to the protein superfamily of medium-length dehydrogenase/reductases (MDRs). Classical ADHs are mostly known in plants for their participation in fermentative metabolism, in which they catalyse the NADH-dependent conversion of acetaldehyde (MeCHO) to ethanol (EtOH). This reaction has the double purpose of detoxifying MeCHO and sustaining the glycolytic flux by NAD<sup>+</sup> regeneration under conditions of impaired mitochondrial respiration. In addition, ADHs are able to catalyse the reverse NAD<sup>+</sup>-dependent conversion of alcohols to aldehydes (*e.g.*, EtOH to MeCHO). Among the enzymes belonging to the MDR superfamily, the class III ADH family includes nitrosogluthione reductase (GSNOR). GSNOR is involved in the detoxification of toxic aldehyde compounds, but is primarily implicated in the degradation of S-nitrosogluthione (GSNO), the most important NO-releasing compound in both plant and non-plant cells. As a relatively stable molecule, GSNO can react with cysteine thiols in proteins in a reaction called S-nitrosylation (or S-nitrosation), which plays a fundamental role in modulating protein function and structure.

When considering the relative content of the different proteinogenic amino acids, cysteine (Cys) is one of the least abundant residues. Nevertheless, Cys plays a key role in enzyme function, protein structure stabilization and coordination of metal ions. Zinc ions are one of the most abundant biologically relevant transition metals, serving both structural and catalytic functions and typically coordinated by four ligands in a tetrahedral geometry. ADHs contain two zinc ions, coordinated either by 4 Cys and by 2 Cys coupled to a histidine and a glutamate that in some cases is replaced by a water molecule. In addition, depending on reactivity and microenvironment, Cys residues can undergo a wide range of redox post-translational modifications (PTMs) that are able to modulate protein function or alter structural conformations. This property makes Cys residues exceptionally important for redox homeostasis in plant cells and are therefore considered as the primary sensor of reactive oxygen and nitrogen species (ROS and RNS, respectively). Numerous proteomic-based studies have identified hundreds of plant proteins susceptible to thiol-based redox modifications. Among metabolism-related proteins, ADH1 (*i.e.*, classical ADH) and GSNOR were recently identified in *Arabidopsis thaliana* as putative targets of S-sulfenylation both under control conditions and after exposure to hydrogen peroxide (H<sub>2</sub>O<sub>2</sub>). In addition, both proteins showed sensitivity toward S-nitrosylation, while other redox modifications, such as S-glutathionylation and thioredoxin-mediated dithiol/disulfide interchanges, specifically target ADH.

Here, we first determined new crystal structures of *Arabidopsis thaliana* ADH1 complexed with NADH (NADH-ADH1) and of GSNOR in the apo-form (apo-GSNOR). This allowed us to broaden our knowledge of the structural landscape of ADHs and to conduct an in-depth structural comparison between the different apo- and holo- forms (NAD<sup>+</sup> and NADH structures). Then, we performed a kinetic analysis to establish specificity toward the enzyme's respective substrates as well as alternative substrates such as long-chain alcohols. The two enzymes exhibit nearly an identical fold, but have striking differences in catalytic behaviour and catalytic-related structural elements. We further examined the content, conservation and accessibility of cysteine thiols in the two enzymes and evaluated their redox sensitivity in the presence of various thiol oxidizing agents. We evidenced similar and prominent redox responsivity of ADHs to thiol switching mechanisms with concomitant destabilization of zinc ion coordination, suggesting that cysteine-based modifications may constitute a mechanism for controlling their activity under physiological conditions and in response to oxidative stress.

## Results

### Arabidopsis ADH1 and GSNOR share a similar fold with identical domain organization

To gain a better understanding of the structural properties and to identify differences between Arabidopsis ADH1 and GSNOR, we expressed and purified both proteins and determined two new structures, NADH-ADH1 and apo-GSNOR. These new structures now provide a complete set of Arabidopsis ADHs in both apo- and holo-forms (**Table 1**). The extensive similarity of the two proteins is first observed by comparative analysis of their primary sequences, both of which comprise 379 amino acids, along with their secondary structures. Despite their different physiological roles, ADH1 and GSNOR share ~59% sequence identity and exhibit a nearly complete conservation of secondary structure composition (**Figure S1**). Based on the complete set of 3D-structures reported (**Table 1**), ADH1 and GSNOR are both homodimers with a similar tertiary structure (**Figure 1a, 1b, and Table 1**).

	PDB ID	Resolution (Å)	Asymmetric unit	Ligand	Oligomeric state	References
	4RQT	2.30	Monomer	Acetate	Dimer	(Chen et al., 2014)
ADH1	4RQU	2.50	Dimer	NAD <sup>+</sup> †	Dimer	(Chen et al., 2014)
	8CON	1.64	Monomer	NADH	Dimer	(this work)
	4JJI‡	1.80	Dimer	NAD <sup>+</sup>	Dimer	-
GSNOR	3UKO‡	1.40	Dimer	NADH	Dimer	-
	8CO4	1.90	Dimer of dimers	-	Dimer	(this work)

**Table 1.** 3D-structures for *A. thaliana* ADH1 and GSNOR in the Protein Data Bank.

†the cofactor is found only in one chain of the dimer (chain B)

‡Crystal structures deposited in the Protein Data Bank

According to the CATH classification (Orengo *et al.*, 1997), each monomer is composed of two domains (**Figure 1a and 1b**). The catalytic domain comprises the N-terminal portion and the C-terminal tail of the protein (residues 1-177 and 327-379) and is formed by eleven  $\beta$ -strands and ten or eleven helices for ADH1 and GSNOR, respectively, with the additional helix inserted between  $\beta$ 5 and  $\beta$ 6 in GSNOR (**Figure 1c and 1d**). The cofactor binding domain has a typical Rossmann fold (residues 178-326), formed by a six-strand parallel  $\beta$ -sheet surrounded by seven helices (**Figure 1c**

and 1d). The interaction between the cofactor binding domains of the two subunits allows the formation of the quaternary assembly, while the catalytic domains are located in the distal portion of the ADH structures (**Figure 1a and 1b**).

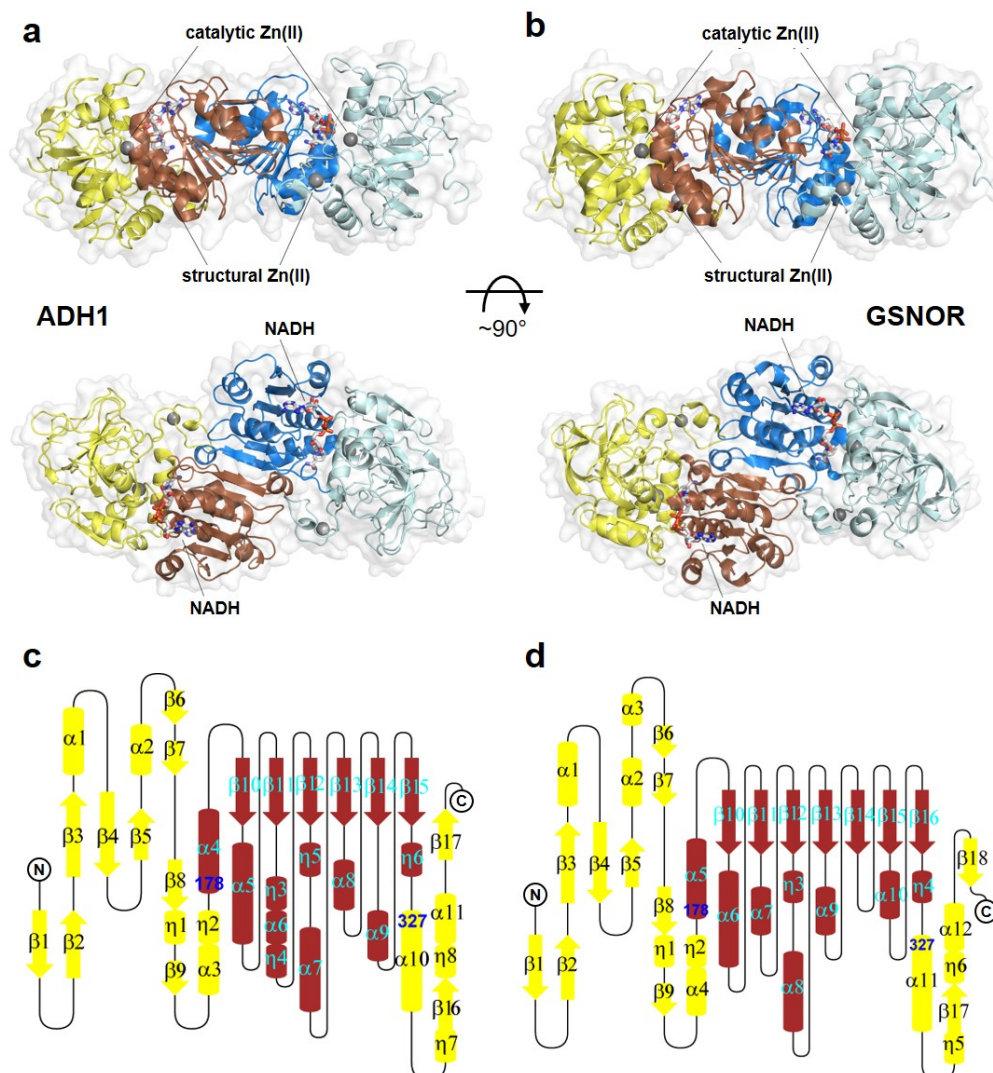


**Figure 1:** Overview of ADH1 and GSNOR structures. Cartoon and surface representation of structures of ADH1 (PDB ID: 8CON) (a) and GSNOR (PDB ID: 3UKO) (b) in the presence of NADH. In the bottom panels the structure is rotated by 90° degrees around the horizontal axis with respect to the upper panels. The two monomers of the dimers are coloured yellow/orange (ADH1) and aquamarine/blue (GSNOR). In each monomer, the catalytic domain is shown in lighter colours (yellow and aquamarine) with respect to the cofactor binding domain (orange and blue). The surface is shown in white. Zinc ions are indicated as Zn(II) (see Figure 2 and related text for further details). Panels (c) and (d) are topology diagrams of ADH1 and GSNOR, respectively. The catalytic domain (yellow) comprises residues 1-177 and 327-379, and is composed by eleven  $\beta$ -strands and ten or eleven helices for ADH1 and GSNOR, respectively. The cofactor binding domain (dark red) comprises residues 178-326 and is composed by a six-strand parallel  $\beta$ -sheet and seven helices. Residues 178 and 327 are highlighted in blue.

The cofactor binding domain hosts NAD<sup>+</sup>/NADH cofactor in a wide pocket at the interface between the two domains (**Figure 1a and 1b**). The conformation of the cofactor is very similar in all monomers, except for chain B of the NAD<sup>+</sup>-GSNOR structure (PDB ID 4JJI) where the nicotinamide-ribose moiety is rotated by about 90° (**Figure S2**).

### Structural and catalytic zinc ions in Arabidopsis ADHs

Arabidopsis ADHs contain two zinc ions having either structural or catalytic role (Xu *et al.*, 2013, Chen *et al.*, 2015), and the effective content of zinc atoms was determined for the purified recombinant proteins using the 4-(2-pyridylazo)resorcinol (PAR) assay. As expected, the number of zinc ions released from ADH1 and GSNOR are  $1.94 \pm 0.14$  and  $2.05 \pm 0.13$ , respectively. In the available structures (Table 1), the structural zinc ion is located in a loop at *ca.* 25 Å from the active site (**Figure 1a and 1b**) and it is coordinated by four cysteines (Cys99, Cys102, Cys105, and Cys113 in both ADHs; **Figures 2a**) in a slightly distorted tetrahedral geometry (root mean square deviations (RMSDs) 0.125 to 0.237 Å with respect to the ideal tetrahedral geometry; **Figure S3**). In contrast, the catalytic zinc ion, which is involved in substrate stabilization/activation, shows a variable number of ligands and coordination geometry (**Figures 2b, 2c, and S4**) as is typical for zinc ions exhibiting catalytic functions (Permyakov, 2021). In all structures, the catalytic zinc ion is bound to Cys47, His69, and Cys177, while there is variability of the fourth ligand (Glu70, water or substrate), and the fifth ligand, when present, is always a water molecule (**Figure S4**). However, in the NADH-ADH1/GSNOR structures, the catalytic zinc ion is found in a distorted tetrahedral coordination geometry with Glu70 directly bound to the metal ion (**Figures 2b and S4**).

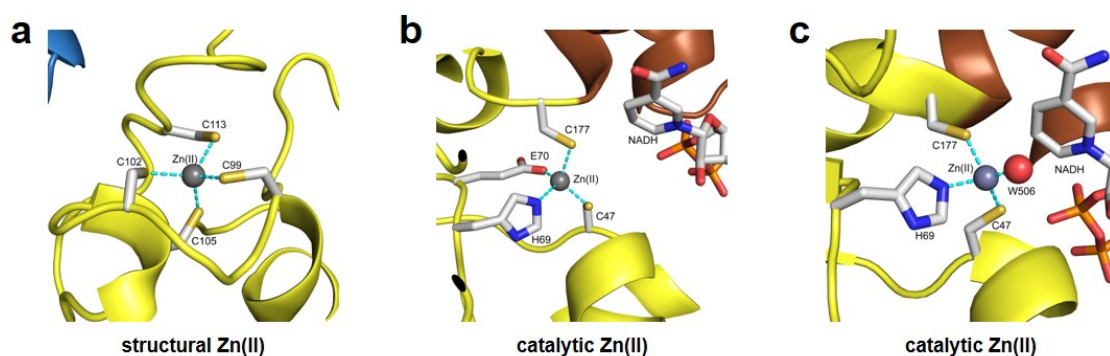


**Figure 2:** Coordination sites of zinc ions in Arabidopsis ADHs. (a) Representation of the coordination environment of the structural zinc ion in ADHs (from NADH-ADH1 structure, PDB ID: 8CON). The metal-coordination bonds are reported as dashed cyan lines. (b) and (c) Representation of the coordination environment of two catalytic zinc ions in ADHs from NADH-ADH1 structure, PDB ID: 8CON and NAD<sup>+</sup>-ADH1 structure chain B, PDB ID: 4RQU,

respectively. The metal coordination bonds are reported as dashed cyan lines. Zinc ions are represented as grey spheres, water molecule as red sphere while the NADH cofactor and protein residues are shown in sticks coloured according to the atom type (C, light grey; O, red; N, blue; S, yellow; P, orange).

### Structural comparison of ADH1 and GSNOR in apo- and holo-forms

In order to highlight significant structural differences between the two enzymes, a comparative analysis was performed by superposing the available 3D-structures (**Table 1**) and calculating the RMSDs of the positions of the C<sub>α</sub> atoms *per* residue and as the average value of the whole protein chain (**Figures 3 and S5, and Tables S1-S3**). The monomers of the apo- and NAD(H)-ADH1 structures are similar having an average RMSD (<RMSD>) of 0.69 ± 0.15 Å, slightly higher than that obtained from the superposition of the apo- and NAD(H)-GSNOR structures (<RMSD> = 0.58 ± 0.16 Å) (**Table S3**). This trend is paralleled by the average RMSD values for the dimers (<RMSD> = 1.13 ± 0.18 Å for ADH1 and <RMSD> = 0.81 ± 0.27 Å for GSNOR; **Tables S3**). Despite the low RMSD values, the superposition of ADH1 monomers (apo- and NAD(H) forms) shows structural deviations especially in the cofactor binding domain with RMSD values *per* monomer up to 4 Å (**Figure S5a and S5c**). In contrast, these differences are not observed among monomers of apo- and holo-GSNOR (**Figure S5b and S5d**). These observations argue that there is conformational variability among different ADH1 forms compared with GSNOR, which appears to be more rigid.

The superposition of ADH1 and GSNOR (*i.e.*, apo-ADH1 vs apo-GSNOR and NAD(H)-ADH1 vs NAD(H)-GSNO) reveals higher structural deviations with RMSD values ranging from 0.93 Å to 1.52 Å for monomers and 1.58 Å to 2.43 Å for dimers (**Table S1-S3**). Major differences are observed in the non-conserved regions that delimit the entrance to the catalytic cavity and that form the cavity itself, including the loop 55-69 following helix α1, residues 115-132 and residues 297-303 (**Figures 3 and S6**). Helix α1 and residues 297-303 are also involved in setting in place the nicotinamide moiety of the cofactor. Residues 115-132, which have RMSD values *per* residue higher than 4 Å (**Figure 3b, 3d, and 3f**), acquire a different conformation in the two enzymes, forming a turn/loop in ADH1 and a helix/loop in GSNOR (**Figures 3a, 3c, 3e, and S1**). Moreover, in ADH1 access to the catalytic cavity appears to be narrowed compared to GSNOR.

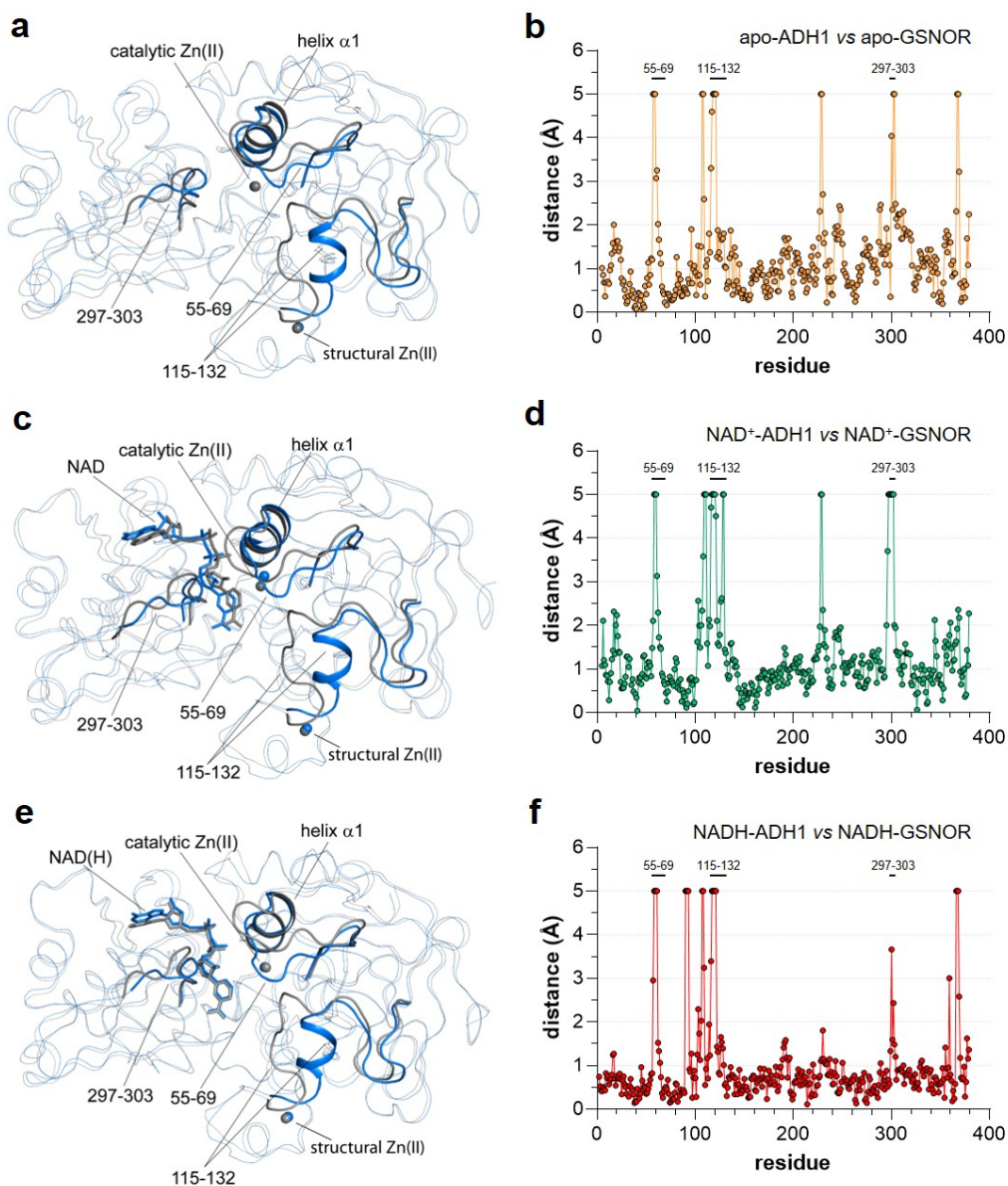


**Figure 3:** ADH1 and GSNOR structural superpositions. Left panels show the  $C_{\alpha}$  atoms superposition of ADH1 (grey) and GSNOR (light blue) monomers in apo-form (a),  $NAD^{+}$ -form (c), and NADH-form (e). The protein backbone is reported as ribbon, zinc ion as sphere and cofactor as sticks. The protein portions delimiting the catalytic cavity and showing major differences are indicated. Right panels report the RMSD values per residue obtained from the  $C_{\alpha}$  atoms superposition of ADH1 and GSNOR monomers in apo-form (b, orange closed circles),  $NAD^{+}$ -form (d, green closed circles), and NADH-form (f, red closed circles). RMSD values equal to or greater than 5 Å are set at 5 Å for clarity.

Notwithstanding the differences in cofactor binding domain and catalytic cavity, the residues involved in cofactor stabilization are almost entirely conserved (Figure 4 and Table S4). Minor differences, which do not alter the cofactor-protein interaction network between the two enzymes,

correspond to Ala205, Arg231, and Thr272 in ADH1, replaced by Val205, Lys231, and Ile272 in GSNOR (**Figure 4 and Table S4**). Conversely, substitution of ADH1 Phe95 for Tyr95 in GSNOR results in an additional interaction (**Figure 4b and Table S4**). The adenine ring of NAD(H) in ADH1 structures is stabilized through a  $\pi$ -stacking interaction with Phe227 and the methyl group of Thr272 and Ala277 (**Figure 4a**). These residues are not conserved in GSNOR and Van der Waals interactions with Ile227, Ile272, and Val277 stabilize the adenine (**Figure 4b**). The stabilization of the nicotinamide ring is conserved in both enzymes and involves Val206, Val297, and the methyl group of Thr181 (**Figure 4a and 4b**).

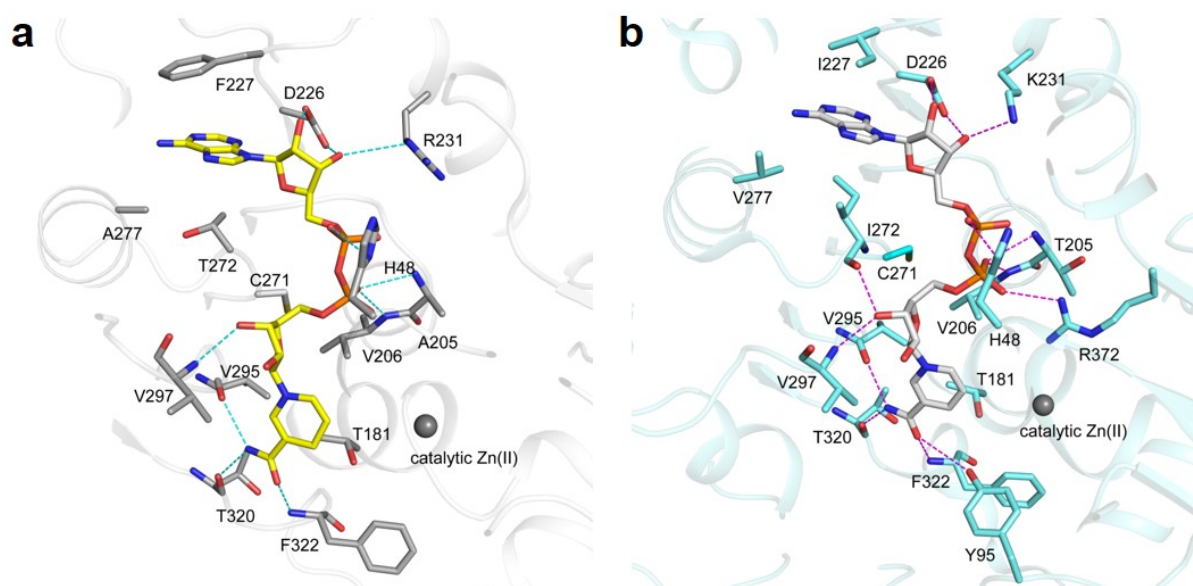


**Figure 4:** Cofactor-protein interactions in *Arabidopsis* ADHs. Interactions between NADH and protein residues in ADH1 (**a**) and GSNOR (**b**). The cofactor and the protein residues are shown as sticks, the catalytic zinc ion is shown as a grey sphere, and the hydrogen-bond interactions (distance  $\leq 3.6$  Å) are indicated as dashed lines. The corresponding distance values observed in different ADH1 and GSNOR monomers are reported in Table S5. Residues forming Van der Waals interactions with the adenine and nicotinamide rings are also shown.

Positioning of zinc ions was analyzed by structural superposition of the ADH structures. While the position of the structural zinc is similar in all apo- and NAD(H)-forms of ADH1 and GSNOR structures, the catalytic zinc ion assumes slightly variable positions especially in the case of NAD<sup>+</sup>-structures (**Figures 3c, S5a, and S5b**). In NADH-structures of both enzymes, the distance of the catalytic zinc ion from the nicotinamide ring (C5N atom) of NAD(H) ranges between 5.0 and 5.9 Å, while it decreases to 3.2 Å in NAD<sup>+</sup>-AtADH1 structure (**Figure 3c**) and increases to 7.8 Å in NAD<sup>+</sup>-AtGSNOR structure (chain B) (**Figure S2**).

Overall, this comparative analysis of the different forms of the two enzymes highlights that despite their structural similarity, specific structural differences are observed in the regions delimiting the shape and size of the catalytic cavity.

### ADH1 and GSNOR exhibit non-redundant catalytic properties

To compare the catalytic behaviour of ADH1 and GSNOR, we first determined the pH optimum of their respective activities: NAD<sup>+</sup>-dependent oxidation of EtOH for ADH1, and NADH-dependent degradation of GSNO for GSNOR. The highest rate of ADH1 for EtOH oxidation was measured at pH 10.0, while GSNOR efficiently degraded GSNO between pH 7.9 and 9.0 (**Figure S7**). At their optimal pH (pH 10 and 7.9 for ADH1 and GSNOR, respectively), the two enzymes possess similar specific activities (**Figure 5a**) with values comparable to paralogs from other organisms (Chang *et al.*, 2021). We then examined whether one protein could act on the other's substrate. The oxidation of ethanol was measured at pH 10, and the degradation of GSNO at pH 7.9. As shown in **Figure 5a**, ADH1 cannot catalyse NADH-dependent degradation of GSNO, and GSNOR cannot use EtOH as a substrate (*i.e.*, undetectable activities). These data indicate that these similar proteins are highly specific for their respective substrates and associated physiological roles.

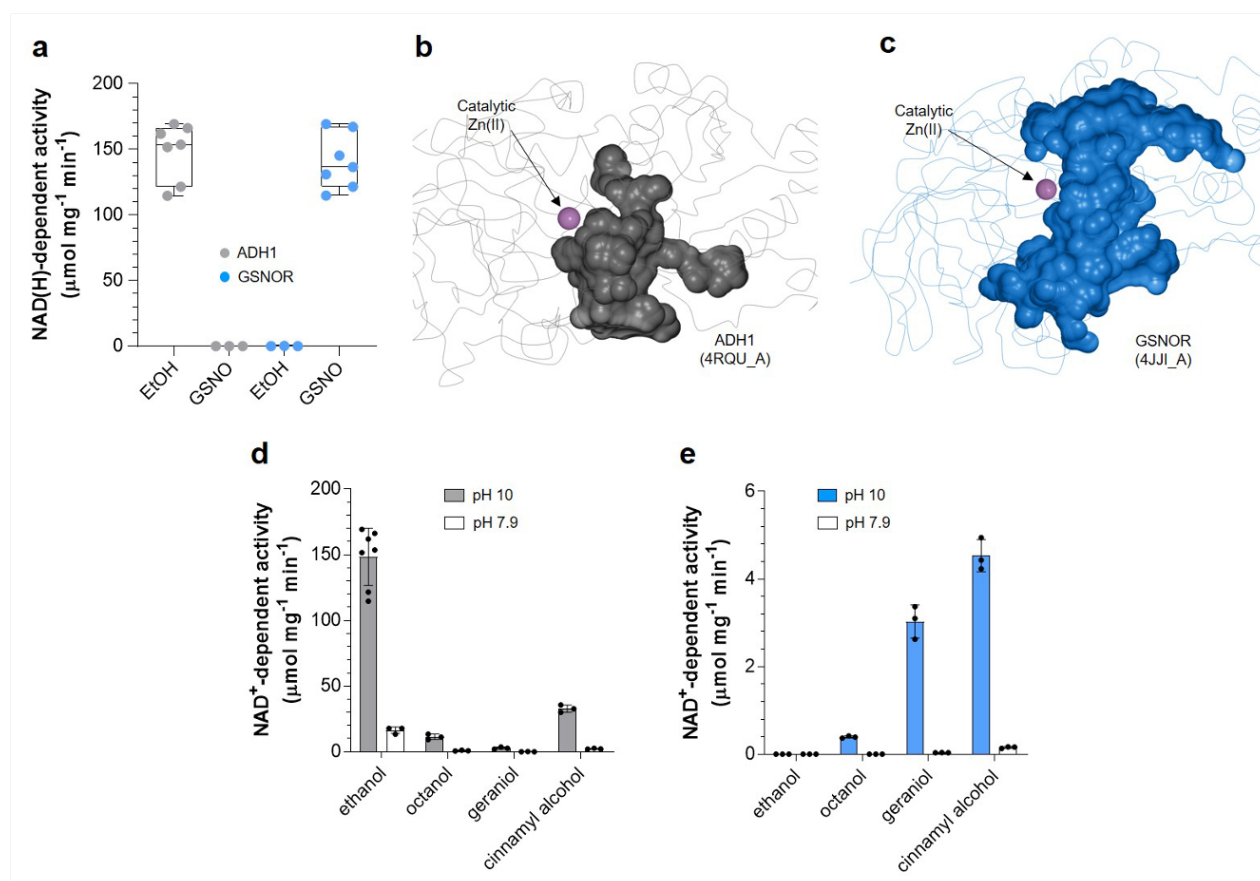


**Figure 5:** Analysis of kinetic properties of ADH1 and GSNOR. **(a)** Specific activities of ADH1 (grey closed circles) and GSNOR (blue closed circles) measured in the presence of 50 mM EtOH and 2 mM NAD<sup>+</sup> (EtOH oxidation, EtOH) or 0.4 mM GSNO and 0.2 mM NADH (GSNO degradation, GSNO). For both enzymes, activity measurements for EtOH oxidation and GSNO degradation were carried out at pH 10 and 7.9, respectively. The box plots are built on the basis of seven biological replicates. Solvent excluded surface of the internal cavity calculated for two representative ADH1 **(b)** and GSNOR **(c)** monomers. The protein backbone is represented by a thick ribbon and the catalytic zinc ion is represented by a violet sphere. **(d)** Specific activities of ADH1 in the presence of ethanol or different long chain alcohols (cinnamyl alcohol, geraniol, and octanol). Activities were determined at pH 10 (grey bars) and 7.9 (white bars). Data are represented as mean  $\pm$  SD ( $n = 3$ ). **(e)** Specific activities of GSNOR in the presence of different long chain alcohols (cinnamyl alcohol, geraniol, and octanol). Activities were determined at pH 10 (blue bars) and 7.9 (white bars). Data are represented as mean  $\pm$  SD ( $n = 3$ ). For panels D and E, long-chain alcohols were used at 5 mM to ensure their solubility in water.

To discern structural differences that might be responsible for their divergent catalytic abilities, the shape and volume of their catalytic cavity were examined. The volume of the internal cavities of each protein monomer without cofactor was calculated using the method described by Damborský and co-workers (Chovancova *et al.*, 2012) that makes use of two probe spheres of different radius. Representative catalytic cavities of ADH1 and GSNOR are depicted in **Figure 5b** and **5c**, while the complete set of calculated cavities is described in **Figure S8**. The calculated cavities of GSNOR are more than twice as large as those of ADH1, with an average volume of  $3722 \pm 395 \text{ \AA}^3$  and  $1567 \pm 122 \text{ \AA}^3$ , respectively. Thus, GSNOR presents a much larger substrate-binding pocket, presumably linked to the ability to better accommodate larger substrates (*e.g.*, GSNO). Consistently, the number of residues involved in the formation of catalytic cavity is higher for GSNOR (93 residues) compared to ADH1 (53 residues) (**Figure S6**). In addition, those residues present in both proteins are only partially conserved (47% sequence identity) (**Figure S6**), indicating that specific residues in the active site contribute to the observed substrate selectivity of these enzymes.

### Catalytic activity of ADH1 and GSNOR with long-chain alcohols

As highlighted in previous studies, plant ADHs can catalyse the reduction of various long-chain alcohols (Achkor *et al.*, 2003, Strommer, 2011, Kubienova *et al.*, 2013). Thus, we examined whether ADH1 and GSNOR could use octanol, geraniol, and cinnamyl alcohol as substrates. As shown in **Figure 5d** and **5e**, both enzymes catalysed the NAD<sup>+</sup>-dependent oxidation of long-chain alcohols at pH 10, though exhibiting largely different specific activities. In particular, ADH1 showed maximal activity in the presence of cinnamyl alcohol ( $32.81 \text{ \mu mol min}^{-1} \text{ mg}^{-1}$ ), which was  $\sim 22\%$  of that

measured with EtOH (**Figure 5d**). Similarly, GSNOR preferentially used cinnamyl alcohol but with a 7-fold lower specific activity compared to ADH1 ( $4.54 \mu\text{mol min}^{-1} \text{mg}^{-1}$ ; **Figure 5e**). When we measured the  $\text{NAD}^+$ -dependent oxidation of octanol, the activity of GSNOR was very low ( $0.39 \mu\text{mol min}^{-1} \text{mg}^{-1}$ ), while ADH1 catalysed the reaction with a specific activity of  $11.35 \mu\text{mol min}^{-1} \text{mg}^{-1}$ , a value that corresponds to  $\sim 8\%$  of EtOH-dependent activity (**Figure 5d and 5e**). Almost identical activities were measured in the presence of geraniol ( $2.82$  and  $3.03 \mu\text{mol min}^{-1} \text{mg}^{-1}$  for ADH1 and GSNOR, respectively; **Figure 5d and 5e**). For all long-chain alcohols, enzyme activities drastically dropped when monitored at pH 7.9, and in some cases, catalysis was almost undetectable (**Figure 5d and 5e**), suggesting that  $\text{NAD}^+$ -dependent oxidizing reactions are strongly favored at alkaline conditions. In sum, these results indicate that these two functionally divergent enzymes share the catalytic ability to oxidize long-chain alcohols, albeit with different catalytic capacities. Thus, the conformation of the active sites in the two ADHs appears adapted to the specific recognition of EtOH and GSNO but has structural similarities that allow both enzymes to use long-chain alcohols as substrates.

### Cysteine conservation, accessibility, and reactivity in Arabidopsis ADHs

ADH1 and GSNOR are cysteine-rich proteins containing 12 and 15 Cys residues, respectively (**Figure S6**). Among protein cysteines, eleven are fully conserved including Cys10, Cys173, Cys271, Cys284, Cys373, and the six invariable zinc-coordinating residues (Cys47 and Cys177 for the catalytic zinc ion, and Cys99, Cys102, Cys105 and Cys113 for the structural zinc ion; **Figures S6**), while Cys243 and Cys65/Cys94/Cys285/Cys370 are exclusively found in ADH1 and GSNOR, respectively (**Figure S6**).

To establish the number of solvent-exposed thiols and their position, we calculated the accessible surface area (ASA) of the entire residue and the  $S_\gamma$  atoms of cysteines (**Table S5**). ASA calculation revealed that ADH1 and GSNOR contain 4 and 7 cysteines, respectively, showing no or very low solvent accessibility (Cys10, 173, 284, and 373 for ADH1; Cys10, 65, 94, 173, 284, 285, and 372 for GSNOR; **Table S5**). Conversely, some cysteine residues stabilizing the structural and catalytic zinc ions are exposed to solvent, although their  $S_\gamma$  atoms show limited accessibility (**Table S5**). Similarly, Cys271 in the apo-forms of both enzymes, Cys243 in apo-ADH1, and Cys370 in apo-GSNOR show ASA values that range between 14 and  $40 \text{ \AA}^2$ , while the accessibility of their thiol group is zero or significantly lower (**Table S5**). Interestingly, in both enzymes Cys271 becomes buried when the cofactor ( $\text{NADH}$  or  $\text{NAD}^+$ ) is bound as the phosphate group and ribose of the nicotinamide moiety are located in front of it (**Figure 4**), reducing its exposure to the solvent (**Table S5**). Cofactor binding

significantly reduces the accessibility of other Cys in GSNOR, namely Cys370 and zinc-coordinating cysteine residues (Cys47, Cys102, and Cys177) (**Table S5**). In summary, the number of solvent-exposed cysteine residues are five for ADH1 (Cys99, 102, 105, 243, and 271) and seven for GSNOR (Cys47, 99, 102, 105, 177, 271, and 370) (**Table S5**).

The number of accessible cysteine thiols in ADH1 and GSNOR was further investigated by thiol titration using Ellman's reagent (5,5'-dithiobis(2-nitrobenzoic acid), DTNB). This analysis showed that each monomer of ADH1 and GSNOR contains ~2 accessible cysteine thiols ( $2.04 \pm 0.19$  and  $2.02 \pm 0.41$  for ADH1 and GSNOR, respectively). Almost identical values were found for the pre-reduced ADH1 and GSNOR, being  $2.22 \pm 0.14$  and  $2.19 \pm 0.25$ , respectively. To evaluate whether derivatization of accessible thiols had an effect on enzyme activities, we examined the redox response of ADH1 and GSNOR to DTNB and the alkylating agent NEM. Although both compounds are reactive toward accessible cysteine residues, DTNB causes reversible thiol modifications (*i.e.*, disulfide bonds), while NEM binds irreversibly. As shown in **Figure 6a**, both thiol-modifying agents caused similar and partial inactivation of ADHs, which retained ~50% (GSNOR) and ~75% (ADH1) of control activity after a 60 min incubation. No further inhibition was observed at longer incubation times (~48% and ~72% residual activity for ADH1 and GSNOR after 2 hours of incubation, respectively). As DTNB forms reversible disulfide bonds, we assessed the recovery of enzyme activity in the presence of the strong reducing agent tris(2-carboxyethyl)phosphine (TCEP). Intriguingly, TCEP largely restored DTNB-dependent inactivation ( $\sim 95 \pm 2\%$  and  $\sim 90 \pm 4\%$  of maximal activity for ADH1 and GSNOR, respectively), indicating that for both ADHs the thiol-derivatization by DTNB does not involve metal-coordinating cysteines since the reduction of these eventually oxidized residues would not allow replenishment of the zinc ion and recovery of enzyme activity.

In total, these results indicate that DTNB/NEM-dependent protein inhibition is caused by derivatization of solvent-accessible cysteine residues other than the metal-coordinating cysteines. As the most likely candidates, we identified Cys271 in both enzymes, Cys243 in ADH1, and Cys370 in GSNOR. However, since the thiol group of these residues is poorly accessible in the enzyme structure we hypothesize that when DTNB or NEM approaches the cysteine residues, their side chains may rotate toward the protein surface making the thiol group available to react.

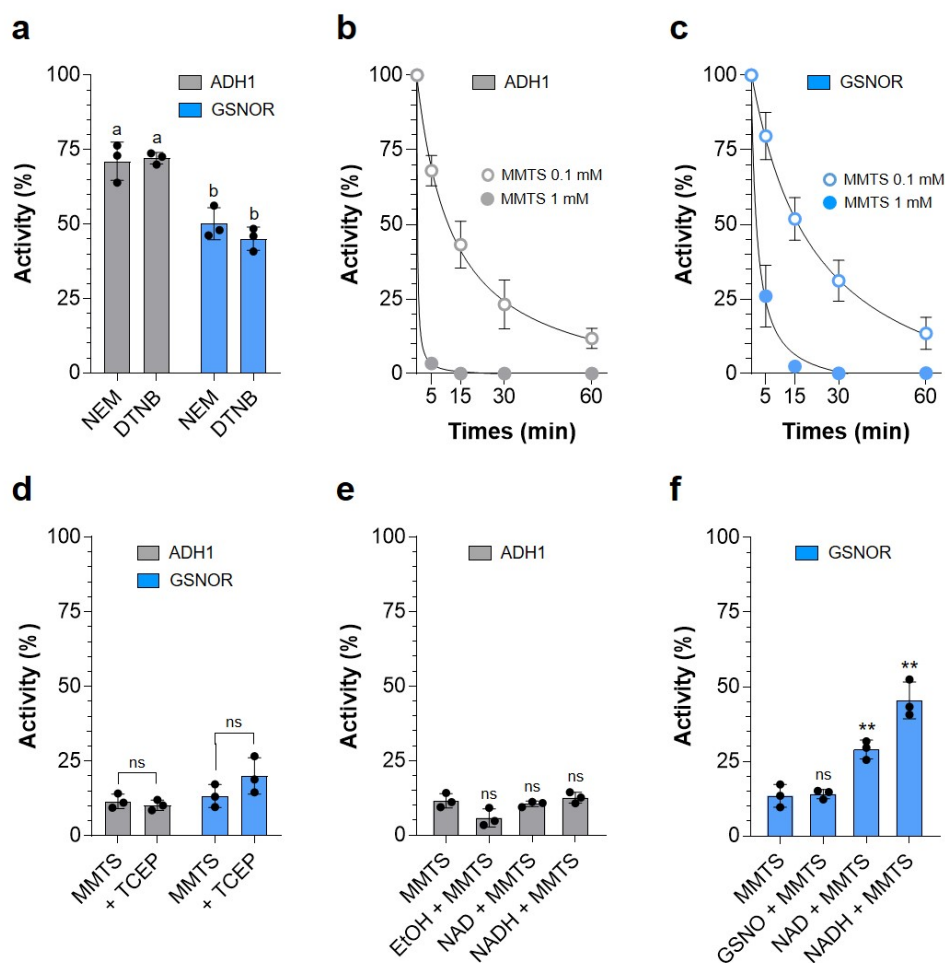


**Figure 6:** Sensitivity of *Arabidopsis* ADHs to thiol-modifying agents. (a) Inactivation treatments of ADH1 (grey bars) and GSNOR (blue bars) with NEM or DTNB. Proteins (2  $\mu$ M) were incubated for 60 min in the presence of 1 mM NEM or 0.2 mM DTNB. Data are represented as mean  $\pm$  SD ( $n = 3$ ). (b) and (c) Inactivation treatments of ADH1 and GSNOR with MMTS. Proteins (2  $\mu$ M) were incubated with 1 mM MMTS (closed grey/blue circles) or with 0.1 mM MMTS (open grey/blue circles). At the indicated times, an aliquot was withdrawn to measure enzyme activity. Data are represented as mean  $\pm$  SD ( $n = 3$ ). (d) and (e) Substrate and cofactor protection of ADH1 (grey bars) and GSNOR (blue bars) from MMTS-dependent inactivation. Proteins were pre-incubated in the presence of cofactors (0.2 mM NAD(H)) or substrates (50 mM EtOH or 0.2 mM GSNO) and then exposed to 0.1 mM MMTS (1 h). Data are represented as mean  $\pm$  SD ( $n = 3$ ). (f) The reversibility of ADH1 (grey bars) and GSNOR (blue bars) inactivation was assessed by addition of 10 mM TCEP after 1 h incubation with 0.1 mM MMTS. Data are represented as mean  $\pm$  SD ( $n = 3$ ). For panels A-F, values are expressed as percentage of protein activity measured under control conditions (see Experimental procedures). Statistical analysis was performed as described in Experimental procedures, \* $p \leq 0.05$ , \*\* $p \leq 0.01$ , \*\*\* $p \leq 0.001$ , \*\*\*\* $p \leq 0.0001$ , ns: not significant. Letters were used to distinguish groups that differ significantly.

### **Arabidopsis ADH1 and GSNOR are both sensitive to the thiol-modifying agent MMTS**

To further investigate the redox sensitivity of ADH1 and GSNOR, we examined the effect of the thiol-modifying agent MMTS, which can reversibly react with both accessible cysteines and metal-coordinating cysteine thiols (Tagliani *et al.*, 2021). As shown in **Figures 6b and 6c**, both enzymes are highly sensitive and exposure to 1 mM MMTS resulted in almost complete inhibition of enzyme activity after incubation for 5 min (ADH1) or 15 min (GSNOR). Inhibition kinetics were slower in the presence of 0.1 mM MMTS, but confirm the greater sensitivity of ADH1 compared with GSNOR (**Figure 6b and 6c**). We then evaluated the reversibility of protein inactivation and the protective effect of substrates (GSNO/EtOH) and cofactors (NAD/NADH) towards MMTS (0.1 mM) (**Figure 6d, 6e, and 6f**). For both enzymes, TCEP was unable to restore enzyme activities (Figure 6d) and pre-incubation with substrates did not affect the extent of inactivation. Cofactors did not provide any protection for ADH1, while they were effective in decreasing MMTS-dependent inhibition of GSNOR (**Figure 6e and 6f**).

The strong and irreversible inhibitory effect of MMTS prompted us to investigate the impact on protein stability and folding by monitoring absorbance at 405 nm to measure changes in turbidity as an assay of protein misfolding and by analysing secondary structure profiles using circular dichroism (CD). Surprisingly, MMTS caused dose-dependent GSNOR aggregation, with maximal turbidity reached after 1 h (1 mM) or 3 h (0.1 mM) (**Figure S9**). In contrast, no structural alteration was detected for ADH1 (**Figure S10**). Noticeably, CD analysis showed that MMTS (0.1 mM, 10:1 molar excess) does not alter the secondary structure of GSNOR significantly, while ADH1 appears to be slightly more sensitive (**Figure S11, Table S6**).

Interference with zinc ion coordination and possible metal release was then examined using the PAR assay after exposure to 1 mM MMTS for 1 h. Each protein released ~1 zinc ion per monomer, the value being  $1.08 \pm 0.34$  and  $1.05 \pm 0.13$  for ADH1 and GSNOR, respectively. Taken together, these results indicate that MMTS causes inhibition of both enzymes by altering the redox state of cysteine residues and particularly those involved in zinc ion coordination with consequent release of the metal. However, MMTS causes loss of structural integrity only for GSNOR.

### **H<sub>2</sub>O<sub>2</sub>-induced oxidation causes irreversible inhibition of ADH1 and GSNOR**

Hydrogen peroxide (H<sub>2</sub>O<sub>2</sub>) is one of the most common reactive oxygen species (ROS) produced by plant cells in response to both normal and stress conditions, and it is known to primarily react with reactive cysteine thiols on proteins (Trost *et al.*, 2017, Zaffagnini *et al.*, 2019a). To evaluate the

propensity of ADH1 and GSNOR to undergo cysteine oxidation, we treated both proteins with 2 mM  $H_2O_2$  and observed a decrease of enzymatic activities (**Figure 7a**). The time course of  $H_2O_2$ -mediated inhibition was much slower than that observed with MMTS, but again, ADH1 was more affected by  $H_2O_2$  compared to GSNOR, retaining ~38% and ~52% residual activity, respectively, after 1 hour of incubation. (**Figure 7a**). A longer incubation (4 h) had a more severe effect on both enzymes, causing almost complete inactivation (~2% and ~10% residual activity, respectively) (**Figure 7a**).

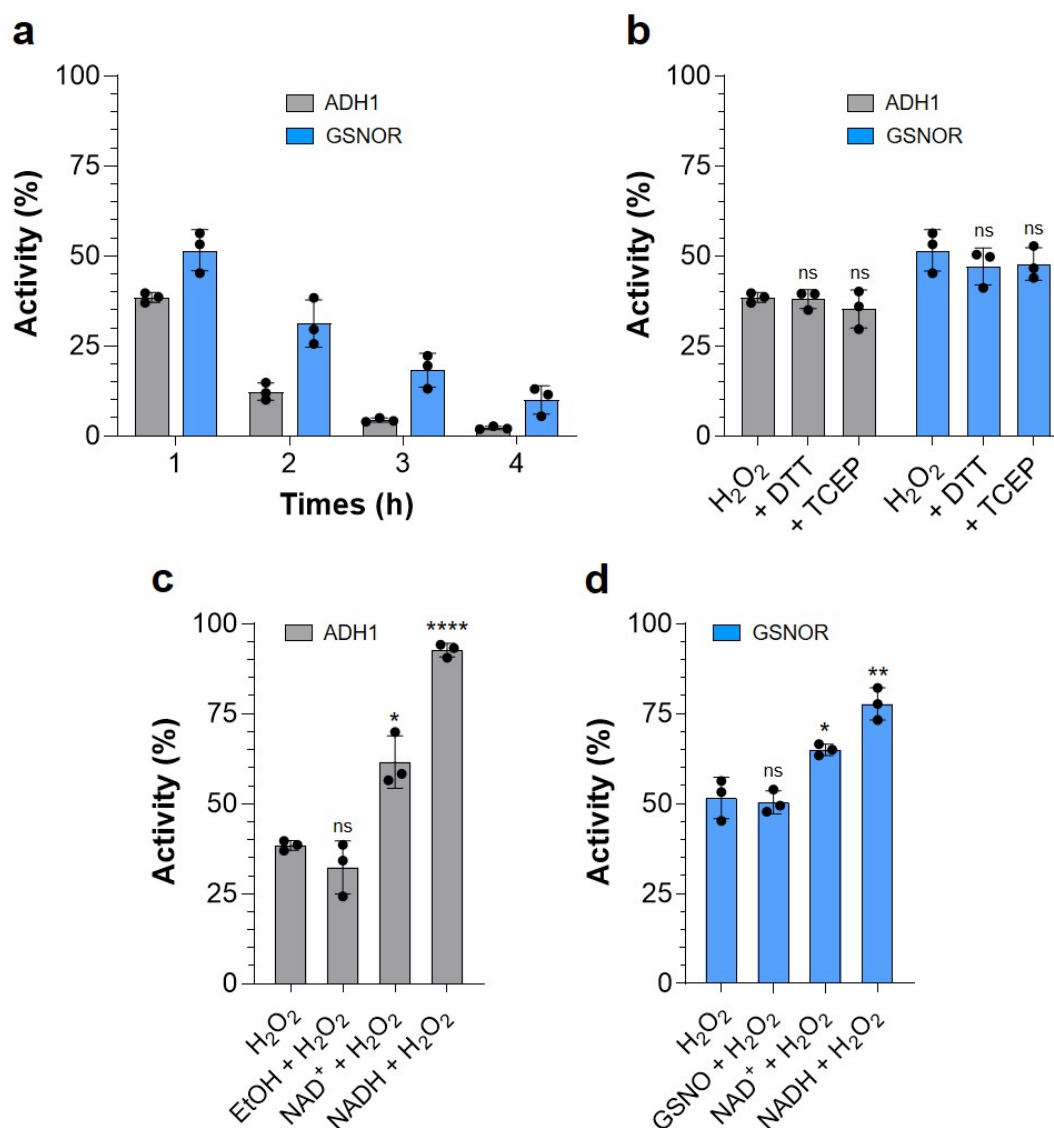


**Figure 7:** Sensitivity of *Arabidopsis* ADHs to  $H_2O_2$ -mediated oxidation. (a) Inactivation treatments of ADH1 (grey bars) and GSNOR (blue bars) with  $H_2O_2$ . Proteins (2  $\mu$ M) were incubated in the presence of 2 mM  $H_2O_2$ . At the indicated times, an aliquot was withdrawn to measure enzyme activity. Data are represented as mean  $\pm$  SD ( $n = 3$ ). (b) The reversibility of ADH1 and GSNOR inactivation was assessed by incubating oxidized proteins (1 h incubation with 2 mM  $H_2O_2$ ) with 10 mM TCEP or 20 mM DTT for 20 min after. Data are represented as mean  $\pm$  SD ( $n = 3$ ). (c) and (d) Substrate and cofactor protection of ADH1 (grey bars) and GSNOR (blue bars) from  $H_2O_2$ -dependent

*inactivation. Proteins (2  $\mu$ M) were pre-incubated with cofactors (0.2 mM NAD(H)) or substrates (50 mM EtOH or 0.2 mM GSNO) and then exposed to 2 mM H<sub>2</sub>O<sub>2</sub> for 1 h. Data are represented as mean  $\pm$  SD ( $n = 3$ ). For panels A-D, values are expressed as percentage of protein activity measured under control conditions (see Experimental procedures). Statistical analysis was performed as described in Experimental procedures, \* $p \leq 0.05$ , \*\* $p \leq 0.01$ , \*\*\* $p \leq 0.001$ , \*\*\*\* $p \leq 0.0001$ , ns: not significant.*

To determine if oxidation of ADH1 and GSNOR could be reversed by reducing treatments, we exploited two different reducing agents (TCEP and dithiothreitol, DTT) added independently to proteins partially inactivated by 1 h incubation with H<sub>2</sub>O<sub>2</sub>. Both reductants were ineffective in restoring protein activities indicating that H<sub>2</sub>O<sub>2</sub> caused cysteine oxidation that irreversibly affects ADH1 and GSNOR functionality (**Figure 7b**). We then evaluated the protective effects of substrates and cofactors toward oxidation and examined the stability of protein folding and zinc ions coordination. Intriguingly, we observed no protection in the presence of their respective substrates (*i.e.* EtOH and GSNO for ADH1 and GSNOR, respectively), while oxidized or reduced cofactors strongly hindered the inhibitory effect of H<sub>2</sub>O<sub>2</sub> with the inactivation of ADH1 almost completely abolished by the presence of NADH (**Figure 7c and 7d**). As evidenced by distortion of CD spectra, H<sub>2</sub>O<sub>2</sub> treatment (2 mM, 200:1 molar excess) altered the secondary structure of both enzymes to similar extents (**Figure S11, Table S7**). However, we observed no alteration in the structural stability for either protein (*i.e.*, no turbidity increase) (**Figures S9 and S10**). Finally, we tested the possible interference of H<sub>2</sub>O<sub>2</sub> on zinc ion coordination. Zinc ion release was determined after 4 h incubation with H<sub>2</sub>O<sub>2</sub>, and we found that  $\sim$ 1 zinc ion was released by each protein monomer ( $0.98 \pm 0.07$  and  $0.92 \pm 0.13$  for ADH1 and GSNOR, respectively).

In total, these results indicate that exposure of Arabidopsis ADHs to H<sub>2</sub>O<sub>2</sub> affects protein catalysis through oxidation of cysteine thiol(s) and destabilization of zinc coordination without altering native protein folding.

## Discussion

We report a detailed structural and biochemical comparison of ADH1 and GSNOR from *A. thaliana*. Despite their different physiological role, ADH1 and GSNOR have relatively high sequence identity and a similar 3D-structure except for the conformation and dimension of the active site (**Figures 3a, 3c, 3e, 5b, 5c, and S8**). These localized structural differences could explain the stringent affinity of ADH1 and GSNOR toward their specific substrates (EtOH and GSNO, respectively) (**Figure 5a**). This is further reinforced by the presence of specific sequences in the active site that distinguish alcohol dehydrogenases capable to process ethanol from those that can degrade GSNO (Thr<sub>60</sub>-Pro-(Leu/Val)<sub>62</sub> and Ser<sub>55</sub>-Gly-(Lys/Ala)-Asp-Pro-Glu-Gly<sub>61</sub> sequences, respectively) (**Figure S6**) (Shafqat *et al.*, 1996, Bui *et al.*, 2019). Both enzymes, however, are capable of oxidizing long-chain alcohols, albeit with different proficiency (**Figure 5d and 5e**). GSNOR activity is significantly lower than ADH1 with octanol and cinnamyl alcohol, probably because its large catalytic cavity prevents efficient binding and orientation of these substrates. Accordingly, the catalytic efficiency of GSNOR slightly improves as substrate hindrance increases (from octanol to geraniol), while an opposite behaviour is observed for ADH1. Both enzymes show the highest activity with the aromatic cinnamyl alcohol, possibly due to stabilizing interactions with aromatic residues located close to the catalytic zinc ion such as Phe95 (in ADH1) or Tyr95 (in GSNOR), Phe143 and Phe322 in both enzymes, and Phe53 and Phe321 only in ADH1. However, we cannot exclude that besides active site size and configuration, additional factors participate in substrate binding and processing. In any case, these data reinforce the potential role of this class of enzymes in controlling the metabolism of alcohols/aldehydes in specific plant tissues as previously observed during fruit ripening and maturation (Kalua and Boss, 2009; Strommer, 2011).

We demonstrated that the activity of both ADH1 and GSNOR responds to thiol-modifying agents as previously reported (Guerra *et al.*, 2016, Kovacs *et al.*, 2016, Ticha *et al.*, 2017, Dumont *et al.*, 2018). DTNB-dependent thiol titration shows that both enzymes contain at least two solvent-accessible cysteine thiols, while ASA calculations indicate that in addition to some zinc-coordinating cysteines, also Cys243 in apo-ADH1, Cys370 in apo-GSNOR and Cys271 in both enzymes, are solvent-exposed (Table S5). When treated with the thiol-modifying agents NEM and DTNB, both enzymes undergo partial inactivation (**Figure 6a**), indicating that derivatization of solvent accessible Cys thiols affects catalytic activity of these enzymes. Among possible cysteine candidates, modified Cys271 could be responsible for the altered enzyme activity since it is located near the cofactor (**Figure 4**), and the modification of its thiol group (*i.e.*, Cys-TNB disulfide or Cys-maleimide) could hinder proper cofactor binding. However, we cannot exclude that the reaction of DTNB/NEM with Cys243 in

ADH1 and Cys370 in GSNOR may also contribute to the inactivation of the proteins. Unlike DTNB and NEM, MMTS and H<sub>2</sub>O<sub>2</sub> led to a complete inactivation of the two enzymes, although with different inhibition kinetics (**Figures 6 and 7**). Previous studies, reported that H<sub>2</sub>O<sub>2</sub>-dependent inactivation of plant GSNOR is reversed by treatment with the reducing agent DTT, whereas oxidative inactivation of plant ADH1 was not reversed by reducing treatments (Kovacs *et al.*, 2016, Dumont *et al.*, 2018). Our results show that inactivation is irreversible for both enzymes and associated to the release of one zinc ion, possibly the catalytic one. Consistently, both enzymes were previously identified as prominent targets of H<sub>2</sub>O<sub>2</sub>-induced oxidation in *A. thaliana* cell cultures, and Cys47 and Cys177, which coordinate the catalytic zinc ion, were identified as target sites (Huang *et al.*, 2019b). Considering the protective effect of substrates/cofactors towards MMTS and H<sub>2</sub>O<sub>2</sub> (**Figures 6 and 7**), we observed that protein substrates (*i.e.*, EtOH and GSNO) were unable to limit the inhibitory effect, while cofactors, notably NADH, effectively counteracted thiol modification. Possible explanations for the protective mechanism of pyridine nucleotides reside in the fact that cofactor binding can directly protect accessible cysteine residues from modifications or induce conformational changes that may alter the protein sensitivity to thiol-modifying agents by changing the microenvironment and/or solvent accessibility of target cysteines. Notably, we observed that for both enzymes the interaction with oxidized or reduced cofactors affects the solvent accessibility of some cysteines including those involved in zinc ion coordination (Table S5).

In conclusion, our data reveal limited and localized structural differences in ADH1 and GSNOR catalytic sites that emphasize their stringent catalytic properties, and we show comparable redox sensitivity of the two enzymes. ADH1 and GSNOR play fundamental physiological roles in plant cells, being specifically involved in hypoxia-induced ethanolic fermentation and control of GSNO homeostasis, respectively (Strommer, 2011, Lindermayr, 2017, Jahnova *et al.*, 2019). In the model plant *A. thaliana*, ADH1 and GSNOR are both encoded by a single gene and constitute the sole enzymes capable of catalysing their respective reactions (NAD<sup>+</sup>-dependent conversion of EtOH to MeCHO and NADH-dependent degradation of GSNO, respectively) (Lee *et al.*, 2008, Xu *et al.*, 2013, Bui *et al.*, 2019). Having unique activities, regulation of ADH1 and GSNOR catalysis by thiol switching mechanisms becomes even more pivotal in controlling their physiological function especially under stress conditions when plant cells experience an over-production of ROS. In this regard, H<sub>2</sub>O<sub>2</sub> is considered the most relevant oxidizing molecule within plant cells and here we demonstrated that both ADHs exhibit marked sensitivity to H<sub>2</sub>O<sub>2</sub> with irreversible impairment of their activity (**Figure 7**). Likewise, altered nitric oxide (NO) homeostasis and treatment with NO donors have been shown to affect the activity of plant ADHs (Frunghillo *et al.*, 2014, Cheng *et al.*, 2015, Guerra *et al.*, 2016, Dumont *et al.*, 2018, Zhan *et al.*, 2018). Specifically, Arabidopsis ADHs are

inhibited by S-nitrosylation, and Cys10, Cys271 and Cys370 have been identified as target residues for GSNOR (Guerra *et al.*, 2016, Zhan *et al.*, 2018). We can therefore postulate that various cysteine-based oxidative modifications (*e.g.*, oxidation to sulfenic or sulfinic/sulfonic acids, S-nitrosylation, and likely S-glutathionylation) can modulate the function of both enzymes and potentially also impact their structural stability. In this regard, it will be crucial to identify cysteine residues that undergo redox modifications by analysing oxidised ADH forms through mass spectrometry and to assess their regulatory role by examining the redox sensitivity of single and/or multiple Cys mutants. What remains to be established is whether these thiol-switching mechanisms effectively occur and their extent under physiological conditions, and with what type of stress or metabolic condition they are associated. Notably, redox-dependent inhibition of ADH activities might represent an important regulatory mechanism to control intracellular GSNO level and activation of ethanol fermentation in response to hypoxic conditions, especially in *A. thaliana*, as both physiological pathways are specifically and uniquely controlled by GSNOR and ADH1.

## Materials and methods

### Cloning, expression, and purification of *A. thaliana* ADH1 and GSNOR

The coding sequence for *Arabidopsis thaliana* ADH1 (At1g77120) was amplified by standard RT-PCR on total *Arabidopsis* RNA extracts using a forward primer introducing a *Nde*I restriction site (in bold) at the start codon: 5'-GGCC**CATATGTCT**ACCACCGGACAGAT-3' and a reverse primer introducing a *Bam*HI restriction site (in bold) downstream of the stop codon: 5'-GGCC**CTCGAGTCAAGCACCCATGGT**GATGAT-3'. *ADH1* was then cloned in a pET-28a vector containing additional codons upstream of the *Nde*I site to express a tagged protein with six N-terminal histidines. The sequence was checked by sequencing. The pET-28a expression vector for *Arabidopsis thaliana* GSNOR (At5g43940) was already available (Guerra *et al.*, 2016). Both constructs were then used to transform *Escherichia coli* BL21(DE3). Bacteria were grown in LB medium supplemented with 50  $\mu\text{g ml}^{-1}$  kanamycin at 37 °C and the production of both proteins was induced with 100  $\mu\text{M}$  isopropyl  $\beta$ -D-1-thiogalactopyranoside overnight at 30 °C. Cells were then harvested by centrifugation (5,000 x *g* for 10 min) and resuspended in 30 mM Tris-HCl pH 7.9 (buffer A). Cell lysis was performed using a combination of lysozyme (100  $\mu\text{g}$  per ml of cells suspension) and sonication (5 cycles of 2 minutes each) (Zaffagnini *et al.*, 2014). Cell debris were removed by centrifugation (15,000 x *g* for 45 min) and the supernatant applied onto a Ni<sup>2+</sup>-Hitrap chelating resin (HIS-Select Nickel Affinity Gel; Sigma-Aldrich) equilibrated with buffer A containing 500 mM NaCl and 5 mM imidazole. The recombinant ADH1 and GSNOR were further purified according to the manufacturer's instructions. The molecular mass and purity of each protein were examined by SDS-PAGE after desalting with PD-10 columns (GE-Healthcare) equilibrated with buffer A. Protein concentration was determined spectrophotometrically using a molar extinction coefficient at 280 nm of 25,440 and 42,400  $\text{M}^{-1} \text{cm}^{-1}$  for of ADH1 and GSNOR, respectively. The resulting homogeneous protein solutions were stored at -20 °C.

### Activity assays

The catalytic activity of both ADH1 and GSNOR was measured spectrophotometrically monitoring the NAD(H) reduction/oxidation at 340 nm. EtOH oxidation was measured in an assay mixture containing 50 mM glycine-NaOH (pH 9.8), 50 mM EtOH, and 2 mM NAD<sup>+</sup>. GSNO-degrading activity was measured in a reaction buffer containing 100 mM Tris-HCl buffer (pH 7.9), 0.4 mM GSNO, and 0.2 mM NADH. For both proteins, the reaction was initiated by the addition of enzymes (10-50 nM) and activity was calculated using the linear variation of absorbance at 340 nm. To

determine the pH optimum, the activity of both proteins was monitored as just described but using different pH buffers. The following buffers (50 mM) were used: potassium phosphate at pH 6.5–7.5; Tris-HCl at pH 7.5–9; and glycine at pH 9–10. Protein activities in the presence of long-chain alcohols (*i.e.* octanol, geraniol, and cinnamyl alcohol) were measured in a reaction mixture containing 50 mM glycine-NaOH (pH 9.8), 5 mM long-chain alcohols, 2 mM NAD<sup>+</sup>, and variable amounts of ADH1 or GSNOR (50-400 nM).

### **DTNB-based thiol titration**

The number of free cysteine thiols in as-purified and pre-reduced ADHs was determined spectrophotometrically under non-denaturing conditions using 5,5'-dithiobis-2-nitrobenzoic acid (DTNB) (Zaffagnini *et al.*, 2014, Zaffagnini *et al.*, 2016b). Pre-reduced proteins were obtained after 30 min incubation with 10 mM DTT following desalting with NAP-5 columns (GE-Healthcare) equilibrated with buffer A. ADHs were incubated at room temperature in 100 mM Tris-HCl (pH 7.9) supplemented with 0.2 mM DTNB. The formation of TNB<sup>-</sup> was measured at 412 nm and the number of free thiols was calculated using a molar extinction coefficient of 14,150 M<sup>-1</sup> cm<sup>-1</sup>.

### **Cysteine-modifying treatments**

Thiol-modifying treatments were performed by incubating ADHs (2 μM) in 50 mM Tris-HCl (pH 7.9) in the presence of 0.2 mM DTNB, or 1 mM NEM, or 0.1/1 mM MMTS, or 2 mM H<sub>2</sub>O<sub>2</sub>. Control incubations were carried out in the absence of thiol-modifying agents. At the indicated time points, an aliquot was withdrawn and enzymatic activities were assessed as described above. To assess the reversibility, treated proteins were incubated in the presence of 10 mM TCEP or DTT and activities were measured after 30 min incubation. The protective effect of substrate(s) or cofactor(s) was carried out by pre-incubating ADH1 with 50 mM EtOH or 0.2 mM NAD(H), and GSNOR with 0.2 mM GSNO or 0.2 mM NAD(H). Residual activities were measured and expressed as a percentage of maximal activity (control conditions).

### **Zinc ion quantification**

The zinc release was measured spectrophotometrically following the bathochromic shift of 4-(2-pyridylazo)resorcinol (PAR). Specifically, 2 μM of ADH1 or GSNOR were incubated in buffer A supplemented with 2 mM H<sub>2</sub>O<sub>2</sub> for 4 h, or 1 mM MMTS for 1 h, or 2.5% SDS in the presence of 1 mM MMTS for 30 min. After incubation, PAR (15-40 μM) was added to ADH1 and GSNOR reaction

mixtures, and the absorbance at 497 nm was monitored over time. Zinc ion released was calculated using a calibration curve with known quantities of ZnCl<sub>2</sub> as standards.

### **Turbidity measurements**

The structural stability of ADHs was assayed spectrophotometrically by measuring the increase in absorbance at 405 nm (Zaffagnini *et al.*, 2019b). Proteins (2 μM) were incubated with 2 mM H<sub>2</sub>O<sub>2</sub> or 0.1/1 mM MMTS and absorbance was monitored for 180 min using a Perkin Elmer VICTOR X3 MultiLabel Plate Reader.

### **Protein crystallization and data collection**

Apo-GSNOR and NADH-ADH1 were crystallized using the hanging drop vapor diffusion method at 20 °C. The drop was obtained by mixing 2 μl of 10 mg mL<sup>-1</sup> (GSNOR) or 5 mg mL<sup>-1</sup> (ADH1) protein solution both in buffer A supplemented with 1 mM EDTA, and an equal volume of a reservoir solution containing 0.1 M Tris-HCl pH 8.5, 0.2 M MgCl<sub>2</sub>, and 12–20% w/v PEG 4 K or 0.1 M HEPES-NaOH pH 7.0–8.0, 2% v/v PEG 400 and 2 M (NH<sub>4</sub>)<sub>2</sub>SO<sub>4</sub> for GSNOR and ADH1, respectively. Crystals with a rod-like (GSNOR) or rhombohedral (ADH1) morphology appeared after about 10 days. The crystals were fished, briefly soaked in a cryo-solution containing the reservoir components plus 20% v/v PEG 400 as cryoprotectant, and then frozen in liquid nitrogen. Diffraction data were collected at 100 K using the synchrotron radiation of the I03 beamline at Diamond (Oxford, UK) or XRD2 beamline at Elettra (Trieste, Italy) with a wavelength of 0.97 or 1.00 Å, a sample-to-detector distance of 217.02 (Eiger2 XE 16M) or 311.29 mm (Pilatus 6M), a beam size of 20x20 or 50x50 μm<sup>2</sup> and an exposition time of 0.08 or 0.1 s for GSNOR and ADH1, respectively. An oscillation angle (Δφ) of 0.1° was used for all crystals. The images were indexed with XDS (Kabsch, 2010) and scaled with AIMLESS (Evans and Murshudov, 2013) from the CCP4 package (Winn *et al.*, 2011). Data collection statistics are reported in Table S7.

### **Structure solution and refinement**

Apo-GSNOR and NADH-ADH1 structures were solved by molecular replacement using the software PHASER (McCoy *et al.*, 2007) and the coordinates of *A. thaliana* NAD<sup>+</sup>-GSNOR (PDB ID 4JJI) and the AlphaFold (Jumper *et al.*, 2021) model of *A. thaliana* ADH1 (AF-P06525) as search models, respectively. Two dimers and one monomer were placed in the asymmetric unit consistently with the calculated Matthews coefficient (Matthews, 1968) of 2.14 Å<sup>3</sup> Da<sup>-1</sup> (solvent content 43%) for GSNOR

and  $2.48 \text{ \AA}^3 \text{ Da}^{-1}$  (solvent content 50%) for ADH1. The initial electron density map of GSNOR showed that the cofactor was absent while an electron density compatible with NADH was clearly observed in ADH1. The refinement was performed with REFMAC 5.8.0135 (Murshudov *et al.*, 2011) selecting 5% of reflections for  $R_{\text{free}}$ , and the manual rebuilding with Coot (Emsley and Cowtan, 2004). Water molecules were automatically added and, after a visual inspection, confirmed in the model only if contoured at  $1.0 \sigma$  on the  $(2F_o - F_c)$  electron density map and they fell into an appropriate hydrogen-bonding environment. Several PEG molecules coming from the crystallization solution were identified and added to the model. The last refinement cycle was performed with PHENIX (Adams *et al.*, 2010). Refinement statistics are reported in Table S7. The stereo-chemical quality of the models was checked with Molprobit (Chen *et al.*, 2010). Molecular graphics images were generated using PyMOL (The PyMOL Molecular Graphics System, Schrödinger, LLC).

### Structure analysis

The structural superposition and the subsequent RMSD calculations were conducted by using the Secondary Structure Matching algorithm in Coot (Emsley and Cowtan, 2004). The analysis of the protein cavity was performed using CAVER 3.0 (Chovancova *et al.*, 2012) and CAVER Analyst 1.0 (Kozlikova *et al.*, 2014) by setting the radius of the small and large probe spheres to 1.4 and 4.9 Å, respectively. The metal binding sites analysis and the pictures of the molecular structures were done using UCSF Chimera (Pettersen *et al.*, 2004) and UCSF ChimeraX (Goddard *et al.*, 2018, Pettersen *et al.*, 2021). The ASA values were calculated by the software Areaimol from the CCP4 package (Winn *et al.*, 2011).

### Circular dichroism analysis

The secondary structures of ADHs were investigated by means of circular dichroism (CD) spectroscopy. Samples of both proteins (10  $\mu\text{M}$ ) were prepared in buffer A and quantified by spectrophotometric analysis at 280 nm in a 1-cm cell ( $\epsilon_{280} = 25,440 \text{ M}^{-1} \text{ cm}^{-1}$  for ADH1 and  $42,400 \text{ M}^{-1} \text{ cm}^{-1}$  for GSNOR) (Pace *et al.*, 1995). Treated samples were obtained by incubating both proteins in the presence of 2 mM  $\text{H}_2\text{O}_2$  (4 h) or 0.1 mM MMTS (1 h for GSNOR, 2 h for ADH1). The far-UV CD spectra (260–190 nm) of all samples were measured at room temperature on a J-715 spectropolarimeter (Jasco, Japan), using a QS-quartz cylindrical cell with 0.2 mm optical pathlength (Hellma Analytics, Germany), a 2 nm spectral bandwidth, a 50 nm/min scanning speed, a 2 s data integration time, a 0.5 nm data interval and an accumulation cycle of 3 scans. The resulting CD spectra

were corrected by subtracting the spectral contribution of solvent and eventual thiol-modifying agents, then converted to molar units per residue ( $\Delta\epsilon_{\text{res}}$ , in  $\text{M}^{-1} \text{cm}^{-1}$ ). The estimation of secondary structures from the CD spectra of native and treated samples was then performed using the CDSSTR algorithm (Sreerama and Woody, 2000) and the SP175 protein reference set (Lees *et al.*, 2006) available on the DichroWeb web server (<http://dichroweb.cryst.bbk.ac.uk/>) (Miles *et al.*, 2022).

### **Replicates and statistical analyses**

All the results reported are representative of at least three independent biological replicates and expressed as mean  $\pm$  S.D. Statistical analysis was performed using unpaired t-test with Welch's correction in the case of two categories or one-way ANOVA followed by a Tukey's post-hoc test for multiple comparisons. P values reported on graphs as follows: \* $p \leq 0.05$ , \*\* $p \leq 0.01$ , \*\*\* $p \leq 0.001$ , \*\*\*\* $p \leq 0.0001$ . Letters were used to distinguish groups that differ significantly, as indicated in figure legends.

## References

- Achkor, H., Diaz, M., Fernandez, M.R., Biosca, J.A., Pares, X. and Martinez, M.C. (2003) Enhanced formaldehyde detoxification by overexpression of glutathione-dependent formaldehyde dehydrogenase from Arabidopsis. *Plant Physiol*, 132, 2248-2255.
- Adams, P.D., Afonine, P.V., Bunkoczi, G., Chen, V.B., Davis, I.W., Echols, N., Headd, J.J., Hung, L.W., Kapral, G.J., Grosse-Kunstleve, R.W., McCoy, A.J., Moriarty, N.W., Oeffner, R., Read, R.J., Richardson, D.C., Richardson, J.S., Terwilliger, T.C. and Zwart, P.H. (2010) PHENIX: a comprehensive Python-based system for macromolecular structure solution. *Acta Crystallogr D Biol Crystallogr*, 66, 213-221.
- Antonio, C., Papke, C., Rocha, M., Diab, H., Limami, A.M., Obata, T., Fernie, A.R. and van Dongen, J.T. (2016) Regulation of Primary Metabolism in Response to Low Oxygen Availability as Revealed by Carbon and Nitrogen Isotope Redistribution. *Plant Physiol*, 170, 43-56.
- Broniowska, K.A., Diers, A.R. and Hogg, N. (2013) S-Nitrosoglutathione. *Biochim Biophys Acta*.
- Bui, L.T., Novi, G., Lombardi, L., Iannuzzi, C., Rossi, J., Santaniello, A., Mensuali, A., Corbineau, F., Giuntoli, B., Perata, P., Zaffagnini, M. and Licausi, F. (2019) Conservation of ethanol fermentation and its regulation in land plants. *J Exp Bot*, 70, 1815-1827.
- Chang, A., Jeske, L., Ulbrich, S., Hofmann, J., Koblitiz, J., Schomburg, I., Neumann-Schaal, M., Jahn, D. and Schomburg, D. (2021) BRENDA, the ELIXIR core data resource in 2021: new developments and updates. *Nucleic Acids Res*, 49, D498-D508.
- Chen, F., Wang, P., An, Y., Huang, J. and Xu, Y. (2015) Structural insight into the conformational change of alcohol dehydrogenase from Arabidopsis thaliana L. during coenzyme binding. *Biochimie*, 108, 33-39.
- Chen, V.B., Arendall, W.B., 3rd, Headd, J.J., Keedy, D.A., Immormino, R.M., Kapral, G.J., Murray, L.W., Richardson, J.S. and Richardson, D.C. (2010) MolProbity: all-atom structure validation for macromolecular crystallography. *Acta Crystallogr D Biol Crystallogr*, 66, 12-21.
- Cheng, T., Chen, J., Ef, A.A., Wang, P., Wang, G., Hu, X. and Shi, J. (2015) Quantitative proteomics analysis reveals that S-nitrosoglutathione reductase (GSNOR) and nitric oxide signaling enhance poplar defense against chilling stress. *Planta*, 242, 1361-1390.
- Chovancova, E., Pavelka, A., Benes, P., Strnad, O., Brezovsky, J., Kozlikova, B., Gora, A., Sustr, V., Klvana, M., Medek, P., Biedermannova, L., Sochor, J. and Damborsky, J. (2012) CAVER 3.0: a tool for the analysis of transport pathways in dynamic protein structures. *PLoS Comput Biol*, 8, e1002708.
- Dixon, D.P., Skipsey, M., Grundy, N.M. and Edwards, R. (2005) Stress-induced protein S-glutathionylation in Arabidopsis. *Plant Physiol*, 138, 2233-2244.
- Dumont, S., Bykova, N.V., Khaou, A., Besserour, Y., Dorval, M. and Rivoal, J. (2018) Arabidopsis thaliana alcohol dehydrogenase is differently affected by several redox modifications. *PLoS One*, 13, e0204530.
- Dupuis, J.H., Wang, S., Song, C. and Yada, R.Y. (2020) The role of disulfide bonds in a Solanum tuberosum saposin-like protein investigated using molecular dynamics. *PLoS One*, 15, e0237884.
- Emsley, P. and Cowtan, K. (2004) Coot: model-building tools for molecular graphics. *Acta Crystallogr D Biol Crystallogr*, 60, 2126-2132.
- Evans, P.R. and Murshudov, G.N. (2013) How good are my data and what is the resolution? *Acta Crystallogr D Biol Crystallogr*, 69, 1204-1214.
- Fares, A., Rossignol, M. and Peltier, J.B. (2011) Proteomics investigation of endogenous S-nitrosylation in Arabidopsis. *Biochem Biophys Res Commun*, 416, 331-336.
- Fliegmann, J. and Sandermann, H., Jr. (1997) Maize glutathione-dependent formaldehyde dehydrogenase cDNA: a novel plant gene of detoxification. *Plant Mol Biol*, 34, 843-854.
- Frungillo, L., Skelly, M.J., Loake, G.J., Spoel, S.H. and Salgado, I. (2014) S-nitrosothiols regulate nitric oxide production and storage in plants through the nitrogen assimilation pathway. *Nat Commun*, 5, 5401.
- Goddard, T.D., Huang, C.C., Meng, E.C., Pettersen, E.F., Couch, G.S., Morris, J.H. and Ferrin, T.E. (2018) UCSF ChimeraX: Meeting modern challenges in visualization and analysis. *Protein Sci*, 27, 14-25.
- Guerra, D., Ballard, K., Truebridge, I. and Vierling, E. (2016) S-Nitrosation of Conserved Cysteines Modulates Activity and Stability of S-Nitrosoglutathione Reductase (GSNOR). *Biochemistry*, 55, 2452-2464.

- Huang, D., Huo, J., Zhang, J., Wang, C., Wang, B., Fang, H. and Liao, W. (2019a) Protein S-nitrosylation in programmed cell death in plants. *Cell Mol Life Sci*, 76, 1877-1887.
- Huang, J., Willems, P., Wei, B., Tian, C., Ferreira, R.B., Bodra, N., Martinez Gache, S.A., Wahni, K., Liu, K., Vertommen, D., Gevaert, K., Carroll, K.S., Van Montagu, M., Yang, J., Van Breusegem, F. and Messens, J. (2019b) Mining for protein S-sulfenylation in Arabidopsis uncovers redox-sensitive sites. *Proc Natl Acad Sci U S A*, 116, 21256-21261.
- Jahnova, J., Luhova, L. and Petrivalsky, M. (2019) S-Nitrosogluthathione Reductase-The Master Regulator of Protein S-Nitrosation in Plant NO Signaling. *Plants (Basel)*, 8.
- Jumper, J., Evans, R., Pritzel, A., Green, T., Figurnov, M., Ronneberger, O., Tunyasuvunakool, K., Bates, R., Zidek, A., Potapenko, A., Bridgland, A., Meyer, C., Kohl, S.A.A., Ballard, A.J., Cowie, A., Romera-Paredes, B., Nikolov, S., Jain, R., Adler, J., Back, T., Petersen, S., Reiman, D., Clancy, E., Zielinski, M., Steinegger, M., Pacholska, M., Berghammer, T., Bodenstein, S., Silver, D., Vinyals, O., Senior, A.W., Kavukcuoglu, K., Kohli, P. and Hassabis, D. (2021) Highly accurate protein structure prediction with AlphaFold. *Nature*, 596, 583-589.
- Kabsch, W. (2010) Xds. *Acta Crystallogr D Biol Crystallogr*, 66, 125-132.
- Kovacs, I., Holzmeister, C., Wirtz, M., Geerlof, A., Frohlich, T., Romling, G., Kuruthukulangarakoola, G.T., Linster, E., Hell, R., Arnold, G.J., Durner, J. and Lindermayr, C. (2016) ROS-Mediated Inhibition of S-nitrosogluthathione Reductase Contributes to the Activation of Anti-oxidative Mechanisms. *Front Plant Sci*, 7, 1669.
- Kozlikova, B., Sebestova, E., Sustr, V., Brezovsky, J., Strnad, O., Daniel, L., Bednar, D., Pavelka, A., Manak, M., Bezdeka, M., Benes, P., Kotry, M., Gora, A., Damborsky, J. and Sochor, J. (2014) CAVER Analyst 1.0: graphic tool for interactive visualization and analysis of tunnels and channels in protein structures. *Bioinformatics*, 30, 2684-2685.
- Krzywoszynska, K., Swiatek-Kozłowska, J., Potocki, S., Ostrowska, M. and Kozłowski, H. (2020) Triplet of cysteines - Coordinational riddle? *J Inorg Biochem*, 204, 110957.
- Kubienova, L., Kopečný, D., Tylichova, M., Briozzo, P., Skopalova, J., Sebelá, M., Navrátil, M., Tache, R., Luhova, L., Barroso, J.B. and Petrivalsky, M. (2013) Structural and functional characterization of a plant S-nitrosogluthathione reductase from *Solanum lycopersicum*. *Biochimie*, 95, 889-902.
- Lee, U., Wie, C., Fernandez, B.O., Feelisch, M. and Vierling, E. (2008) Modulation of nitrosative stress by S-nitrosogluthathione reductase is critical for thermotolerance and plant growth in Arabidopsis. *Plant Cell*, 20, 786-802.
- Lees, J.G., Miles, A.J., Wien, F. and Wallace, B.A. (2006) A reference database for circular dichroism spectroscopy covering fold and secondary structure space. *Bioinformatics*, 22, 1955-1962.
- Lindermayr, C. (2017) Crosstalk between reactive oxygen species and nitric oxide in plants: Key role of S-nitrosogluthathione reductase. *Free Radic Biol Med*.
- Liu, L., Hausladen, A., Zeng, M., Que, L., Heitman, J. and Stamler, J.S. (2001) A metabolic enzyme for S-nitrosothiol conserved from bacteria to humans. *Nature*, 410, 490-494.
- Loreti, E., van Veen, H. and Perata, P. (2016) Plant responses to flooding stress. *Curr Opin Plant Biol*, 33, 64-71.
- Marshall, R.S., Frigerio, L. and Roberts, L.M. (2010) Disulfide formation in plant storage vacuoles permits assembly of a multimeric lectin. *Biochem J*, 427, 513-521.
- Matthews, B.W. (1968) Solvent content of protein crystals. *J Mol Biol*, 33, 491-497.
- Mattioli, E.J., Rossi, J., Meloni, M., De Mia, M., Marchand, C.H., Tagliani, A., Fanti, S., Falini, G., Trost, P., Lemaire, S.D., Fermani, S., Calvaresi, M. and Zaffagnini, M. (2022) Structural snapshots of nitrosogluthathione binding and reactivity underlying S-nitrosylation of photosynthetic GAPDH. *Redox biology*, 54, 102387.
- McCoy, A.J., Grosse-Kunstleve, R.W., Adams, P.D., Winn, M.D., Storoni, L.C. and Read, R.J. (2007) Phaser crystallographic software. *J Appl Crystallogr*, 40, 658-674.
- Miles, A.J., Ramalli, S.G. and Wallace, B.A. (2022) DichroWeb, a website for calculating protein secondary structure from circular dichroism spectroscopic data. *Protein Sci*, 31, 37-46.
- Murshudov, G.N., Skubak, P., Lebedev, A.A., Pannu, N.S., Steiner, R.A., Nicholls, R.A., Winn, M.D., Long, F. and Vagin, A.A. (2011) REFMAC5 for the refinement of macromolecular crystal structures. *Acta Crystallogr D Biol Crystallogr*, 67, 355-367.
- Orengo, C.A., Michie, A.D., Jones, S., Jones, D.T., Swindells, M.B. and Thornton, J.M. (1997) CATH--a hierarchic classification of protein domain structures. *Structure*, 5, 1093-1108.

- Pace, C.N., Vajdos, F., Fee, L., Grimsley, G. and Gray, T. (1995) How to measure and predict the molar absorption coefficient of a protein. *Protein Sci*, 4, 2411-2423.
- Pace, N.J. and Weerapana, E. (2014) Zinc-binding cysteines: diverse functions and structural motifs. *Biomolecules*, 4, 419-434.
- Paulsen, C.E. and Carroll, K.S. (2013) Cysteine-mediated redox signaling: chemistry, biology, and tools for discovery. *Chemical reviews*, 113, 4633-4679.
- Permyakov, E.A. (2021) Metal Binding Proteins. 1, 261-292.
- Persson, B., Hedlund, J. and Jornvall, H. (2008) Medium- and short-chain dehydrogenase/reductase gene and protein families : the MDR superfamily. *Cell Mol Life Sci*, 65, 3879-3894.
- Pettersen, E.F., Goddard, T.D., Huang, C.C., Couch, G.S., Greenblatt, D.M., Meng, E.C. and Ferrin, T.E. (2004) UCSF Chimera--a visualization system for exploratory research and analysis. *J Comput Chem*, 25, 1605-1612.
- Pettersen, E.F., Goddard, T.D., Huang, C.C., Meng, E.C., Couch, G.S., Croll, T.I., Morris, J.H. and Ferrin, T.E. (2021) UCSF ChimeraX: Structure visualization for researchers, educators, and developers. *Protein Sci*, 30, 70-82.
- Poole, L.B. (2015) The basics of thiols and cysteines in redox biology and chemistry. *Free Radic Biol Med*, 80, 148-157.
- Shafqat, J., El-Ahmad, M., Danielsson, O., Martinez, M.C., Persson, B., Pares, X. and Jornvall, H. (1996) Pea formaldehyde-active class III alcohol dehydrogenase: common derivation of the plant and animal forms but not of the corresponding ethanol-active forms (classes I and P). *Proc Natl Acad Sci U S A*, 93, 5595-5599.
- Sreerama, N. and Woody, R.W. (2000) Estimation of protein secondary structure from circular dichroism spectra: comparison of CONTIN, SELCON, and CDSSTR methods with an expanded reference set. *Anal Biochem*, 287, 252-260.
- Strommer, J. (2011) The plant ADH gene family. *Plant J*, 66, 128-142.
- Tagliani, A., Rossi, J., Marchand, C.H., De Mia, M., Tedesco, D., Gurrieri, L., Meloni, M., Falini, G., Trost, P., Lemaire, S.D., Fermani, S. and Zaffagnini, M. (2021) Structural and functional insights into nitrosogluthione reductase from *Chlamydomonas reinhardtii*. *Redox biology*, 38, 101806.
- Ticha, T., Lochman, J., Cincalova, L., Luhova, L. and Petrivalsky, M. (2017) Redox regulation of plant S-nitrosogluthione reductase activity through post-translational modifications of cysteine residues. *Biochem Biophys Res Commun*, 494, 27-33.
- Trivedi, M.V., Laurence, J.S. and Siahaan, T.J. (2009) The role of thiols and disulfides on protein stability. *Curr Protein Pept Sci*, 10, 614-625.
- Trost, P., Fermani, S., Calvaresi, M. and Zaffagnini, M. (2017) Biochemical basis of sulphenomics: how protein sulphenic acids may be stabilized by the protein microenvironment. *Plant Cell Environ*, 40, 483-490.
- Wei, B., Willems, P., Huang, J., Tian, C., Yang, J., Messens, J. and Van Breusegem, F. (2020) Identification of Sulfenylated Cysteines in *Arabidopsis thaliana* Proteins Using a Disulfide-Linked Peptide Reporter. *Front Plant Sci*, 11, 777.
- Winn, M.D., Ballard, C.C., Cowtan, K.D., Dodson, E.J., Emsley, P., Evans, P.R., Keegan, R.M., Krissinel, E.B., Leslie, A.G., McCoy, A., McNicholas, S.J., Murshudov, G.N., Pannu, N.S., Potterton, E.A., Powell, H.R., Read, R.J., Vagin, A. and Wilson, K.S. (2011) Overview of the CCP4 suite and current developments. *Acta Crystallogr D Biol Crystallogr*, 67, 235-242.
- Xu, S., Guerra, D., Lee, U. and Vierling, E. (2013) S-nitrosogluthione reductases are low-copy number, cysteine-rich proteins in plants that control multiple developmental and defense responses in *Arabidopsis*. *Front Plant Sci*, 4, 430.
- Yamazaki, D., Motohashi, K., Kasama, T., Hara, Y. and Hisabori, T. (2004) Target proteins of the cytosolic thioredoxins in *Arabidopsis thaliana*. *Plant Cell Physiol*, 45, 18-27.
- Zaffagnini, M., De Mia, M., Morisse, S., Di Giacinto, N., Marchand, C.H., Maes, A., Lemaire, S.D. and Trost, P. (2016a) Protein S-nitrosylation in photosynthetic organisms: A comprehensive overview with future perspectives. *Biochim Biophys Acta*, 1864, 952-966.
- Zaffagnini, M., Fermani, S., Calvaresi, M., Orru, R., Iommarini, L., Sparla, F., Falini, G., Bottoni, A. and Trost, P. (2016b) Tuning Cysteine Reactivity and Sulfenic Acid Stability by Protein Microenvironment in Glyceraldehyde-3-Phosphate Dehydrogenases of *Arabidopsis thaliana*. *Antioxid Redox Signal*, 24, 502-517.
- Zaffagnini, M., Fermani, S., Marchand, C.H., Costa, A., Sparla, F., Rouhier, N., Geigenberger, P., Lemaire, S.D. and Trost, P. (2019a) Redox Homeostasis in Photosynthetic Organisms: Novel and Established Thiol-Based Molecular Mechanisms. *Antioxid Redox Signal*, 31, 155-210.

- Zaffagnini, M., Marchand, C.H., Malferrari, M., Murail, S., Bonacchi, S., Genovese, D., Montalti, M., Venturoli, G., Falini, G., Baaden, M., Lemaire, S.D., Fermani, S. and Trost, P. (2019b) Glutathionylation primes soluble glyceraldehyde-3-phosphate dehydrogenase for late collapse into insoluble aggregates. *Proc Natl Acad Sci U S A*, 116, 26057-26065.
- Zaffagnini, M., Michelet, L., Sciabolini, C., Di Giacinto, N., Morisse, S., Marchand, C.H., Trost, P., Fermani, S. and Lemaire, S.D. (2014) High-resolution crystal structure and redox properties of chloroplastic triosephosphate isomerase from *Chlamydomonas reinhardtii*. *Mol Plant*, 7, 101-120.
- Zhan, N., Wang, C., Chen, L., Yang, H., Feng, J., Gong, X., Ren, B., Wu, R., Mu, J., Li, Y., Liu, Z., Zhou, Y., Peng, J., Wang, K., Huang, X., Xiao, S. and Zuo, J. (2018) S-Nitrosylation Targets GSNO Reductase for Selective Autophagy during Hypoxia Responses in Plants. *Mol Cell*, 71, 142-154 e146.
- Zhang, T., Ma, M., Chen, T., Zhang, L., Fan, L., Zhang, W., Wei, B., Li, S., Xuan, W., Noctor, G. and Han, Y. (2020) Glutathione-dependent denitrosation of GSNOR1 promotes oxidative signalling downstream of H<sub>2</sub>O<sub>2</sub>. *Plant Cell Environ.*



**CHAPTER V: “In-depth dissection of biochemical features of alcohol dehydrogenase from *Arabidopsis thaliana* and related physiological insights”**

*This chapter is based on a manuscript in preparation*

## Summary

Oxygen shortages represent a stress circumstance to which plants are often subjected. To overcome this stressful situation, many adaptative strategies are put in place, mostly consisting in morpho-physiological modifications and major metabolic rearrangement. Specifically, there is a shift in the metabolic strategy for energy production as a result of the blockage of oxidative phosphorylation due to the low availability of oxygen as final acceptor of the mitochondrial electron transport chain. In such conditions, the energy production is entrusted exclusively to glycolysis coupled with  $\text{NAD}^+$  regenerative pathways, which include ethanol fermentation. Ethanol fermentation proceeds through the decarboxylation of pyruvate to acetaldehyde (MeCHO) catalyzed by the enzyme pyruvate decarboxylase (PDC), followed by the reduction of MeCHO to ethanol (EtOH) catalyzed by alcohol dehydrogenase (ADH). These two enzymes are part of the anaerobic polypeptides (ANPs) whose expression depends on a group of transcription factors called hypoxia-associated ethylene response factor group VII (ERF-VII). The stability of these transcription factors depends on oxygen levels, thereby connecting oxygen sensing and downstream response. In fact, in normoxic conditions they are degraded through a Cys-branch of the N-degron pathway, conversely being stabilized in low oxygen conditions. Under hypoxia, ERF-VIIs induce the expression of a cluster of genes called Hypoxia-Responsive Genes (HRGs), mainly involved in anaerobic fermentation, saccharose metabolism, control of reactive species and transcriptional control.

In this work we aimed at characterizing the functional features of ADH in the model plant *Arabidopsis thaliana*. We performed biochemical and thermodynamic analysis on the recombinant enzyme, particularly focusing on its catalytic role related to the NADH-dependent conversion of MeCHO to EtOH. By optimizing the catalytic assay for measuring such activity, we determined the relative kinetic parameters, namely Michaelis-Menten constant ( $K_m$ ), turnover number ( $k_{\text{cat}}$ ), and catalytic efficiency ( $k_{\text{cat}}/K_m$ ). The same kinetic parameters were also determined for the reverse activity, *i.e.*,  $\text{NAD}^+$ - oxidation of EtOH. In addition, thermodynamic analysis was carried out to compare the enthalpic and entropic determinants of the binding of MeCHO or EtOH into ADH catalytic pocket. Taken together, these results reveal that the NADH-dependent acetaldehyde reduction is the catalytically favored ADH-related reaction.

To gain a deeper understanding of ADH role, we employed protein extracts from 7-days old *Arabidopsis* seedlings. We combined immunodetection analysis to establish the presence of

ADH with activity assays to monitor ADH-related activities. Our data show that also in a physiological context the NADH-dependent acetaldehyde reduction is the most represented activity, being highly induced upon hypoxic circumstances. Interestingly, such activity was strongly represented even upon restoration of normoxic conditions, suggesting a substantial latency time for the recovery of physiological oxygen-dependent metabolism.

Finally, we unraveled a MeCHO detoxification system involving NADPH as cofactor. Apart from the involvement of enzymes that have yet to be identified, we demonstrated that ADH largely participates in this detoxification system, indicating that this enzyme not only use NAD(H) as a cofactor but is also able to use the reducing power of NADPH, although with lower affinity as determined by kinetic analysis performed on recombinant enzyme.

## Results

### **Biochemical analyses of ADH identify NADH-dependent acetaldehyde reduction as the catalytically favored reaction**

Over the last two decades, the NAD<sup>+</sup>-dependent oxidation of ethanol (EtOH) has been the only activity examined when studying plant ADH. However, since it is well known that the physiological activity in plant is the opposite reaction, *i.e.*, NADH-dependent reduction of acetaldehyde (MeCHO), in this work we resumed and optimized activity assays to evaluate both reactions. This allowed us to perform an in-depth biochemical characterization of the recombinant ADH from *Arabidopsis thaliana* (AtADH). We assayed the ADH-related activities consisting in the conversion of MeCHO into EtOH and *vice versa* by following the absorbance at 340 nm related to NADH consumption and production. For each reaction, maximal activity (*i.e.*, specific activity) was determined after establishing saturating concentrations for both substrates (MeCHO and EtOH at 15 and 50 mM, respectively) and cofactors (NADH and NAD<sup>+</sup> at 0.2 and 2 mM, respectively). In addition, we analyzed the dependency of ADH catalytic capacity on pH. As shown in **Figure 1**, the two ADH-related activities measured at varying pH show a typical Gaussian pattern whose peak represents the relative pH *optimum*.

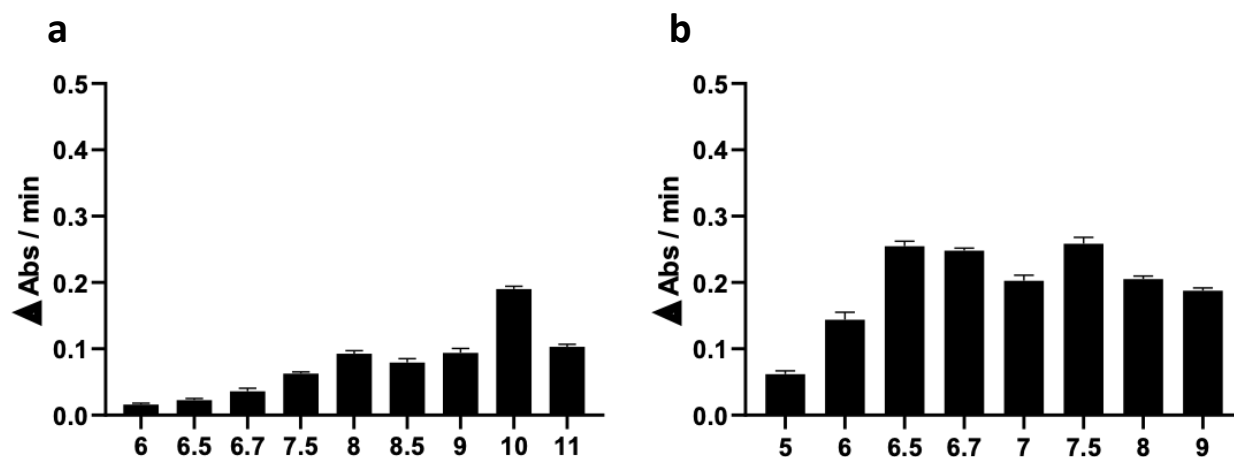


**Figure 1:** Graphs of pH dependency of the two ADH-related activities ( $\Delta Abs_{340nm}/min$ ), displaying a typical gaussian distribution. The activity of reduction of acetaldehyde (a) was measured with 2 nM of recombinant AtADH, while oxidation of ethanol (b) was measured with 10 nM.

The pH *optimum* determined in relation to the activity of reduction of MeCHO (**Figure 1**) is situated in a range between 6.5 and 7.5. Subsequent analyses were conducted at pH 6.7, a value that is close to the physiological range (7-7.5, (Zhou et al., 2021)), especially considering the slight cytoplasmic acidification due to the induction of lactic fermentation at the onset of hypoxic/anoxic conditions (Ismond et al., 2003), in which ADH is induced. As opposite, the pH *optimum* relative to the conversion of EtOH into MeCHO is far from physiological values, being highly alkaline (pH 9.8) (**Figure 1**). Once set up the optimized conditions for assaying ADH activities, we determined the correlation between catalysis and enzyme concentration. As shown in **Figure 2**, both activities display a linear proportionality with enzyme concentration. In addition, the reduction of MeCHO displays higher catalytic rate compared to the NAD-dependent oxidation of EtOH.

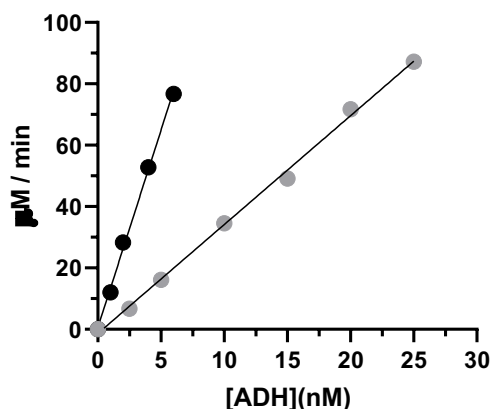


**Figure 2:** Linear dependence of the two ADH-related activities ( $\mu\text{M}/\text{min}$ ) on enzyme concentration. Maximal activities were measured at their respective optima of pH, in a 0-6 nM range for reduction of acetaldehyde (black dots) and in a 0-25 nM range for oxidation of ethanol (grey dots).

Kinetic parameters ( $k_{cat}$  and  $K_m$ ) were determined at the relative pH *optima* using variable substrates and cofactors concentrations. Plotting the activity data *versus* substrate concentrations resulted in typical hyperbolic responses (**Figure 3**) deriving by the analysis of the corresponding curves by non-linear regression with the Michaelis-Menten equation.

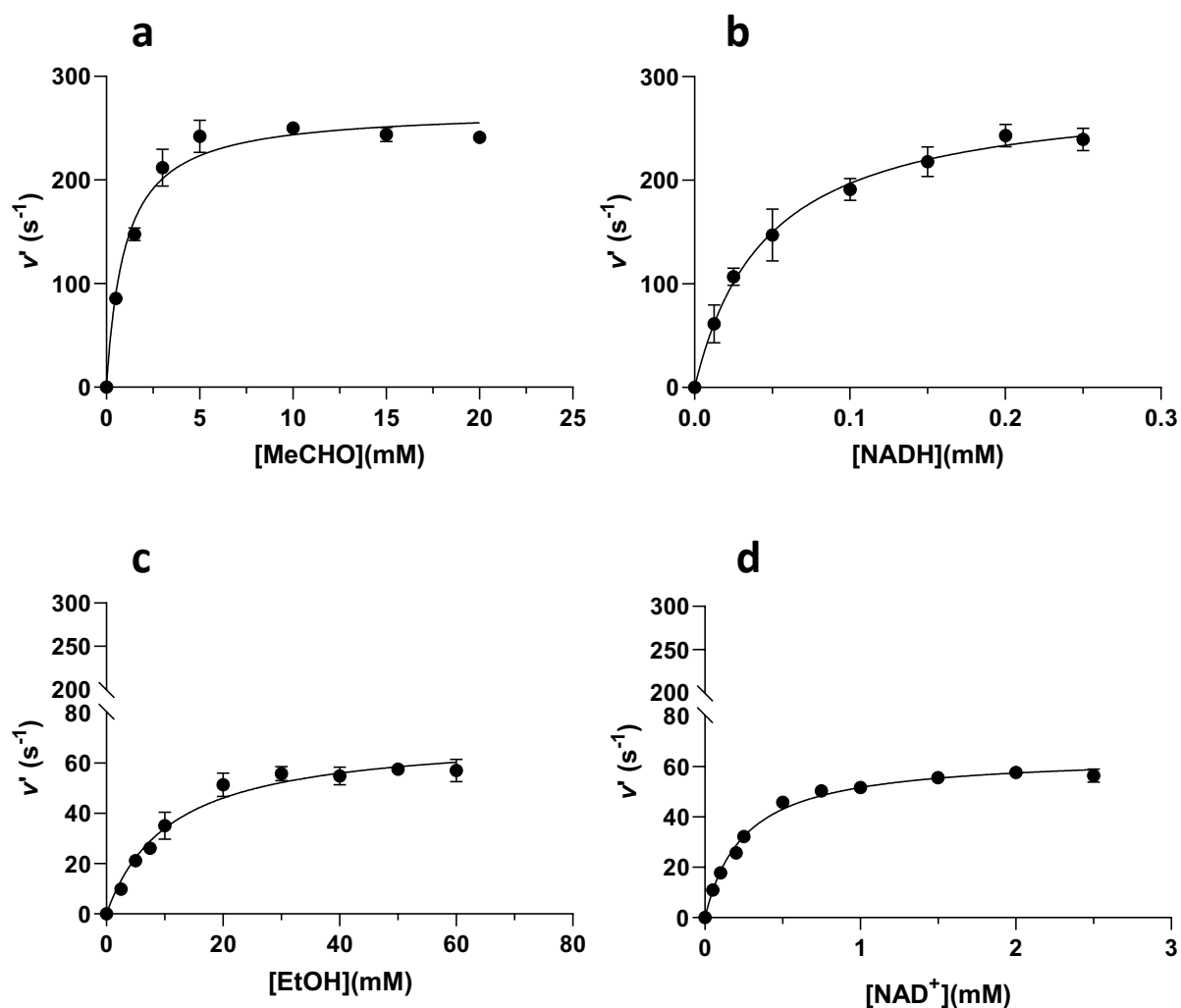


**Figure 3:** Variations of apparent velocity ( $v'$ ) in ADH-related activities measured at their respective optimum of pH, in the presence of varying concentrations of substrates (a, c) or cofactors (b, d).

	$K_{cat}$ (s <sup>-1</sup> )	$K_m$ (mM)	$K_{cat}/K_m$ (M <sup>-1</sup> s <sup>-1</sup> )
<b>MeCHO</b>	268.1 ± 6.8	1 ± 0.1	268100
<b>EtOH</b>	71.3 ± 3.6	11 ± 0.4	6481.82

	$K_{cat}$ (s <sup>-1</sup> )	$K_m$ (mM)	$K_{cat}/K_m$ (M <sup>-1</sup> s <sup>-1</sup> )
<b>NADH</b>	288.8 ± 1.4	0.05 ± 0.01	5776
<b>NAD<sup>+</sup></b>	64.6 ± 1.1	0.25 ± 0.01	258.4

**Table 1:** Turnover numbers ( $k_{cat}$ ) and Michaelis-Menten constants ( $K_m$ ) obtained by analyzing graphs in Figure 3 with non-linear regression using the Michaelis-Menten equation. Catalytic efficiency values ( $k_{cat}/K_m$ ) were obtained dividing the values of  $k_{cat}$  by the relative  $K_m$  value.

The resulting  $k_{cat}$  values (*i.e.*, turnover numbers) relative to the conversion of MeCHO into EtOH and EtOH into MeCHO are 268 s<sup>-1</sup> and 71 s<sup>-1</sup> (**Table 1**), respectively. This indicates that NADH-dependent reduction of MeCHO is ~4-times faster compared to the opposite reaction. Looking at the values of Michaelis-Menten constants ( $K_m$ ),  $K_{m(\text{MeCHO})}$  and  $K_{m(\text{NADH})}$  are respectively 1 and 0.05 mM, while  $K_{m(\text{EtOH})}$  and  $K_{m(\text{NAD}^+)}$  resulted to be 11 and 0.25 mM. By comparing these values, it emerges that the substrate and cofactor affinities relative to MeCHO reduction are much higher compared to EtOH catalysis. The resulting catalytic efficiencies ( $k_{cat}/K_m$ ) for MeCHO and EtOH are 268 and 6 mM<sup>-1</sup>s<sup>-1</sup>, while are 5776 and 258 mM<sup>-1</sup>s<sup>-1</sup> for NADH and NAD<sup>+</sup>, respectively) (**Table 1**). The derived ratios of catalytic efficiencies in relation to substrates (catalytic efficiency<sub>(MeCHO)</sub> / catalytic efficiency<sub>(EtOH)</sub>) or cofactors (catalytic efficiency<sub>(NADH)</sub> / catalytic efficiency<sub>(NAD<sup>+</sup>)</sub>) were found to be 41 or 22, respectively. These values clearly indicate the reaction of conversion of MeCHO into EtOH as the most catalytically favored, coherently with the physiological role assigned to plant ADH in the context of ethanol fermentation.

### Computational analysis displays thermodynamic differences in the propensity of MeCHO/EtOH to bind the catalytic pocket of ADH

To explore the molecular basis of the catalytic preference for NADH-dependent MeCHO reduction, we performed thermodynamic analysis in collaboration with Prof. Matteo Calvaresi and Dr. Edoardo Jun Mattioli (Department of Chemistry "Giacomo Ciamician", University of Bologna). In particular, the binding free energy ( $\Delta G = \Delta H - T\Delta S$ ) relative to the placement of the two substrates (MeCHO/EtOH) into the ADH active site was determined. Calculation of the enthalpy of binding ( $\Delta H$ ) revealed a similar enthalpy contribution (**Table 2**) due to the high structural similarity between the two molecules which results in their similar interaction with the catalytic pocket (**Figure 4**). Despite this, the entropic term ( $\Delta S$ ) relative to MeCHO and EtOH binding shows greater difference (**Table 2**), being the  $\Delta S$  relative to EtOH binding more significant. This is due to the more flexible structure of EtOH, requiring a greater structural rearrangement for the optimization of the interactions with ADH. For this reason, the formation of the EtOH-ADH complex leads to a greater decrease in disorder (*i.e.*, entropy change,  $\Delta S$ ) in respect to the formation of the MeCHO-ADH complex. The entropic component results in a more negative value of binding free energy ( $\Delta G = \Delta H - T\Delta S$ ) correlated to the formation of the ADH complex with MeCHO rather than EtOH, indicating a thermodynamic propensity for the formation of the former.

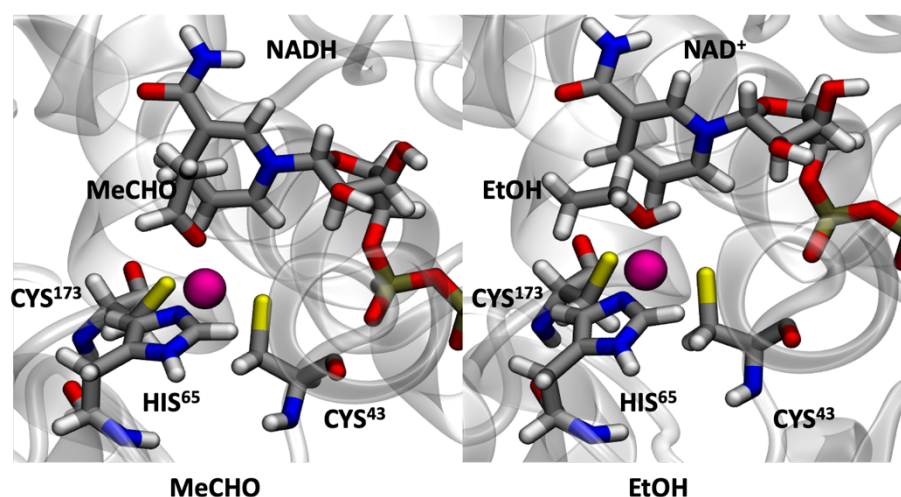


**Figure 4:** Interactions of the substrates (MeCHO or EtOH) into the catalytic pocket of ADH. Catalytic zinc ions (magenta sphere) and cofactors (NADH or NAD<sup>+</sup>) are also represented.

	MeCHO	EtOH
$\Delta H$ (kcal/mol)	-21.0	-19.6
$T\Delta S$ (kcal/mol)	-0.8	-4.9
$\Delta G = \Delta H - T\Delta S$ (kcal/mol)	-20.2	-14.7

**Table 2:** calculated values of enthalpy change ( $\Delta H$ ), entropy change ( $\Delta S$ ) and binding free energy ( $\Delta G$ ) related to the binding of the two substrates (MeCHO/EtOH) into ADH catalytic pocket.

After establishing that in a physiological pH (*i.e.*, pH 6.7) EtOH is thermodynamically less favored to form the binding complex (EtOH-ADH), we investigated how pH influences the affinity of ADH towards EtOH by determining the  $K_m$  (EtOH) at pH 6.7. The resulting  $K_m$  value (obtained by the analysis of the data in **Figure 5**) is equal to  $9.3 \pm 0.1$  mM, being similar to the  $K_m$  (EtOH) value measured at pH 9.8 (**Figure 3 panel c, Table 1**). This suggests that the affinity of ADH towards EtOH is not affected by pH. To establish whether pH influences the velocity of ADH in catalyzing the reaction of oxidation of EtOH, we measured specific activities at different pH conditions, finding that at pH 6.7 it is  $\sim 7$ -fold lower compared to the specific activity value determined at pH 9.8, being  $11.31 \pm 0.23 \mu\text{mol min}^{-1} \text{mg}^{-1}$  and  $72.12 \pm 7.51 \mu\text{mol min}^{-1} \text{mg}^{-1}$ , respectively.

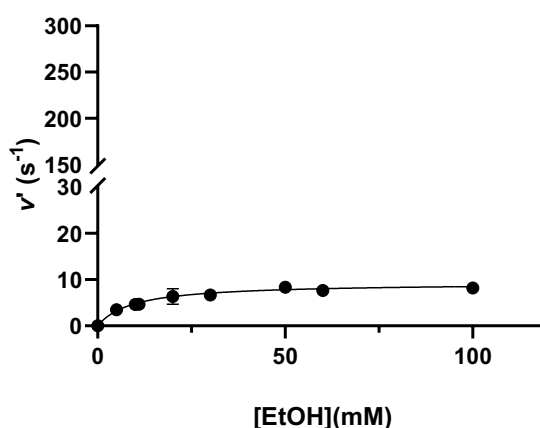


**Figure 5:** Variations of apparent velocity ( $v'$ ) of ethanol oxidation activity measured at pH 6.7, in the presence of varying concentrations of EtOH and saturating concentration of  $\text{NAD}^+$  (2 mM).

In conclusion, our data demonstrate that the binding of MeCHO into the ADH catalytic pocket is thermodynamically favored compared to the binding of EtOH. However, the lower propensity for the EtOH/ADH binding is not influenced by the pH, which only affects the catalytic rate of the EtOH oxidation reaction. This is consistent with theoretical knowledge regarding the mechanism of reversible interconversion of an alcohol into an aldehyde, consisting of the addition or removal of molecular hydrogen from the substrate. In fact, it is well known that basic environments promote deprotonation. In the case of ethanol oxidation, deprotonation of the alcohol is necessary for the subsequent oxidative reaction and for this reason, basic environments favor the mechanism for oxidation of EtOH into MeCHO.

### ***Ex-vivo* analysis confirm the hypoxic ADH induction and identify the NADH-dependent MeCHO reduction as the prominent ADH-related activity**

To gain insight into the physiological role of ADH, we carried out a series of activity assays coupled with immunoblot analysis using protein extracts from Arabidopsis seedlings exposed to variable oxygen conditions (*i.e.*, normoxia *versus* hypoxia *versus* reoxygenation, see below for further details). In addition, analyses were conducted using WT plants and plants lacking the *ADH* gene (*adh1*). The experimental set-up foresaw the use of seven days-grown Arabidopsis seedlings (WT and *adh1* plants) subjected to control conditions (normoxia, 21% O<sub>2</sub> v/v), low oxygen conditions for 12 h (hypoxia, 1% O<sub>2</sub> v/v), or low oxygen conditions followed by reoxygenation conditions in which the oxygen percentage was restored to 21% O<sub>2</sub>. At different time points (6, 24, and 36 h), samples were collected and immediately frozen in liquid nitrogen for protein extraction and experimental analysis.

Before analyzing protein extract, we tested the sensitivity of the anti-ADH antibody in western blot analysis using the recombinant form of Arabidopsis ADH and GSNOR, with the latter being an enzyme that shares with ADH a high sequence homology and membership of the alcohol dehydrogenase family. As shown in **Figure 6**, we observed a signal proportional to the amount of ADH used, while no signal was detected in the presence of GSNOR. This indicates that the antibody is sensible and strictly specific to ADH making immunodetection analyses conducted on protein extracts reliable.

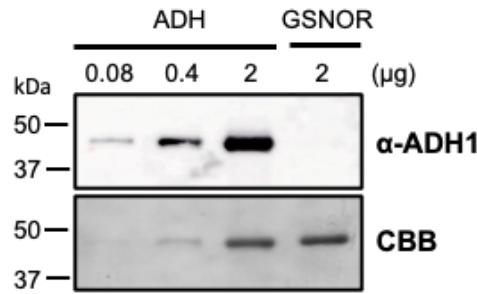


**Figure 6:** Anti-ADH antibody specificity. Immunodetection was carried out using anti-ADH antibody ( $\alpha$ -ADH) against AtADH and AtGSNOR. Coomassie Brilliant Blue (CBB) staining was used as loading control. The recombinant enzymes were loaded at the indicated quantity ( $\mu$ g).

Since the induction of ADH expression under conditions of oxygen deprivation is well established (Dennis et al., 2000; Dolferus et al., 1994; Licausi et al., 2011), we first immunodetected the presence of ADH protein in protein extracts subjected to different level of oxygen in both WT and *adh1* mutant lines (**Figure 7**). As expected, almost no ADH-related signal is detected in normoxic conditions, while we observed the appearance of a strong signal following hypoxic treatment, confirming the accumulation of ADH in response to oxygen depletion. No signal was observed in the *adh1* mutant in both normoxic and hypoxic conditions. When analyzing the WT samples subjected to the restoration of normoxic conditions (*i.e.*, reoxygenation), we observed a stable ADH signal slightly decreasing only at 36 hours of reoxygenation, indicating the presence of the protein even after the loss of hypoxic conditions. This paves the way for important questions about the persistence of hypoxia response in a context where the stressful condition is no longer present. Hypothetically, the activation of the cascade upon the hypoxic signal is triggered faster through transcription and translation, while its deactivation, which should go through protein degradation, is a much slower process. This may reflect an inherent slowness of the process or an actual physiological constrain, and future studies are needed to address this question.

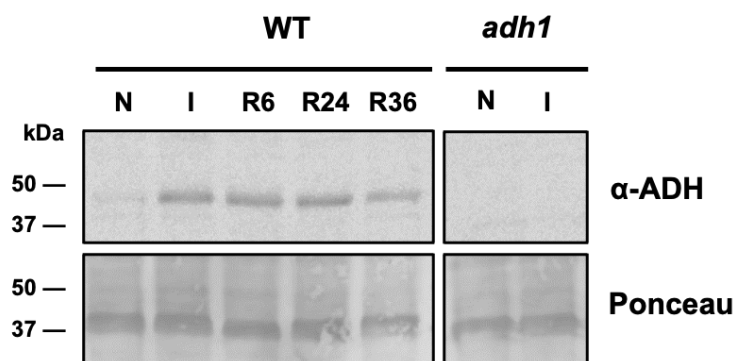


**Figure 7:** Immunodetection with anti-ADH antibody ( $\alpha$ -ADH) (upper part) and loading control with Red Ponceau staining (lower part), in wild type (WT) or mutant (*adh1*) genetic backgrounds. The different samples were subjected to different oxygenation conditions (N: 12 h normoxic conditions, I: 12 h hypoxic conditions, R: 12 h hypoxia followed by 6 h, 24 h or 36 h of normoxia). In every lane, the same quantity of *Arabidopsis* protein extract was loaded (40  $\mu$ g).

To dissect the role of ADH in different conditions of oxygenation, we measured the  $\text{NAD}^+$ -dependent oxidation of EtOH and the NADH-dependent reduction of MeCHO in WT samples (**Figure 8**). As expected, both activities are highly induced in response to hypoxic conditions. Between the two, the activity of reduction of MeCHO in the presence of NADH results to be the most represented (**Figure 8a**). In fact, upon hypoxic treatment, it is  $\sim 6$  folds higher than the activity of oxidation of EtOH (104.18  $\text{nmol min}^{-1} \text{mg}^{-1}$  and 18.19  $\text{nmol min}^{-1} \text{mg}^{-1}$ , respectively) (**Figure 8**). This is coherent with our biochemical data indicating the activity of reduction of MeCHO as catalytically favored. Interestingly, high activity of MeCHO reduction was also registered in samples receiving the reoxygenation treatment (up to 123.82  $\text{nmol min}^{-1} \text{mg}^{-1}$ ), displaying a slight decrease only after 36 h. This trend reflects well the accumulation pattern of ADH detected by immunoblotting (**Figure 7**), indicating a rather good correlation between protein quantity and catalytic activity.

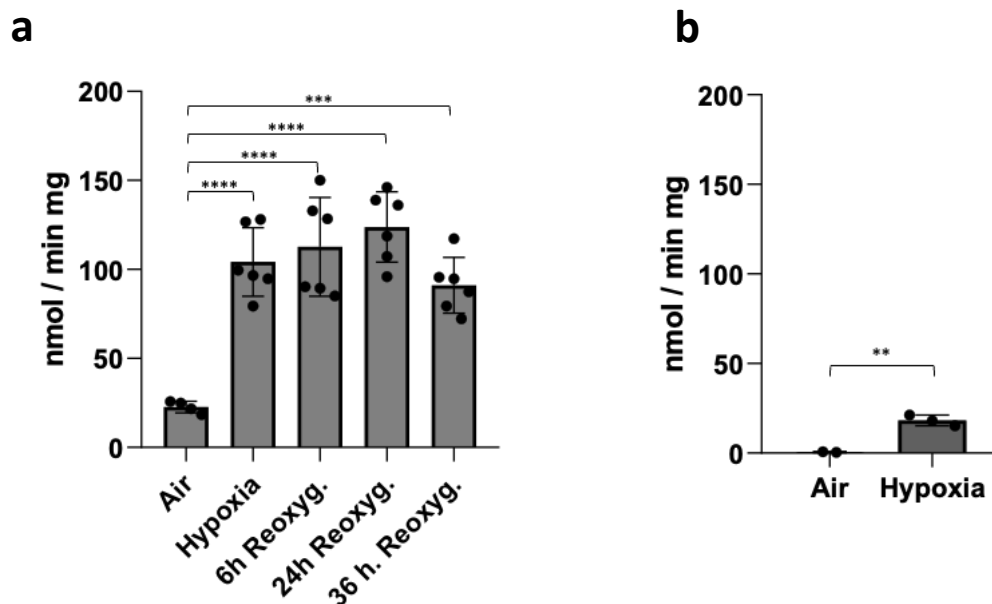


**Figure 8.** Specific activities of NADH-dependent reduction of MeCHO (a) or NAD<sup>+</sup>-dependent oxidation of EtOH (b) in 7-day-old *Arabidopsis* seedlings with a wild type genetic background, subjected to different oxygenation treatments (Air: 12 h normoxic conditions (21% O<sub>2</sub> v/v), Hypoxia: 12 h hypoxic conditions (1% O<sub>2</sub> v/v), Reoxygenation: 12 h hypoxia (1% O<sub>2</sub> v/v) followed by 6 h, 24 h or 36 h of normoxia (21% O<sub>2</sub> v/v)). Bars represent the average of at least three biological replicates. Asterisks indicate level of statistical significance: \*  $p \leq 0.05$ , \*\*  $p \leq 0.01$ , \*\*\*  $p \leq 0.001$ , \*\*\*\*  $p \leq 0.0001$

### Identification of a new MeCHO detoxification system based on the reductive power of NADPH

As already mentioned, western blot carried out on *adh1* samples with *adh1* genetic background displayed no ADH-related signal (**Figure 7**), confirming the proper knockout nature of this T-DNA mutant line obtained by the disruption of the single *Arabidopsis* ADH gene (ADH1) (Dolferus et al., 1990). However, the possible functional redundancy of ADH still remained to be evaluated *in vivo*. To this end, we performed activity assays in *adh1* mutant line, observing no NAD(H)-dependent activity even following the hypoxic treatment (**Figure 9**). This suggests that only ADH is able to fulfill this catalytic role in the assayed conditions. For this reason, an accumulation of MeCHO should occur in *adh1* mutant line since no other enzyme is able to catalyze the reduction of MeCHO in the presence of NADH. Contrary to what expected, a striking mild phenotype is displayed in *adh1*, even after hypoxic treatment (Bui et al., 2019), where the PDC-related activity producing MeCHO is induced (Ismond et al., 2003). This

evidence led us to investigate the presence of alternative detoxification system based on NADPH as an alternative cofactor.

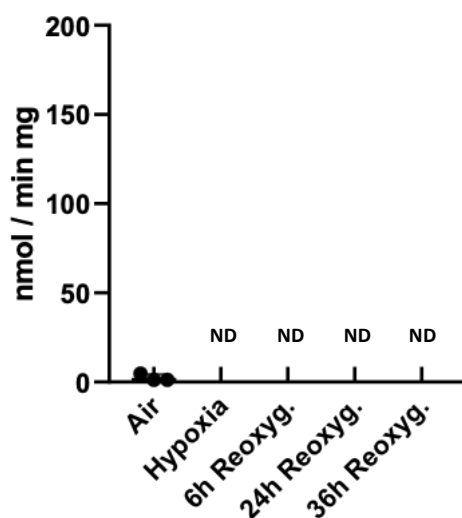


**Figure 9:** Specific activities of NADH-dependent reduction of MeCHO in 7-day-old *Arabidopsis* seedlings *adh1* mutant line subjected to different oxygenation treatments (Air: 12 h normoxic conditions (21% O<sub>2</sub> v/v), Hypoxia: 12 h hypoxic conditions (1% O<sub>2</sub> v/v), Reoxygenation: 12 h hypoxia (1% O<sub>2</sub> v/v) followed by 6 h, 24 h or 36 h of normoxia (21% O<sub>2</sub> v/v)). Only in the case of air treatment it was possible to measure an activity. In the case of other treatments, the activities resulted to be not detectable (ND).

To address this point, we first tested the ability of the protein extract from WT plants to reduce MeCHO in the presence of NADPH (**Figure 10**). We surprisingly detected such activity, finding an induction upon the establishment of hypoxic conditions (36.96 nmol/min mg) compared to air conditions (18.42 nmol min<sup>-1</sup> mg<sup>-1</sup>). Interestingly, this activity slightly increased even following reoxygenation (76.80 nmol min<sup>-1</sup> mg<sup>-1</sup>).

To better understand the involvement of ADH in this alternative detoxification system, we tested the NADPH-dependent activity in the *adh1* mutant line (**Figure 11**). Also in this case, a NADPH-dependent activity of reduction of MeCHO is found, although less represented than in the wild type. In this case, the activity measured is characterized by an absence of a hypoxia-mediated induction (air: 5.30 nmol min<sup>-1</sup> mg<sup>-1</sup>, hypoxia: 4.01 nmol min<sup>-1</sup> mg<sup>-1</sup>). As in the wild type, a slight increase in reoxygenation conditions is observed (up to 11.32 nmol min<sup>-1</sup> mg<sup>-1</sup>).

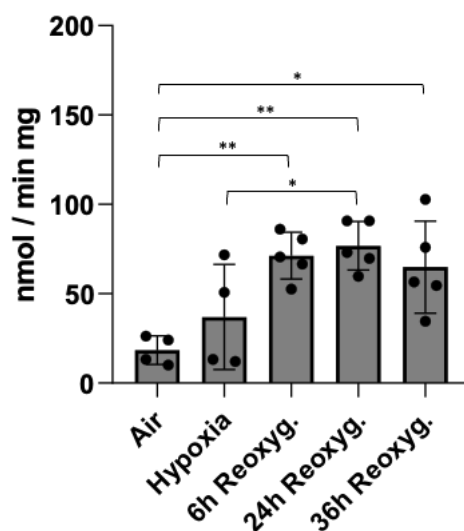


**Figure 10:** Specific activities of NADPH-dependent reduction of MeCHO in 7-day-old *Arabidopsis* seedlings with a wild type genetic background, subjected to different oxygenation treatments (Air: 12 h normoxic conditions (21% O<sub>2</sub> v/v), Hypoxia: 12 h hypoxic conditions (1% O<sub>2</sub> v/v), Reoxygenation: 12 h hypoxia (1% O<sub>2</sub> v/v) followed by 6 h, 24 h or 36 h of normoxia (21% O<sub>2</sub> v/v)). Bars represent the average of at least three biological replicates. Asterisks indicate level of statistical significance: \*  $p \leq 0.05$ , \*\*  $p \leq 0.01$

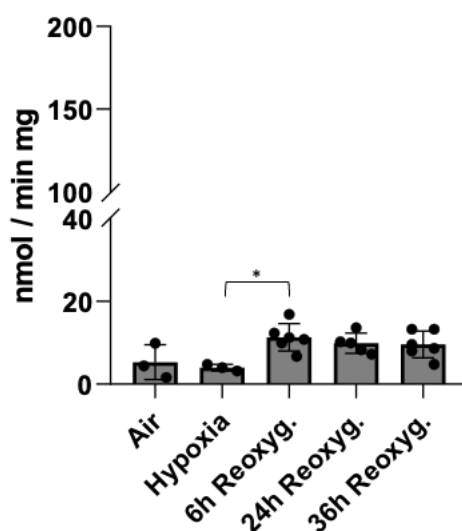


**Figure 11:** Specific activities of NADPH-dependent reduction of MeCHO in 7-day-old *Arabidopsis* seedlings *adh1* mutant line subjected to different oxygenation treatments (Air: 12 h normoxic conditions (21% O<sub>2</sub> v/v), Hypoxia: 12 h hypoxic conditions (1% O<sub>2</sub> v/v), Reoxygenation: 12 h hypoxia (1% O<sub>2</sub> v/v) or followed by 6 h, 24 h or 36 h of normoxia (21% O<sub>2</sub> v/v)). Bars represent the average of at least three biological replicates. Asterisks indicate level of statistical significance: \*  $p \leq 0.05$ .

The fact that wild type extracts display higher NADPH-dependent MeCHO reduction compared to the *adh1* mutant line led us to hypothesize that ADH is highly responsible for this alternative MeCHO detoxification system, despite ADH catalysis has always been considered as NAD(H)-dependent.

To further investigate the cofactor specificity of ADH, we employed the recombinant enzyme to test its ability to catalyze the reduction of MeCHO in the presence of NADPH. We measured a specific activity equal to  $(105.7 \pm 9.01 \mu\text{mol min}^{-1} \text{mg}^{-1})$ , a value about 3 times lower than specific activity of the NADH-dependent reaction  $(303.67 \pm 19.75 \mu\text{mol min}^{-1} \text{mg}^{-1})$ . The relative  $K_m$  and  $k_{cat}$  values were also determined (**Figure 12**).

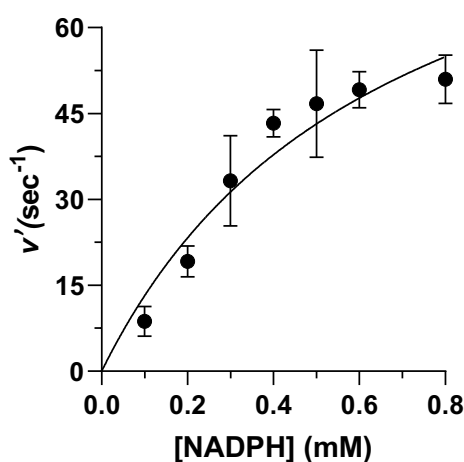


**Figure 12:** variation of apparent velocity ( $v'$ ) in NADPH-dependent reduction of MeCHO measured at the optimum of pH (6.7), in the presence of varying concentrations of NADPH and saturating concentration of MeCHO (15 mM).

As shown in **Figure 12**, ADH followed a Michaelis-Menten kinetics with a  $K_m(\text{NADPH})$  of  $0.74 \pm 0.19$  mM, a value that is about 16 times higher than the  $K_m(\text{NADH})$ , indicating a much lower affinity of AtADH for NADPH compared to NADH. At the same time, the  $k_{cat}(\text{NADPH})$ , which is  $108.7 \pm 8.24$ , is around 3 times lower than the  $k_{cat}(\text{NADH})$  (**Table 1**).

In conclusion, our data demonstrate that ADH is not strictly dependent on NAD(H) as a cofactor but is also able to use NADPH to catalyze the reduction of MeCHO, although with lower catalytic efficiency. Further studies are indeed required to investigate the structural determinants involved in NADPH binding and to shed light on the *in vivo* relevance of this unexpected activity.

## Discussion

The classic alcohol dehydrogenase (ADH, alcohol:NAD<sup>+</sup> oxidoreductase, EC 1.1.1.1) is a Zn-binding enzyme whose active form is a homodimer, relying on NAD(H) as a cofactor to interconvert EtOH to MeCHO.

Plant ADHs are known for their involvement in fermentative metabolism during the acclimation response to low oxygen conditions (Pucciariello & Perata, 2012), where they catalyze the conversion of acetaldehyde (MeCHO) into ethanol (EtOH) while yielding NAD<sup>+</sup> necessary to sustain glycolysis. ADH induction in plants subjected to anaerobic conditions has been established in the 1950s (App & Meiss, 1958). However, more recently mounting evidence has assigned key roles to ADH under circumstances other than stressful conditions, including developmental stages and tissue-specific functional specialization. For example, ADH expression and activity has been reported in the kernels and anthers of maize (Schwartz, 1971) and during shoot meristem development whereby hypoxic niches are important to regulate the production of new leaves (Weits et al., 2019). Except for a few *Arabidopsis* species, most of the plants carry multiple ADH genes (Strommer, 2011).

In animals, classical ADHs include many isoforms with tissue-specific expression, involved in many different metabolic pathways such as ethanol oxidation, norepinephrine, dopamine, serotonin and bile acid metabolism and oxidation of retinol (Thompson et al., 2018). The major ADH expression and activity is typically found in liver where it is responsible for EtOH metabolism catalyzing the conversion of EtOH to MeCHO.

To date, recent biochemical studies on plant ADH focused on the activity of conversion of EtOH to MeCHO, not representing the main physiological role of plant ADH. In this study, we provided a functional study of ADH from *Arabidopsis thaliana*, particularly focusing on its activity of conversion of MeCHO to EtOH, for which the role in plants has been well established. Our results unequivocally demonstrate the higher catalytic capacity of ADH in catalyzing MeCHO conversion reaction rather than EtOH conversion, both in terms of substrate affinity ( $K_m$ ) and in terms of catalytic proficiency ( $k_{cat}$ ). Moreover, we observed that the MeCHO-related reaction has its *optimum* of pH in the physiologic range, while EtOH-related reaction has its *optimum* in highly alkaline pH range, further indicating that in a physiological environment the former reaction is catalytically favored. Although biochemical analyses revealed the higher affinity for NADH compared to NAD<sup>+</sup> (*i.e.*, lower  $K_m$  value), the understanding of how these two cofactors may compete in the binding of ADH is an intriguing

point, since it is well established that *in vivo* the  $\text{NAD}^+/\text{NADH}$  ratio is highly shifted toward the oxidized form (Steinbeck et al., 2020; Williamson et al., 1967).

The greater predisposition of ADH for the binding of MeCHO as opposed to EtOH has been further confirmed by thermodynamic analysis. More in detail, we carried out a comparison between the binding energy ( $\Delta G$ ) related to the binding of MeCHO or EtOH in the catalytic pocket of ADH. The analysis unveiled a notably similar enthalpic contribution ( $\Delta H$ ) in the binding of both molecules. Nevertheless, the entropic contribution ( $\Delta S$ ) is more favorable for the binding of MeCHO as compared to EtOH, leading to a more negative  $\Delta G$  for the former. This result uncovered the thermodynamic preference for the formation of the MeCHO-ADH complex as opposed to the EtOH-ADH complex. In a future perspective, an approach integrating computational and thermodynamic analyses could be employed to pinpoint the critical amino acid residues determining the higher plant ADH affinity for MeCHO, making a comparison with animal ADH where EtOH binding is favored. This would help to unravel the basis of this functional differentiation in enzymes sharing an evolutionary history, reflected in their highly similar 3D-structure.

In the second phase of our study, we used protein extracts obtained from Arabidopsis plants to conduct immunodetection experiments and biochemical analyses. Through these investigations, we successfully validated the upregulation of ADH under hypoxic conditions. Furthermore, our findings confirmed the prevalence of its NADH-dependent MeCHO reduction activity. This suggests a significant role for ADH in responding to low oxygen levels and underscores its involvement in the reduction of MeCHO using NADH as a cofactor. Moreover, we demonstrated the stability of the enzyme even upon the restoration of normoxic conditions following a period of hypoxia. This opens avenues for future experimental perspectives aimed at deciphering the timing of deactivation of the hypoxic response, an issue that has so far gathered limited experimental data.

Conclusively, given the identification of ADH as the sole enzymatic system accountable for the NADH-dependent MeCHO detoxification, along with the observation of a mild phenotype in the ADH mutant knockout (not expected in the case of MeCHO accumulation), we conducted experiments to explore the hypothetical existence of a MeCHO detoxification system relying on NADPH as an alternative cofactor. Intriguingly, we identified a NADPH-dependent detoxification activity in protein extracts. This activity is highly dependent on the presence of ADH, as it is only partially retained in *adh1* mutant line. This finding suggests the involvement of other enzymatic systems whose identity is yet to be investigated and whose

presence could be very relevant in a physiological context, considering that the NADPH/NADH cytosolic ratio is estimated to be between 3 and 8 (Smith et al., 2021). A possible enzymatic class to be explored in this sense is the aldo-keto reductase (AKR) protein superfamily, but further studies are required to correlate this class of enzymes to the control of MeCHO toxicity (Treffon et al., 2021).

Overall, our findings shed light on the biochemical and thermodynamic features of ADH, offering new insights into its role in a physiological context. Our data represent a contribution for a deeper understanding of plant adaptations to environmental stress, a topic of major interest in the face of evolving environmental challenges.

## Materials and methods

### Expression and purification of recombinant AtADH

AtADH1 coding sequence supplemented with 6 N-terminal histidines was cloned in a pET-28a expression vector, which was subsequently used to transform *Escherichia coli* BL21(DE3). Bacteria were grown in LB medium supplemented with 50  $\mu\text{g ml}^{-1}$  kanamycin at 37 °C and the production of the protein of interest was induced with 100  $\mu\text{M}$  isopropyl  $\beta$ -D-1-thiogalactopyranoside overnight at 30 °C. Cells were then harvested by centrifugation (5,000 g for 10 min) and resuspended in 30 mM Tris-HCl pH 7.9. Cell lysis was performed using a combination of lysozyme (100  $\mu\text{g per ml}$  of cells suspension) and sonication (5 cycles of 2 minutes each, waves amplitude set to 10 microns peak to peak). Cell debris were removed by centrifugation (15,000 g for 45 min) and the supernatant applied onto a Ni<sup>2+</sup>-Hitrap chelating resin (HIS-Select Nickel Affinity Gel; Sigma-Aldrich) equilibrated with 30 mM Tris-HCl (pH 7.9) containing 500 mM NaCl and 5 mM imidazole. The recombinant AtADH was purified according to the manufacturer's instructions. The molecular mass and purity of ADH was examined by SDS-PAGE after desalting with PD-10 columns (GE-Healthcare) equilibrated with 30 mM Tris-HCl pH 7.9. Protein concentration was determined spectrophotometrically using a molar extinction coefficient at 280 nm of 25,440  $\text{M}^{-1} \text{cm}^{-1}$ . The resulting homogeneous protein solutions were stored at -20 °C.

### Activity measurements

The catalytic activity of ADH was measured spectrophotometrically by monitoring the NADP(H) reduction/oxidation at 340 nm. EtOH oxidation activity was measured in an assay mixture containing 50 mM glycine- NaOH (pH 9.8), 50 mM EtOH, and 2 mM NAD<sup>+</sup>, starting the reaction with 10 nM ADH. NAD(P)H-dependent reduction of MeCHO was measured in an assay mixture containing 50 mM K-P (pH 6.7), 15 mM MeCHO and 0.2 mM NAD(P)H starting the reaction with 2 nM ADH. To determine the pH optimum, ADH activity was monitored as just described but using different pH buffers. The following buffers were used: potassium phosphate at pH 6.5–7.5; Tris-HCl at pH 7.5–9; and glycine at pH 9–10.

### Determination of kinetic parameters

Kinetic analysis for determination of apparent  $K_m$  for cofactors was accomplished by varying the concentrations of NADH (0 – 0.25 mM), NADPH (0 – 0.8 mM) at fixed concentration of MeCHO (15 mM) and varying the concentrations of NAD<sup>+</sup> (0 – 2.5 mM) at fixed EtOH concentration (50 mM). Determination of apparent  $K_m$  for substrates was accomplished by varying the concentrations of MeCHO (0 – 20 mM) or EtOH (0 – 60 mM) at fixed concentration of NADH (0.2 mM) or NAD<sup>+</sup> (2 mM). The reactions of NAD(P)H-dependent MeCHO reduction or NAD<sup>+</sup>-dependent EtOH oxidation were started by adding 2 nM or 10 nM ADH, respectively. Three independent experiments were performed at each substrate/cofactor concentration and apparent kinetic parameters ( $K'_m$  and  $k'_{cat}$ ) were calculated by nonlinear regression using the Michaelis- Menten equation with the GraphPad software.

### Thermodynamic calculations

Thermodynamic analysis in collaboration with Prof. Matteo Calvaresi and Dr. Edoardo Jun Mattioli (Department of Chemistry "Giacomo Ciamician", University of Bologna). All calculations were carried out using the Amber16 software package. Starting from ADH 3D-structures (PDBs: 4RQT and 4RQU), enzyme-substrate complexes (i.e., MeCHO-NADH and EtOH-NAD<sup>+</sup>) were built computationally using the VMD alignment tool. ADH was modeled using FF14SB, while cofactors (NADH and NAD<sup>+</sup>) were modeled with force field parameters calculated by Ryde. EtOH and MeCHO were modeled using the GAFF force field, and atomic charges were determined using the Merz–Singh–Kollman scheme. 500 steps of steepest descent minimization, followed by additional 950 steps of conjugate gradient minimization

were performed with SANDER. Geometry optimizations were carried out in Poisson-Boltzmann implicit solvation model. From the minimized structures, MM/PBSA method was used to calculate the binding enthalpy ( $\Delta H$ ). Entropy variation ( $\Delta S$ ) of the binding process was calculated using normal mode analysis as implemented in AMBER.

### **Growth of Arabidopsis seedlings**

In *ex vivo* experiments Arabidopsis thaliana Col-0 (Columbia-0) ecotype was used as the wild type. The T-DNA insertion mutant line *adh1* (N552699) was obtained from the Nottingham Arabidopsis Stock Centre (NASC). For cultivation in axenic culture using 6-well plates, Arabidopsis seeds were surface sterilized with 70% ethanol (v/v) followed by 0.4% NaClO (v/v) and rinsed six times with sterile distilled water. Seeds were sown in liquid half-strength MS medium (pH 5.8) supplemented with 1% (w/v) sucrose, then stratified at 4 °C in the dark for 3 d and transferred to growth chamber conditions under temperatures of 23 °C/18 °C (day/night) and a light cycle of 12 h/12 h (light/dark) with 80–120  $\mu\text{mol photons m}^{-2} \text{s}^{-1}$  irradiance. After 7 days, seedlings were subjected to treatment. Hypoxic treatments were applied in the dark to avoid oxygen release by photosynthesis. Pre-mixed gas bottles containing 99% N<sub>2</sub> and 1% O<sub>2</sub> (v/v) were used to provide the desired hypoxic atmosphere to the plants, in plexiglas boxes. Aerobic controls were obtained by flushing compressed air in a similar way.

### **Protein extracts**

Briefly, seedlings extract (200 mg) was prepared by homogenization of material in ice-cold extraction buffer containing 50 mM Tris-HCl buffer (pH 7.5), 0.5 mM EDTA, 1 mM phenylmethylsulfonyl fluoride (PMSF), and 10 mM DTT. The extracts were then centrifuged (10 000 g for 15 min at 4 °C) to remove insoluble material. Protein amounts were measured using the Bradford method (Bradford, 1976) with BSA as a standard.

### ***Ex vivo* activity measurements**

*Ex vivo* kinetic assays were carried out by employing the protocol for activity determination reported above. Background activities were determined by omitting the substrate from the cuvette and subtracted from the total activity. Activities were obtained using protein amounts between 50 and 200  $\mu\text{g}$ .

**Immunodetection analyses**

40 µg of total proteins from the cleared supernatant were denatured and separated by SDS–PAGE. ADH immunodetection was performed by means of a polyclonal anti- ADH antibody (Agrisera, cat. no. AS10 685, working dilution 1/3000) and an anti-rabbit horseradish peroxidase (HRP)-conjugated secondary antibody (Agrisera, cat. no. AS09 602, working dilution 1/20 000). Luminescence was elicited by incubation of the membrane with the LiteAblot Turbo ECL Substrate (EuroClone) and imaged with a ChemiDoc.

**Replicates and statistical analyses**

All the results reported are representative of at least three independent biological replicates and expressed as mean ± S.D. Statistical analysis was performed using unpaired t-test with Welch's correction in the case of two categories or one-way ANOVA followed by a Tukey's post-hoc test for multiple comparisons. P values reported on graphs as follows: \* $p \leq 0.05$ , \*\* $p \leq 0.01$ , \*\*\* $p \leq 0.001$ , \*\*\*\* $p \leq 0.0001$ .

- Anderson, L. E. (1973). Regulation of pea leaf ribulose-5-phosphate kinase activity. *Biochimica et Biophysica Acta (BBA)-Enzymology*, 321(2), 484–488.
- App, A. A., & Meiss, A. N. (1958). Effect of aeration on rice alcohol dehydrogenase. *Archives of Biochemistry and Biophysics*, 77(1), 181–190.
- Baudouin, E. (2011). The language of nitric oxide signalling. *Plant Biology*, 13(2), 233–242. <https://doi.org/https://doi.org/10.1111/j.1438-8677.2010.00403.x>
- Bedhomme, M., Adamo, M., Marchand, C. H., Couturier, J., Rouhier, N., Lemaire, S. D., Zaffagnini, M., & Trost, P. (2012). Glutathionylation of cytosolic glyceraldehyde-3-phosphate dehydrogenase from the model plant *Arabidopsis thaliana* is reversed by both glutaredoxins and thioredoxins in vitro. *Biochemical Journal*, 445(3), 337–347.
- Boisset, N. D., Favoino, G., Meloni, M., Jomat, L., Cassier-Chauvat, C., Zaffagnini, M., Lemaire, S. D., & Crozet, P. (2023). Phosphoribulokinase abundance is not limiting the Calvin-Benson-Bassham cycle in *Chlamydomonas reinhardtii*. *Frontiers in Plant Science*, 14(August), 1–12. <https://doi.org/10.3389/fpls.2023.1230723>
- Buchanan, B. B. (1991). Regulation of CO<sub>2</sub> assimilation in oxygenic photosynthesis: The ferredoxin/thioredoxin system: Perspective on its discovery, present status, and future development. *Archives of Biochemistry and Biophysics*, 288(1), 1–9. [https://doi.org/https://doi.org/10.1016/0003-9861\(91\)90157-E](https://doi.org/https://doi.org/10.1016/0003-9861(91)90157-E)
- Buchanan, B. B., Schürmann, P., Wolosiuk, R. A., & Jacquot, J.-P. (2002). The ferredoxin/thioredoxin system: from discovery to molecular structures and beyond. *Photosynthesis Research*, 73(1), 215–222. <https://doi.org/10.1023/A:1020407432008>
- Bui, L. T., Novi, G., Lombardi, L., Iannuzzi, C., Rossi, J., Santaniello, A., Mensuali, A., Corbineau, F., Giuntoli, B., Perata, P., Zaffagnini, M., & Licausi, F. (2019). Conservation of ethanol fermentation and its regulation in land plants. *Journal of Experimental Botany*, 70(6), 1815–1827. <https://doi.org/10.1093/jxb/erz052>
- Burney, J. A., Davis, S. J., & Lobell, D. B. (2010). Greenhouse gas mitigation by agricultural intensification. *Proceedings of the National Academy of Sciences of the United States of America*, 107(26), 12052–12057. <https://doi.org/10.1073/pnas.0914216107>
- Crawford, N. M., Galli, M., Tischner, R., Heimer, Y. M., Okamoto, M., & Mack, A. (2006). Response to Zemojtel *et al*: Plant nitric oxide synthase: back to square one. *Trends in Plant Science*, 11(11), 526–527. <https://doi.org/10.1016/j.tplants.2006.09.007>
- Dewbre, C. J., Soglo, Production, F., Cervantes-Godoy, J., PIN, Amegnaglo, Y. Y., Akpa, A. F., Bickel, M., Sanyang, S., Ly, S., Kuiseu, J., Ama, S., Gautier, B. P., Officer, E. S., Officer, E. S., Eberlin, R., Officer, P., Branch, P. A., Oduro-ofori, E., ... Swanson, B. E. (2014). The future of food and agriculture: trends and challenges. In *The future of food and agriculture: trends and challenges* (Vol. 4, Issue 4).
- Del Castello, F., Nejamkin, A., Cassia, R., Correa-Aragunde, N., Fernández, B., Foresi, N., Lombardo, C., Ramirez, L., & Lamattina, L. (2019). The era of nitric oxide in plant biology: Twenty years tying up loose ends. *Nitric Oxide*, 85, 17–27. <https://doi.org/https://doi.org/10.1016/j.niox.2019.01.013>

- Dennis, E. S., Dolferus, R., Ellis, M., Rahman, M., Wu, Y., Hoeren, F. U., Grover, A., Ismond, K. P., Good, A. G., & Peacock, W. J. (2000). Molecular strategies for improving waterlogging tolerance in plants. *Journal of Experimental Botany*, *51*(342), 89–97. <https://doi.org/10.1093/jexbot/51.342.89>
- Dolferus, R., Jacobs, M., Peacock, W. J., & Dennis, E. S. (1994). Differential interactions of promoter elements in stress responses of the Arabidopsis Adh gene. *Plant Physiology*, *105*(4), 1075–1087. <https://doi.org/10.1104/pp.105.4.1075>
- Dolferus, R., Van Den Bossche, D., & Jacobs, M. (1990). Sequence analysis of two null-mutant alleles of the single Arabidopsis Adh locus. *Molecular and General Genetics MGG*, *224*(2), 297–302. <https://doi.org/10.1007/BF00271565>
- Dumont, S., Bykova, N. V., Khaou, A., Besserour, Y., Dorval, M., & Rivoal, J. (2018). Arabidopsis thaliana alcohol dehydrogenase is differently affected by several redox modifications. *PLoS ONE*, *13*(9). <https://doi.org/10.1371/journal.pone.0204530>
- Eklund, H., Nordström, B., Zeppezauer, E., Söderlund, G., Ohlsson, I., Boiwe, T., Söderberg, B.-O., Tapia, O., Brändén, C.-I., & Åkeson, Å. (1976). Three-dimensional structure of horse liver alcohol dehydrogenase at 2.4 Å resolution. *Journal of Molecular Biology*, *102*(1), 27–59. [https://doi.org/https://doi.org/10.1016/0022-2836\(76\)90072-3](https://doi.org/https://doi.org/10.1016/0022-2836(76)90072-3)
- Evans, L. T., & Fischer, R. A. (1999). Yield Potential: Its Definition, Measurement, and Significance. *Crop Science*, *39*(6), 1544–1551. <https://doi.org/https://doi.org/10.2135/cropsci1999.3961544x>
- Feechan, A., Kwon, E., Yun, B.-W., Wang, Y., Pallas, J. A., & Loake, G. J. (2005). A central role for S-nitrosothiols in plant disease resistance. *Proceedings of the National Academy of Sciences*, *102*(22), 8054–8059. <https://doi.org/10.1073/pnas.0501456102>
- Fermani, S., Trivelli, X., Sparla, F., Thumiger, A., Calvaresi, M., Marri, L., Falini, G., Zerbetto, F., & Trost, P. (2012). Conformational Selection and Folding-upon-binding of Intrinsically Disordered Protein CP12 Regulate Photosynthetic Enzymes Assembly\*. *Journal of Biological Chemistry*, *287*(25), 21372–21383. <https://doi.org/https://doi.org/10.1074/jbc.M112.350355>
- Foster, M. W., Liu, L., Zeng, M., Hess, D. T., & Stamler, J. S. (2009). A Genetic Analysis of Nitrosative Stress. *Biochemistry*, *48*(4), 792–799. <https://doi.org/10.1021/bi801813n>
- Gasch, P., Funding, M., Müller, J. T., Lee, T., Bailey-Serres, J., & Mustroph, A. (2016). Redundant ERF-VII transcription factors bind to an evolutionarily conserved cis-motif to regulate hypoxia-responsive gene expression in arabidopsis. *Plant Cell*. <https://doi.org/10.1105/tpc.15.00866>
- Gurrieri, L., Del, A., Demitri, N., Falini, G., Viorel, N., & Zaffagnini, M. (2019). *Arabidopsis and Chlamydomonas phosphoribulokinase crystal structures complete the redox structural proteome of the Calvin – Benson cycle*. 1–6. <https://doi.org/10.1073/pnas.1820639116>
- Gurrieri, L., Fermani, S., Zaffagnini, M., Sparla, F., & Trost, P. (2021). Calvin–Benson cycle regulation is getting complex. *Trends in Plant Science*, *26*(9), 898–912. <https://doi.org/10.1016/j.tplants.2021.03.008>
- Gütle, D. D., Roret, T., Müller, S. J., Couturier, J., Lemaire, S. D., Hecker, A., Dhalleine, T., Buchanan, B. B., Reski, R., Einsle, O., & Jacquot, J. P. (2016). Chloroplast FBPase and SBPase are thioredoxin-linked enzymes with similar architecture but different evolutionary histories.

- Proceedings of the National Academy of Sciences of the United States of America*, 113(24), 6779–6784. <https://doi.org/10.1073/pnas.1606241113>
- Holtgrefe, S., Gohlke, J., Starmann, J., Druce, S., Klocke, S., Altmann, B., Wojtera, J., Lindermayr, C., & Scheibe, R. (2008). Regulation of plant cytosolic glyceraldehyde 3-phosphate dehydrogenase isoforms by thiol modifications. *Physiologia Plantarum*, 133(2), 211–228.
- Hurwitz, J., Weissbach, A., Horecker, B. L., & Smyrniotis, P. Z. (1956). Spinach phosphoribulokinase. *Journal of Biological Chemistry*, 218(2), 769–783.
- Ifuku, K., Endo, T., Shikanai, T., & Aro, E.-M. (2011). Structure of the chloroplast NADH dehydrogenase-like complex: nomenclature for nuclear-encoded subunits. *Plant and Cell Physiology*, 52(9), 1560–1568.
- Ismond, K. P., Dolferus, R., De Pauw, M., Dennis, E. S., & Good, A. G. (2003). Enhanced low oxygen survival in Arabidopsis through increased metabolic flux in the fermentative pathway. *Plant Physiology*, 132(3), 1292–1302. <https://doi.org/10.1104/pp.103.022244>
- Jablonsky, J., Bauwe, H., & Wolkenhauer, O. (2011). Modeling the Calvin-Benson cycle. *BMC Systems Biology*, 5. <https://doi.org/10.1186/1752-0509-5-185>
- Jahnová, J., Luhová, L., & Petřivalský, M. (2019). S-nitrosoglutathione reductase—the master regulator of protein S-nitrosation in plant NO signaling. *Plants*, 8(2), 48.
- Janasch, M., Asplund-Samuelsson, J., Steuer, R., & Hudson, E. P. (2019). Kinetic modeling of the Calvin cycle identifies flux control and stable metabolomes in Synechocystis carbon fixation. *Journal of Experimental Botany*, 70(3), 1017–1031. <https://doi.org/10.1093/jxb/ery382>
- Johnson, J. R., Cobb, B. G., & Drew, M. C. (1994). Hypoxic induction of anoxia tolerance in roots of Adh1 null Zea mays L. *Plant Physiology*, 105(1), 61–67. <https://doi.org/10.1104/pp.105.1.61>
- Johnson, M. P. (2016). Photosynthesis. *Essays in Biochemistry*, 60(3), 255–273. <https://doi.org/10.1042/EBC20160016>
- Knaff, D. B. (1996). Ferredoxin and ferredoxin-dependent enzymes. In *Oxygenic photosynthesis: the light reactions* (pp. 333–361). Springer.
- Kono, T., Mehrotra, S., Endo, C., Kizu, N., Matusda, M., Kimura, H., Mizohata, E., Inoue, T., Hasunuma, T., Yokota, A., Matsumura, H., & Ashida, H. (2017). A RuBisCO-mediated carbon metabolic pathway in methanogenic archaea. *Nature Communications*, 8(1), 14007. <https://doi.org/10.1038/ncomms14007>
- Kovacs, I., Holzmeister, C., Wirtz, M., Geerlof, A., Fröhlich, T., Römmling, G., Kuruthukulangarakoola, G. T., Linster, E., Hell, R., Arnold, G. J., Durner, J., & Lindermayr, C. (2016). ROS-Mediated Inhibition of S-nitrosoglutathione Reductase Contributes to the Activation of Anti-oxidative Mechanisms. In *Frontiers in Plant Science* (Vol. 7). <https://www.frontiersin.org/articles/10.3389/fpls.2016.01669>
- Kubienová, L., Kopečný, D., Tylichová, M., Briozzo, P., Skopalová, J., Šebela, M., Navrátil, M., Tâche, R., Luhová, L., Barroso, J. B., & Petřivalský, M. (2013). Structural and functional characterization of a plant S-nitrosoglutathione reductase from Solanum lycopersicum. *Biochimie*, 95(4), 889–902. <https://doi.org/https://doi.org/10.1016/j.biochi.2012.12.009>

- Lee, U., Wie, C., Fernandez, B. O., Feelisch, M., & Vierling, E. (2008). Modulation of Nitrosative Stress by S-Nitrosoglutathione Reductase Is Critical for Thermotolerance and Plant Growth in Arabidopsis. *The Plant Cell*, *20*(3), 786–802. <https://doi.org/10.1105/tpc.107.052647>
- Licausi, F., Kosmacz, M., Weits, D. A., Giuntoli, B., Giorgi, F. M., Voeselek, L. A. C. J., Perata, P., & Van Dongen, J. T. (2011). Oxygen sensing in plants is mediated by an N-end rule pathway for protein destabilization. *Nature*, *479*(7373), 419–422. <https://doi.org/10.1038/nature10536>
- Lin, A., Wang, Y., Tang, J., Xue, P., Li, C., Liu, L., Hu, B., Yang, F., Loake, G. J., & Chu, C. (2012). Nitric Oxide and Protein S-Nitrosylation Are Integral to Hydrogen Peroxide-Induced Leaf Cell Death in Rice. *Plant Physiology*, *158*(1), 451–464. <https://doi.org/10.1104/pp.111.184531>
- Liu, L., Hausladen, A., Zeng, M., Que, L., Heitman, J., & Stamler, J. S. (2001). A metabolic enzyme for S-nitrosothiol conserved from bacteria to humans. *Nature*, *410*(6827), 490–494. <https://doi.org/10.1038/35068596>
- Long, S. P., ZHU, X., Naidu, S. L., & Ort, D. R. (2006). Can improvement in photosynthesis increase crop yields? *Plant, Cell & Environment*, *29*(3), 315–330.
- López-Gómez, P., Buezo, J., Urrea, M., Cornejo, A., Esteban, R., de Los Reyes, J. F., Urarte, E., Rodríguez-Dobrevá, E., Chamizo-Ampudia, A., & Eguaras, A. (2024). A new oxidative pathway of nitric oxide production from oximes in plants. *Molecular Plant*, *17*(1), 178–198.
- Loreti, E., & Perata, P. (2020). The Many Facets of Hypoxia in Plants. *Plants*, *9*(6), 745. <https://doi.org/10.3390/plants9060745>
- Marri, L., Trost, P., Trivelli, X., Gonnelli, L., Pupillo, P., & Sparla, F. (2008). Spontaneous assembly of photosynthetic supramolecular complexes as mediated by the intrinsically unstructured protein CP12. *The Journal of Biological Chemistry*, *283*(4), 1831–1838. <https://doi.org/10.1074/jbc.M705650200>
- Marsden, W. J. N., & Codd, G. A. (1984). Purification and molecular and catalytic properties of phosphoribulokinase from the cyanobacterium *Chlorogloeopsis fritschii*. *Microbiology*, *130*(4), 999–1006.
- Matamoros, M., Cutrona, M., Wienkoop, S., Begara Morales, J., Sandal, N., Orera, I., Barroso, J., Stougaard, J., & Becana, M. (2019). Altered Plant and Nodule Development and Protein S-Nitrosylation in Lotus japonicus Mutants Deficient in S-Nitrosoglutathione Reductases. *Plant & Cell Physiology*, *61*. <https://doi.org/10.1093/pcp/pcz182>
- Mcfarlane, C. (2019). Structural basis of light-induced redox regulation in the Calvin–Benson cycle in cyanobacteria. *Proceedings of the National Academy of Sciences*, *116*. <https://doi.org/10.1073/pnas.1906722116>
- Meloni, M., Gurrieri, L., Fermani, S., Velie, L., Sparla, F., Crozet, P., Henri, J., & Zaffagnini, M. (2023). Ribulose-1,5-bisphosphate regeneration in the Calvin-Benson-Bassham cycle: Focus on the last three enzymatic steps that allow the formation of Rubisco substrate. *Frontiers in Plant Science*, *14*(February), 1–13. <https://doi.org/10.3389/fpls.2023.1130430>
- Michelet, L., Zaffagnini, M., Morisse, S., Sparla, F., Pérez-Pérez, M. E., Francia, F., Danon, A., Marchand, C. H., Fermani, S., Trost, P., & Lemaire, S. D. (2013). Redox regulation of the Calvin-Benson cycle: Something old, something new. *Frontiers in Plant Science*, *4*(NOV), 1–21. <https://doi.org/10.3389/fpls.2013.00470>

- Michels, A. K., Wedel, N., & Kroth, P. G. (2005). Diatom plastids possess a phosphoribulokinase with an altered regulation and no oxidative pentose phosphate pathway. *Plant Physiology*, *137*(3), 911–920.
- Mithran, M., Paparelli, E., Novi, G., Perata, P., & Loreti, E. (2014). Analysis of the role of the pyruvate decarboxylase gene family in *Arabidopsis thaliana* under low-oxygen conditions. *Plant Biology*, *16*(1), 28–34. <https://doi.org/10.1111/plb.12005>
- Mittler, R. (2002). Oxidative stress, antioxidants and stress tolerance. *Trends in Plant Science*, *7*(9), 405–410. [https://doi.org/10.1016/S1360-1385\(02\)02312-9](https://doi.org/10.1016/S1360-1385(02)02312-9)
- Morisse, S., Zaffagnini, M., Gao, X. H., Lemaire, S. D., & Marchand, C. H. (2014). Insight into protein S-nitrosylation in *Chlamydomonas reinhardtii*. *Antioxidants & Redox Signaling*, *21*(9), 1271–1284. <https://doi.org/10.1089/ars.2013.5632>
- Munekage, Y., Hojo, M., Meurer, J., Endo, T., Tasaka, M., & Shikanai, T. (2002). PGR5 is involved in cyclic electron flow around photosystem I and is essential for photoprotection in *Arabidopsis*. *Cell*, *110*(3), 361–371.
- Neill, S., Barros, R., Bright, J., Desikan, R., Hancock, J., Harrison, J., Morris, P., Ribeiro, D., & Wilson, I. (2008). Nitric oxide, stomatal closure, and abiotic stress. *Journal of Experimental Botany*, *59*(2), 165–176. <https://doi.org/10.1093/jxb/erm293>
- Perata, P., & Alpi, A. (1993). Plant responses to anaerobiosis. *Plant Science*, *93*(1), 1–17. [https://doi.org/https://doi.org/10.1016/0168-9452\(93\)90029-Y](https://doi.org/https://doi.org/10.1016/0168-9452(93)90029-Y)
- Pérez-Pérez, M. E., Mauriès, A., Maes, A., Tourasse, N. J., Hamon, M., Lemaire, S. D., & Marchand, C. H. (2017). The Deep Thio redoxome in *Chlamydomonas reinhardtii*: New Insights into Redox Regulation. *Molecular Plant*, *10*(8), 1107–1125. <https://doi.org/10.1016/j.molp.2017.07.009>
- Persson, B., Hedlund, J., & Jörnvall, H. (2008). Medium- and short-chain dehydrogenase/reductase gene and protein families : the MDR superfamily. *Cellular and Molecular Life Sciences : CMLS*, *65*(24), 3879–3894. <https://doi.org/10.1007/s00018-008-8587-z>
- Plapp, B. V. (2010). Conformational changes and catalysis by alcohol dehydrogenase. *Archives of Biochemistry and Biophysics*, *493*(1), 3–12. <https://doi.org/10.1016/j.abb.2009.07.001>
- Poole, L. B. (2015). The basics of thiols and cysteines in redox biology and chemistry. *Free Radical Biology and Medicine*, *80*, 148–157. <https://doi.org/10.1016/j.freeradbiomed.2014.11.013>
- Pucciariello, C., & Perata, P. (2012). Flooding tolerance in plants. *Plant Stress Physiology*, 148–170.
- Pucciariello, C., & Perata, P. (2017). *New insights into reactive oxygen species and nitric oxide signalling under low oxygen in plants*. 473–482. <https://doi.org/10.1111/pce.12715>
- Raines, C. A. (2003). The Calvin cycle revisited. *Photosynthesis Research*, *75*(1), 1–10. <https://doi.org/10.1023/A:1022421515027>
- Raines, C. A. (2022). Improving plant productivity by re-tuning the regeneration of RuBP in the Calvin–Benson–Bassham cycle. *New Phytologist*, *236*(2), 350–356. <https://doi.org/10.1111/nph.18394>
- Roesler, K. R., & Ogren, W. L. (1990). *Chlamydomonas reinhardtii* phosphoribulokinase: Sequence, purification, and kinetics. *Plant Physiology*, *93*(1), 188–193.

- Saika, H., Matsumura, H., Takano, T., Tsutsumi, N., & Nakazono, M. (2006). A Point Mutation of Adh1 Gene is Involved in the Repression of Coleoptile Elongation under Submergence in Rice. *Breeding Science - BREEDING SCI*, *56*, 69–74. <https://doi.org/10.1270/jsbbs.56.69>
- Sanghani, P. C., Stone, C. L., Ray, B. D., Pindel, E. V., Hurley, T. D., & Bosron, W. F. (2000). Kinetic Mechanism of Human Glutathione-Dependent Formaldehyde Dehydrogenase. *Biochemistry*, *39*(35), 10720–10729. <https://doi.org/10.1021/bi9929711>
- Schwartz, D. (1971). Genetic control of alcohol dehydrogenase—a competition model for regulation of gene action. *Genetics*, *67*(3), 411.
- Seelert, H., Poetsch, A., Dencher, N. A., Engel, A., Stahlberg, H., & Müller, D. J. (2000). Proton-powered turbine of a plant motor. *Nature*, *405*(6785), 418–419. <https://doi.org/10.1038/35013148>
- Sewelam, N., Kazan, K., & Schenk, P. M. (2016). Global plant stress signaling: Reactive oxygen species at the cross-road. *Frontiers in Plant Science*, *7*(FEB2016), 1–21. <https://doi.org/10.3389/fpls.2016.00187>
- Shafqat, J., El-Ahmad, M., Danielsson, O., Martínez, M. C., Persson, B., Parés, X., & Jörnvall, H. (1996). Pea formaldehyde-active class III alcohol dehydrogenase: Common derivation of the plant and animal forms but not of the corresponding ethanol-active forms (classes I and P). *Proceedings of the National Academy of Sciences of the United States of America*, *93*(11), 5595–5599. <https://doi.org/10.1073/pnas.93.11.5595>
- Shiao, T., Ellis, M. H., Dolferus, R., Dennis, E. S., & Doran, P. M. (2002). Overexpression of alcohol dehydrogenase or pyruvate decarboxylase improves growth of hairy roots at reduced oxygen concentrations. *Biotechnology and Bioengineering*, *77*(4), 455–461. <https://doi.org/https://doi.org/10.1002/bit.10147>
- Simkin, A. J., López-Calcagno, P. E., & Raines, C. A. (2019). Feeding the world: Improving photosynthetic efficiency for sustainable crop production. *Journal of Experimental Botany*, *70*(4), 1119–1140. <https://doi.org/10.1093/jxb/ery445>
- Smith, E. N., Schwarzländer, M., Ratcliffe, R. G., & Kruger, N. J. (2021). Shining a light on NAD- and NADP-based metabolism in plants. *Trends in Plant Science*, *26*(10), 1072–1086. <https://doi.org/https://doi.org/10.1016/j.tplants.2021.06.010>
- Steinbeck, J., Fuchs, P., Negroni, Y. L., Elsässer, M., Lichtenauer, S., Stockdreher, Y., Feitosa-Araujo, E., Kroll, J. B., Niemeier, J. O., Humberg, C., Smith, E. N., Mai, M., Nunes-Nesi, A., Meyer, A. J., Zottini, M., Morgan, B., Wagner, S., & Schwarzländer, M. (2020). In vivo nadh/nad1 biosensing reveals the dynamics of cytosolic redox metabolism in plants. *Plant Cell*, *32*(10), 3324–3345. <https://doi.org/10.1105/tpc.20.00241>
- Strommer, J. (2011). The plant ADH gene family. *Plant Journal*, *66*(1), 128–142. <https://doi.org/10.1111/j.1365-313X.2010.04458.x>
- Suorsa, M. (2015). Cyclic electron flow provides acclimatory plasticity for the photosynthetic machinery under various environmental conditions and developmental stages. In *Frontiers in Plant Science* (Vol. 6). <https://www.frontiersin.org/articles/10.3389/fpls.2015.00800>
- Surek, B., Heilbronn, A., Austen, A., & Latzko, E. (1985). Purification and characterization of phosphoribulokinase from wheat leaves. *Planta*, *165*, 507–512.

- Tabita, F. R. (1988). Molecular and cellular regulation of autotrophic carbon dioxide fixation in microorganisms. *Microbiological Reviews*, *52*(2), 155–189.
- Tagliani, A., Rossi, J., Marchand, C. H., De Mia, M., Tedesco, D., Gurrieri, L., Meloni, M., Falini, G., Trost, P., Lemaire, S. D., Fermani, S., & Zaffagnini, M. (2021). Structural and functional insights into nitrosogluthione reductase from *Chlamydomonas reinhardtii*. *Redox Biology*, *38*(November 2020). <https://doi.org/10.1016/j.redox.2020.101806>
- Thieulin-pardo, G., Lignon, S., & Gontero, B. (2015). *Molecular BioSystems Phosphoribulokinase from Chlamydomonas reinhardtii : a Benson – Calvin cycle enzyme enslaved to its cysteine residues*. *14*, 1134–1145. <https://doi.org/10.1039/c5mb00035a>
- Thompson, C. E., Freitas, L. B., & Salzano, F. M. (2018). Molecular evolution and functional divergence of alcohol dehydrogenases in animals, fungi and plants. *Genetics and Molecular Biology*, *41*(1), 341–354. <https://doi.org/10.1590/1678-4685-GMB-2017-0047>
- Thomson, C. J., & Greenway, H. (1991). Metabolic Evidence for Stelar Anoxia in Maize Roots Exposed to Low O<sub>2</sub> Concentrations 1. *Plant Physiology*, *96*(4), 1294–1301. <https://doi.org/10.1104/pp.96.4.1294>
- Tichá, T., Lochman, J., Činčalová, L., Luhová, L., & Petřivalský, M. (2017). Redox regulation of plant S-nitrosogluthione reductase activity through post-translational modifications of cysteine residues. *Biochemical and Biophysical Research Communications*, *494*(1), 27–33. <https://doi.org/https://doi.org/10.1016/j.bbrc.2017.10.090>
- Tilman, D., & Clark, M. (2015). Food, Agriculture & the Environment: Can We Feed the World & Save the Earth? *Daedalus*, *144*(4), 8–23. [https://doi.org/10.1162/DAED\\_a\\_00350](https://doi.org/10.1162/DAED_a_00350)
- Treffon, P., Rossi, J., Gabellini, G., Trost, P., Zaffagnini, M., & Vierling, E. (2021). Quantitative proteome profiling of a S-nitrosogluthione reductase (GSNOR) null mutant reveals a new class of enzymes involved in nitric oxide homeostasis in plants. *Frontiers in Plant Science*, *12*, 787435.
- Trost, P., Fermani, S., Calvaresi, M., & Zaffagnini, M. (2017). Biochemical basis of sulphenomics: how protein sulphenic acids may be stabilized by the protein microenvironment. *Plant Cell and Environment*, *40*(4), 483–490. <https://doi.org/10.1111/pce.12791>
- Ventura, I., Brunello, L., Iacopino, S., Valeri, M. C., Novi, G., Dornbusch, T., Perata, P., & Loreti, E. (2020). Arabidopsis phenotyping reveals the importance of alcohol dehydrogenase and pyruvate decarboxylase for aerobic plant growth. *Scientific Reports*, *10*(1), 16669. <https://doi.org/10.1038/s41598-020-73704-x>
- Wadano, A., Kamata, Y., Iwaki, T., Nishikawa, K., & Hirahashi, T. (1995). Purification and characterization of phosphoribulokinase from the cyanobacterium *Synechococcus* PCC7942. *Plant and Cell Physiology*, *36*(7), 1381–1385.
- Weits, D. A., Kunkowska, A. B., Kamps, N. C. W., Portz, K. M. S., Packbier, N. K., Nemeč Venzá, Z., Gaillochet, C., Lohmann, J. U., Pedersen, O., & van Dongen, J. T. (2019). An apical hypoxic niche sets the pace of shoot meristem activity. *Nature*, *569*(7758), 714–717.
- Williamson, D. H., Lund, P., & Krebs, H. A. (1967). The redox state of free nicotinamide-adenine dinucleotide in the cytoplasm and mitochondria of rat liver. *Biochemical Journal*, *103*(2), 514–527. <https://doi.org/10.1042/bj1030514>

- Winkler, M., Hemschemeier, A., Jacobs, J., Stripp, S., & Happe, T. (2010). Multiple ferredoxin isoforms in *Chlamydomonas reinhardtii* – Their role under stress conditions and biotechnological implications. *European Journal of Cell Biology*, *89*(12), 998–1004. <https://doi.org/https://doi.org/10.1016/j.ejcb.2010.06.018>
- Yu, A., Xie, Y., Pan, X., Zhang, H., Cao, P., Su, X., Chang, W., & Li, M. (2020). Photosynthetic Phosphoribulokinase Structures: Enzymatic Mechanisms and the Redox Regulation of the Calvin-Benson-Bassham Cycle[OPEN]. *The Plant Cell*, *32*(5), 1556–1573. <https://doi.org/10.1105/tpc.19.00642>
- Zaffagnini, M., Bedhomme, M., Groni, H., Marchand, C. H., Puppo, C., Gontero, B., Cassier-Chauvat, C., Decottignies, P., & Lemaire, S. D. (2012). Glutathionylation in the Photosynthetic Model Organism *Chlamydomonas reinhardtii*: A Proteomic Survey\*. *Molecular & Cellular Proteomics*, *11*(2), M111.014142. <https://doi.org/https://doi.org/10.1074/mcp.M111.014142>
- Zaffagnini, M., De Mia, M., Morisse, S., Di Giacinto, N., Marchand, C. H., Maes, A., Lemaire, S. D., & Trost, P. (2016). Protein S-nitrosylation in photosynthetic organisms: A comprehensive overview with future perspectives. *Biochimica et Biophysica Acta (BBA) - Proteins and Proteomics*, *1864*(8), 952–966. <https://doi.org/https://doi.org/10.1016/j.bbapap.2016.02.006>
- Zaffagnini, M., Fermani, S., Calvaresi, M., Orrù, R., Iommarini, L., Sparla, F., Falini, G., Bottoni, A., & Trost, P. (2016). Tuning Cysteine Reactivity and Sulfenic Acid Stability by Protein Microenvironment in Glyceraldehyde-3-Phosphate Dehydrogenases of *Arabidopsis thaliana*. *Antioxidants and Redox Signaling*, *24*(9), 502–517. <https://doi.org/10.1089/ars.2015.6417>
- Zaffagnini, M., Fermani, S., Marchand, C. H., Costa, A., Sparla, F., Rouhier, N., Geigenberger, P., Lemaire, S. D., & Trost, P. (2019). Redox Homeostasis in Photosynthetic Organisms: Novel and Established Thiol-Based Molecular Mechanisms. *Antioxidants and Redox Signaling*, *31*(3), 155–210. <https://doi.org/10.1089/ars.2018.7617>
- Zaffagnini, M., Morisse, S., Bedhomme, M., Marchand, C. H., Festa, M., Rouhier, N., Lemaire, S. D., & Trost, P. (2013). Mechanisms of nitrosylation and denitrosylation of cytoplasmic glyceraldehyde-3-phosphate dehydrogenase from *Arabidopsis thaliana*. *Journal of Biological Chemistry*, *288*(31), 22777–22789.
- Zemojtel, T., Fröhlich, A., Palmieri, M. C., Kolanczyk, M., Mikula, I., Wyrwicz, L. S., Wanker, E. E., Mundlos, S., Vingron, M., Martasek, P., & Durner, J. (2006). Plant nitric oxide synthase: a never-ending story? *Trends in Plant Science*, *11*(11), 524–525. <https://doi.org/10.1016/j.tplants.2006.09.008>
- Zhou, J.-Y., Hao, D.-L., & Yang, G.-Z. (2021). Regulation of Cytosolic pH: The Contributions of Plant Plasma Membrane H<sup>+</sup>-ATPases and Multiple Transporters. In *International Journal of Molecular Sciences* (Vol. 22, Issue 23). <https://doi.org/10.3390/ijms222312998>

## Conclusions

Photosynthesis is a complex biological process characterized by the integration of a photochemical phase and a metabolic phase, resulting in the conversion of electromagnetic energy into chemical energy. The photochemical phase involves a linear electron flow (LEF), wherein electrons are transferred from the primary electron donor, H<sub>2</sub>O, oxidized at the level of photosystem II (PSII), to the terminal electron acceptor, NADP<sup>+</sup>, which undergoes reduction at the acceptor side of photosystem I (PSI). The metabolic phase of photosynthesis is represented by the Calvin-Benson-Bassham (CBB) cycle, a pathway ensuring most of the entry of inorganic carbon (*i.e.*, carbon dioxide CO<sub>2</sub>), into the Earth's biosphere, providing carbon skeletons essential for all biological reactions.

Notably, photosynthesis is a tightly regulated process. Sophisticated mechanisms are requisite to maintain the balance between the two phases, ensuring redox homeostasis. Furthermore, the functionality of both photochemical and metabolic phases must adapt to a dynamic environment characterized by fluctuations in light intensity and timing, temperature, water availability, or the occurrence of stressful conditions. In fact, each environmental variable can represent a sub-optimal constrain for a particular photosynthetic step, requiring a subsequent tuning of the other components of the process. For this reason, the photochemical phase includes alternative pathways of electron transport acting as regulatory valves to optimize the stoichiometry of ATP and NADPH required for efficient carbon fixation. Concerning the CBB cycle, the main established regulatory mechanisms depend on cysteine-based redox post-translational modifications (PTMs).

World population is increasing together with the demand of food, feed, energy. For this reason, agronomic techniques must adapt accordingly to enhance productivity while limiting the consume of natural resources. It has been demonstrated that energy conversion, intended as the capacity of photosynthetic organisms to convert solar energy into biomass, is the agronomic determinant with the greatest leeway for improvement. Limitations for energy conversion can be directly attributed to kinetic bottlenecks within the CBB cycle since its slow turnover leads to overreduction of the photosynthetic electron transfer with consequent dissipation of excess solar energy. To date, most research efforts have focused on the carbon-fixing enzyme ribulose-1,5-bisphosphate carboxylase/oxygenase (Rubisco), considered as the major CBB cycle

limiting step. However, CBB cycle is co-limited by the phase of regeneration of the substrate for Rubisco (*i.e.*, ribulose-1,5-bisphosphate, RuBP), as demonstrated by several attempts of overexpression of specific enzymes such as fructose-1,6-bisphosphatase (FBPase) and sedoheptulose-1,7-bisphosphatase (SBPase), leading to an increased photosynthetic efficiency (Simkin et al., 2019). However, the identification of the steps retaining major metabolic control is far from being elucidated. This goal is particularly tricky if we consider that metabolic constraints may change accordingly to many environmental variables. For this reason, bioinformatic and modeling approaches are crucial to dissect the dynamic behavior of the CBB-cycle-system, representing a powerful tool for addressing future biotechnological efforts. In this context, obtaining a comprehensive dataset encompassing the biochemical and regulatory characteristics of all relevant enzymes, coupled with high-throughput metabolomic analyses, is imperative to ensure the reliability and utility of modeling approaches. In this regard, the significance of fundamental research becomes evident.

This part of my thesis project is focused on the study of three enzymes participating in the CBB-cycle of the green microalga *Chlamydomonas reinhardtii*, considered as a robust model system for the study of photosynthesis. The study of each enzyme was tackled by following different approaches in the attempt to address different scientific questions.

The first case study (**Chapter I**) regards the investigation of the molecular mechanisms involved in the S-nitrosylation of the CBB cycle enzyme glyceraldehyde-3-phosphate dehydrogenase (GAPDH) from *C. reinhardtii* (CrGAPA). This enzyme was previously identified through proteomic approaches as a target of S-nitrosylation, which represents an important redox modification able to control multiple cellular processes. In this work we demonstrated that nitrosoglutathione (GSNO), one of the main cellular nitric oxide releasing compounds, is able to mediate S-nitrosylation of GAPDH, causing the reversible inhibition of enzyme activity. The subsequent combination of biochemical, structural, and computational approaches allowed the identification of the structural determinants controlling GSNO binding and reactivity. Moreover, the molecular mechanisms underlying the GSNO-dependent oxidation of plant GAPDH were dissected. Thanks to these analyses, we were able to pinpoint key protein residues in the determination of the redox sensitivity of CrGAPA to GSNO-dependent S-nitrosylation and their relative contribution in modulating the activation barrier of the trans-nitrosylation reaction. Notably, although a great number of S-nitrosylation targets have been identified, some of which have been biochemically confirmed, little is known about

the mechanistic features of this redox modification. To this regard, the approach presented in this work could help expanding this investigation.

The second part of my work (**Chapter II**) regards a morpho-functional study of the CBB cycle enzyme ribulose-5-phosphate epimerase from *C. reinhardtii* (CrRPE), by following primarily an *in vitro* approach aimed at the characterization of the recombinant enzyme. The definition of the enzyme structural determinants together with a thorough biochemical investigation permitted to gain insights into the structure-function relationship. Being an amphibolic enzyme participating both in the CBB cycle and in the pentose phosphate pathway, RPE can bidirectionally catalyze its reaction. However, the kinetic analysis we carried out demonstrated that the enzyme does not retain a catalytic propensity for a reaction over the other, suggesting that in the cellular context the catalytic direction depends on the relative concentration of substrates. Considering that CrRPE was identified as a putative target of multiple thiol-based redox modifications, we evaluated the possible modulation of its catalysis mediated by redox-modifying molecules. No change in RPE activity was found, although other possible outcomes of redox modifications (*e.g.*, regulation of protein interactions with other macromolecules, change in protein localization) cannot be excluded and requires future investigations. Finally, phosphorylation sites in the proximity of the active site were identified, but further analyses are needed to uncover their possible physiological meaning.

As already mentioned, our understanding of the critical bottleneck in the CBB cycle is still deficient. To this regard, the objective of the following study (**Chapter III**) was to figure out whether the enzymatic step catalyzed by the enzyme phosphoribulokinase (PRK) in *C. reinhardtii* may represent a kinetic bottleneck in the CBB cycle. To this end, we first analyzed and functionally complemented the *knock-out* PRK mutant, confirming the essentiality of this enzyme for photoautotrophic growth. Subsequently, we employed synthetic approaches to generate *Chlamydomonas* mutant lines retaining diverse levels of PRK expression. To figure out the physiological output of differential PRK expression, we correlated the relative accumulation levels of the enzyme to algal growth capacity. Our analysis revealed that, in the conditions tested, overexpression of PRK does not improve *Chlamydomonas* growth. This evidence suggests that the catalytic step catalyzed by PRK may not represent a kinetic bottleneck in CBB cycle. Noteworthy, PRK is subjected to multiple levels of regulation whose mechanisms have been well established by *in vitro* approaches. However, to date little is known about the *in vivo* implications of such regulatory mechanisms and whether there may be conditions under which they can represent a metabolic constraint.

As we all know, climate change imposes new challenges particularly concerning our ability to cultivate food plants in adverse environmental circumstances. Among such conditions, flooding caused by extreme climate events represents a condition increasingly affecting cultivations, fields, and plant yield. In this context, possessing a profound understanding of the physiology of cultivars and model systems could enhance our capability to face future challenges. One of the enzymes with a well-established role in plant adaptation to stress conditions is alcohol dehydrogenase (ADH). This enzyme is involved in the fermentative metabolism, playing a crucial role in plant acclimatization to conditions characterized by oxygen deficiency. In the following research (**Chapter V**), we conducted a functional analysis of ADH from the model plant *Arabidopsis thaliana*. In particular, we focused on the biochemical features dissecting its physiological activity, which involves the NADH-dependent reduction of acetaldehyde (MeCHO). The combination of biochemical and computational analysis permitted us to identify this reaction as both catalytically and thermodynamically favored, as opposed to the ADH-related EtOH oxidation. Furthermore, experiments carried out on *Arabidopsis* protein extracts successfully validated the *in vivo* inducibility of ADH expression and activity upon the occurrence of hypoxic conditions and identified ADH as the sole enzymatic system able to carry out the MeCHO detoxification using NADH as a source of reducing equivalents. Notably, we observed the persistence of ADH even upon the restoration of normoxic conditions following a period of hypoxia. This evidence offers opportunities for future experimental avenues aimed at unraveling the timing of deactivation of the hypoxic response, an intriguing aspect that has so far gathered limited experimental data. Finally, we identified a NADPH-dependent MeCHO detoxification activity in protein extracts, highly dependent on the presence of ADH but also depending, though partially, on other enzymatic players yet to be identified. Our findings reveal that ADH catalysis is not strictly dependent on the use of NAD(H) as a cofactor but rather, it is also able to exploit the reducing power of NADPH. Considering the NADPH/NADH cytosolic ratio as between 3 and 8 (Smith et al., 2021), this alternative ADH catalysis suggests its potential physiological roles beyond ethanolic fermentation, whose discovery calls for new investigations.

Finally, **Chapter IV** consists in a structural-functional comparison between ADH and nitrosogluthathione reductase (GSNOR) from *A. thaliana*, both belonging to the protein superfamily of medium-length dehydrogenase/reductases (MDRs). Like ADH, GSNOR is a crucial enzyme in stress response conditions as it catalyses the NADH-dependent reduction of

nitrosoglutathione (GSNO), the major nitric oxide reservoir of the cell and a trans-nitrosylating agent. This renders GSNOR a key controller of the intracellular levels of protein nitrosothiols. In our research we revealed a nearly identical fold in the 3D-structure of ADH and GSNOR but striking differences in their catalytic behaviour and catalytic-related structural elements. Moreover, starting from an examination of the content, conservation and accessibility of cysteine thiols we evaluated their redox sensitivity and observed similar and prominent redox responsiveness of both of the enzymes to thiol switching mechanisms. Nevertheless, the physiological significance of redox PTMs associated to such thiol switches still requires evaluation. Considering the pivotal physiological roles of ADH and GSNOR, any regulatory mechanism influencing their activities could exert a significant impact on the overall physiological context.